Nucleosynthesis in Stellar Models across Initial Masses and Metallicities and Implications for Chemical Evolution

by

Christian Heiko Ritter
B.Sc., Goethe University Frankfurt, 2011
M.Sc., Goethe University Frankfurt, 2013

A Dissertation Submitted in Partial Fulfillment of the
Requirements for the Degree of

DOCTOR OF PHILOSOPHY

in the Department of Physics and Astronomy

Nucleosynthesis in Stellar Models across Initial Masses and Metallicities and Implications for Chemical Evolution

by

Christian Heiko Ritter
B.Sc., Goethe University Frankfurt, 2011
M.Sc., Goethe University Frankfurt, 2013

Supervisory Committee

Dr. Falk Herwig, Supervisor
(Department of Physics and Astronomy, University of Victoria)

Dr. Kim Venn, Departmental Member
(Department of Physics and Astronomy, University of Victoria)

Dr. Adam Monahan, Outside Member
(School of Earth and Ocean Sciences, University of Victoria)

Dr. Jeremy Heyl, External Member
(Department of Physics and Astronomy, University of British Columbia)

ABSTRACT

Tracing the element enrichment in the Universe requires to understand the element production in stellar models which is not well understood, in particular at low metallicity. In this thesis a variety of nucleosynthesis processes in stellar models across initial masses and metallicities is investigated and their relevance for chemical evolution explored.

Stellar nucleosynthesis is investigated in asymptotic giant branch (AGB) models and massive star models with initial masses between $1\,M_\odot$ and $25\,M_\odot$ for metal fractions of $Z = 0.02, 0.01, 0.006, 0.001, 0.0001$. A yield grid with elements from H to Bi is calculated. It serves as an input for chemical evolution simulations. AGB models are computed towards the end of the AGB phase and massive star models are calculated until core collapse followed by explosive core-collapse nucleosynthesis. The simulations include convective boundary mixing in all AGB star models and feature efficient hot-bottom burning and hot dredge-up in AGB models as well the predictions of both heavy elements and CNO species under hot-bottom burning conditions. H-ingestion events in the low-mass low-Z AGB model with initial mass of $1\,M_\odot$ at $Z = 0.0001$ result in the production of large amounts of heavy elements. In super-AGB models H ingestion could potentially lead to the intermediate neutron-capture process.

To model the chemical enrichment and feedback of simple stellar populations in hydrodynamic simulations and semi-analytic models of galaxy formation the SYGMA module is created and its functionality is verified through a comparison with a widely adopted code. A comparison of ejecta of simple stellar populations based on yields of this work with a commonly adopted yield set shows up to a factor of 3.5 and 4.8 less C and N enrichment from AGB stars at low metallicity which is attributed to complete stellar models, the modeling of the AGB stage and hot-bottom burning in super-AGB stars. Analysis of two different core-collapse supernova fallback prescriptions show that the total amount of Fe enrichment by massive stars differs by up to two at $Z = 0.02$.

Insights into the chemical evolution at very low metallicity as motivated by the observations of extremely metal poor stars require to understand the H-ingestion events common in stellar models of low metallicity. The occurrence of H ingestion events in super-AGB stars is investigated and identified as a possible site for the production of heavy elements through the intermediate neutron capture process. The peculiar abundance of some C-Enhanced Metal Poor stars are explained with simple

models of the intermediate neutron capture process. Initial efforts to model this heavy element production in 3D hydrodynamic simulations are presented.

For the first time the nucleosynthesis of interacting convective O and C shells in massive star models is investigated in detail. 1D calculations based on input from 3D hydrodynamic simulations of the O shell show that such interactions can boost the production of odd-Z elements P, Cl, K and Sc if large entrainment rates associated with O-C shell merger are assumed. Such shell merger lead in stellar evolution models to overproduction factors beyond 1 dex and p-process overproduction factors above 1 dex for ^{130,132}Ba and heavier isotopes. Chemical evolution models are able to reproduce the Galactic abundance trends of these odd-Z elements if O-C shell merger occur in more than 50% of all massive stars.

Contents

List of Tables

List of Figures

Co-authorship

This thesis has been entirely written by me. All work was done in collaboration with my supervisor Dr. Falk Herwig as well as researchers from various institutions. If a work is presented in depth in a chapter or section and is available in an advanced draft form, submitted or published I provide the references, co-author names and abstract.

I have performed the stellar evolution calculations of AGB models and the post-processing nucleosynthesis calculations of AGB models, massive star models and core-collapse SN explosions in Chapter 2. The stellar evolution simulations of massive stars were performed by Dr. Sam Jones. Post-processing codes and the semi-analytic explosion code are provided by the NuGrid collaboration, in particular by Dr. Marco Pignatari and Dr. Chris Fryer. I have analyzed all the stellar evolution and post-processing nucleosynthesis simulations.

The simple stellar populations code SYGMA was developed by me and I have produced all results up to and including Section 3.2 of Chapter 3. For that purpose I have learned from the GCE code from Dr. Chris Fryer. I have added a continuous star formation rate for SYGMA and with Dr. Benoit Côté I created the galactic chemical evolution code OMEGA which application I summarize (Section 3.3). To foster scientific outreach I have created a website for the codes and developed teaching material.

In Chapter 4 I have analyzed the hot-dredge up and H ingestion events in super-AGB models (Section 4.2). In collaboration with the visiting research student Laurent Dardelet we have compared the signatures of CEMP-r/s stars with i-process nucleosynthesis predictions (Section 4.3). I have developed and applied a nucleosynthesis code which post-processes 3D hydrodynamic simulations. The code uses the nucleosynthesis routines of the NuGrid collaboration. I have provided Prof. Paul Woodward with nucleosynthesis modules to be included in the PPMstar code.

I have analyzed the nucleosynthesis in O-C shell merger in Chapter 5. The calculations are based on input from 3D hydrodynamic simulations of massive stars which are performed by Dr. Robert Andrassy. I have investigated the nucleosynthesis in a variety of 1D stellar models and 1D setups and analyzed the impact on Galactic chemical evolution.

ACKNOWLEDGEMENTS

In contrast to the early days of scientific work today scientific break throughs are rarely made without support and deep insight provided by scientific collaborators. I would like to thank my supervisor Dr. Falk Herwig whose dedication, patience and advice guided me towards a deeper understanding of science. I appreciate the feedback of my supervisory committee Dr. Kim Venn, Dr. Adam Monahan, and the external member Dr. J. Heyl which improved this thesis.

I value especially the collaboration with Dr. Benoit Côté who I consider a close friend and mentor. I value the friendships with many members of the NuGrid collaboration, in particular Dr. Marco Pignatari, Dr. Sam Jones, Dr. Raphael Hirschi and Dr. Reto Trappitsch. I am thankful to Dr. Robert Andrassy who provided me with insights into stellar hydrodynamics and Dr. Pavel Denisenkov for advice and encouragement.

I would also thank my previous supervisor Prof. Dr. René Reifarth for his guidance through my B.Sc. and M.Sc. and towards the PhD at the University of Victoria.

Thanks to all my fellow Astronomy students with whom I share a bond of friendship, in particular my office mates Azadeh Fattahi, Kyle Oman, Connor Bottrell and Austin Davis. I enjoyed the company of Mike Chen, Clare Higgs, Masen Lamb, Sébastien Lavoie, Trystyn Berg and Ondrea Clarkson. I appreciate the advice and orientation provided by Cory Shankman.

I would like to thank the NiteShifters Toastmasters team including Muyang Zhong and Marius Miklea for being great mentors. I am grateful to my friends David Guo and Lichen Liang.

Finally I would like to thank my wife Xiwen Wang for her love and for sharing both, the good and bad sides our life. I appreciate my brother Nicolas Ritter for being a great brother. I am most in depth to my parents who supported my own decisions and let me go on my own journey to explore and experience. Thank you for your sacrifices.

DEDICATION

To all my family, near and far.

Chapter 1

Introduction

Ten years after Hans Bethe proposal of fusion inside stars in 1939 Chamberlain and Aller (1951) observed differences in the surface abundance of stars. Stars are indeed producer of elements and therefore do not exhibit the same chemical composition! Hoyle (1954) explained that stars of many generations pollute the interstellar medium leading to a continuous enrichment of gas in the Universe, called chemical evolution. The amount of enrichment is characterized by the term metallicity or metal mass fraction Z where metals are in the astronomy jargon all elements heavier than helium.

Stellar nucleosynthesis theory made an enormous step forward with the work by Burbidge et al. (1957) which outlines many nuclear processes responsible for nucleosynthesis which were confirmed through observations in the following decades. In the 1960s computer were able to simulate stellar evolution and reaction networks during the main sequence phase (Henyey, Forbes, and Gould 1964) and with different initial compositions such as $Z = 0$ (Ezer 1961). Since then more complex models allowed to simulate the advanced stages of stellar evolution and the prediction of the element production in stellar models of various initial masses and compositions (e.g. Woosley, Heger, and Weaver 2002; Herwig 2005).

The observation of many metal-poor stars led Eggen, Lynden-Bell, and Sandage (1962) to propose a correlation between metallicity and eccentricity, pointing to the halo as the origin of many metal-poor stars. During the formation of large structures such as the Milky Way element synthesis and mixing have lead to distinct metal enrichment of different sites. One has to understand the interplay of many generations of stars in conjunction with galactic structural evolution to understand the observed abundances observed in stars of different age. Hence galactic chemical evolution models were developed from simple 1-zone closed-box models (Schmidt 1963;

Timmes, Woosley, and Weaver 1995) to sophisticated 3D hydrodynamic cosmological simulations with gas and dark matter (e.g. Schaye et al. 2015).

Complementary, large-scale spectroscopic surveys such as the HK survey (Beers, Preston, and Shectman 1985) and the Hamburg/ESO survey (Christlieb et al. 2008) provide a wealth of observational data, including the stellar abundance of metal-poor stars, which help to constrain the chemical evolution of the Milky Way and small systems such as dwarf galaxies and globular clusters (e.g. Venn et al. 2012).

1.1 Motivation and goals

Despite the immense comprehensive amount of knowledge of stellar nucleosynthesis an investigation across the wide initial mass and metallicity range is still missing and pursued in this work. I outline the problems and specific goals of this thesis in Section 1.1 and introduce the basics of stellar nucleosynthesis in Section 1.2 and chemical evolution in Section 1.3.

1.1.1 Stellar yields

The ejecta of stars, the stellar yield, have been calculated by various groups since the early stage of stellar evolution modeling. Because stellar evolution depends crucially on initial mass (Fig. 1.1) AGB yields and massive star yields are often published by separate groups.

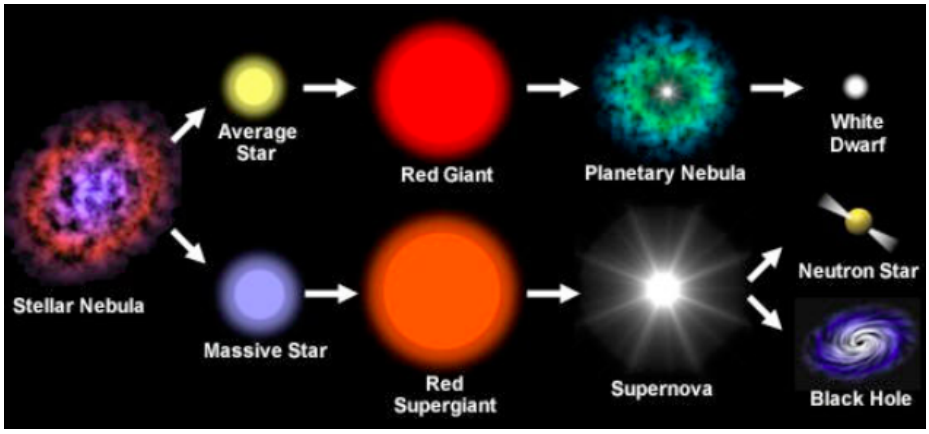

Figure 1.1: Stages of stellar evolution for low- and intermediate-mass stars (top) and massive stars (bottom) pictured by an artist. Figure adopted from seasky.org.

Those yield sets differ in nuclear physics. The revision of cross sections, for example due to new experimental measurements, can have a strong impact on stellar structure and final yields (Herwig and Austin 2004) which makes yield calculations based on the same nuclear reactions necessary. Model assumptions such as mass loss, mixing processes at convective boundaries and fallback in core-collapse supernova have a strong impact on stellar evolution and often differ between sets.

The difference in published massive star yields are analyzed in Gibson (2002) and for AGB yields in Tosi (2007). Recently, Romano et al. (2010) compared the impact of yield set combinations on Galactic chemical evolution and found large differences such as of ≈0.5 dex for [C/O] (Fig. 1.2). Their recommended set includes yields

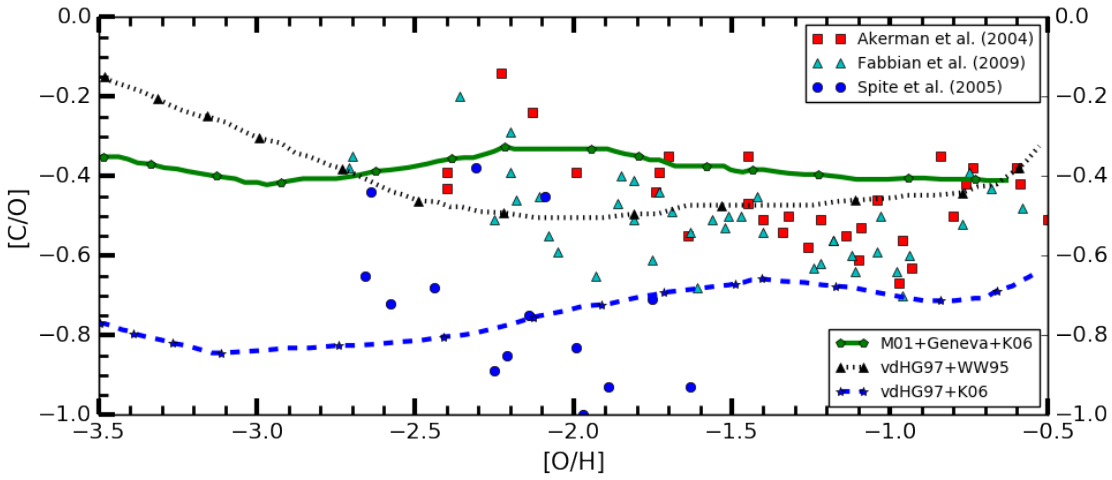

Figure 1.2: Predicted chemical evolution trends of [C/O] for three yield set combinations in comparison with Galactic halo stars. Observational data from Spite et al. (2005), Fabbian et al. (2009), Akerman et al. (2004) is plotted with STELLAB (Section 3.3). Chemical evolution data is extracted from Romano et al. (2010) and for details about the yield sets see Section 2.1.

from Marigo (2001a), the Geneva group (Hirschi, Meynet, and Maeder 2005a) and (Kobayashi et al. 2006). The impact of the different assumptions are nearly impossible to quantify and Tosi (2007) demand for chemical evolution an *optimal* set of yields containing all major isotopes and which includes the whole range of stellar masses and many metallicities.

The Padua group has published the most recent complete self-consistent yield set of AGB and massive stars in Portinari, Chiosi, and Bressan (1998) and Marigo (2001a). Drawbacks of this set are that AGB models are not based on full stellar

evolution simulations ('synthetic models'), the explosion yields are not consistent (based on yields by Woosley and Weaver 1995) and they include only isotopes up to Fe. Additionally, they apply now out-dated nuclear physics. Because of the lack of alternatives these yields are still in use (e.g. in Vogelsberger et al. 2013; Yates et al. 2013). My goal is to provide stellar yields of AGB models and massive star models for chemical evolution simulations based on consistent nuclear physics, the same model assumptions and for isotopes and elements up to Bi (Chapter 2).

1.1.2 Chemical evolution

By the end of the 1970s it was clear that dark matter (halos) play an important role in the formation of galaxies. Dark matter was applied in cosmological simulations since the early 1990s (Mo, van den Bosch, and White 2010). To model the chemical enrichment in galaxies by taking into account gas and dark matter as well as inhomogeneous mixing cosmological hydrodynamical simulation are employed (e.g. EAGLE and Illustris simulations Schaye et al. 2015; Vogelsberger et al. 2014). Such simulations include the three components dark matter, gas and stars which make them computational expensive (Fig. 1.3). Other strategies are semi-analytic models

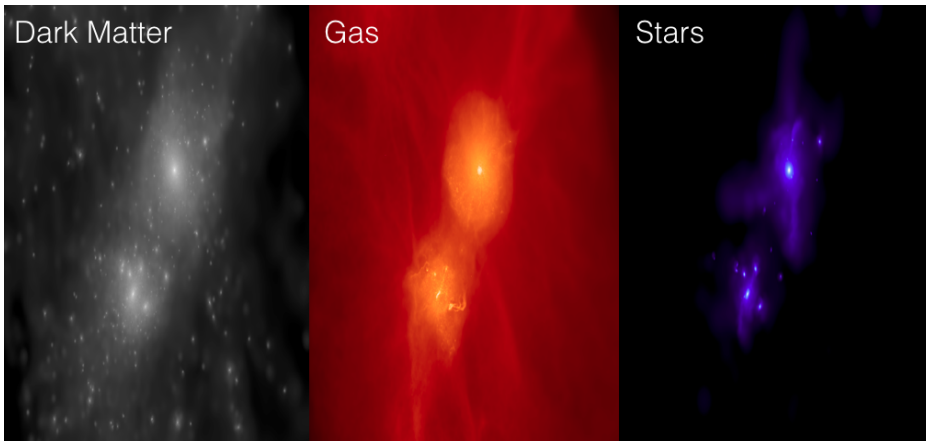

Figure 1.3: Stars, gas and dark matter in a cosmological hydrodynamical simulation of the Local-Group environment (Fattahi et al. 2016; Sawala et al. 2016).

which post-process dark matter N-body simulations. This is used to follow chemical enrichment on smaller, galactic scales (e.g. recent work by Côté, Martel, and Drissen 2013; Crosby et al. 2013).

To model chemical enrichment in such simulations a gas (star) particle returns stellar ejecta over time. These star particles are treated as a simple stellar population

and their ejecta need to be pre-calculated and provided as an input. Codes to calculate those ejecta are not publicly available which makes it challenging to reproduce their results. Furthermore they often provide limited choice of stellar evolution parameters such as the initial mass function. Additionally, those codes typically do not include exotic sources such as neutron-star (NS) mergers required to trace r-process enrichment (Wiersma et al. 2009).

Usually only a small number of elements up to Fe are followed in simulations with dark matter and gas which affect the efficiency of radiative gas cooling (Scannapieco et al. 2005). Very recently heavy elements are included (e.g. Shen et al. 2015) and SSP ejecta for heavier elements are required. SSP ejecta of all elements would provide strong constraints for comparison with observations.

To model the chemical enrichment in chemical evolution simulations, my aim is to provide an open-source code which allows to compute the ejecta of SSPs and other stellar parameter (Chapter 3). Various chemical evolution assumptions should be provided for specific applications and any yield sets should be handled, including my yield set with elements up to Bi (Chapter 2).

1.1.3 Reactive-convective nucleosynthesis

AGB stars

Large Galactic surveys allow to find stars at lower and lower metallicity with the currently lowest measured value of [Fe/H] below -7.1 (Keller et al. 2014). Those observations motivate to investigate stellar models down to extreme low and zero metallicity. Such stellar evolution simulations reveal H ingestion in He-burning zones in low and zero-metallicity AGB stars (Fujimoto, Ikeda, and Iben 2000), in He-core flashes in low-Z low-mass stars (Campbell, Lugaro, and Karakas 2010) and in very late thermal pulses of post-AGB stars (Herwig et al. 2011).

The ingested H burns on the same time scale as it is mixed and its burning affects the fluid flow. 3D hydrodynamic simulations of H ingestion in the post-AGB star Sakurai's object show that such a reactive-convective regime cannot be properly described with the mixing length theory and the assumption of spherically symmetry, both applied in stellar evolution models Herwig et al. (2011), Herwig et al. (2014), and Woodward, Herwig, and Lin (2015).

Herwig et al. (2011) found that the H ingestion peculiar nucleosynthesis and the production of heavy elements via a intermediate neutron-capture (i) process (Fig. 1.5).

In recent years a number of observations require the i process to explain abundance signatures. Those include open-cluster stars Mishenina et al. (2015), low-Z post-AGB stars in the Magellanic clouds Lugaro et al. (2015), low-metallicity stars (Roederer et al. 2016) as well as pre-solar grains (Jadhav et al. 2013; Fujiya et al. 2013) Those observations have not been connected to any site and Sakurai's object remains the only confirmed site.

Previous studies used 1-zone and 1D approximations of i-process nucleosynthesis while reliable predictions require comprehensive nucleosynthesis in 3D hydrodynamic simulations which is currently not computationally feasible. I aim to develop an approach to handle large networks in hydrodynamic simulations to provide accurate predicitons of i-process nucleosynthesis in 3D.

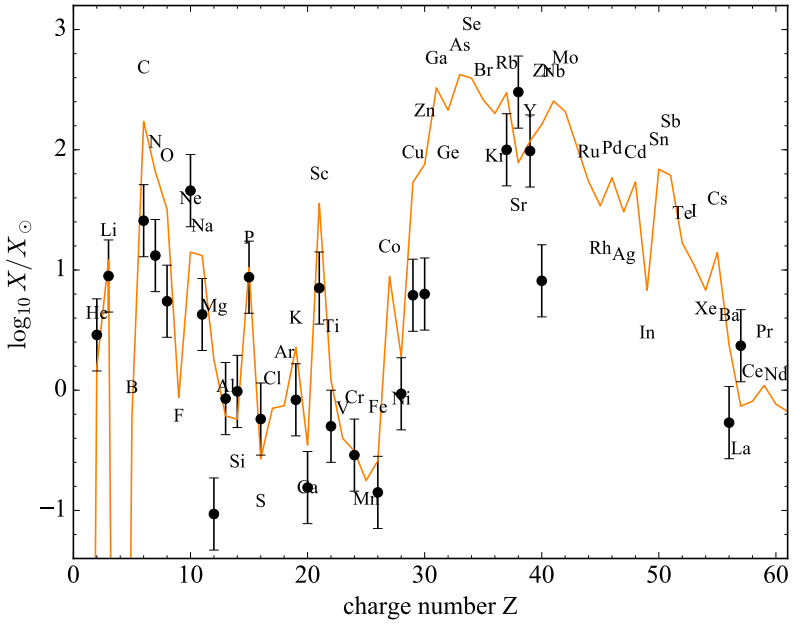

Figure 1.4: i-process nucleosynthesis predictions (line) based on the H ingestion in a AGB star model in comparison with observational data of Sakurai's object as in Herwig et al. (2011).

Massive stars

In shell O burning of massive star evolution the nuclear burning time scales and convective turnover time scale become comparable which requires multi-D hydrodynamic simulations (Bazan and Arnett 1994). Similar to H ingestion into a He-burning shell

in AGB models the ingestion of C-shell material into the convective O shell in massive star models may lead to a convective-reactive regime.

Meakin and Arnett (2006a) investigated the interaction of the C shell and O shell with 2D hydrodynamic simulations and suggested that the ingestion of C shell material into the O shell could rapidly transition into a situation with accerating entrainment rates. With increasing entrainment rates both shells could merge. Hydrodynamic simulations of the O shell showed that the entrainment processes require 3D models (Jones et al. 2016c).

O-C shell mergers in stellar models have been mentioned in passing in the literature (Rauscher et al. 2002; Tur, Heger, and Austin 2007). But neither the nucleosynthesis nor the hydrodynamic processes of such shell mergers have been investigated in detail in part due to the computational limitations. Large networks are needed to follow the nucleosynthesis in the O shell and C shell and are not computationally feasible in 3D hydrodynamic simulations. I plan to get insight into the nucleosynthesis of O-C shell merger with 3D hydrodynamic simulations and a 3D-1D approach to compute the comprehensive nucleosynthesis. To estimate the impact on the Galactic production I aim to apply my galactic chemical evolution model (Chapter 3).

I will present an introduction to stellar evolution and nucleosynthesis in Section 1.2. The principles of element evolution on larger scales, the galactic chemical evolution, is explained in Section 1.3. A short overview over stellar hydrodynamics is provided in Section 1.2.4.

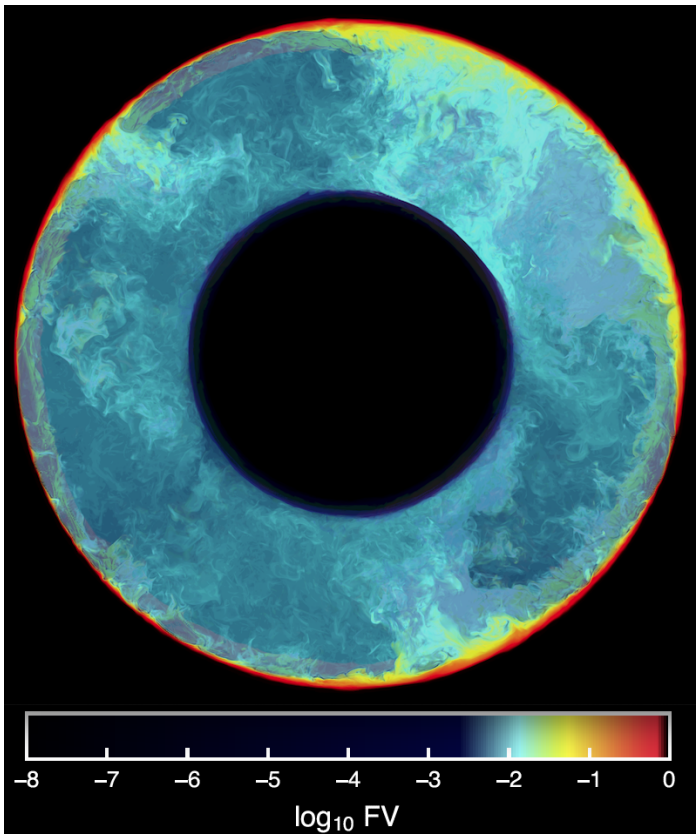

Figure 1.5: Fractional volume of entrained C-shell fluid in sphere slice after 1.67 min of entrainment in a hydrodynamic simulation of the O shell of Jones et al. (2016c). The large-scale plumes of downflows indicate the divergence from spherical symmetry and the necessity for 3D simulations.

1.2 Stellar nucleosynthesis

1.2.1 Stellar modeling

The simulation of a star is a complex multi-physics problem in 3D which spans extremely short and long time and space scales. A variety of simplifications are applied to allow the modeling of most stellar phases and are, in part, related to the involved time scales. The following time scales and basic equations are from Kippenhahn and Weigert (1990).

The Kelvin-Helmoltz time-scale τ_{KH} is the time it would take to radiate away all gravitational energy and is defined as

$$\tau_{KH} = \frac{|E_g|}{L} \approx \frac{GM^2}{2R} \tag{1.1}$$

where E_g is the gravitational energy, L is the energy radiated away (luminosity). G is the gravitational constant, R the radius and M the mass. The nuclear time scale τ_n is the time it would take to radiate away all the energy available through nuclear reactions E_n and is defined as

$$\tau_n = \frac{E_n}{L}. \tag{1.2}$$

To estimate the time until a perturbation in a stellar model reaches hydrostatic equilibrium the hydrostatic (dynamic) time scale τ_{hydro} is derived in Kippenhahn and Weigert (1990) as

$$\tau_{hydro} \approx (\frac{R^3}{GM})^{1/2}. \tag{1.3}$$

The assumption of spherically symmetry allows to describe the stellar model in 1D. In hydrostatic equilibrium which is assumed during stellar evolution $\tau_{KH} \gg \tau_{hydro}$ and $\tau_n \gg \tau_{hydro}$. Based on these assumptions one can derive the structure equations Eq. 1.5 and 1.6 where r and m are the radial coordinate and mass coordinate, respectively. ρ is the density, P the pressure and G the gravitational constant.

To model the energy transport under the assumption of $\tau_n \gg \tau_{KH}$ the energy equation can be written as Eq. 1.7 where ϵ_n is the energy release due to nuclear reactions and ϵ_ν is the energy lost due to neutrinos. The energy transport and the temperature gradient depend on the the properties of the layer such as the convective stability. The temperature gradient $\Delta = dlnT/dlnP$ is set with Eq. 1.8 where T is the temperature and P is the pressure. Δ_{rad} is in radiative layers given as

$$\Delta_{rad} = \frac{dlnT}{dlnP}|_{rad} = \frac{3}{16\pi acG}\frac{\kappa LP}{mT^4} \tag{1.4}$$

and for convective layers derived from the mixing theory applied in the stellar model (Böhm-Vitense 1958). a is the radiation-density constant, c is the velocity of light and G is the gravitational constant.

The change in abundance of species i due to nuclear production reactions r_{ji} and destruction reactions r_{ik} is given through the change of its mass fraction X_i in Eq. 1.9. The indices j and k span all N relevant nuclei.

$$\frac{dr}{dm} = \frac{1}{4\pi r^2 \rho}, \tag{1.5}$$

$$\frac{dP}{dm} = -\frac{Gm}{4\pi r^4}, \tag{1.6}$$

$$\frac{dL}{dm} = \epsilon_n - \epsilon_\nu \tag{1.7}$$

$$\frac{dT}{dm} = -\frac{GmT}{4\pi r^4 P}\Delta, \tag{1.8}$$

$$\frac{dX_i}{dt} = \frac{m_i}{\rho}\sum_j r_{ji} - \sum_k r_{ik} \tag{1.9}$$

Variables in the basic equations Eq. 1.5 to Eq. 1.9 are related through additional quantities such as the equation of state $\sigma(P, T, X_i)$.

1.2.2 Stellar phases

Stellar evolution can be separated in distinct phases according to stellar characteristics which depend on the initial mass of the stellar model and to lesser extent on its metallicity. Stellar models above $0.08\,\mathrm{M}_\odot$ ignite H in their center at $T \approx 10^7$ K (Kippenhahn and Weigert 1990) and evolve to the main sequence (MS, Fig. 1.6). The latter is the longest burning phase of their evolution (Table 1.1).

RGB stars

After exhaustion of central H the core shrinks and H burning starts in a shell surrounding the core. The envelope expands due to shell burning and low-mass and intermediate mass stars with masses below $\approx 8\,\mathrm{M}_\odot$ evolve into red giants (Fig. 1.6). Stars above this threshold mass are classified as massive stars and they evolve into supergiants (Fig. 1.7).

Horizontal branch

The growing H-free core becomes highly degenerate in low-mass models with initial masses above $\approx 0.8\,\mathrm{M}_\odot$ and below $\approx 1.8\,\mathrm{M}_\odot$ and central He burning commences in a flash at the tip of the RGB (Fig. 1.6). Core He burning takes place via the triple-alpha reaction at $T \approx 10^8$ K. Lower core densities in stellar models of higher initial mass lead to a slow onset of He burning.

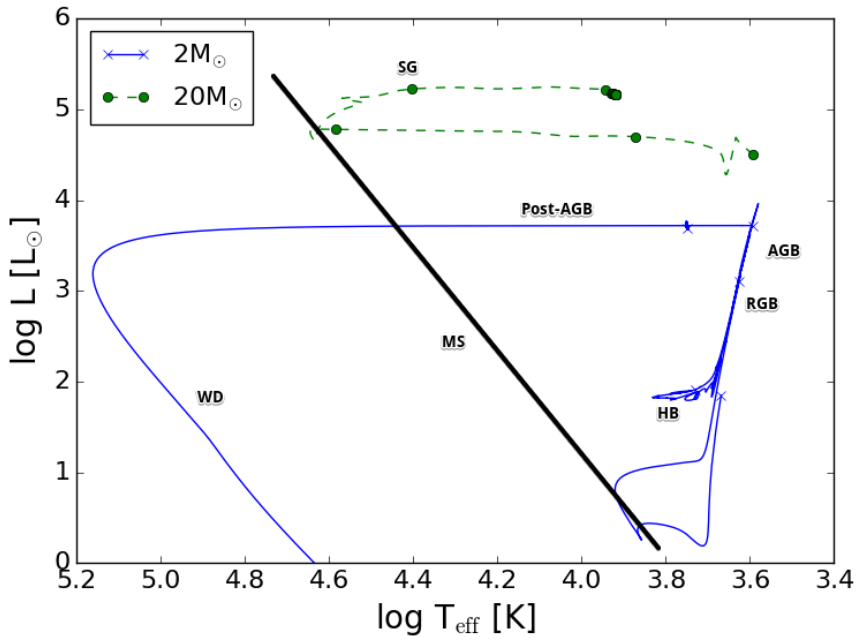

Figure 1.6: Hertzsprung-Russell diagram including the stellar models with initial mass of $2\,M_\odot$ and $20\,M_\odot$ at $Z = 0.0001$. Marked are the stellar phases main sequence (MS, including track populated), horizontal branch (HB), red giant branch (RGB), supergiant (SG), asymptotic giant branch (AGB), post-AGB and white dwarf (WD).

AGB stars

In low-mass models and most intermediate-mass models a degenerate C/O core forms after central He burning (Fig. 1.7). With the alternation of H-shell and He-shell burning these stellar models enter the complex thermal-pulse (TP) asymptotic giant branch (AGB) phase (Fig. 1.6, Herwig 2005; Herwig 2013). In the most massive intermediate-mass models the cores are only partly degenerate which allows C burning and the formation of a O/Ne/Mg core before the onset of the TP-AGB phase (Siess 2010). These stars are referred to as Super-AGB (S-AGB) stars (Fig. 1.7).

Massive stars

After central He burning non-degenerate conditions lead to the onset of central C burning via the ^{12}C-^{12}C reaction at $T \approx 10^9$ K (Woosley, Heger, and Weaver 2002). After exhaustion of C burning proceeds in the surrounding shell and central Ne burning starts via photo-disintegration at $T \approx 1.5 \times 10^9$ K (Thielemann et al. 2011a). In the next stage O is burned via ^{16}O-^{16}O reaction which produces Si. In the last stage

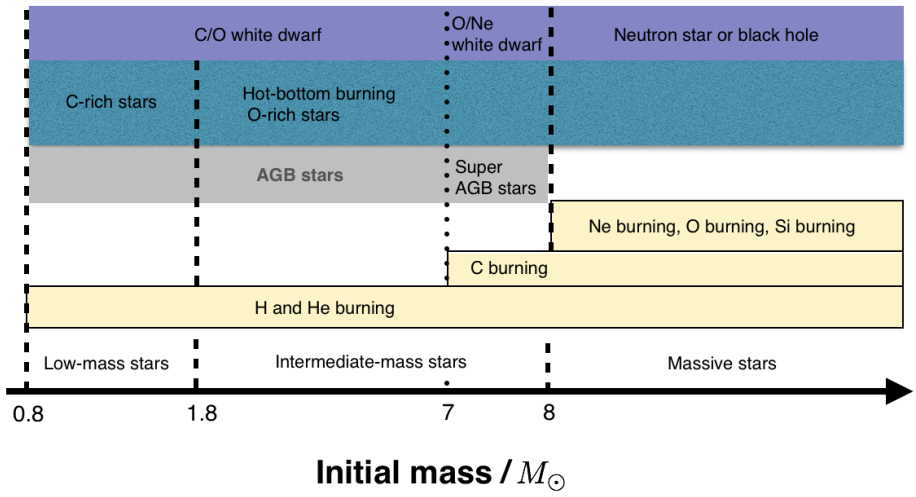

Figure 1.7: Stellar classification similar to Herwig (2005). Distinguished is between the different burning phases, stellar characteristics and the final fates which all depend on metallicity.

Si is burned in the core and shell which leads to the production of large amounts of the Fe-peak elements Cr, Mn, Fe, Co and Ni. In these advanced stages the burning time scales become subsequent shorter due to energy loss via neutrinos. The time scales decrease to months and days in the core while outer layers and stellar surface are frozen out (Table 1.1).

Core-collapse and supernova explosion

With the growth of the Fe core in the massive star model the gravitational force eventually overcomes the degeneracy pressure provided by the electrons. The following collapse is accelerated due to electron capture and/or endoergic photo-disintegration of nuclei which further reduces the pressure (Thielemann et al. 2011a). In some massive stars collapse is halted at extreme nuclear densities of $\approx 10^{14}$ gcm^{-3} due to degeneracy pressure of the neutrons and a proto-neutron star forms. Infalling layers bounce back at the remnant and the reverse shock, if sufficiently energetic, launches a supernova explosion with energies of $\approx 10^{51}$ erg $= 10^{44}$ J (Thielemann et al. 2011a). The high shock temperatures throughout the onion-shell structure of the star allow to synthesize elements on short time scale of seconds which are either ejected or fall back onto the remnant (Arnett 1996). Other stellar models collapse directly to a black hole without neutron star formation and do not ejecta any matter.

Table 1.1: Nuclear burning times Δt of a low-mass stellar model with initial mass of $2\,M_\odot$ and massive star model with initial mass of $20\,M_\odot$ at solar metallicity. Data of the massive star model is taken from Thielemann et al. (2011a).

Burning phase	Δt [yr]
M_{ini}=2 $M_\odot$	
H burning	1.3×10^9
He burning	2.0×10^8
M_{ini}=20 $M_\odot$	
H burning	1.3×10^7
He burning	9.5×10^5
C burning	3.0×10^2
Ne burning	3.8×10^{-1}
O burning	5.0×10^{-1}
Ne burning	5.5×10^{-3}

1.2.3 Nucleosynthesis

Nuclear reactions

Charged-particle reactions are the main source of energy generation in stars and are responsible for the creation of elements up to iron (Iliadis 2007). The endothermic nature of the the fusion of Fe nuclei stops the production of heavier nuclei. Elements beyond Fe are mainly produced through neutron-capture reactions and are separated into the slow neutron capture process (s process, Fig. 1.8) with neutron densities of 10^9 cm^{-3} (Straniero et al. 1995; Gallino et al. 1998) the rapid neutron-capture process (r process) 10^{23} cm^{-3} (Thielemann et al. 2011b). Each process is thought to produce about half the heavy elements up to Bi (Herwig 2005; Heil et al. 2007; Thielemann et al. 2011b). 35 proton-rich isotopes are identified as p nuclei and most of them are produced in the p process (Arnould and Goriely 2003; Pignatari et al. 2016c).

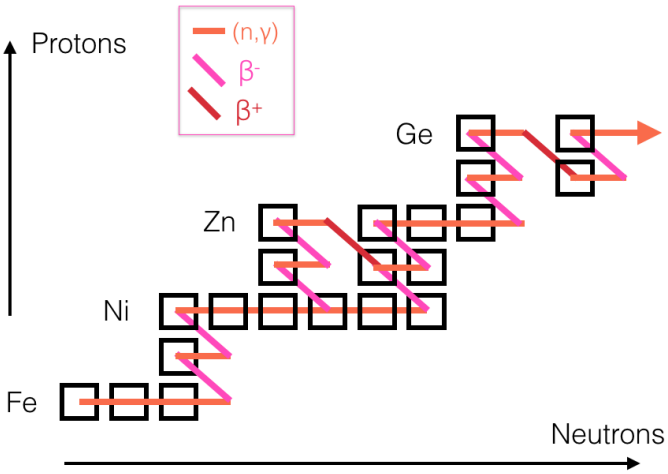

Figure 1.8: Sketch of the s process path in the isotopic chart starting from Fe. It is differentiated between neutron captures, β^- decays and β^+ decays.

To model the thermonuclear reactions the reaction rate per particle pair $< \sigma v >$ is required. It depends on temperature and the cross section of the reaction (Iliadis 2007). For example with $< \sigma v >$ the mean lifetime of a nucleus ^{12}C against destruction through proton capture is calculated with

$$\tau_p(^{12}C) = \frac{1.}{< \sigma v > N_A X(H)\ \rho} \tag{1.10}$$

where $X(H)$ is the mass fraction of hydrogen, ρ is the density and N_A is the Avogadro's constant (Iliadis 2007).

Only large nucleosynthesis networks with ten thousands of reactions and hundreds to thousands of isotopes can model the production of elements in the stellar models.

Nuclear cross sections are important constituents of reaction networks. They are deduced from experiments (Rolfs and Rodney 2005) and, if not available, from theoretical work (Hauser and Feshbach 1952; Rauscher and Thielemann 2000). Most nuclear information is still theoretical (Rauscher et al. 2002). The revision of cross sections, for example due to new experimental measurements, can have a strong impact on stellar structure and final yields when applied in stellar evolution simulations (Herwig and Austin 2004; Pignatari et al. 2013b).

Post processing

In stellar evolution simulations the Henyey method (Kippenhahn and Weigert 1990) is applied to solve the basic equations of a stellar model on a 1D grid (Section 1.2.1). Such computations are very expensive when hundreds or thousands of species are considered (Eq. 1.9). Typically only a small network which accounts for most energy generation and structure properties is applied in stellar evolution simulations. The comprehensive nucleosynthesis is done in a post-processing step. In this step mixing and burning operators are solved separately. Stellar parameters such as temperature and density are tracked during the stellar evolution computation and provided as an input in the post-processing code. While this method allows the modeling of large networks some of its drawbacks are discussed in Chapter 2.

1.2.4 Stellar hydrodynamics

Stellar evolution simulations include comprehensive microphysics and macrophysics over long time scales which requires simplified model assumptions. Examples are spherically symmetry, hydrostatic equilibrium and time-and space averaged mixing (Böhm-Vitense 1958). The latter demands the convective turnover time scale τ_{mix} to be much shorter than the burning time scale τ_{nuc} which prevails in many stellar stages.

When the burning time scale decreases drastically such as in the advanced stage of massive stars (Table 1.1) τ_{nuc} can become comparable with τ_{mix} and averaging mixing in time and space is an insufficient approximation. Hydrodynamic simulations allow to describe flow properties accurately on short time scales but require simplified physics due to their large computational cost. In such simulations solved explicitly

on a grid the time step size is limited by the sound crossing time through one grid cell. The Courant-Friedrichs-Lewy condition defines the maximum time step Δt in 1D as

$$\Delta t = \frac{\Delta x}{u} \tag{1.11}$$

where Δx is the grid size and u is the fluid velocity (Herwig 2013).

One example is H ingestion into He-burning convective zone of the post-AGB star Sakurai's object where $\tau_{nuc} \approx \tau_{mix}$ in some layers and the nuclear energy release feeds back into the flow to change its properties (Herwig et al. 2011). Such reactive-convective events in flows of global scale are required to model the whole convective zone in 3D and are computationally extremely expensive (Porter, Woodward, and Jacobs 2000; Herwig et al. 2011). With the setup of Herwig et al. (2011) the modeling the He convective zone requires time steps of $\Delta t \approx 0.01$ s while the convective turnover time scale is $\tau_{mix} \approx 1000$ s which requires millions of time steps. A simple equation of state such as the monoatomic ideal equation of state is applied for He-shell flash convection (Woodward, Herwig, and Lin 2015). The entrainment of H-rich fluid into the He convective shell is non-spherical and of turbulent character (Fig. 1.9).

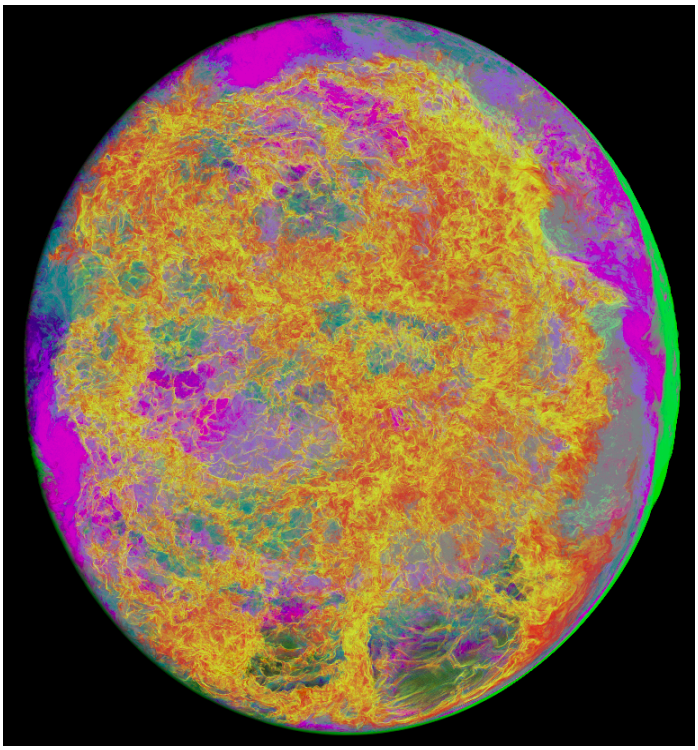

Figure 1.9: Volume fraction of entrained H-rich fluid of the hydrodynamic simulation of Sakurai's object of Herwig et al. (2014).

The simplified microphysics requires the application of small networks and nucleosynthesis in advanced burning stages in massive stars or heavy element production cannot be accurately modeled. For the post-AGB star Sakurai's object (Fig. 1.9) only a 2-species network was applied. For multiple burning shells in massive stars a larger network of 38 species is applied (Arnett and Meakin 2011) while accurate predictions require hundreds or thousands of species.

1.3 Chemical evolution

1.3.1 Simple stellar populations

Over billions of years many generations of stars were born into a unique environment, defined by the cumulative ejecta of previous generations (Hoyle 1954). The basic building block of each galaxy is a stellar population (Fig. 1.10). *Simple* stellar populations (SSPs) are groups of stars formed from the same gas homogeneous mixed gas cloud and hence have the same initial composition.

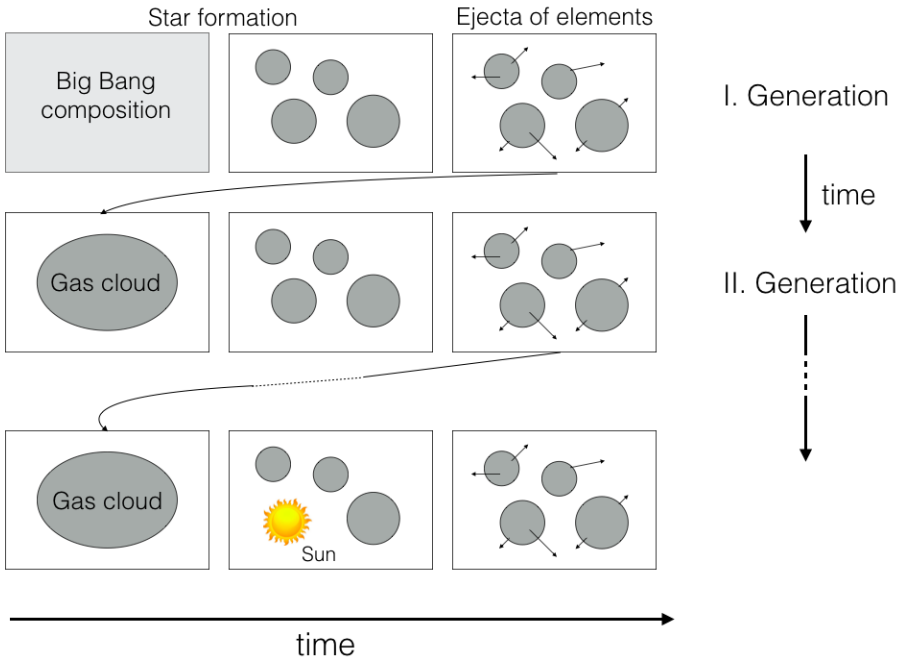

Figure 1.10: Sketch of the chemical evolution since the Big Bang with contributions from stellar populations of many generations. After a unknown number of generations our Sun was formed out of a gas cloud.

Chemical evolution parameters define the star-formation properties such as how

many stars formed of which initial mass. The initial mass function ξ together with the total mass of the SSP define how many stars are formed in the initial mass interval [m_1,m_2] via

$$N = A \int_{m_1}^{m_2} \xi(m')\, dm' \tag{1.12}$$

where the normalization constant A is derived from the total gas mass. Determination of observed stellar masses help to define the initial mass range in which stars are formed (see compilation in Côté et al. 2016d). The amount of massive star ejecta depends critically on the explodability of the massive star which defines if a star explodes as a core-collapse SN (Sukhbold and Woosley 2014; Ertl et al. 2016).

To trace the chemical enrichment by SSPs a fundamental ingredient are stellar yields which are needed for a range of initial masses and metallicities (Côté et al. 2016b). Analyzing the ejecta of SSPs can provide valuable insights without the application of more complex galaxy models as shown in Section 3.2.

1.3.2 Simple galaxy models

To model Galactic chemical evolution 1-zone closed-box models were applied early on (Schmidt 1963; Tinsley 1980). These models assume an isolated system in which stars eject their matter instantaneously after birth into a homogenous-mixed box (McWilliam 1997). Over the years more complex chemical evolution models emerged, taking into account infall, outflow and different properties of the galactic structure (Timmes, Woosley, and Weaver 1995; Nomoto, Kobayashi, and Tominaga 2013).

In such models the basic equation which governs the evolution of gas mass $M(t)$ from t^* to $t^* + \Delta t$ is given as

$$M(t^* + \Delta t) = [\dot{M_{ej}}(t^*) - \dot{M_*}(t^*) + \dot{M_{in}}(t^*) - \dot{M_{out}}(t^*)]\Delta t + M(t^*) \tag{1.13}$$

where $\dot{M_{ej}}(t)$ is the rate of stellar ejecta and $\dot{M_*}(t)$ is the star formation rate. The inflow rate is given as $\dot{M_{in}}(t)$ and the outflow rate as $\dot{M_{out}}(t)$. In a simple approach $\dot{M_{in}}(t)$ is coupled to $\dot{M_{out}}(t)$ which in turn is connected with the star formation rate but other varieties of inflow and outflow models exist(see comparisons in Côté et al. 2016c). To solve Eq. 1.13 the star formation history is required and derived from observations or derived from the current gas density.

Constraints are stellar abundances including (I) the solar system abundance distribution, (II) the age-metallicity relationship in the solar neighbourhood and (III)

the G dwarf distribution (Timmes, Woosley, and Weaver 1995). A 1-zone galaxy code was created as as part of this work (Section 3.3).

1.3.3 Cosmological simulations

While 1-zone chemical evolution models describe homogenously mixed systems fairly well (e.g. Timmes, Woosley, and Weaver 1995) they fail to model the inhomogeneous mixing present during the assembly of the Milky Way from smaller galaxies. The formation of dark matter halos described by cosmological N-body simulations are not taken into account in those models.

In some sophisticated N-body simulation gas and stars are tracked which is computational very expensive (e.g. EAGLE and Illustries simulations Schaye et al. 2015; Vogelsberger et al. 2014). Only a limited number of elements can be included.

Another method is to use the information about the assembly of dark matter and halos in a post-processing step in semi-analytic models (Côté, Martel, and Drissen 2013; Crosby et al. 2013). While those are less expensive and might be able to carry more elements the feedback of gas and stars onto dark matter is not taken into account (Sawala et al. 2013; Sawala et al. 2015).

In those large-scale simulations enrichment by single stars cannot be traced and instead star particles describe the chemical enrichment. Those particles are treated as simple stellar populations.

1.4 Thesis outline

Chapter 2: Yields for chemical evolution

In Chapter 2 I describe the methods to calculate the stellar evolution models of AGB stars, massive stars as well as the simulation of core-collapse supernova explosions. The stellar evolution simulations are analyzed with focus on peculiarities at low metallicity and the results of the extensive post-processing nucleosynthesis are presented. In a discussion I outline the shortcomings of my approaches and results.

Chapter 3: Applications of yields in chemical evolution studies

I describe my investigations into the chemical evolution of simple stellar populations and the Milky Way based on the stellar yields calculated in Chapter 2. First I present

the simple stellar population code SYGMA, its application with different yield input and in comparison with other works. I will outline my contribution to develop the galaxy framework NuPyCEE which includes the chemical evolution code for galaxies OMEGA. The investigations into galactic chemical evolution assumptions with the latter code are summarized. Finally I address my efforts to make the code available to the scientific community for research and for teaching.

Chapter 4: H-ingestion flashes and I process

In this section H ingestion events and i process nucleosynthesis are analyzed. In particular I compare the result of simple i-process 1-zone models with the abundance C-Enhanced Metal Poor (CEMP-r/s) stars. I present my efforts to predict the elements produced via i process in 3D with the building of a 3D nucleosynthesis framework to post-process the output of 3D hydrodynamic simulations.

Chapter 5: O-C shell merger in massive stars

The comprehensive nucleosynthesis in O-C shell mergers of massive star models is analyzed. I investigate the element production in 1D stellar evolution models and in a convective O-C shell merger model informed by 3D hydrodynamic simulations. The impact of O-C shell mergers on the Galactic production is tested with (Chapter 2), the galactic chemical evolution code (Chapter 3) and results are compared with disk and halo stars.

Chapter 2

Yields for chemical evolution

In this chapter I investigate the nucleosynthesis of AGB models and massive star models with metallicities from $Z = 0.02$ down to $Z = 0.0001$ with particular focus on the effect of low metallicity. Stellar yields between H and Bi are derived and serve as an input for chemical evolution simulations in Chapter 3.

Draft of C. Ritter, F. Herwig, S. Jones, M. Pignatari, C. Fryer, R. Hirschi, to be submitted to MNRAS

Abstract

We provide a significant extension of the NuGrid Set 1 (Pignatari et al. 2016a). Set 1 extension adopts the same physics assumptions for stellar models as Set 1.The combined data set now spans the initial masses $M_{ini}/\,\mathrm{M}_\odot$ = 1, 1.65, 2, 3, 4, 5, 6, 7, 12, 15, 20, 25 for $Z = 0.02, 0.01, 0.006, 0.001, 0.0001$ with α-enhanced composition for the lowest three Z. All stellar evolution models are computed with the MESA stellar evolution code and post-processed with the NuGrid MPPNP code. Most AGB models are computed towards the end of the asymptotic giant branch phase or to the WD stage. Massive star models are calculated until core collapse followed by simple 1D models for the explosive core-collapse nucleosynthesis as in Set 1. We include metallicity-dependent mass loss and convective boundary mixing in all asymptotic giant branch (AGB) star models. These massive AGB models at low Z experience efficient hot-bottom burning and hot dredge-up. In this case we reduce the convective boundary mixing to take into account its energetic feedback. We find H-ingestion events in these low-mass low-Z AGB models which lead for the $1\,\mathrm{M}_\odot$, $Z = 0.0001$ model to the production of large amounts of heavy-element. H ingestion appears in

super-AGB models which could potentially lead to the intermediate neutron-capture process. The massive star models of $20\,M_\odot$ and $25\,M_\odot$ at $Z = 0.0001$ produce light elements via H ingestion which leads to peculiar nucleosynthesis signatures due to the explosive nucleosynthesis. We have applied a new nested-network post-processing scheme that allows to simulate in detail both heavy elements and CNO species under hot-bottom burning conditions. The element production through the main and weak s process, and of the γ process with respect to metallicity is analyzed. We find that convective O-C shell merger in some stellar models lead to the strong production of odd-Z elements P, Cl, K and Sc. All post-processing calculations use the same nuclear reaction rates. Complete yield data tables and derived data products are provided online, including the entire simulation database and the profile evolution of all models. We provide the "NuGridSet explorer" at http://wendi.nugridstars.org for interactive exploration of the extended Set 1 database.

2.1 Introduction

Stellar yields data are a fundamental input for galactical chemical evolution models (e.g. Romano et al. 2010; Nomoto, Kobayashi, and Tominaga 2013; Mollá et al. 2015), hydrodynamic models and chemodynamic models (e.g. Scannapieco et al. 2005; Few et al. 2012; Côté, Martel, and Drissen 2013; Schaye et al. 2015). Gibson (2002) and Romano et al. (2010) showed that results of chemical evolution model are strongly affected by uncertainties related to the choice of the yield set. Romano et al. (2010) for example found 0.6 dex differences in [C/O] ratio and 0.8 dex for [C/Fe] in their galaxy models. Tosi (2007) demanded an optimal yield set which spans the whole mass range and the whole metallicities with all major isotopes. A consistent choice of nuclear and stellar physics input is crucial in such a yield set.

In most cases yields for asymptotic giant branch (AGB) models are combined with yield sets of massive stars which all stem from different stellar evolution models. Widely used yield sets of massive stars are those of Woosley and Weaver (1995), Portinari, Chiosi, and Bressan (1998), Chieffi and Limongi (2004), Kobayashi et al. (2006), the Geneva group (e.g. Hirschi, Meynet, and Maeder 2005b) which differ in nuclear physics input and model assumptions such as mass loss and rotation. Yields provided with a explosive contribution differ in their explosion prescription. These assumptions considerably impact the final yields (Romano et al. 2010). AGB star yields are given by e.g., van den Hoek and Groenewegen (1996), Marigo (2001b), Karakas (2010), Straniero, Cristallo, and Piersanti (2014) and Cristallo et al. (2015), which differ in their treatment of nuclear physics, the AGB phase and the mixing model and hence their final yields. Recent works applying some of those yields are Few et al. (2012) and Spitoni et al. (2016).

Wiersma et al. (2009) and Yates et al. (2013) apply as input for simple stellar population models yields of the Padova group which are based on AGB models by Marigo (2001b) and massive star models by Portinari, Chiosi, and Bressan (1998) and inherit some consistency. But the models use simplifications to reduce computational cost, such as synthetic AGB modeling, that are not necessary anymore. To reach a higher degree of consistency Pignatari et al. (2016a) (P16 in the following) published AGB *and* massive star models and their yields of $Z = 0.02$ and $Z = 0.01$. While their yields are calculated with the same nuclear-physics input they are based on different stellar models: MESA (Paxton et al. 2011) for AGB star models and GENEC (Eggenberger et al. 2008) for massive star models.

In this paper we provide a new set of models and stellar yields which use updated nuclear-physics input as in P16, but are calculated with the same stellar evolution code, MESA. We recalculate massive star models of $15\,M_\odot$, $20\,M_\odot$ and $25\,M_\odot$ provided in P16 with MESA to reach consistency at solar and half-solar metallicity. We increase the initial mass range of massive star models towards the lower end by adding stellar models of $12\,M_\odot$. P16 provides AGB models up to $5\,M_\odot$ and does not include super-AGB (SAGB) star models, which among other isotopes are important producers of ^{13}C and ^{14}N, in particular at low Z (e.g. Siess 2010; Ventura and D'Antona 2011; Karakas, García-Hernández, and Lugaro 2012; Ventura et al. 2013; Gil-Pons et al. 2013; Doherty et al. 2014). In this paper we include S-AGB star models at all metallicities and we extend the mass grid of P16 for *each metallicity* to $M_{ini}/\,M_\odot =$ 1, 1.65, 2, 3, 4, 5, 6, 7.

Stellar models and recent observations indicate that massive AGB stars and S-AGB stars experience hot-bottom burning (HBB, Sackmann and Boothroyd 1992; Lattanzio et al. 1996; Doherty et al. 2010; García-Hernández et al. 1992; Ventura et al. 2015). There are two options to resolve HBB in stellar models: either to couple the mixing and burning operators or choose time steps smaller than the convective turnover timescale τ_{conv} (e.g. $\tau_{conv} \sim$ hrs for the stellar model of $4\,M_\odot$ at $Z = 0.0001$). At present coupled codes require long computing-time to handle large networks and heavy element nucleosynthesis. Post-processing codes would need to resolve the extremely short mixing time scale when HBB convective-reactive conditions are relevant. In this work we present a nested-network post-processing approach which allows to predict the correct nucleosynthesis of CNO species and s-process elements also in these conditions, which we apply in all stellar models experiencing HBB.

With the convective boundary mixing prescription in this work, which is derived from hydrodynamic simulations, mixing and ^{13}C-pocket formation in AGB models is obtained self-consistently at all Z. In order to resolve the chemical evolution history in different galactic systems, we need to define the number of masses and metallicities required. Côté et al. (2016b) show that adding more masses to the grid provided in this work is not necessary. The authors conclude that the metallicity range is more important than the number of metallicities within that range and hence we refrain from providing a denser metallicity grid. P16 includes stellar models of solar and half-solar metallicity.

In this work we present models down to $Z = 0.0001$ which are in part an extension of the work by P16. Below $Z = 0.01$, we calculate stellar evolution and

post-processing tracks based on α-enhanced initial abundance which leads to [Fe/H] = -1.18, 1.96 and -2.97 for $Z = 0.006, 0.001$ and $Z = 0.0001$. Ingestion events are common at low and zero-metallicity in AGB models of low mass (e.g. Fujimoto, Ikeda, and Iben 2000; Cristallo et al. 2009), in He-core flash in low-Z low-mass models (e.g. Campbell, Lugaro, and Karakas 2010) but also in S-AGB models in a wide range of metallicities (e.g. Gil-Pons and Doherty 2010; Jones et al. 2016a). The energy release due to H ingestion might violate the treatment of convection via mixing-length theory (Herwig 2001) and/or the assumption of hydrostatic equilibrium or in S-AGB models (Jones et al. 2016a). The 3D hydrodynamic simulations of H ingestion of the post-AGB star Sakurai's object show that 1D and 3D predictions differ (Herwig et al. 2011; Herwig et al. 2014). The predictive power of 1D stellar evolution models to describe H ingestion events might be limited.

Yield tables are typically provided in the literature but the access to the full stellar models is limited. We provide a full web access of the stellar evolution and post-processing data including yield tables at http://www.nugridstars.org/data-and-software/yields/set-1. An interactive interface allows to retrieve data based on ipython notebooks and is accessible through the NuGrid web interface WENDI[1].

The paper is organized as follows: in Sect. 2.2 we describe the methods used to perform the stellar evolution simulations, CCSN explosions and post-processing. In Sect. 2.3 we introduce the general properties of stellar models and features related to the low metallicity. In Sect. 2.4 we analyze the final yields at low Z. The latter are grouped by nucleosynthesis process. We discuss this work in Sect. 2.5 and compare the results with available literature. In Sect. 2.6 we summarize the results.

[1] http://wendi.nugridstars.org

2.2 Methods

2.2.1 Stellar evolution

We adopt the physics assumptions of P16. In the following we describe additional methods and assumptions applied in this work.

Initial composition, network and opacities

We use solar-scaled but α-enhanced initial abundance at $Z = 0.006$ and below. The abundances are scaled from Grevesse and Noels (1993) and with the isotopic percentage from Lodders (2003) as described in P16. Enhanced species are ^{12}C, ^{16}O, ^{20}Ne, ^{24}Mg, ^{28}Si, ^{32}S, ^{36}Ar, ^{40}Ca and ^{48}Ti. The enhancements were derived from fits of halo and disk stars from Reddy, Lambert, and Allende Prieto (2006) and references therein. For each enhanced isotope X_α we apply Eq. 2.1 where A_α and B_α were derived from the fits for metallicities $-1 \leq$ [Fe/H] ≤ 0 (Reddy, Lambert, and Allende Prieto 2006). In the case of [Fe/H] < -1 we apply $[X_\alpha/\mathrm{Fe}] = -A_\alpha + B_\alpha$ for Eq. 2.1.

$$[X_\alpha/\mathrm{Fe}] = A_\alpha[\mathrm{Fe/H}] + B_\alpha \tag{2.1}$$

For isotopes of Ne, S and Ar values from Kobayashi et al. (2006) were adopted. The resulting $[X_\alpha/\mathrm{Fe}]$ and mass fractions for $Z = 0.0001$ are shown in Table 2.1. The fit result of [O/Fe] $= 0.89$ is at the top of the [O/Fe] distribution but within the maximum given in (Reddy, Lambert, and Allende Prieto 2006). For the initial abundance of Li in AGB models with initial mass above $3\,\mathrm{M}_\odot$ we choose as a lower limit the Li plateau (Sbordone et al. 2010) . In other stellar models an unrealistic initial Li abundance was unintentionally adopted In these low-mass stellar models up to the initial mass of $3\,\mathrm{M}_\odot$ we employ the *agb.net* network in agreement with P16. For stellar models with initial masses of $4\,\mathrm{M}_\odot$ and above we use a network which includes necessary C-burning reactions. The choice of opacities is the same as in P16.

Choice of MESA revision

We utilize the stellar evolution code MESA. MESA rev. 3372 is used for AGB models in P16 while we use in this work rev. 3709. We compared stellar structure and post-processing results of both revisions for stellar models of $3\,\mathrm{M}_\odot$ and $5\,\mathrm{M}_\odot$ and do not find major differences. The structural evolution of the H-free and He-free boundaries

for different MESA revisions are shown in Fig. 2.1.

For rev. 3709 we adopted the opacity settings of rev. 3372, including the temperature-dependent transition between opacity tables, which results in a better agreement with P16 (kap in Fig. 2.1). The differences between the revision of P16 and this work (rev. 3709, kap) in Fig. 2.1 are less than 1%.

Rev. 4631 was at the time of the calculations the latest MESA revision and was not adopted due to various physics updates since rev. 3372 which lead to differences in the structural evolution (Fig. 2.1).

Mass loss

The difficulty to predict mass loss has led to the development of semi-empirical prescriptions for many evolutionary phases (e.g. Vassiliadis and Wood 1993; van Loon et al. 2005). Such prescriptions describe observed properties while mass loss is still a major uncertainty in stellar evolution (Willson 2000; Willson 2007). As in P16 we apply the mass loss prescription by Reimers (1975) for the RGB phase and the prescription of Blöcker and Schönberner (1995) for the AGB phase. Both prescription are based on the mass, luminosity and radius of the stellar model. The parameter $\eta_{Bloecker}$ is increased to mimic the effect of the C-rich dust-driven phase as described in P16. A proper dependence of the mass loss on metallicity based on observations is not available yet but efforts have been made (Rosenfield et al. 2014).

Our approach provides a mass-metallicity dependence of AGB mass loss which gives results that are consistent with the assumption made in P16 for solar-like metallicity and Herwig (2004) for low Z. We fit $\eta_{Bloecker}$ in the mass-metallicity plane to derive a metallicity-dependent mass loss. We use $\eta_{Bloecker}$ as applied in P16 for stellar models with $M_{ini}/\,\mathrm{M}_{\odot}$= 1.65, 2, 5 at solar and half-solar metallicity. We derive values of $\eta_{Bloecker}$ for stellar models with $M_{ini}/\,\mathrm{M}_{\odot} = 2$, 3, 4, 5, 6 at $Z = 0.0001$ from Herwig (2004). We compare their mass loss rates with mass loss rates of these stellar models for which we apply the Blöcker and Schönberner (1995) prescription and derive an average $\eta_{Bloecker}$ which reproduces the mass loss of Herwig (2004).

The resulting spline fits of $\eta_{Bloecker}$ in the mass-metallicity plane are shown in Fig. 2.2. We have also added ad-hoc values for stellar models of $M_{ini}/\,\mathrm{M}_{\odot} = 4$, 6, 7, 8 for solar and half-solar metallicity to achieve a smooth transition between initial masses of $1\,\mathrm{M}_{\odot}$ and $8\,\mathrm{M}_{\odot}$. Note that those values do not change the general trends. Our fit follows the general assumption that $\eta_{Bloecker}$ (and with it the mass loss)

decreases for lower metallicity (Willson 2000, atmosphere-wind models). Rosenfield et al. (2014) recently observed in low-mass low-Z AGB stars a trend of shorter AGB lifetimes with initial mass which is qualitatively in agreement with these fit result. The mass loss for stellar models with initial masses of $M_{ini}/\,\mathrm{M}_{\odot} = 1,\ 3,\ 5,\ 6$ at $Z = 0.0001$ based on the fits is shown in Fig. 2.2.

The choice of the mass loss prescription adopted in the massive star models depends on the effective temperature T_{eff} and the surface hydrogen mass fraction X(H) as in Glebbeek et al. (2009). For $T_{eff} \leq 10^4$ K we adopt the mass loss rate of de Jager, Nieuwenhuijzen, and van der Hucht (1988). If $T_{eff} > 10^4$ K and $X(H) < 0.4$ we use the rates by Nugis and Lamers (2000). For $X(H) < 0.4$ the de Jager, Nieuwenhuijzen, and van der Hucht (1988) rate transits into the Vink, de Koter, and Lamers (2001) rate up to $T_{eff} = 1.1 \times 10^4$ K and the de Jager, Nieuwenhuijzen, and van der Hucht (1988) rate is adopted for higher T_{eff}. The Nugis and Lamers (2000) and Vink, de Koter, and Lamers (2001) rates depend explicitly on metallicity. See Glebbeek et al. (2009) for further details. A correction factor of 0.8 is adopted for mass loss rates of massive star models as deduced for MS OB stars in Maeder and Meynet (2001).

Hot-bottom burning

HBB is the activation of the CNO cycle at the hot bottom of the convective envelope in massive and S-AGB stars (Scalo, Despain, and Ulrich 1975; Sackmann and Boothroyd 1992). Higher temperatures in the AGB envelopes at lower metallicity lead to the activation of HBB at lower initial mass compared to AGB models of higher metallicity. This increases the number of stars which experience HBB with decreasing metallicity.

During HBB the mixing timescale of the convective envelope τ_{conv} and burning timescales of CNO reactions τ_p can reach the same order as shown for stellar model with initial mass of $4\,\mathrm{M}_{\odot}$ at $Z = 0.0001$ in Fig. 2.4. The coupling of mixing and burning operators in stellar evolution codes allow to resolve HBB correctly. Post-processing codes decouple mixing and burning in order to be able to solve differential equations for large reaction networks which allow to predict heavy elements. To model HBB in the decoupled approach it is necessary to resolve the mixing timescale at the bottom of the convective envelope which can be extremely short compared to the interpulse phases of tens of thousands of years. We find a convective mixing timescale of hours in these stellar model with initial mass of $4\,\mathrm{M}_{\odot}$ at $Z = 0.0001$ (Fig. 2.4). Cristallo et al. (2015) who predict heavy elements with a large network in

their stellar evolution code approximate CNO production due to HBB with a burn-mix-burn step.

To predict realistic CNO elements *and* heavy elements we have developed a method to solve the coupled mixing and burning equations for a small network which includes species which are affected by HBB. Simultaneously, we solve the large decoupled network for the whole stellar model. After each time step the coupled solution is merged into the large network. The small network includes the CNO, NeNa and MgAl cycles and isotopes up to ^{35}Cl similar to Siess (2010). The comparison of the surface C/O ratio between the coupled and the nested-network solution is shown in Fig. 2.4. The decoupled solution overestimates the surface C/O ratio compared to the coupled solution from MESA. Our nested-network method results in the same evolution of the surface C/O ratio..

The final stellar yields of CNO isotopes based on the nested-network method are similar to Herwig (2004, H04) and Karakas (2010, K10) who couple mixing and burning (Table 2.3). Both studies do not predict s-process isotopes. Our low ^{12}C/^{13}C and ^{12}C/^{16}O ratio in comparison with Cristallo et al. (2015, p. C15) indicates that the mix-burn-mix time step approximation of the coupled mixing and burning in Cristallo et al. (2015) might not be an adequate treatment of HBB nucleosynthesis. Our nested-network solution allows to predict Li production via HBB because we resolve the Cameron-Fowler mechanism through the coupling of mixing and burning. To predict CNO isotopes and heavy elements we apply the nested-network method for all stellar models which undergo HBB.

Convective boundary mixing treatment

We apply convective boundary mixing (CBM) at all convective boundaries modeled with an exponential declining velocity field beyond the convective boundary (Freytag, Ludwig, and Steffen 1996; Herwig 2000). A CBM efficiency of $f = 0.014$ is used at all convective boundaries except for the bottom of the pulse-driven convective zone (PDCZ) and during the third dredge-up (TDUP) of the thermal-pulse (TP)-AGB stage. Motivated by 2D and 3D simulations of Herwig et al. (2007) a lower CBM efficiency of $f_{PDCZ} = 0.008$ is applied at the PDCZ boundary. An increased mixing efficiency of $f_{CE} = 0.126$ is applied at the bottom of the convective envelope during the TDUP which is calibrated for low-mass stellar models to produce the ^{13}C pocket (Herwig, Langer, and Lugaro 2003). This approach is the same as in P16.

The continuation of HBB during TDUP leads to a increase of the TDUP efficiency and is referred to as hot dredge-up (HDUP, Herwig 2004; Herwig and Austin 2004). The application of CBM at the bottom of the convective envelope results in strong burning of the mixed protons below the envelope and extreme TDUP efficiencies in these massive AGB models at low Z. For the calibrated value $f_{CE} = 0.126$ the TDUP penetrates into the C/O core after the sixth TP of the stellar model with initial mass of $5\,M_\odot$ at $Z = 0.0001$ as shown in the Kippenhahn diagram in Fig. 2.3. This finding is in agreement with Herwig (2004) who found that the HDUP can penetrate into the C/O core and terminate the AGB phase (see also Goriely and Siess 2004). The abundance profile during a TDUP at the bottom of the convective envelope shows the peak of nuclear burning in the CBM region which lifts the radiative gradient and hence leads to a deeper penetration of the envelope into the He intershell (Fig. 2.3). The reduction of f_{CEB} to 0.01 prevents the extreme TDUP.

The efficiency of CBM at the lower boundary of the convective envelope in massive and S-AGB is not known. Investigations of the impact of CBM efficiency on structure and nucleosynthesis such as for S-AGB models by Jones et al. (2016a) are required. We assume that the CBM is weakened due to buoyancy of the mixed and burning material and that the resulting CBM efficiency is reduced. We limit CBM by reducing f_{CE} for stellar models with initial mass of $4\,M_\odot$ and above which experience HDUP. Table 2.2 shows the choice of CBM efficiencies at different convective boundaries applied in this work. With this approach we prevent in these stellar models the termination of the AGB phase due to too extreme boundary mixing.

2.2.2 Explosion

We use the semi-analytic approach for core-collapse supernova explosions of P16. The method drives a shock off the proto-neutron star based on a mass cut derived from Fryer et al. (2012). The mass cuts depend non-linear on initial mass and metallicity and are available for delayed and a rapid explosion prescription. The mass coordinates based on these models are shown in Table 2.5. For stellar models such as the stellar model of $15\,M_\odot$ at $Z = 0.006$ the mass cut is deeper located than than the outer layers of the Fe core as visible from the Fe-core masses in Table 2.4.

One of the big uncertainties in the yields is the position of the mass cut. The data from Fryer et al. (2012) were based on fits to the stellar structures produced by comparing the models from a range of stellar evolution codes (Woosley, Heger,

and Weaver 2002; Limongi and Chieffi 2006; Young et al. 2009). These mass-cut prescriptions were then validated against the compact remnant mass distribution (Belczynski et al. 2012). For these stellar evolution models, the mass cut is fairly similar for models with zero age main sequence models with masses below $25\,M_\odot$. However, in particular for the $12\,M_\odot$ model, the core from the MESA model is much larger than that produced by the Kepler code. This corresponds to much higher densities in the inner $2\,M_\odot$ and, with the Fryer et al. (2012) analysis, we expect the MESA models to collapse down to a black hole rather than explode to produce a low-mass neutron star. In part, this is caused by the use of a small network in the MESA code during Si burning.

At earlier times, the MESA models with initial mass of $12\,M_\odot$ and Geneva models with initial mass of $15\,M_\odot$ look very similar and, to provide a first estimate from the yields of the MESA models, we use the mass cut and energies used for Geneva models with initial mass of $15\,M_\odot$ of P16. The differences between the MESA and Geneva models in more massive progenitors is less extreme and, for these models, we use the same mass cut and explosion energy for both code results.

2.2.3 Nucleosynthesis code and processed data

We use the post-processing multi-zone code MPPNP and the same reaction network as in P16. The yields and overproduction factors in this work were calculated according to Eq. (8), (9) and (10) in P16.

Table 2.1: Mass fractions of α-enhanced isotopes for $Z = 0.0001$ derived from Reddy, Lambert, and Allende Prieto (2006) and Kobayashi et al. (2006). The solar normalization based on Grevesse and Noels (1993) and Lodders (2003) as introduced in Sec. 2.2.1.

Isotope	$[X_i/Fe]$	X_i
^{12}C	0.562	1.25E-05
^{16}O	0.886	7.41E-05
^{20}Ne	0.5	5.75E-06
^{24}Mg	0.411	1.51E-06
^{28}Si	0.307	1.51E-06
^{32}S	0.435	1.09E-05
^{36}Ar	0.3	1.64E-07
^{40}Ca	0.222	1.21E-07
^{48}Ti	0.251	5.38E-09

Table 2.2: CBM efficiencies f for the diffusive CBM mechanism in the range of initial masses M. f_{CE} is adopted at the bottom boundary of the convective envelope while f_{PDCZ} is adopted at the bottom boundary of the PDCZ. 'burn' or 'non-burn' stand for burning or no burning at the bottom of the respective convective zone.

$M < 4\,M_\odot$			$M \geq 4\,M_\odot$		
f_{CE}		f_{PDCZ}	f_{CE}		f_{PDCZ}
burn	non-burn	burn	burn	non-burn	burn
0.014	0.126	0.008	0.0035	0.126	0.008

Table 2.3: The final yields for the stellar model with initial mass of $4\,M_\odot$ at $Z = 0.0001$ in comparison with yields of H04, K10 and C15. Units are in $M_\odot$.

specie	this work	H04	K10	C15
CNO isotopes				
C-12	6.948E-04	4.587E-04	2.787E-03	1.274E-02
C-13	9.086E-05	4.372E-05	4.059E-04	1.856E-04
N-14	4.691E-03	1.680E-03	2.405E-02	3.405E-04
O-16	1.824E-04	3.008E-04	6.094E-04	9.350E-04
isotopic ratios				
C-12/C-13	7.65	10.49	6.87	68.64
C-12/O-16	3.81	1.52	4.5	13.63
s-process isotopes				
Sr-88	8.969E-10			2.238E-08
Zr-90	1.520E-10			4.399E-09
Ba-136	2.236E-11			1.029E-09
Pb-208	1.465E-10			1.284E-08

Table 2.4: Fe core mass of massive star models presented in this work. The Fe core boundary is defined where the mass fraction of Fe, Co and Ni falls below 50%. Units are in $M_\odot$.

initial mass	Z=0.02	Z=0.01	Z=0.006	Z=0.001	Z=0.0001
12	1.60	1.52	1.55	1.50	1.64
15	1.46	1.50	1.66	1.55	1.53
20	1.68	1.32	2.02	2.08	1.65
25	1.55	1.78	1.66	1.56	1.69

Table 2.5: Remnant masses of massive star models according to Fryer et al. (2012) for the two delayed and rapid explosion prescriptions. The model with initial mass of $25\,M_\odot$ at $Z = 0.02$ based on the rapid explosion prescription collapses directly into a black hole. Units are in $M_\odot$.

initial mass	$Z = 0.02$		$Z = 0.01$		$Z = 0.006$		$Z = 0.001$		$Z = 0.0001$	
	delay	*rapid*	*delay*	*rapid*	*delay*	*rapid*	*delay*	*rapid*	*delay*	*rapid*
12	1.61	1.44	1.61	1.44	1.62	1.44	1.62	1.44	1.62	1.44
15	1.61	1.44	1.61	1.44	1.62	1.44	1.62	1.44	1.62	1.44
20	2.73	2.7	2.77	1.83	2.79	1.77	2.81	1.76	2.82	1.76
25	5.71	-	6.05	9.84	6.18	7.84	6.35	5.88	6.38	5.61

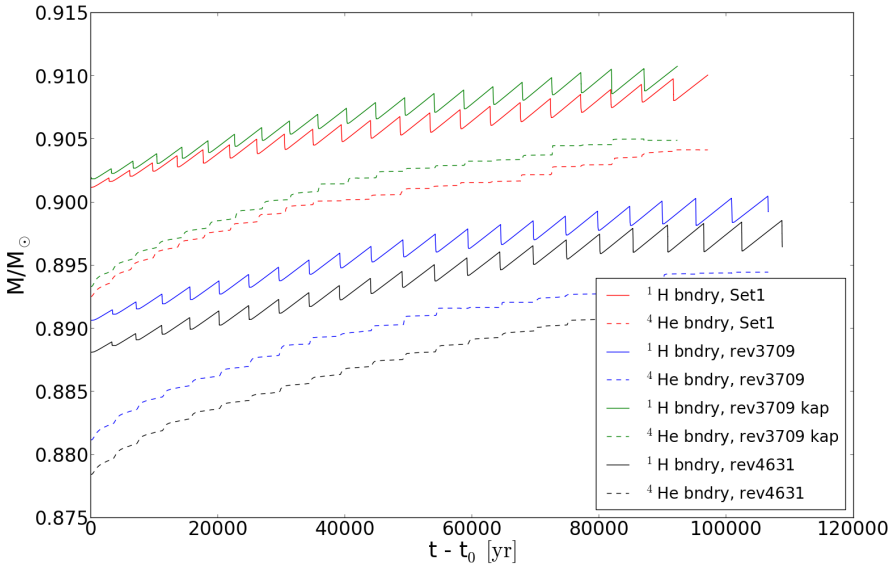

Figure 2.1: Evolution of the ^{1}H-free and ^{4}He-free core boundaries for MESA rev. 3332 (Set1), 3709, 3709 with modified opacities and rev. 4631. t_0 corresponds to the first TP at the beginning of the TP-AGB phase.

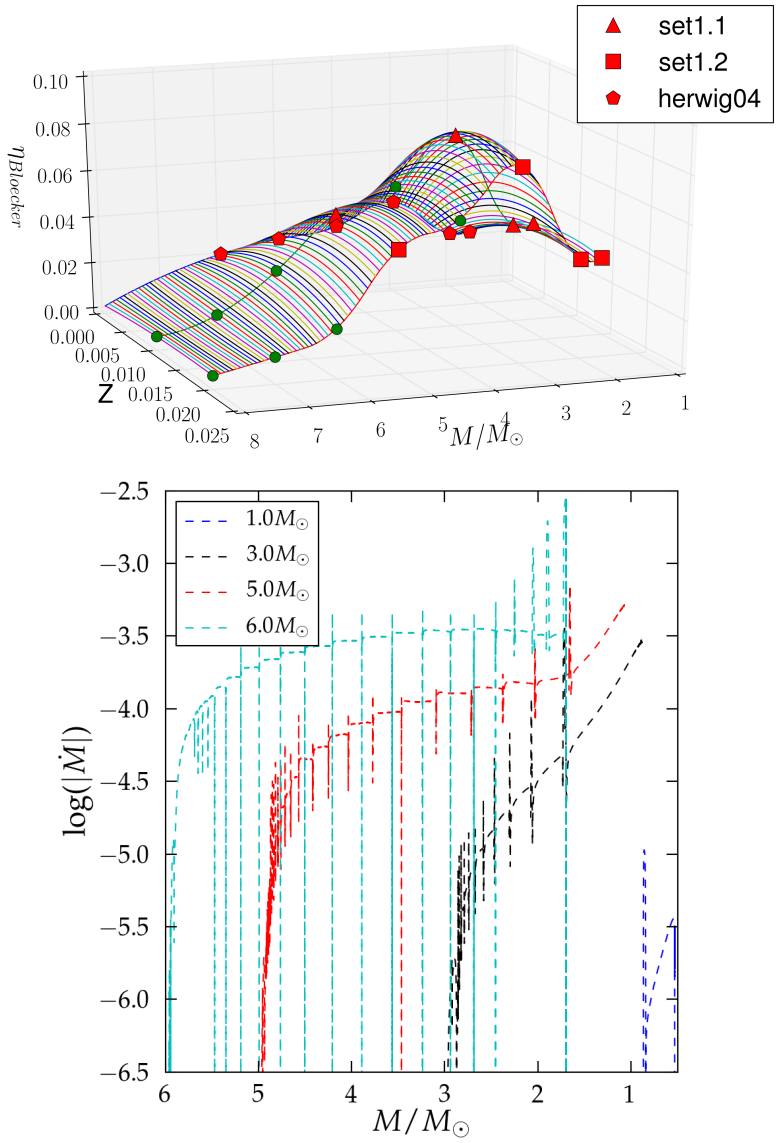

Figure 2.2: 3D spline fit of $\eta_{Bloecker}$ dependent of mass and metallicity based on Herwig (2004) and P16 (left). The green circles represent additional ad-hoc values. Mass loss $\dot{M}$ in $M_\odot/yr$ for stellar models of $Z = 0.0001$ based on the mass-metallicity fits of $\eta_{Bloecker}$ (right).

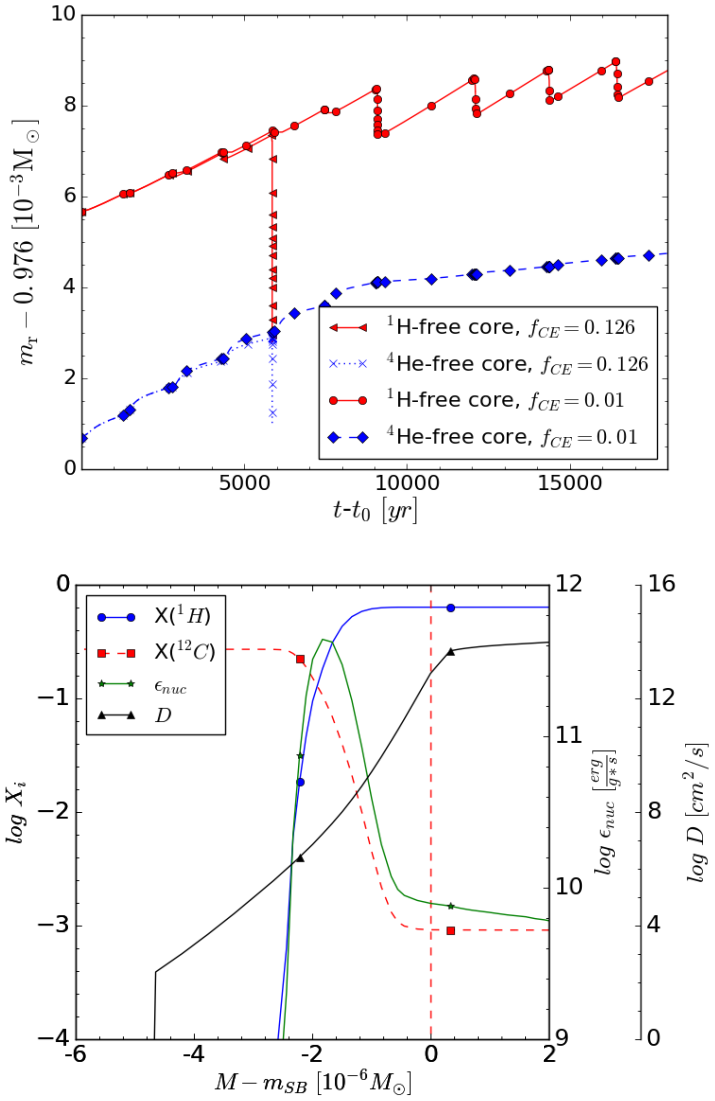

Figure 2.3: Evolution of H-free and He-free cores for $f_{CE} = 0.126$ and $f_{CE} = 0.01$ for stellar models with initial mass of $5\,\mathrm{M}_\odot$ at $Z = 0.0001$ (left). t_0 marks the beginning of the TP-AGB phase. Abundance profile and energy release due to H mixing through the bottom of the convective envelope during HDUP at $\approx (t - t_0) = 7800\,yr$ for the case of $f_{CE} = 0.01$ (right).

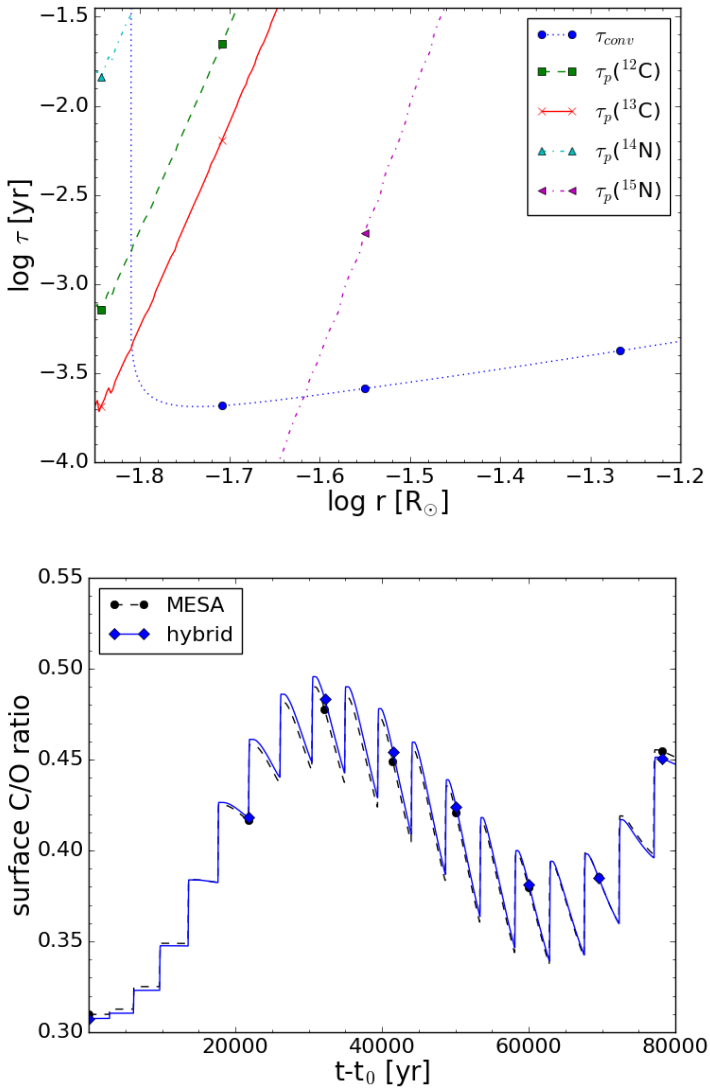

Figure 2.4: Convective turnover timescale τ_{conv} and CNO reaction timescales τ_p relevant for HBB at the bottom of the convective envelope of the stellar model with initial mass of $4\,M_\odot$ at $Z = 0.0001$ (top). The evolution of the surface C/O number ratio based on the coupled solution of MESA and based on the nested-network method (hybrid, bottom). t_0 marks the beginning of the TP-AGB phase.

2.3 Results of stellar evolution and explosion

2.3.1 General properties

Stellar evolution tracks

AGB stars

The influence of metallicity on the stellar evolution is visible in the Hertzsprung-Russell diagram (HRD) with the stellar models with initial mass of $3\,M_\odot$ and $5\,M_\odot$ shown in Fig. 2.5. The shift of the tracks of lower metallicity to higher luminosities and higher surface temperatures is the result of the larger core masses and lower opacities of the envelopes. The central temperature-density tracks of models with initial mass of $5\,M_\odot$ are separated from models with initial mass of $3\,M_\odot$. The central densities ρ_c depend on stellar mass M as $\rho_c \propto M^{-2}$ under the assumption of constant temperature during each burning phase (Woosley, Heger, and Weaver 2002). Lower metallicity models behave as models with higher initial masses which is visible in the approach of the $3\,M_\odot$ tracks at low metallicities towards the $5\,M_\odot$ tracks.

We find He-core flashes in stellar models with $M_{ini} \leq 1.65\,M_\odot$ for $Z = 0.006$, $Z = 0.001$ and $Z = 0.0001$. First dredge-up appears at $Z = 0.006$ and $Z = 0.001$ in all these AGB models but at $Z = 0.0001$ only in stellar models with $M_{ini} \leq 2\,M_\odot$. We find second dredge-up for models with $M_{ini} \geq 4\,M_\odot$ and $M_{ini} \geq 3\,M_\odot$ at $Z = 0.006$ and $Z = 0.001$ respectively. Core flash, first dredge-up and second dredge-up at $Z = 0.006$ show the same initial-mass dependence as the AGB models at $Z = 0.01$ in P16. The dependence of average luminosity on average core mass for stellar models of $Z = 0.006$, $Z = 0.001$ and $Z = 0.0001$ is shown in Fig. 2.10 and follows the core-mass luminosity relationship $logL(M_c) = 1.7414M_c + 2.8799$ given in Blöcker (1993).

All these stellar models with initial mass of $7\,M_\odot$ ignite C and reach the S-AGB stage. The stellar models with initial mass of $6\,M_\odot$ show C ignition and the inward propagation of the C flame at $Z = 0.001$ and $Z = 0.0001$. In the stellar models with $M_{ini} \leq 6\,M_\odot$ at $Z = 0.006$ the convective flames have disappeared and nuclear burning takes place under radiative conditions. For models with initial mass of $4\,M_\odot$ the maximum temperatures in the C/O core do not exceed $T \approx 3 \times 10^8$ K, far below the peak temperature of $T \approx 6 \times 10^8$ K found for M_{up}[2] by Siess (2007). We refer to Farmer, Fields, and Timmes (2015) for more detailed studies of the onset of C burning in MESA.

[2] M_{up} is traditionally referred to as the lower mass of C ignition (e.g. Becker and Iben 1980)

Stellar parameters of the TP-AGB phase for each initial mass and metallicity are shown in Table 2.11. We present in Table 2.12 the detailed TP properties for stellar models of $Z = 0.0001$. The structure evolution of models with initial mass of $3\,M_\odot$, $5\,M_\odot$ and $7\,M_\odot$ at $Z = 0.0001$ are shown in the Kippenhahn diagrams in Fig. 2.6. The final core mass and lifetimes for AGB models are shown in Table 2.6.

We compare stellar models with initial mass of $2\,M_\odot$ and $5\,M_\odot$ at $Z = 0.001$ with models of Weiss and Ferguson (2009) who calculated models with the same initial masses at $Z = 0.004$ and with α-enhanced initial abundances. The core mass of these two stellar models at the first TP are $0.63\,M_\odot$ and $0.985\,M_\odot$ while Weiss and Ferguson (2009) got $0.494\,M_\odot$ and $0.908\,M_\odot$. As Pignatari et al. (2016a) we find larger core masses compared to Weiss and Ferguson (2009). Our number of thermal pulses of the stellar models are 14 and 32 while Weiss and Ferguson (2009) have 10 and 38. The final surface C/O ratio of these stellar models is 3.243 and 3.379 compared to theirs of 3.449 and 0.772. The C/O ratio of the $5\,M_\odot$ model is larger than one because of the decreasing strength of HBB in the last four pulses.

The evolution of the surface C/O ratio is altered by TDUP and HBB in massive AGB models (Lattanzio et al. 1996; Lattanzio et al. 1997; Lattanzio and Boothroyd 1997; Frost et al. 1998). The surface C/O ratios for stellar models of $Z = 0.0001$ in Fig. 2.8 reveal a complex behaviour. While at $Z = 0.02$ low mass stellar models steadily increase their surface C/O ratio (see Fig. 4 in Pignatari et al. 2016a), at low Z the first pulses can lead to a surface enhancement close to or even above the He-intershell C/O ratio as shown in Fig. 2.8. Due to a steady decrease of the C/O ratio in the He intershell over time the TDUP leads to a decline in the surface C/O ratio. Stellar models at higher Z such as the model with initial mass of $1.65\,M_\odot$ at $Z = 0.001$ experience only an increase of the surface C/O ratio during their evolution. For models with higher initial mass a higher C/O intershell ratio is reached which leads to a higher C/O surface enhancement in the non-HBB models.

The TDUP strength is described by the dredge-up parameter λ_{DUP} and shows a strong metallicity-dependent behaviour. In Fig. 2.9 we compare the stellar models with initial mass of $2\,M_\odot$ and $7\,M_\odot$ at $Z = 0.006$ and $Z = 0.0001$. While the $2\,M_\odot$ model at $Z = 0.006$ is very similar to the model of $2\,M_\odot$ at $Z = 0.01$ shown in Fig. 5 of Pignatari et al. (2016a), the $2\,M_\odot$ model at $Z = 0.0001$ reaches $\lambda_{DUP} \approx 1$, similar to the stellar model of the same initial mass and metallicity in Herwig (2004). The maximum of λ_{DUP} and total dredged-up mass increase up to $3\,M_\odot$ for $Z = 0.006$ and up to $2\,M_\odot$ for $Z = 0.001$ and $Z = 0.0001$. For low-mass models both quantities

decline towards higher initial masses (Table 2.12). In comparison, Fishlock et al. (2014) found that the 2.5 $M_\odot$ and 2.75 $M_\odot$ models at $Z = 0.001$ dredge-up the most material. In intermediate-mass stellar models we find a decrease of the total mass dredged up in contrast to Fishlock et al. (2014) who reach another maximum at 4 $M_\odot$.

Our final core masses are larger at lower Z for most stellar models which is visible in the initial-final mass relation (IFMR) of Fig. 2.11. The core masses of models from P16 are added for comparison. The IFMRs in Weiss and Ferguson (2009) which spans from 1 $M_\odot$ to 6 $M_\odot$ and covers $Z = 0.02$ down to $Z = 0.0005$ show in general a smaller final core mass than these stellar models and those by P16. The spread in metallicity is more pronounced for these models. Our IFMR covers the upper part of the compiled data of observed open cluster objects shown in Fig. 10 of Weiss and Ferguson (2009). The AGB phase of the stellar model with initial mass of 1 $M_\odot$ at $Z = 0.0001$ is terminated due to a H-ingestion event which prevents further core growth.

Massive stars

We compare these solar-metallicity models with the MESA models of Jones et al. (2015, J15). We show the He-free core mass, C/O core mass and final mass of stellar models with $M_{ini}/\,M_\odot = 12,\ 15,\ 20$ in Table 2.7. Our models of all initial masses agree with J15. We show in Fig. 2.5 the HRDs and $T_c - \rho_c$ diagram of stellar models with initial mass of 15 $M_\odot$. We find similar trends with metallicity in the HRD as for AGB models. The central conditions for these 15 $M_\odot$ models are not very sensitive to metallicity.

P16 found the final fate of massive stellar models to be the red super giant phase which is in agreement with Peters and Hirschi (2013). All these massive star models experience the same phase except stellar models of 20 $M_\odot$ and 25 $M_\odot$ at $Z = 0.0001$. The latter move from the blue region of the HRD in the region of yellow supergiants but not further, similar to models of Pop III stars of (Heger and Woosley 2010). Due to their low metallicity the stellar models with initial mass of 20 $M_\odot$ and 25 $M_\odot$ experience negligible mass loss and their intermediate convective zones have the largest extend of all models. This leads to higher compactness which favours the blue region of the HRD (Peters and Hirschi 2013).

All these stellar models with initial mass of 20 $M_\odot$ and 25 $M_\odot$ burn C under radiative conditions consistent with solar-Z and PopIII models (Heger and Woosley 2010, P16). We show the lifetimes of the core-burning stages in Table 2.10. The definition of the lifetimes are given in P16. Most burning stages and the total lifetime

are shorter for higher initial masses and lower metallicities.

The structural differences of stellar models with initial mass of $25\,M_\odot$ at $Z = 0.001$ and $Z = 0.0001$ are shown in the Kippenhahn diagram in Fig. 2.7. Contacts between convective burning shells occur in different advanced burning stages and can have ,in particular for a complete shell merger, a profound impact on stellar structure. The contact between the convective H-burning shell and convective He-burning shell leads in the stellar model with initial mass of $25\,M_\odot$ $Z = 0.0001$ to a H-ingestion event. The occurrence of shell merger is affected by considerable uncertainties (Woosley, Heger, and Weaver 2002) and requires studies with 3D hydrodynamic simulations (e.g. Meakin and Arnett 2007a; Jones et al. 2016c).

The final core masses of the He, CO and Si cores as well as total mass are shown in Table 2.9. The definitions of the core masses are in P16. The total mass increases for lower metallicity for all initial masses. We do not find a clear trend of the core masses with metallicity. We compare the final core masses of these stellar models with initial mass of $15\,M_\odot$ and $25\,M_\odot$ for $Z = 0.006$ with those of Meynet and Maeder (2002, p. M02) at $Z = 0.004$ and Pignatari et al. (2016a) at $Z = 0.01$ in Table 2.8. Our H-free core masses are $5.09\,M_\odot$ and $9.66\,M_\odot$ while M02 got $4.45\,M_\odot$ and $8.44\,M_\odot$. P16 got $4.811\,M_\odot$ and $9.39\,M_\odot$. Our results are in better agreement with P16 who got larger values than M02 despite of the metallicity difference. For the C/O core we get $3.27\,M_\odot$ and $7.26\,M_\odot$ compared to $2.27\,M_\odot$ and $5.35\,M_\odot$ from M02. P16 got $2.84\,M_\odot$ and $6.45\,M_\odot$. The mass of the Si core is $2.02\,M_\odot$ and $1.99\,M_\odot$ and P16 got $1.70\,M_\odot$ and $1.85\,M_\odot$.

Core-collapse supernova

The explosion energy and remnant mass of a progenitor depends on the pre-SN structure. The explosion properties determine the stellar layers that are ejected and the shock conditions. We show a profile of maximum temperatures and densities reached during the shock passage for stellar models of $Z = 0.006$ and $Z = 0.001$ in Fig. 2.12 . The differences in shock temperature profiles of the stellar models result from the different density profile (slopes) of the progenitor models (Herant and Woosley 1994). The shock temperature for stellar models with initial mass of $12\,M_\odot$ and $15\,M_\odot$ at $Z = 0.006$ are the largest of all metallicities. Up to $Z = 0.006$ stellar models with initial mass of $15\,M_\odot$ reach the highest shock temperatures and densities followed by the $12\,M_\odot$ models but at higher Z the trend is reversed. The pre-SN structure of these

stellar models do not always show trends with metallicity and the same counts for the shock temperatures. There is no trend of increasing Fe-core mass with initial mass and metallicity and instead the stellar models with initial mass of $20\,M_\odot$ show the largest Fe core masses. This is in supported by recent studies of Ugliano et al. (2012) and Sukhbold and Woosley (2014) who imply that there is no such (continuous) compactness trend with initial mass and metallicity. The maximum temperatures and densities of these delayed explosions at $Z = 0.02$ are similar to those shown in Fig. 31 of P16 for stellar models with $M_{ini}/\,M_\odot = 15$, 20, 25. We find qualitatively the same increase with initial mass but lower explosion temperatures except for the model with initial mass of $25\,M_\odot$. The different explosion conditions might be attributed to the pre-SN structures which were calculated with different stellar evolution codes.

2.3.2 Features at low metallicity

H ingestion

H-ingestion episodes are found in many phases of stellar evolution such as in low and zero-metallicity AGB models (Fujimoto, Ikeda, and Iben 2000) and in very late thermal pulses in models of post-AGB stars (Herwig et al. 2011). At the first TP of the AGB model with initial mass of $1\,M_\odot$ at $Z = 0.0001$ the PDCZ penetrates slightly into the H-rich envelope. A strong neutron burst follows and the production of heavy elements. In the following TP the convective He-burning zone reaches strongly out into the convective envelope which leads to very effective H ingestion and surface enrichment. A H-ingestion flash (HIF) with $L_H \approx 10^{10}\,L_\odot$ occurs. The HIF terminates the AGB phase as shown in the Kippenhahn diagram in Fig. 2.14. The conditions are similar to those found in Iwamoto et al. (2004).

The stellar model of $1\,M_\odot$ at $Z = 0.006$ experiences a He-shell flash when it leaves the highly luminous horizontal evolution towards the WD cooling track. This LTP expands and reaches out into the convective envelope which leads to H ingestion and a born-again phase (Herwig 2001; Herwig et al. 2011). The calculation is terminated six years after the H ingestion due to convergence problems. The H ingestion leads in the He intershell to the production of heavy elements up to the first s-process peak which are mixed to the surface. Due to the energy release of H burning a stable layer forms within the PDCZ and the convective zone splits. The inefficient mass loss together with the short time scale of years lead only to a minor contribution of heavy elements to the total stellar yields.

In these S-AGB models the time between TP and TDUP becomes shorter for lower Z as reported in Jones et al. (2016a). In rare cases this leads for AGB models below $Z = 0.01$ to H ingestion into the PDCZ We find H ingestion during the 29th TP of the stellar model with initial mass of $7\,M_\odot$ at $Z = 0.001$. This leads to neutron densities of up to $N_n = 10^{12}\mathrm{cm}^{-3}$ in the deepest layers of the PDCZ for about five days. The splitting of the PDCZ due to H burning prevents the transport of material from the deep layers to the surface. An efficient envelope enrichment of heavy elements is limited due to the small He-intershell mass and the small amounts of dredged-up material compared to the initially massive AGB envelope (Jones et al. 2016a). Element nucleosynthesis of HIFs do not contribute significantly to the stellar yields.

Stellar models of $20\,M_\odot$ and $25\,M_\odot$ of $Z = 0.0001$ experience H ingestion at the beginning of convective C shell burning and during O shell burning respectively. At higher metallicity we find H ingestion in the stellar model with initial mass of $20\,M_\odot$ at $Z = 0.001$ and in the stellar model of $12\,M_\odot$ at $Z = 0.006$. In both models H ingestion events occur during Si shell burning. The bottom of the convective envelope which reaches into the convective He shell is modeled without CBM in all four massive star models. The penetration into the convective He-burning layer is visible for the model of $25\,M_\odot$ at $Z = 0.0001$ in Fig. 2.7. The resulting energy release leads to the formation of two extended convective regions which persist until collapse. We find at the bottom of the He-shell convective zone neutron densities close to $N_n = 10^{11}\mathrm{cm}^{-3}$ which remain for days until core collapse. There is only a minor production of heavy elements but lighter elements such as F are effectively produced and contribute a relevant fraction of the total stellar yields. The mixing between the H-burning shell and He-burning shell in massive stars have been reported for models at low Z in Woosley and Weaver (1995), for Pop III models in Heger and Woosley (2010) and for rotating models in Hirschi (2007).

Herwig et al. (2011) and Herwig et al. (2014) who investigated the post-AGB star Sakurai's object with 3D hydrodynamic simulations showed that the stellar evolution assumptions of spherical symmetry and the approximation of mixing via mixing length theory of convection might not be sufficient to describe the flow properties of the ingested H. This suggests to study the H-ingestion events found in this work with 3D hydrodynamics simulations.

Hot bottom burning

The temperature at the bottom of the convective envelope T_{CEB} increases with increasing initial mass and for most initial masses increases with decreasing metallicity (Fig. 2.10) and reaches up to $T_{CEB} = 233.9$ MK. In S-AGB models with initial mass of $7\,M_\odot$ at $Z = 0.0001$ and $Z = 0.006$ temperatures reach more than $T_{CEB} = 150$ MK which allows the activation of the NeNa and MgAl cycles. The stellar model with initial mass of $3\,M_\odot$ at $Z = 0.0001$ reaches $T_{CEB} = 40$ MK which leads to HBB. Models of the same mass but of higher Z do not experience HBB (Table 2.11). The threshold initial mass for HBB in Ventura et al. (2013) was found to be $3\,M_\odot$ at $Z = 0.0003$ and $3.5\,M_\odot$ at $Z = 0.008$ which is similar to these values. HBB is active in stellar models of masses as low as $3\,M_\odot$ in agreement with models of $Z = 0.001$ of Fishlock et al. (2014).

Effects of HDUP and dredge-out

Herwig (2004) find that HDUP is characterized by extreme H-burning luminosities L_H during the TDUP. For stellar models with $M_{ini} \leq 4\,M_\odot$ and $Z = 0.0001$ L_H often exceeds the peak He-burning luminosities. Under the most extreme conditions in models with initial mass of $6\,M_\odot$ and $7\,M_\odot$ we find $L_H > 10^9 L_\odot$. At higher metallicities L_H is lower. With reduced CBM (see Sec. 2.2.1) less H is mixed down into the He intershell which decreases the size of ^{13}C pockets. The ^{13}C-pocket size decreases with initial mass and reaches for S-AGB models down to $10^{-7}\,M_\odot$ at $Z = 0.0001$. Dredge-out is found in the most massive AGBs models during second DUP when the convective He-burning shell grows in mass and merges with the convective envelope. This leads to the enrichment of the surface with products of He-shell burning (Ritossa, García-Berro, and Iben 1999). The entrained H ignites as a flash. H-burning and mixing timescales can become comparable (Gil-Pons and Doherty 2010; Jones et al. 2016a). We find dredge-out in S-AGB models with initial mass of $7\,M_\odot$ at Z=0.001 and Z=0.0001. The flash at $Z = 0.0001$ produces up to $L_H \approx 10^8\,L_\odot$. The maximum H-burning luminosities agree well with Jones et al. (2016a). Our stellar models with dredge-out are of lower initial mass than the lower initial mass limit of dredge-out of $\approx 9\,M_\odot$ and above as reported by Gil-Pons and Doherty (2010).

Carbon flame quenching in S-AGB stars

In these S-AGB model with initial mass of $7\,M_\odot$ at $Z = 0.006$ the propagation of the C flame toward the center is quenched as shown in Fig. 2.13 (Denissenkov et al. 2013). The result is a hybrid core. It consists of a inner C-O core of $\approx 0.145\,M_\odot$ surrounded by thicker layers of O, Ne and Mg. For stellar models with initial mass of $7\,M_\odot$ the first C-burning flash occurs at $Z = 0.0001$ closer to the center than at higher metallicity. The C-burning front propagates outwards via a sequence of additional flashes (Fig. 2.13). The location of the first C ignition is located further outwards for models of higher metallicity due to the higher degeneracy of the core (García-Berro, Ritossa, and Iben 1997; Siess 2007). The onset of C burning coincides with the beginning of the second DUP for the stellar model with initial mass of $7\,M_\odot$ at $Z = 0.006$. At higher metallicity the C burning starts earlier than at lower metallicity. The difference in metallicity has a qualitatively similar effect on convective C burning as the difference in initial mass between $7.6\,M_\odot$ and $9\,M_\odot$ shown in Fig. 3 in Farmer, Fields, and Timmes (2015). Possible implications of hybrid WD's are discussed in Denissenkov et al. (2015).

Table 2.6: Final core masses $M_{\rm final}$ and total lifetime $\tau_{\rm total}$ for $Z = 0.0001$. We provide tables for other metallicities online.

initial mass	$M_{\rm Final}$	$\tau_{\rm total}$
$[\,{\rm M}_\odot]$	$[\,{\rm M}_\odot]$	$[yr]$
1.0	0.592	5.670E+09
1.65	0.637	1.211E+09
2.0	0.665	6.972E+08
3.0	0.852	2.471E+08
4.0	0.905	1.347E+08
5.0	0.992	8.123E+07
6.0	1.125	5.642E+07
7.0	1.272	4.217E+07

Table 2.7: Comparison of the He core mass ($M_\alpha^{75\%}$), CO core mass ($M_{\rm CO}$) and final core mass ($M_{\rm final}$) of this work with J15. Core masses are in ${\rm M}_\odot$.

initial mass	$12\,{\rm M}_\odot$		$15\,{\rm M}_\odot$		$20\,{\rm M}_\odot$	
	this work	J15	this work	J15	this work	J15
$M_\alpha^{75\%}$	4.76	4.76	6.77	6.77	9.13	9.13
$M_{\rm CO}$	2.99	2.99	4.65	4.65	6.82	6.82
$M_{\rm Final}$	12.15	12.15	15.40	15.40	12.81	12.82

Table 2.8: Comparison of the He core mass ($M_\alpha^{75\%}$), CO core mass ($M_{\rm CO}$) and Si core mass $M_{\rm Si}$ of this work with M02 and P16. Core masses are in ${\rm M}_\odot$.

initial mass	$15\,{\rm M}_\odot$			$25\,{\rm M}_\odot$		
	this work	M02	P16	this work	M02	P16
$M_\alpha^{75\%}$	5.09	4.45	4.81	9.66	8.44	9.39
$M_{\rm CO}$	3.27	2.27	2.84	7.26	5.35	6.45
$M_{\rm Si}$	2.02		1.7	1.99		1.85

Table 2.9: Core masses for massive star models. For each model the final core mass ($M_{\rm final}$), He core mass ($M_\alpha^{75\%}$), CO core mass ($M_{\rm CO}$) and Si core mass ($M_{\rm Si}$) are shown. Values with * were taken at maximum of the sum of Si+Ar+Ca+Ti. Core masses are in $M_\odot$.

initial mass	$M_{\rm Final}$	$M_\alpha^{75\%}$	$M_{\rm CO}$	$M_{\rm Si}$	$M_{\rm Final}$	$M_\alpha^{75\%}$	$M_{\rm CO}$	$M_{\rm Si}$
	$Z = 0.02$				$Z = 0.01$			
12.0	11.09	3.427	2.014	1.600	10.95	3.665	2.182	1.607
15.0	12.15	4.760	2.989	1.551	13.36	4.946	3.134	1.615
20.0	15.40	6.768	4.651	2.142	17.11	7.209	5.069	1.356
25.0	12.81	9.129	6.815	1.550*	19.73	9.394	7.056	1.808
	$Z = 0.006$				$Z = 0.001$			
12.0	10.71	3.861	2.295	1.617	11.92	4.015	2.392	1.710*
15.0	14.07	5.090	3.265	2.018	14.88	5.231	3.325	1.789
20.0	18.56	7.303	5.158	2.219	19.74	7.567	5.414	2.081
25.0	20.65	9.664	7.264	1.985	24.59	9.715	7.096	2.008
	$Z = 0.0001$							
12.0	11.96	4.142	2.496	1.637				
15.0	14.97	5.275	3.341	1.837				
20.0	19.98	6.429	5.100	1.653*				
25.0	24.96	9.652	6.977	1.982				

Table 2.10: Lifetimes of major central burning stages of massive star models. Shown are lifetimes for H burning, $\tau_{\rm H}$, He burning, $\tau_{\rm He}$, C burning, $\tau_{\rm C}$, Ne burning $\tau_{\rm Ne}$, O burning, $\tau_{\rm O}$, Si burning, $\tau_{\rm Si}$, and the total lifetime of the stellar models, $\tau_{\rm total}$. Times in yr. The complete table is available online.

Model	$\tau_{\rm H}$	$\tau_{\rm He}$	$\tau_{\rm C}$	$\tau_{\rm Ne}$	$\tau_{\rm O}$	$\tau_{\rm Si}$	$\tau_{\rm total}$
			Z = 0.02				
12	1.742E+07	1.669E+06	1.046E+04	1.046E+01	2.973E+00	1.895E-01	1.935E+07
15	1.243E+07	1.250E+06	1.835E+03	2.829E+00	1.361E+00	8.840E-02	1.386E+07
20	8.687E+06	8.209E+05	1.270E+02	1.811E+00	7.086E-01	5.071E-02	9.596E+06
25	6.873E+06	6.426E+05	2.525E+02	5.303E-01	1.390E-01	1.385E-02	7.585E+06

Table 2.11: Model properties of the TP-AGB phase for $Z = 0.006$, 0.001 and 0.0001. The complete table is available online.

M_{ini}	m_c	$logL_*$	R_*	N_{TP}	N_{TDUP}	t_{TPI}	ΔM_{Dmax}	M_D	t_{ip}	M_{lost}	$logT_{CEB,max}$	$logT_{PDCZ,max}$	M_{PDCZ}	$logL_{He,max}$	$logL_{max}$
$[M_\odot]$	$[M_\odot]$	$[L_\odot]$	$[R_\odot]$			$[10^6 yr]$	$[10^{-2}M_\odot]$	$[10^{-2}M_\odot]$	$[yr]$	$[M_\odot]$	$[K]$	$[K]$	$[10^{-2}M_\odot]$	$[L_\odot]$	$[L_\odot]$
Z=0.0001															
1.00	0.532	3.19	75	2	1	5.726E+03	2.485	2.485	274820	0.33	6.266	8.312	3.986	6.72	3.63
1.65	0.589	3.77	161	12	11	1.231E+03	0.702	5.482	91155	0.99	6.870	8.461	2.956	7.53	4.05
2.00	0.655	3.97	205	11	10	7.494E+02	0.895	6.242	56131	1.31	7.114	8.490	1.906	7.89	4.14
3.00	0.848	4.29	295	11	10	2.722E+02	0.242	1.897	8765	2.01	7.715	8.514	0.569	7.63	4.48
4.00	0.899	4.43	345	19	18	1.414E+02	0.246	2.506	5253	3.01	7.979	8.541	0.376	8.00	4.55
5.00	0.982	4.59	413	29	20	8.805E+01	0.111	1.331	2228	3.93	8.057	8.553	0.165	7.82	4.76
6.00	1.124	4.83	572	19	16	6.115E+01	0.038	0.428	824	4.52	8.141	8.561	0.049	7.07	4.96
7.00	1.272	5.05	743	27	21	4.557E+01	0.007	0.091	134	4.70	8.369	8.597	0.009	6.72	5.10

M_{ini}: Initial stellar mass.
m_c: H-free core mass at the first TP.
L_*: Approximated mean stellar luminosity.
R_* : Approximated mean stellar radius.
N_{TP}: Number of TPs.
N_{TDUP} : Number of TPs with TDUP.
t_{TPI}: Time at first TP.
ΔM_{Dmax}: Maximum dredged-up mass after a single TP.
M_D: Total dredged-up mass of all TPs.
t_{ip} : Average interpulse duration of TPs.
M_{lost}: Total mass lost during the TP-AGB phase.
$T_{PDCZ,max}$: Maximum temperature during the TP-AGB phase.
M_{PDCZ}: Maximum size of PDCZ.
$logL_{He,max}$: Maximum He luminosity during TP-AGB phase.
$logL_{max}$: Maximum total luminosity during TP-AGB phase.

Table 2.12: TP-AGB properties for models at $Z = 0.0001$. The complete table is available online.

TP	t_{TP}	$logT_{FBOT}$	$logT_{HES}$	$logT_{HS}$	$logT_{CEB}$	m_{FBOT}	m_{HTP}	$m_{D,max}$	M_*
	$[yr]$	$[K]$	$[K]$	$[K]$	$[K]$	$[M_\odot]$	$[M_\odot]$	$[M_\odot]$	$[M_\odot]$
$M = 1.0M_\odot$									
1	0.00E+00	8.31	8.16	7.75	5.98	0.4926	0.5324	0.5358	0.867
2	2.75E+05	8.09	0.00	0.00	0.00	0.5218	0.5374	0.0000	0.867

TP: TP number.
t_{TP}: Time since the first TP.
T_{FBOT}: Largest temperature at the bottom of the PDCZ.
T_{HES}: Temperature in the He-burning shell during deepest extend of TDUP.
T_{CEB}: Temperature at the bottom of the convective envelope during deepest extend of TDUP.
m_{FBOT}: Minium mass coordinate of the bottom of the He-flash convective zone.
$m_{D,max}$: Mass coordinate of the H-free core at the time of the TP.
M_*: Stellar mass at the TP.

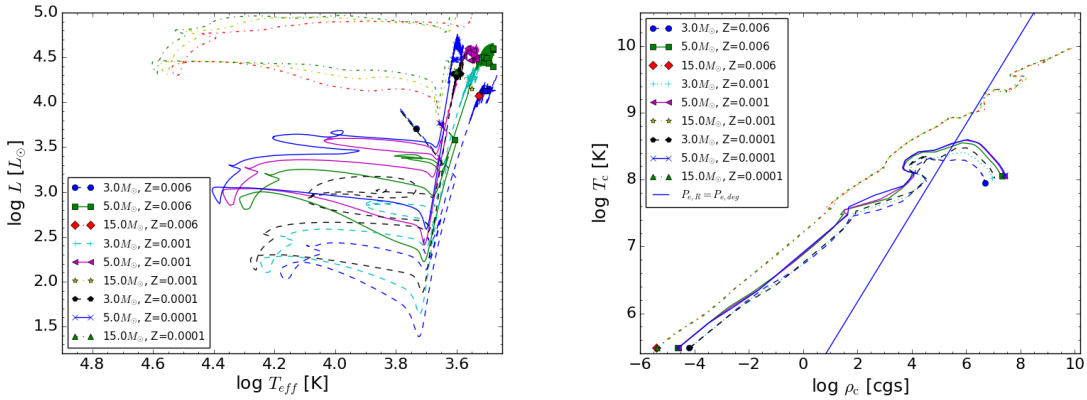

Figure 2.5: Comparison of HRD's (left) and central temperatures T_c and densities ρ_c (right) for AGB models with initial mass of $3\,\mathrm{M}_\odot$ and $5\,\mathrm{M}_\odot$ and massive star models with initial mass of $15\,\mathrm{M}_\odot$ for $Z = 0.006$, $Z = 0.001$ and $Z = 0.0001$. $P_{e,R}$ and $P_{e,deg}$ denote the pressure for a non-degenerate ideal gas and non-relativistic degenerate gas.

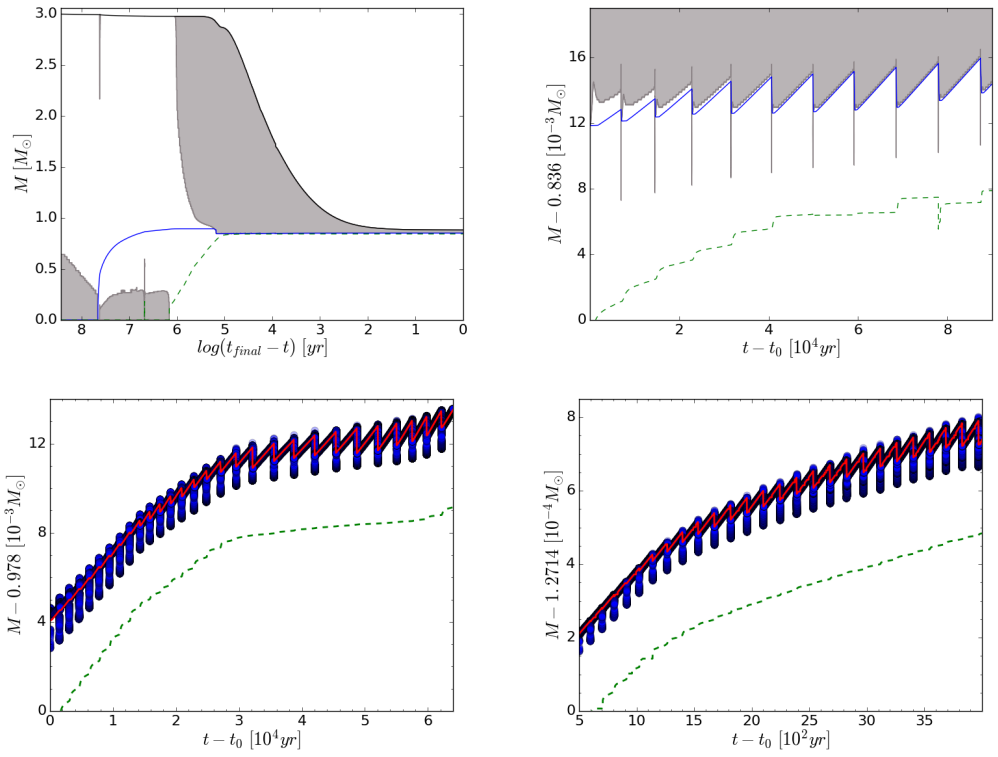

Figure 2.6: Kippenhahn diagrams of a AGB model with initial mass of $3\,M_\odot$ at $Z = 0.0001$ with its pre-AGB phase (top, left) and TP-AGB phase (top, right). Grey areas mark the convective zones. The H-free and He-free core boundaries are displayed by blue solid and green dashed lines. The TP-AGB phase of a massive AGB model with initial mass of $5\,M_\odot$ (bottom, left) and S-AGB model with initial mass of $7\,M_\odot$ (bottom, right) at $Z = 0.0001$ are shown.

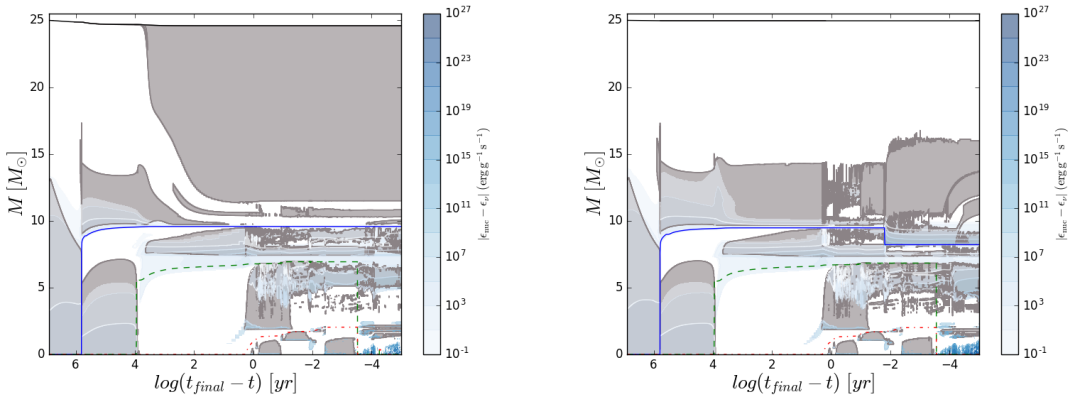

Figure 2.7: Kippenhahn diagrams for two stellar models with initial mass of 25 $M_\odot$ at $Z = 0.001$ (left) and $Z = 0.0001$ (right). Convective zones are marked as gray areas. The purple solid line and green dashed line represent H-free and He-free cores respectively. The red dot-dashed line represent the C-free core. t^* is the time until the infall velocity reaches 1000km/s. Also displayed is the nuclear energy generation ϵ_{nuc}. The specific energy loss rate due to neutrino production via nuclear reaction ϵ_ν is subtracted.

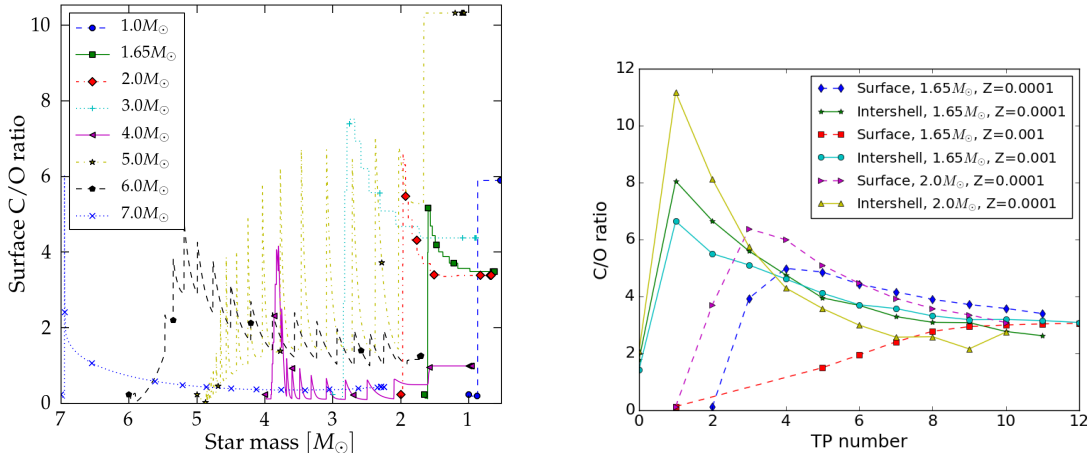

Figure 2.8: Surface C/O ratio versus total stellar mass for $Z = 0.0001$ (left). The He intershell and surface C/O ratio for each TP of two stellar models with initial mass of 1.65 $M_\odot$ and 2 $M_\odot$.

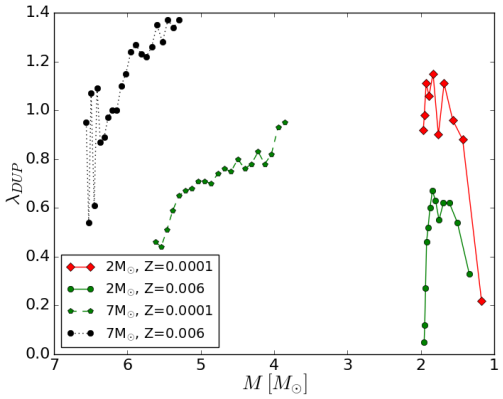

Figure 2.9: Metallicity dependence of the DUP parameter λ shown at the example of low-mass AGB models and a S-AGB models with initial masses of $2\,\mathrm{M}_\odot$ and $7\,\mathrm{M}_\odot$ for $Z = 0.0001$ and $Z = 0.006$.

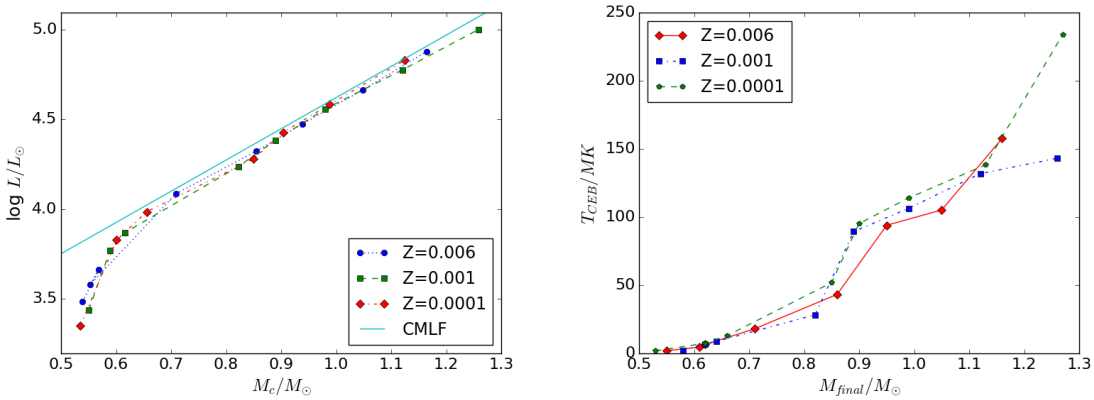

Figure 2.10: Average luminosity versus average core mass of the TP-AGB stage for stellar models at $Z = 0.006, 0.001$ and 0.0001 in comparison with the core-luminosity relation (CMLF, left). Maximum temperature at the bottom of the convective envelope T_{CEB} versus final core mass during the AGB evolution (right).

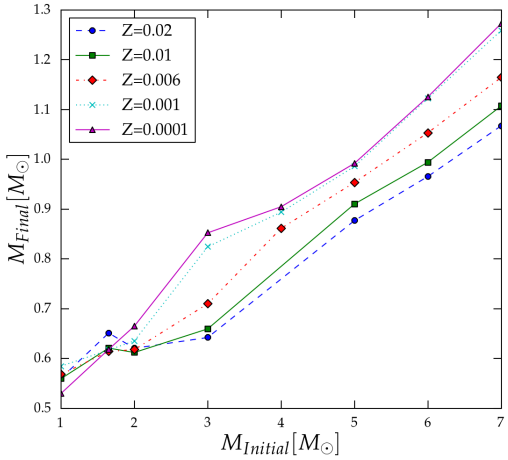

Figure 2.11: Initial-final mass relation for AGB models of this work with AGB models at $Z = 0.02$ and $Z = 0.01$ from P16.

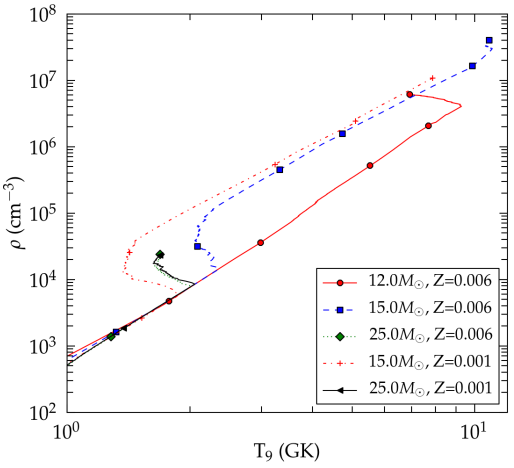

Figure 2.12: Maximum temperature T_9 and density ρ of each zone during the CCSN explosion for massive star models of different initial masses at $Z = 0.006$ and $Z = 0.001$.

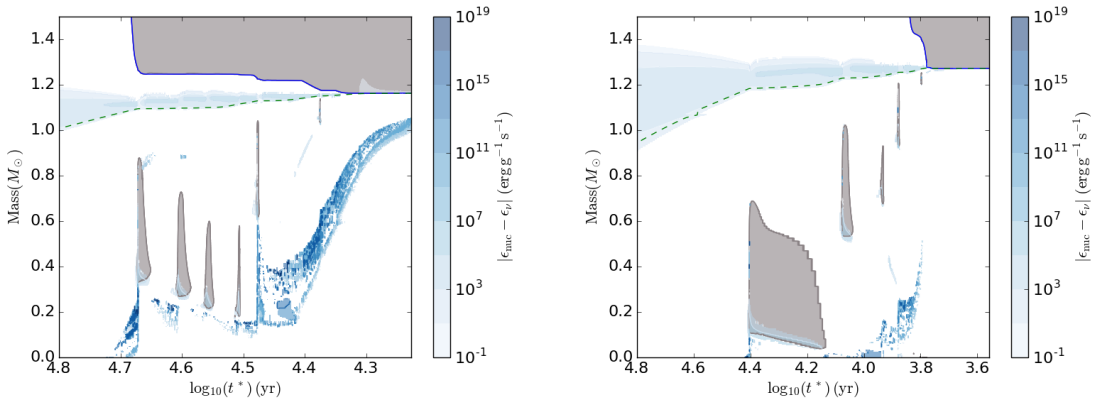

Figure 2.13: Kippenhahn diagrams of the core evolution of two S-AGB models with initial mass of $7\,M_\odot$ at $Z = 0.006$ (left) and $Z = 0.0001$ (right). t^* represents the time until the first thermal pulse. For more details see Fig. 2.7.

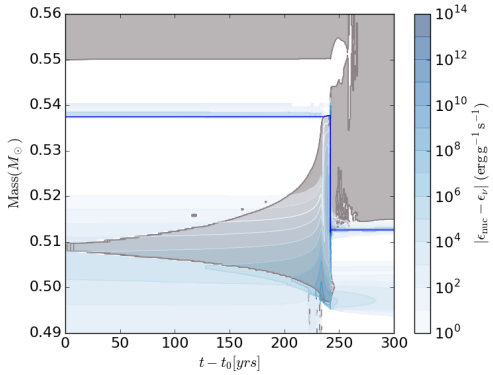

Figure 2.14: H-ingestion in the AGB model with initial mass of $1\,M_\odot$ at $Z = 0.0001$. The H ingestion during the second thermal pulse terminates the TP-AGB phase. t_0 is the time of the appearance of the PDCZ.

2.4 Post-processing nucleosynthesis results

This section complements P16 ($Z \geq 0.01$) and focusses on results obtained for $Z \leq 0.006$. The discussion includes the weak and main s process (Käppeler, Beer, and Wisshak 1989; Straniero et al. 1995; Gallino et al. 1998; Käppeler et al. 2011), the α-process (Woosley and Hoffman 1992; Magkotsios et al. 2010) and p process (Rayet et al. 1995; Arnould and Goriely 2003). Overproduction factors provide a quick overview of which stellar models at which metallicity contribute which elements (Figs. 2.15 through 2.22). We distinguish between yields only from stellar winds, wind yields plus pre-SN yields and the final yields which include wind yields plus SN yields (P16). Final yields are shown for $Z = 0.0001$ in Table 2.13, and all others are available online.

The odd-even effect increases in model predictions with decreasing metallicity (Truran and Arnett 1971). We find this odd-even effect of different strength for intermediate elements in the massive star models (Fig. 2.24).

2.4.1 Dredge-up and dredge-out

In the AGB models with initial mass of $1.65\,M_\odot$ He originates mostly from the first dredge-up. For higher initial masses the contribution of the second dredge-up increases while the contribution of the first dredge-up decreases. Stellar models of the same initial mass experience deeper first dredge-up at higher metallicity. The initial mass above which the second dredge-up is responsible for most He is $2\,M_\odot$ at $Z = 0.0001$ and $3\,M_\odot$ at $Z = 0.006$. The largest overproduction of He of AGB models occurs at the highest initial masses.

C is primary produced during He burning in AGB models and massive star models (Herwig 2004; Woosley and Weaver 1995). The overproduction factors of AGB models peak at the initial mass of $2\,M_\odot$ for $Z = 0.006$ and $Z = 0.001$ and at the initial mass of $1.65\,M_\odot$ for $Z = 0.0001$ (Fig. 2.25). The total amount of dredged-up material reaches a maximum in these three initial stellar models (Table 2.11). The largest overproduction factors of AGB models are slightly larger than those found in massive star models. We find dredge-out (Ritossa, García-Berro, and Iben 1999) in stellar models with initial mass of $7\,M_\odot$ at $Z = 0.001$ and $Z = 0.0001$ where it is the main source of surface enrichment of C.

O is primarily produced in AGB models in the He intershell and during He- and Ne-burning layers of massive star models (Woosley, Heger, and Weaver 2002). The

CBM prescription applied in these AGB models at the bottom of the PDCZ (Herwig et al. 2007) leads to O enhancement in the He intershell of $X(^{16}\mathrm{O}) \approx 15\%$ compared to 2% without CBM (Herwig 2005). In these AGB models O is mostly produced at low initial masses where it is dredged up from the He intershell (Fig. 2.25). The largest overproduction factors of O in AGB models are at the initial mass of $2\,\mathrm{M}_\odot$ at $Z = 0.006$ and $Z = 0.001$. At $Z = 0.0001$ the stellar model of $1.65\,\mathrm{M}_\odot$ has the largest overproduction factor of O.

2.4.2 HBB nucleosynthesis

Li is produced during HBB through the Cameron-Fowler mechanism in massive AGB models ($T_{CEB} \geq 30$MK, Cameron and Fowler 1971; Sackmann and Boothroyd 1992). We improved over the approach of P16 and resolve the simultaneous burning and mixing of CNO isotopes while still including all heavy species in the calculation (Sect. 2.3.2). Li is effectively produced in all these massive AGB models and the largest yields for each metallicity result from these most massive AGB models (Fig. 2.15 to Fig. 2.19).

HBB in AGB models synthesizes large amounts of primary N while the pre-explosive CN cycle in the external He-rich layers produce most N in massive star models which is secondary (Woosley, Heger, and Weaver 2002). The overproduction factors of N strongly increase for these stellar models with initial mass above $3\,\mathrm{M}_\odot$ at $Z = 0.001$ and $Z = 0.0001$ due to HBB (Fig. 2.25). The production of N increases in stellar models at lower metallicity due to the larger temperatures at the bottom of the convective envelope T_{CEB} (Table 2.11).

In these most massive AGB models the activation of the (complete) CNO cycle at $T_{CEB} \approx 80$ MK due to HBB leads to effective O destruction (Fig. 2.25) as in Ventura et al. (2013). More efficient destruction of O occurs at lower Z due to higher T_{CEB}. The highest overproduction factors of all these stellar models are found in the massive star models where most production takes place in the pre-SN stage. In the massive star models the amount of O increases with initial mass up to $20\,\mathrm{M}_\odot$ while at $25\,\mathrm{M}_\odot$ large parts of the O shell are not ejected due to fallback (Fig. 2.25).

2.4.3 C/Si zone and n process

Neutron-rich isotopes are produced in the He shell and upper part of the C shell via the n process during the explosive nucleosynthesis of massive star models (Thiele-

mann, Arnould, and Hillebrandt 1979; Rauscher et al. 2002). In these layers O is transformed through α-chains into isotopes up to ^{28}Si which leads to the formation of a C/Si zone (Pignatari et al. 2013a). We find the C/Si zone in all these massive star models. As fallback in the most massive stellar models with initial mass of $25\,M_\odot$ prevents the ejection of deeper layers the more external located C/Si zone and n-process nucleosynthesis become more relevant for the total production. In the stellar model with initial mass of $25\,M_\odot$ at $Z = 0.006$ the largest contribution to the neutron-rich ^{40}Ar originates from the n process in the C/Si zone.

The C/Si zone in the stellar model at $Z = 0.006$ is broader in mass and the efficiency of the n process is larger than in the stellar model at $Z = 0.0001$ (Fig. 2.29). The efficiency of the n process production decreases with metallicity as indicated in the decrease of the yields of its tracer ^{30}Si in stellar models with initial mass of $25\,M_\odot$.

2.4.4 Shell merger nucleosynthesis

During Si shell burning convective O-C shell mergers occur in the massive star models with initial mass of $12\,M_\odot$, $15\,M_\odot$, $20\,M_\odot$ at $Z = 0.01$ and $15\,M_\odot$ at $Z = 0.02$. In these models the convective O shell increases in mass and touches the C-shell. C-shell material is mixed into the O shell until both convective shells fully merge. Burning of the ingested Ne results in large overproduction factors of the odd-Z elements P, Cl, K and Sc in Fig. 2.20 (Ritter et al. 2017, in prep.)

In the stellar model with initial mass of $20\,M_\odot$ at $Z = 0.01$ the convective Si burning shell grows in mass until it reaches the C shell. In the following merger of the convective Si-O shell and convective C shell Fe-peak elements are transported out of the deeper layers which fall back onto the remnant during CCSN. This boosts the production of Fe peak elements, in particular Cr (Fig. 2.20).

The stellar evolution assumptions of these stellar models such as the approximation of spherical symmetry do not describe accurately the interaction of convective C, O and Si burning shells (Meakin and Arnett 2006b; Arnett and Meakin 2011). Instead, 3D hydrodynamic simulations are required to analyze the dynamics of the convective shells and the nucleosynthesis and will be discussed in more detail in Ritter et al. (2017, in prep. , Chapter 5).

2.4.5 Fe-peak elements

The synthesis of Fe-peak elements are largely independent of the initial metallicity (Woosley, Heger, and Weaver 2002). The odd-even effect decreases for Fe-peak nuclei in these massive star models such as in the stellar model with initial masses of $12\,M_\odot$ (Fig. 2.24). Fallback leads to a lower amount of Fe-peak elements ejected these stellar models with initial mass of $20\,M_\odot$ and prevents any Fe ejection in stellar models with initial mass of $25\,M_\odot$ (Fig. 2.20 to Fig. 2.22). In the stellar model with initial mass of $15\,M_\odot$ the ratio of explosive production to pre-SN production of Fe peak elements increases towards lower metallicity (Fig. 2.23). In contrast, for stellar models with initial mass of $20\,M_\odot$ we find for the model of $Z = 0.006$ the largest ratio which might be due to the larger cores mass of this model (Si core mass in Table 2.9). To the production of Fe-peak elements in explosive Si burning comes a significant contribution from α-rich freeze-out in stellar models with initial mass of $12\,M_\odot$ and $15\,M_\odot$ (Section 2.4.7). The interplay of the core masses at collapse (Table 2.9) and the effect of fallback (Table 2.5 results in large variations of the Fe-peak elements with initial mass and metallicity.

2.4.6 H-ingestion nucleosynthesis

Li is effectively produced due to H ingestion events in the massive star models with initial mass of $20\,M_\odot$ and $25\,M_\odot$ at $Z = 0.0001$ (Fig. 2.22). The amount of Li produced in the stellar model of $25\,M_\odot$ is similar to the production in the most massive AGB models at $Z = 0.0001$. An initial Li abundance well below the Li plateau was unintentionally adopted in these stellar models which does not affect the Li production. The burning of ingested H produces to the most N of all stellar models at $Z = 0.0001$. At higher metallicity hot-bottom burning AGB models are the largest producer. The explosion further increases the amount of N in the layers enriched by the ingested H in stellar model with initial mass of $25\,M_\odot$ at $Z = 0.0001$ of this work similar to massive star models at low-Z (Woosley and Weaver 1995) and Pop III models (Heger and Woosley 2010). The radiative envelopes of both stellar models prevent surface enrichment.

As previously reported by Pignatari et al. (2015) ^{15}N is effectively produced in the region of pre-SN H ingestion during the explosive nucleosynthesis in models of this work. Relative to its pre-SN abundance ^{15}N is orders of magnitude more produced than ^{14}N as visible in the ratio of SN yields to pre-SN yields of these stellar model

with initial mass of $20\,M_\odot$ in Fig. 2.23. The ingestion events might be a relevant source of primary production of ^{14}N and ^{15}N at low Z in contrast to rotating massive star models (e.g. Hirschi 2007) which fail to produce the $^{14}N/^{15}N$ ratio observed in the Sun (Pignatari et al. 2015). ^{19}F is efficiently produced through $^{15}N(\alpha,\gamma)^{19}F$ in these stellar model with initial mass of $25\,M_\odot$ (Fig. 2.22).

In the first TP of the stellar model with initial mass of $1\,M_\odot$ at $Z = 0.0001$ the ingestion of H leads efficient production of heavy elements up to Pb. During the second TP the PDCZ growths in mass and reaches out into the convective envelope (Fig. 2.14). Heavy elements are transported to the surface which results in large overproduction factors from the first s-process peak up to Pb (Fig. 2.19).

2.4.7 α process

Matter in nuclear statistical equilibrium (NSE) during the CCSN explosion which experience fast expansion and cooling experiences an α-rich freeze-out (Woosley, Arnett, and Clayton 1973; Woosley and Hoffman 1992). Such α-rich freeze out conditions are reached in these stellar models with initial mass of $12\,M_\odot$ and $15\,M_\odot$ (Fig. 2.26). A larger α-rich freeze-out layer formed during the explosive nucleosynthesis of the stellar models with initial mass of $15\,M_\odot$ compared to the stellar models with initial mass of $12\,M_\odot$ leads to a stronger production of Fe-peak elements compared to the production in explosive Si burning. The NSE layers in the stellar models with initial mass of $15\,M_\odot$ produce elements up to Mo in agreement with P16 (their Fig. 24). The massive star models of lower initial mass produce only elements up to Ge and Br at $Z = 0.001$ and $Z = 0.001$ respectively (Fig. 2.26). At lower metallicity heavier elements are produced in the NSE region than in stellar models of higher metallicity (Fig. 2.26).

2.4.8 Weak s-process

The weak s process takes place at the end of core He-burning and during the convective C shell burning in massive star models and is metallicity dependent (e.g. Prantzos, Hashimoto, and Nomoto 1990; Käppeler, Beer, and Wisshak 1989; Käppeler et al. 2011). We compare the heavy element production up to the first s-process peak which results from the weak s process these stellar models with initial mass of $25\,M_\odot$ with element production from the main s process these models with initial mass of $3\,M_\odot$ and $5\,M_\odot$ for $Z = 0.006$, $Z = 0.001$ and $Z = 0.0001$ (Fig. 2.27). The weak s-process

production is overall the largest at $Z = 0.006$ but drops for lower metallicities due to the lower amounts of Fe seeds and poisoning through the initially enhanced ^{16}O. The latter is known to reduce the s-process efficiency drastically (Baraffe, El Eid, and Prantzos 1992; Pignatari and Gallino 2007). The overproduction factors of elements above As in the massive star model at $Z = 0.0001$ are below those of the AGB models (Fig. 2.27).

The overproduction factors of the s-only isotopes ^{70}Ge, ^{76}Se, ^{80,82}Kr and ^{86,87}Sr of the stellar models with initial mass of $25\,M_\odot$ at $Z = 0.006$, $Z = 0.001$ and $Z = 0.0001$ show the strong decrease in the s-process efficiency below $Z = 0.001$ (Fig. 2.28). In these massive star models most production of ^{70}Ge takes place in the pre-explosive nucleosynthesis as indicated by the overproduction factors of the pre-explosive ejecta compared to the explosive ejecta for the model at $Z = 0.006$ (Fig. 2.28). In stellar models of lower initial mass the explosive nucleosynthesis produces further ^{70}Ge which increases the overproduction factors of the explosive ejecta over that of the pre-explosive ejecta. The strong production in the stellar model with initial mass of $15\,M_\odot$ origins from a shocked thin Fe core layer.

2.4.9 Main s-process

The main s process takes place in the ^{13}C-pocket of low-mass AGB stars and in the PDCZ of massive AGB stars and is of secondary nature (Gallino et al. 1998; Busso, Gallino, and Wasserburg 1999). In these AGB models the ^{13}C-pocket size $M_{^{13}C}$ depends on the efficiency of the CBM and decreases at $Z = 0.0001$ from the $M_{^{13}C} \approx 10^{-5}\,M_\odot$ in the model with initial mass of $2\,M_\odot$ to $M_{^{13}C} \approx 10^{-8}\,M_\odot$ in the model with initial mass of $7\,M_\odot$. $M_{^{13}C}$ in model of $2\,M_\odot$ is similar to the size of $2 - 3 \times 10^{-5}\,M_\odot$ as in Lugaro et al. (2003) and P16. The decreasing pocket size with initial mass leads to a drastic decrease of s-process production in massive AGB and S-AGB models.

We compare the overproduction factors of heavy elements of these low-mass AGB models, massive AGB models and S-AGB models with AGB models of $Z = 0.02$ from P16 (Fig. 2.31). In stellar models with initial mass of $1\,M_\odot$ at $Z = 0.006$ and $Z = 0.001$ inefficient TDUP leads to little surface enrichment except for the model at $Z = 0.0001$ which experiences H ingestion (Section 2.4.6). For stellar models with $M_{ini} \leq 2\,M_\odot$ the total dredged-up mass M_D increases with initial mass which leads to an increase of the overproduction factors of heavy elements with initial mass

(Table 2.12). The overproduction factors of peak s-proces elements tend to decrease for $M_{ini} > 3\,M_\odot$ because of the larger envelope masses dilute the heavy elements, a decrease of M_D and smaller ^{13}C pockets (Table 2.12).

With decreasing metallicity lower initial masses have the largest overproduction factors (Fig. 2.31). The largest overproduction factors of Sr and Pb are present in low-mass AGB models with initial masses below $4\,M_\odot$. The overproduction factors are the largest around Zr at the first s-process peak due to efficient production of ^{96}Zr in the TP of AGB models with initial mass of $3\,M_\odot$, $4\,M_\odot$ and $5\,M_\odot$ (Fig. 2.31). Rb is also efficient produced in the TP of massive AGB stars and its ratio to Sr, which is mostly produced in low-mass AGB models, increases from low-mass AGB stars to massive AGB stars. At lower metallicity the higher pulse temperature T_{PDCZ} results in a larger Rb/Sr ratio in the stellar models with initial mass of $2\,M_\odot$ (Fig. 2.31).

^{87}Rb and ^{88}Sr have the largest overproduction factors in models of $4\,M_\odot$ at $Z = 0.006$ in agreement with models of the same initial mass at $Z = 0.01$ of P16. ^{208}Pb has the highest overproduction factors in the stellar model with initial mass of $3\,M_\odot$ at $Z = 0.006$ in agreement with AGB models at $Z = 0.01$ of P16.

2.4.10 p-process

The p process takes place in explosive Ne and O burning of CCSN models where heavy seed nuclei are destroyed through photo-disintegration and proton capture (Woosley and Howard 1978). In the massive star models presented here the lightest p nuclei ^{74}Se, ^{78}Kr and ^{84}Sr are more strongly produced than most heavier p-process isotopes in stellar models with initial mass up to $20\,M_\odot$ (Fig. 2.30). These isotopes are formed in the deepest layers of explosive O burning due to their light masses and strong fallback prevents any production of ^{74}Se, ^{78}Kr and ^{84}Sr in the massive star models with initial mass of $25\,M_\odot$. In the latter models only the heaviest p nuclei such as ^{180}Ta and ^{180}W are ejected.

Models with initial mass of $15\,M_\odot$ produce the majority of p-process isotopes from the α-rich freeze-out layers. For increasing metallicity the relative contribution of the α-rich freeze-out material to the total amount of produced ^{74}Se, ^{78}Kr and ^{84}Sr decreases. At $Z = 0.006$ the production in α-rich freeze-out layers of the model of $15\,M_\odot$ would become negligible. But in this model an additional production of light p nuclei takes place in a shocked and ejected thin Fe core layer.

The dominant production of $^{92,94}Mo$, including contributions to $^{96,98}Ru$, occurs in

the same α-rich freeze-out layers as ^{74}Se, ^{78}Kr and ^{84}Sr. Heavier p-process isotopes are mostly produced in O and Ne shell burning of these massive star models which is the only p-process site in stellar models with initial mass of $20\,M_\odot$ and $25\,M_\odot$ because of the lack of α-rich freeze-out layers. In stellar models with initial mass of $20\,M_\odot$ we find larger production than in those of $12\,M_\odot$ (Fig. 2.30).

Table 2.13: Yields derived from stellar winds, pre-SN and SN ejecta for $Z = 0.0001$. The SN ejecta is produced with the delayed explosion prescription.

wind												
specie	1 $M_\odot$	1.65 $M_\odot$	2 $M_\odot$	3 $M_\odot$	4 $M_\odot$	5 $M_\odot$	6 $M_\odot$	7 $M_\odot$	12 $M_\odot$	15 $M_\odot$	20 $M_\odot$	25 $M_\odot$
C	8.708E-03	2.147E-02	2.356E-02	8.884E-03	1.988E-03	7.856E-04	2.937E-04	1.797E-03	4.031E-07	2.472E-07	2.913E-07	4.980E-07
N	7.763E-05	5.710E-05	3.870E-05	3.408E-05	1.019E-02	4.692E-03	2.360E-03	8.018E-03	4.301E-07	2.674E-07	2.471E-08	4.223E-08
O	1.835E-03	8.626E-03	9.952E-03	2.781E-03	4.080E-03	1.833E-04	2.239E-04	3.249E-03	2.939E-06	1.671E-06	1.721E-06	2.942E-06
F	3.522E-08	2.432E-06	2.565E-06	3.756E-08	7.060E-09	1.065E-09	6.403E-10	9.822E-09	2.166E-11	1.246E-11	1.304E-11	2.229E-11
Ne	1.487E-05	8.758E-04	9.089E-04	1.138E-04	2.528E-04	4.369E-05	5.373E-05	1.268E-04	2.461E-07	1.412E-07	1.371E-07	2.344E-07
Na	1.903E-07	6.951E-06	6.375E-06	1.020E-06	1.500E-06	3.222E-07	1.138E-07	5.084E-07	8.330E-09	4.204E-09	9.296E-10	1.589E-09
Mg	1.005E-06	5.403E-05	9.078E-05	3.960E-05	1.193E-04	2.429E-05	1.937E-05	4.907E-05	7.500E-08	4.634E-08	3.896E-08	6.660E-08
Al	3.506E-08	3.905E-07	8.674E-07	6.366E-07	2.057E-06	2.275E-06	1.841E-06	1.037E-06	3.202E-09	1.937E-09	1.506E-09	2.575E-09
Si	7.645E-07	1.791E-06	2.559E-06	3.970E-06	6.714E-06	7.136E-06	1.495E-05	9.418E-06	6.802E-08	3.953E-08	3.666E-08	6.266E-08
S	5.121E-07	1.134E-06	1.469E-06	2.391E-06	3.455E-06	4.471E-06	5.436E-06	6.386E-06	4.806E-08	2.793E-08	2.590E-08	4.427E-08
Ar	8.228E-08	1.820E-07	2.359E-07	3.843E-07	5.537E-07	7.182E-07	8.738E-07	1.027E-06	7.738E-09	4.498E-09	4.170E-09	7.129E-09
Ca	5.590E-08	1.240E-07	1.607E-07	2.630E-07	3.790E-07	4.920E-07	5.993E-07	7.038E-07	5.303E-09	3.082E-09	2.858E-09	4.885E-09
Fe	6.453E-07	1.451E-06	1.881E-06	3.073E-06	4.429E-06	5.754E-06	7.012E-06	8.238E-06	6.202E-08	3.605E-08	3.342E-08	5.714E-08
Sr	6.005E-09	3.708E-09	2.515E-09	1.657E-09	2.446E-09	1.014E-09	3.665E-10	3.752E-10	2.619E-12	1.522E-12	1.411E-12	2.412E-12
Ba	3.250E-09	2.820E-10	2.351E-10	4.156E-10	9.354E-10	2.492E-10	9.297E-11	1.114E-10	7.818E-13	4.544E-13	4.213E-13	7.202E-13
Eu	3.857E-12	6.504E-13	9.461E-13	1.386E-12	2.736E-12	1.848E-12	1.967E-12	2.290E-12	1.849E-14	1.075E-14	9.967E-15	1.704E-14
Pb	3.221E-10	4.503E-10	7.906E-10	2.868E-10	5.420E-10	2.010E-10	8.544E-11	9.068E-11	6.482E-13	3.768E-13	3.493E-13	5.972E-13

wind + pre-SN ejecta					Wind + SN ejecta			
specie	12 $M_\odot$	15 $M_\odot$	20 $M_\odot$	25 $M_\odot$	12 $M_\odot$	15 $M_\odot$	20 $M_\odot$	25 $M_\odot$
C	1.294E-01	1.686E-01	2.128E-01	2.320E-01	1.226E-01	1.646E-01	1.956E-01	2.037E-01
N	2.159E-04	3.034E-04	2.001E-02	1.041E-02	2.164E-04	3.050E-04	2.320E-02	2.813E-02
O	7.383E-01	1.339E+00	2.044E+00	7.407E-01	2.828E-01	1.176E+00	2.043E+00	7.062E-01
F	2.482E-08	3.120E-08	7.212E-08	3.463E-07	2.752E-08	4.500E-08	9.317E-08	2.585E-06
Ne	6.624E-02	1.989E-01	2.638E-01	8.609E-02	6.669E-03	1.469E-01	1.607E-01	1.227E-01
Na	2.475E-04	8.799E-04	1.662E-03	1.031E-03	1.812E-05	5.359E-04	6.145E-04	1.018E-03
Mg	6.435E-02	7.448E-02	1.011E-01	4.728E-03	1.638E-02	7.562E-02	1.160E-01	2.178E-02
Al	1.640E-03	1.436E-03	1.536E-03	7.644E-05	6.219E-05	1.157E-03	1.505E-03	1.315E-04
Si	4.380E-02	1.183E-01	2.093E-02	1.294E-04	9.289E-02	1.078E-01	1.138E-01	2.063E-02
S	6.015E-03	7.430E-02	4.377E-04	2.055E-05	5.446E-02	4.459E-02	2.999E-02	2.046E-03
Ar	3.365E-04	8.531E-03	3.551E-06	3.270E-06	1.083E-02	7.684E-03	3.495E-03	1.122E-05
Ca	3.565E-06	3.916E-05	1.977E-06	2.233E-06	8.686E-03	5.152E-03	1.363E-03	2.159E-06
Fe	1.204E-02	3.753E-05	2.378E-05	2.648E-05	2.443E-01	5.073E-02	7.649E-05	2.524E-05
Sr	9.471E-10	1.915E-09	3.577E-09	2.253E-09	7.219E-10	4.976E-08	3.417E-09	2.215E-09
Ba	2.181E-10	3.039E-10	4.202E-10	3.869E-10	1.771E-10	2.812E-10	3.836E-10	3.739E-10
Eu	3.695E-12	4.508E-12	5.702E-12	6.867E-12	3.874E-12	4.845E-12	5.932E-12	7.541E-12
Pb	1.697E-10	2.311E-10	3.149E-10	3.012E-10	1.450E-10	2.163E-10	2.869E-10	3.093E-10

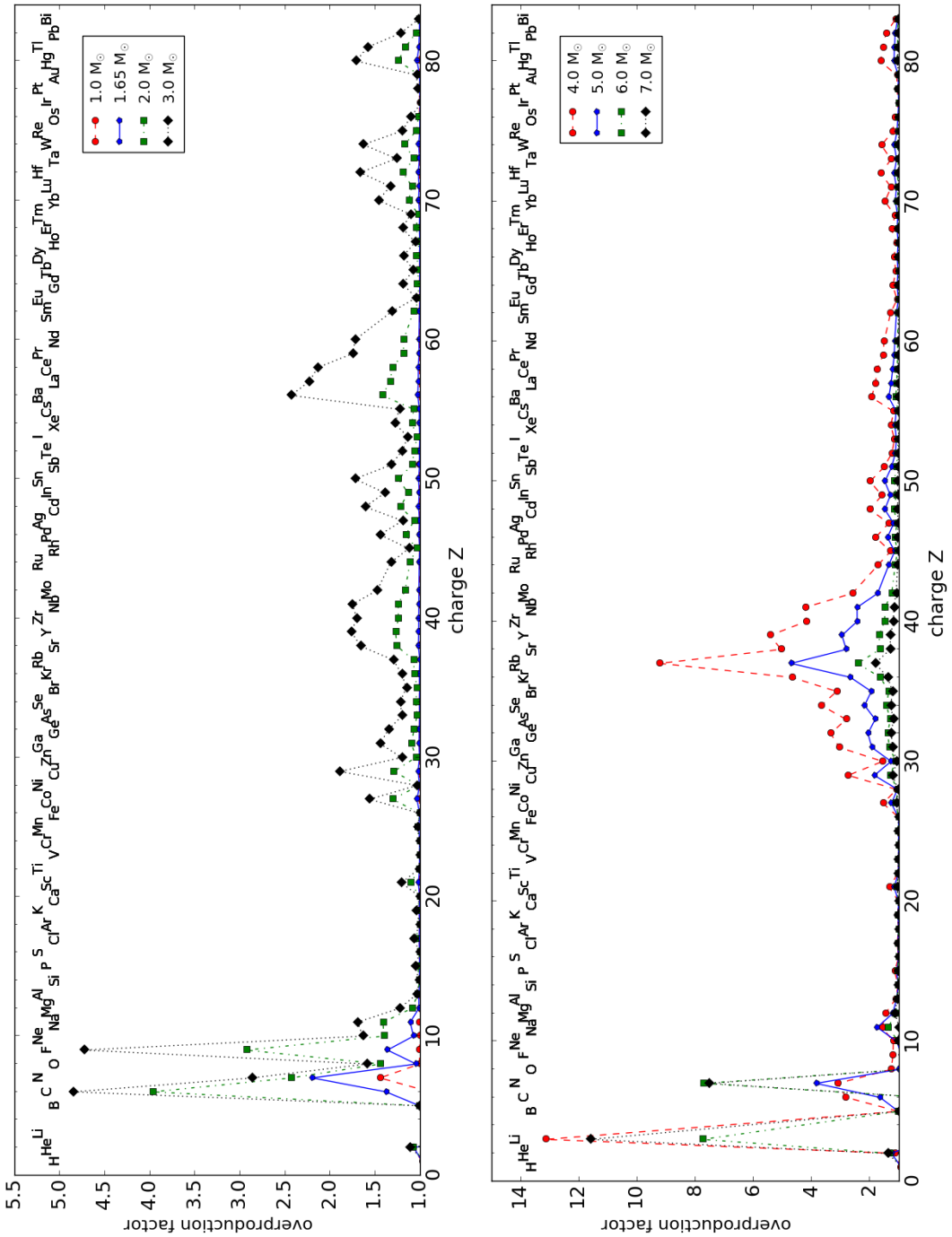

Figure 2.15: Overproduction factors versus charge number of final yields of AGB models at $Z = 0.02$ with stellar models with initial mass of $1.65\,\mathrm{M}_\odot$, $2\,\mathrm{M}_\odot$, $3\,\mathrm{M}_\odot$, $4\,\mathrm{M}_\odot$ and $5\,\mathrm{M}_\odot$ of P16.

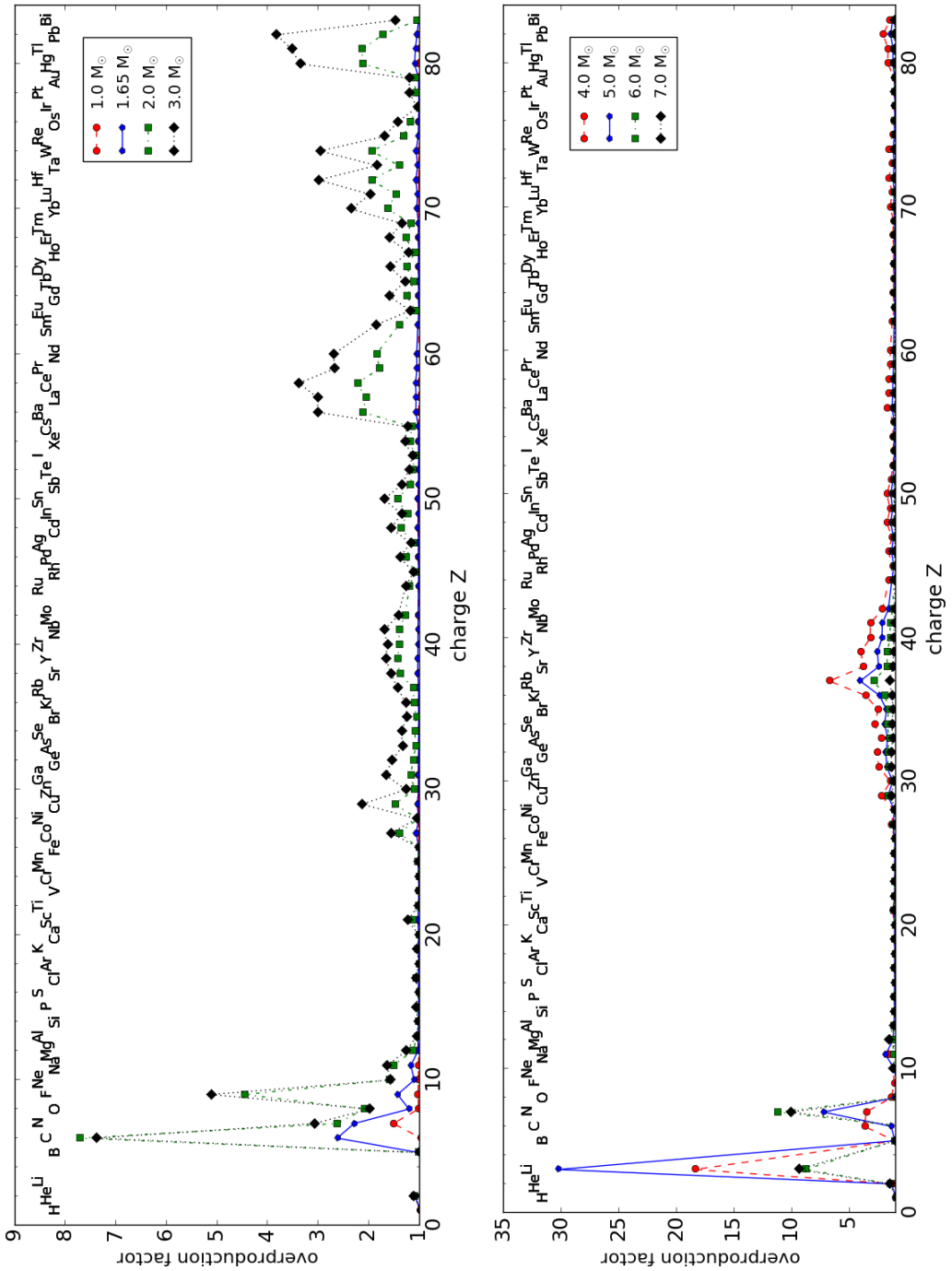

Figure 2.16: Overproduction factors versus charge number of final yields of AGB models at $Z = 0.01$ with stellar models with initial mass of $1.65\,\mathrm{M}_\odot$, $2\,\mathrm{M}_\odot$, $3\,\mathrm{M}_\odot$, $4\,\mathrm{M}_\odot$ and $5\,\mathrm{M}_\odot$ of P16.

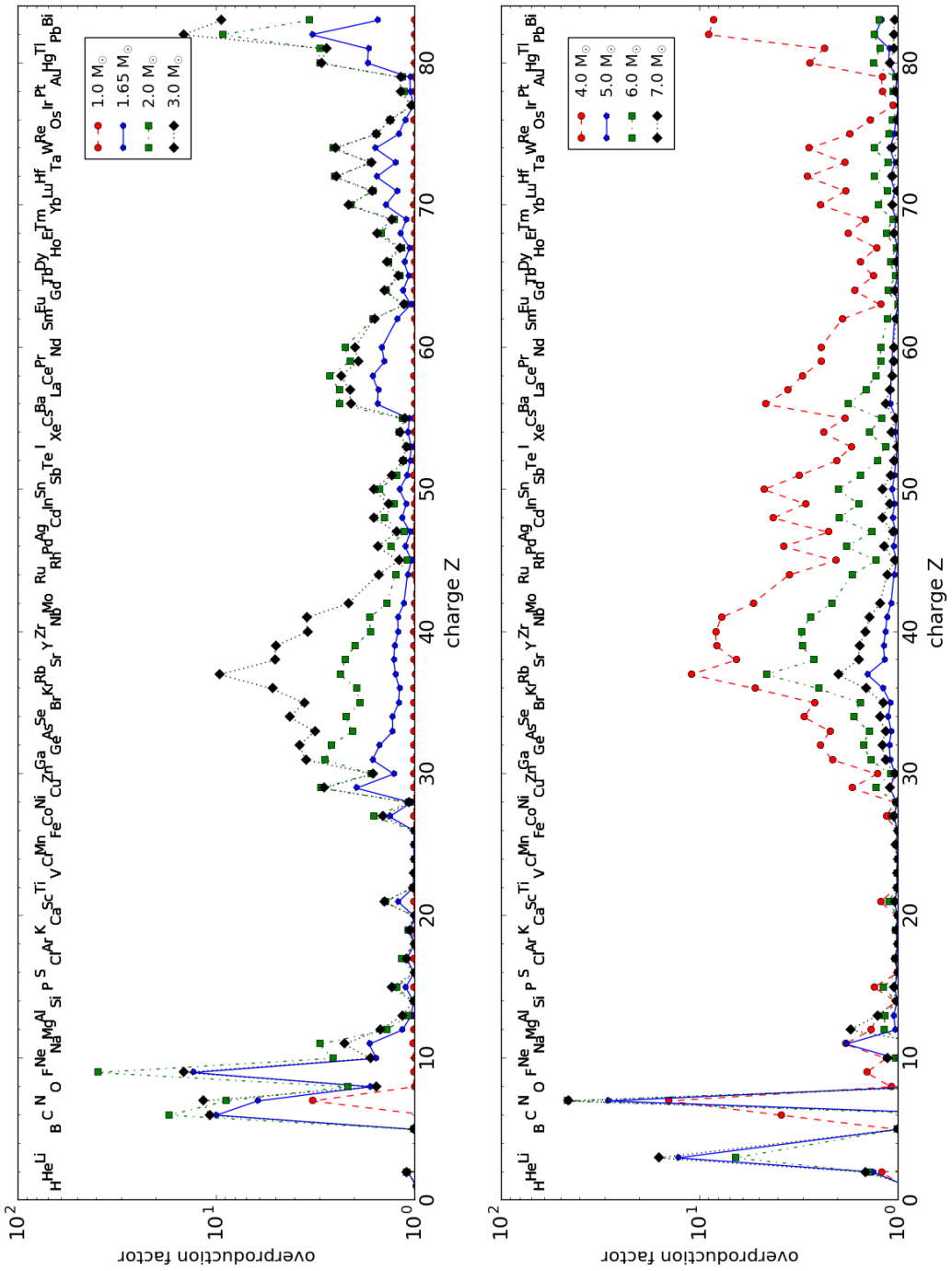

Figure 2.17: Overproduction factors versus charge number of final yields of AGB models at $Z = 0.006$.

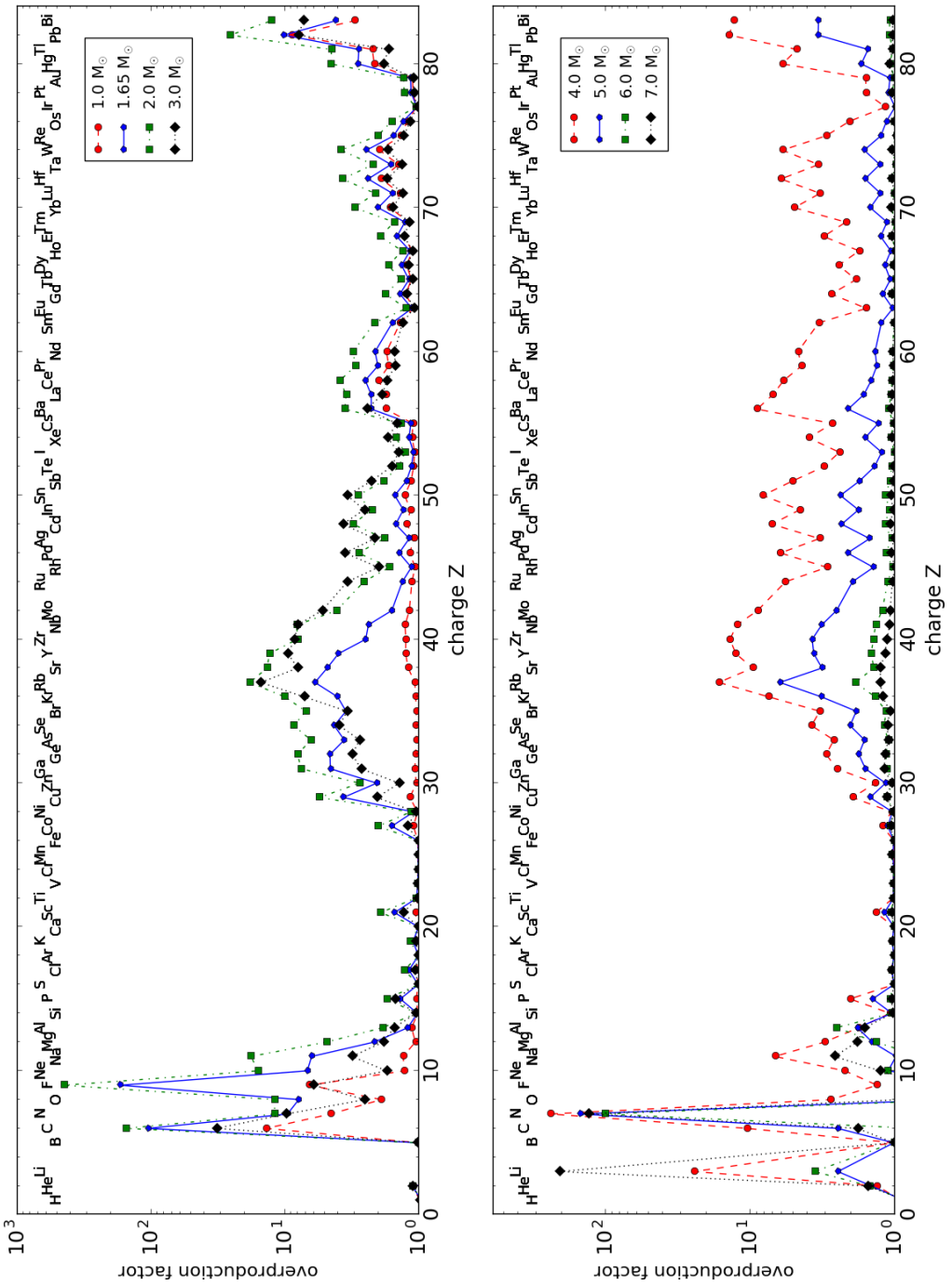

Figure 2.18: Overproduction factors versus charge number of final yields of AGB models at $Z = 0.001$.

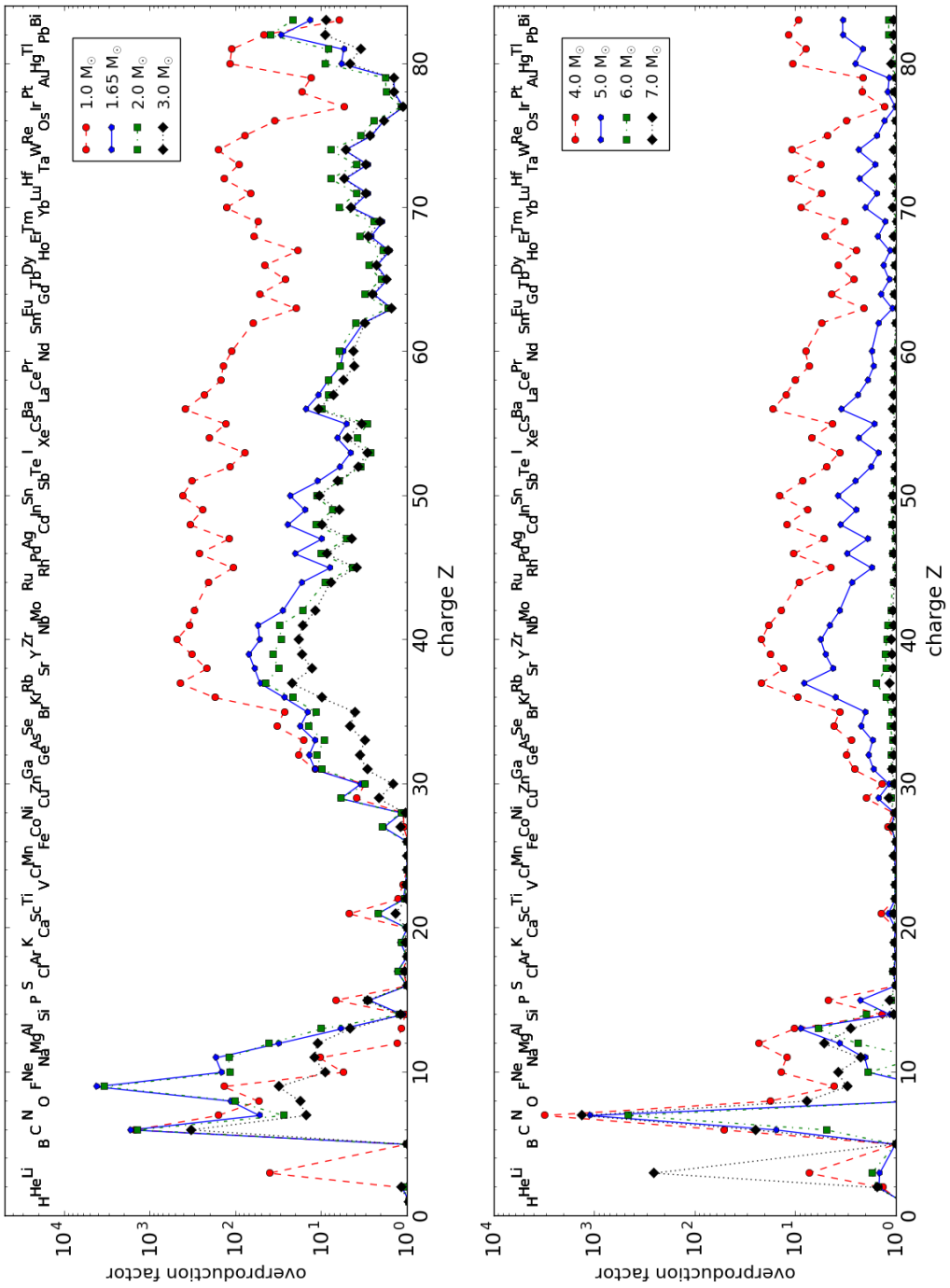

Figure 2.19: Overproduction factors versus charge number of final yields of AGB models at $Z = 0.0001$.

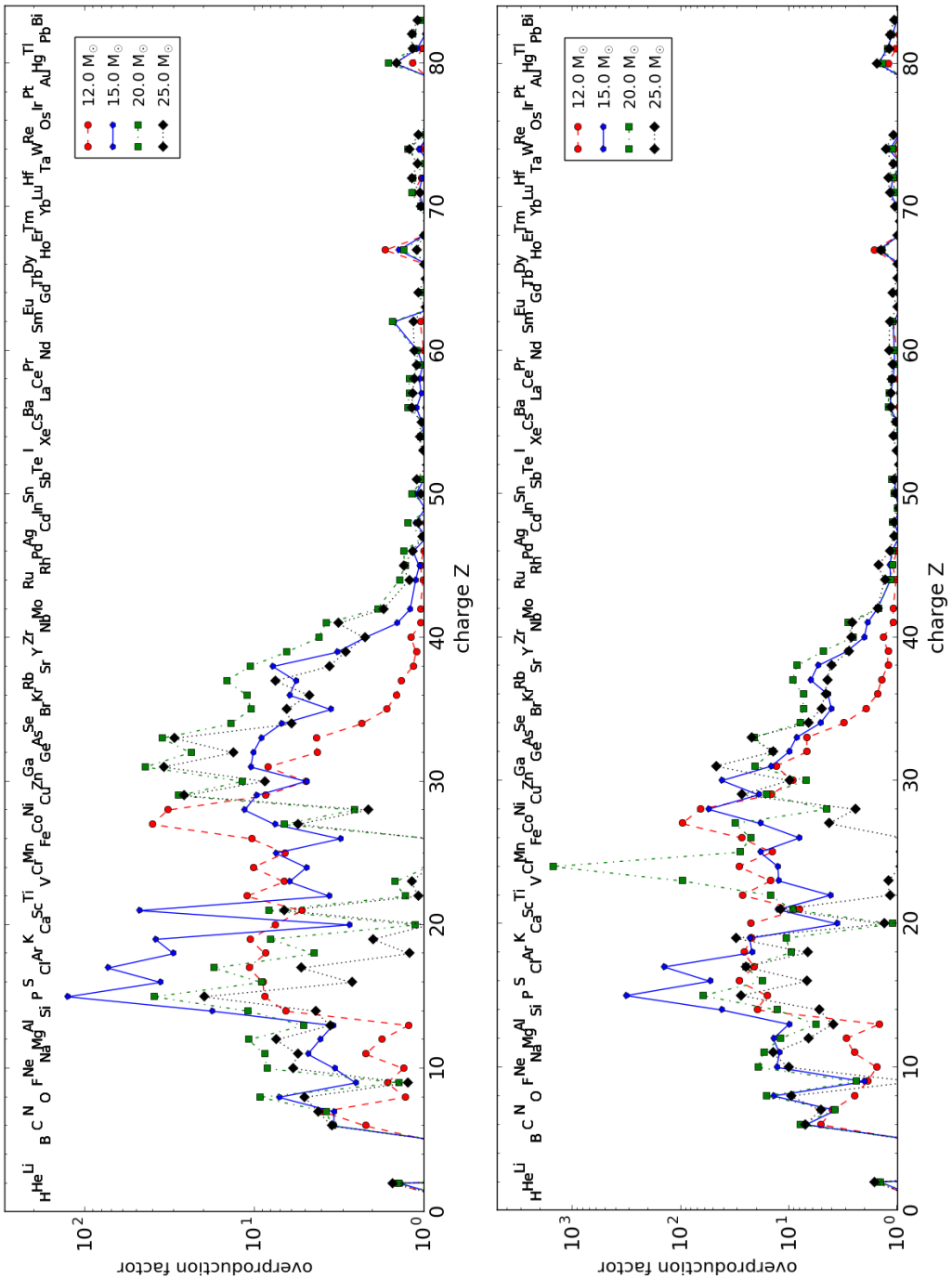

Figure 2.20: Overproduction factors of final yields massive star models at $Z = 0.02$ (top) and $Z = 0.01$ (bottom).

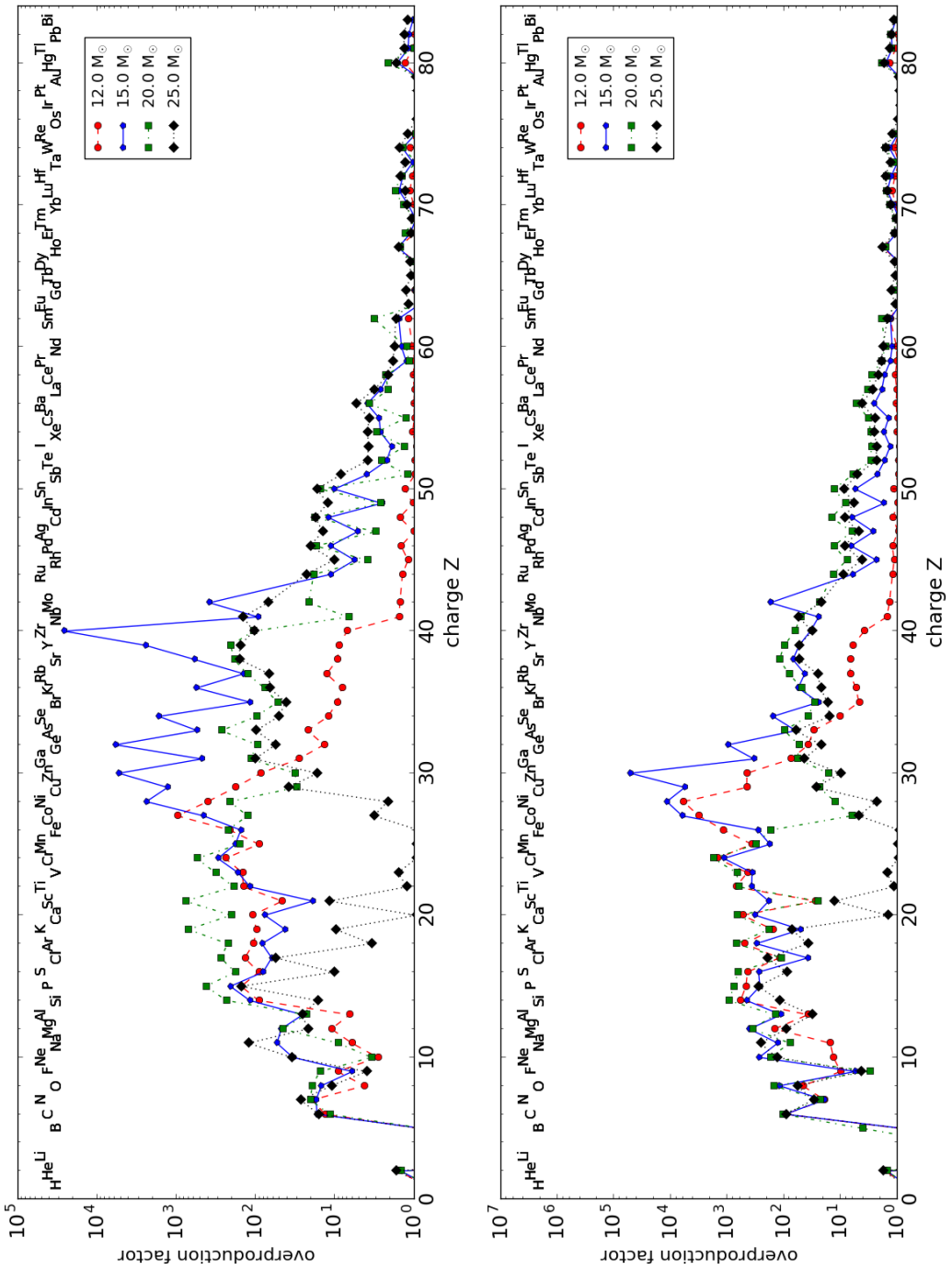

Figure 2.21: Overproduction factors versus charge number of massive star models at $Z = 0.006$ (top) and $Z = 0.001$ (bottom).

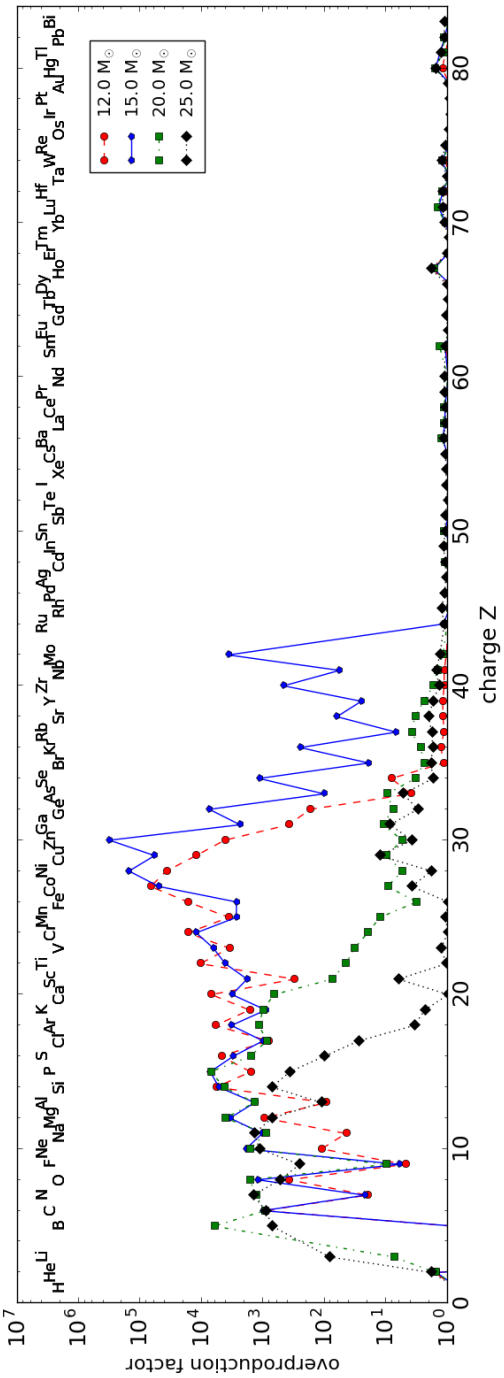

Figure 2.22: Overproduction factors versus charge number of final yields of massive star models at $Z = 0.0001$.

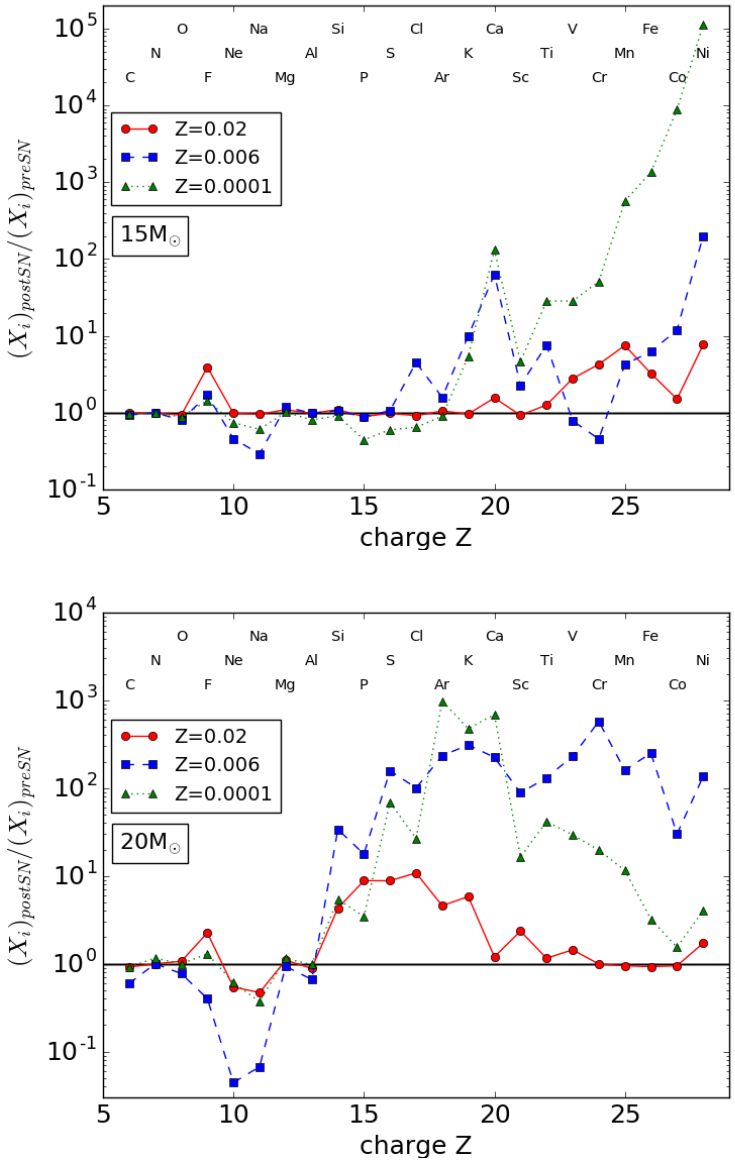

Figure 2.23: Ratio of SN to pre-SN yields versus charge number of stellar models with initial mass of $15\,\mathrm{M}_\odot$ and $20\,\mathrm{M}_\odot$ for $Z = 0.02$, $Z = 0.006$ and $Z = 0.0001$.

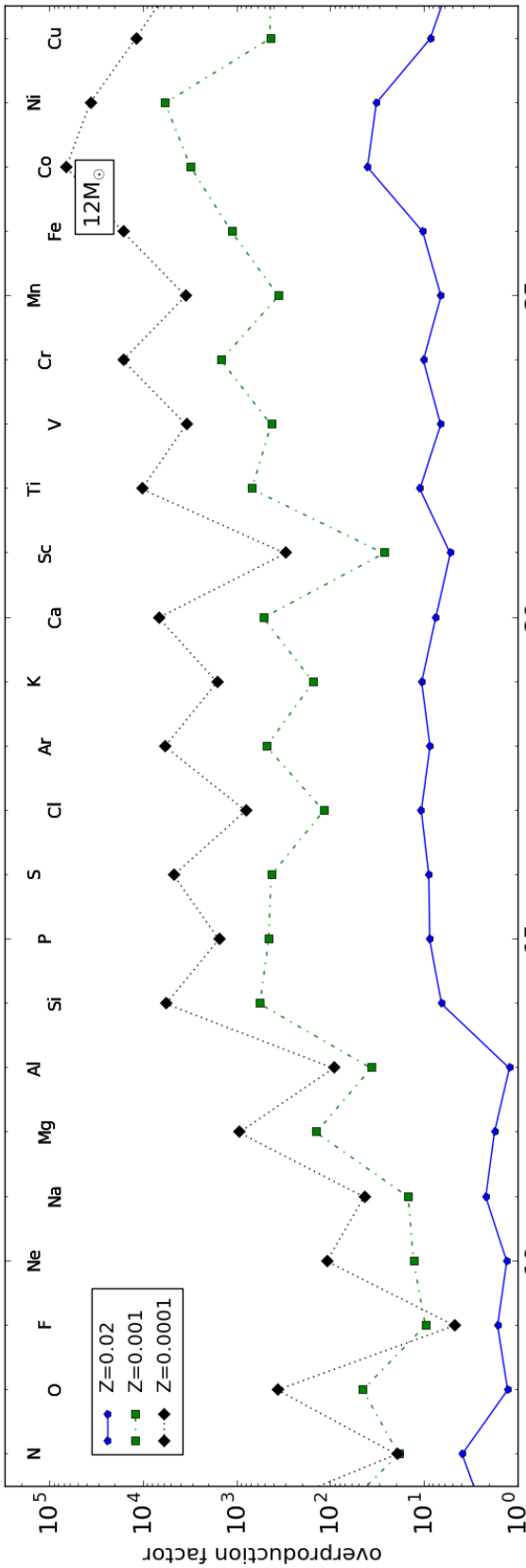

Figure 2.24: Overproduction factors of elements up to the Fe peak versus charge number of final yields of stellar models with initial mass of $12\,\mathrm{M}_\odot$ at $Z = 0.02$, $Z = 0.001$ and $Z = 0.0001$.

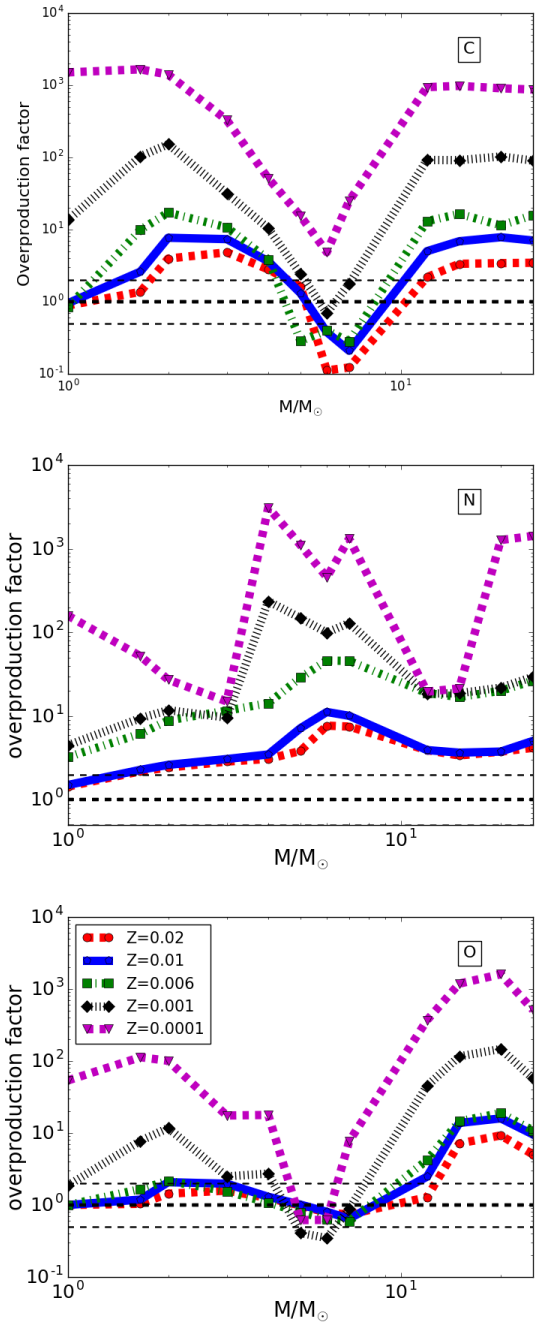

Figure 2.25: Overproduction factors of C, N, and O versus initial mass of final yields of AGB models and massive star models. The dashed horizontal lines indicate the values 0.5, 1 and 2. Included are AGB yields for $Z = 0.02$ and $Z = 0.01$ from P16. Plots for all stable elements and many isotopes at all metallicities presented in this work are available online at `http://nugridstars.org/data-and-software/yields/set-1`.

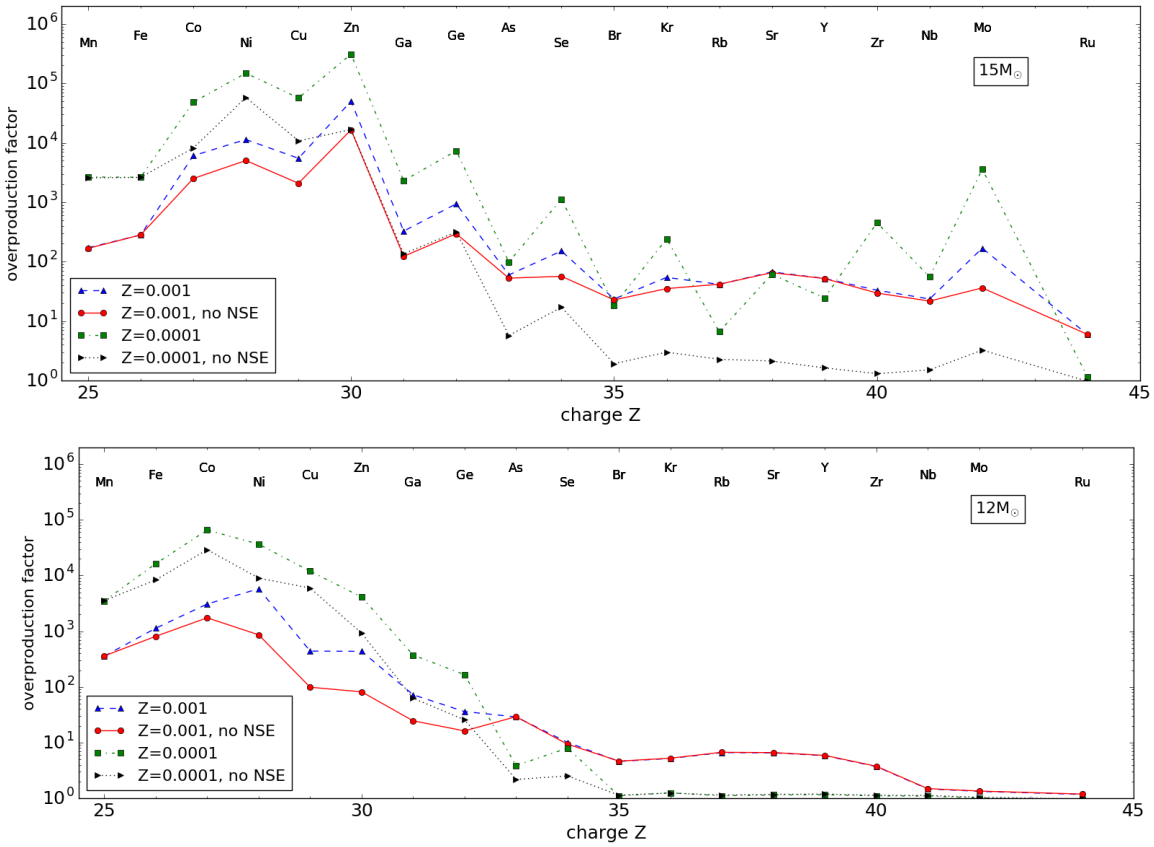

Figure 2.26: Overproduction factors versus charge number for stellar models with initial mass of $12\,M_\odot$ and $15\,M_\odot$ at $Z = 0.001$ and $Z = 0.0001$. Shown are the production factors of final yields under the assumption of fallback of the layers which went into NSE (no NSE).

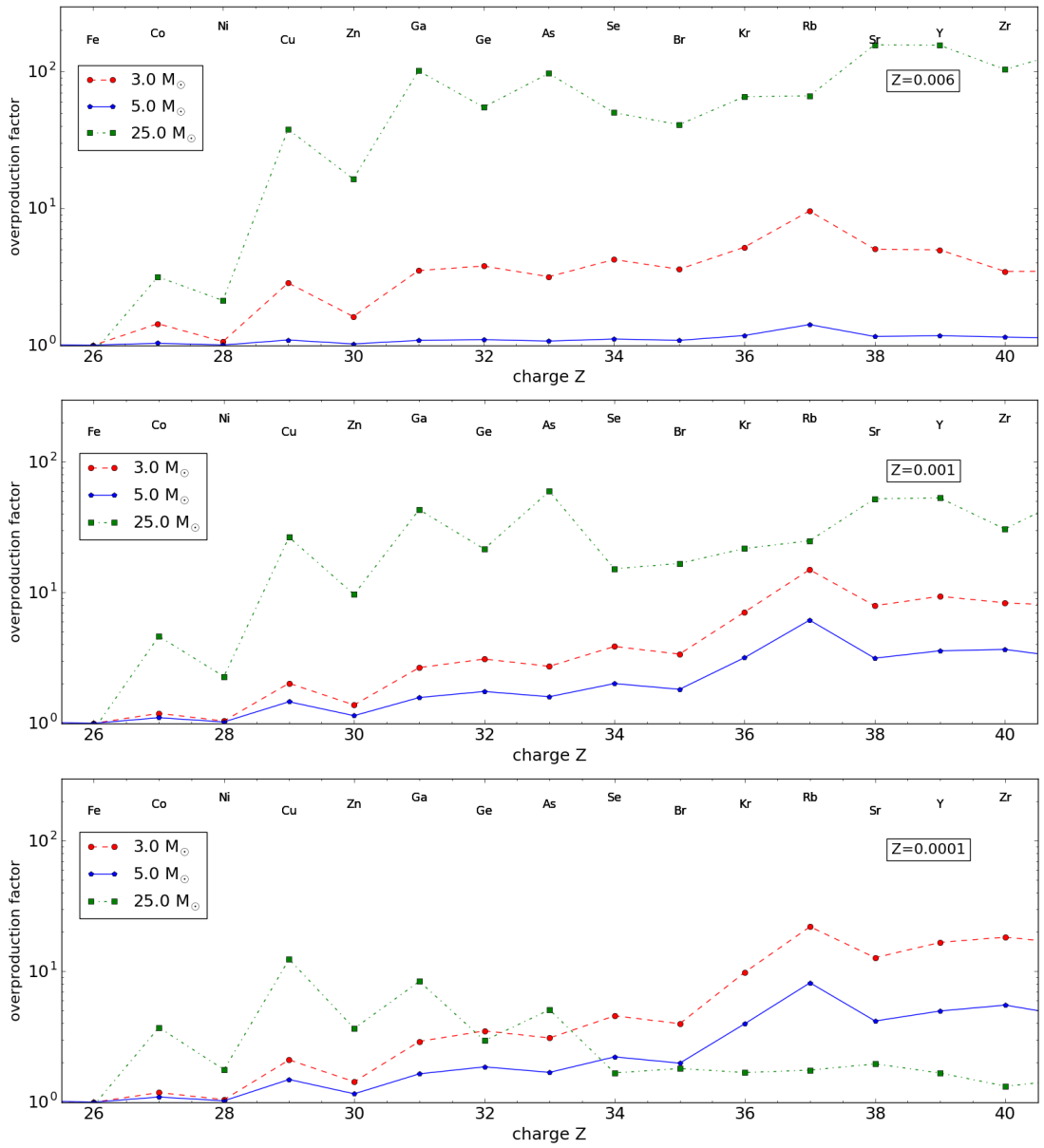

Figure 2.27: Comparison of overproduction factors versus charge of stellar models with initial mass of $3\,M_\odot$ and $5\,M_\odot$ (main s-process) and of stellar models with initial mass of $25\,M_\odot$ at $Z = 0.006, 0.001$ and 0.0001 (weak s process).

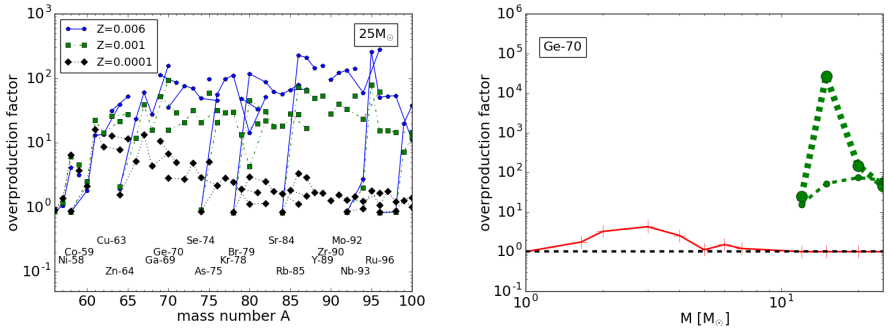

Figure 2.28: Overproduction factors versus mass number of final yields of stars with initial mass of $25\,\mathrm{M}_\odot$ at $Z = 0.006$, $Z = 0.001$ and $Z = 0.0001$ with focus on the weak s-only isotopes ^{70}Ge, ^{76}Se,^{80,82}Kr and ^{86,87}Sr (left). The overproduction factors versus initial mass of ^{70}Ge at $Z = 0.006$ for stellar wind ejecta (solid line), pre-explosive ejecta (small circles) and explosive ejecta (large circles) with delayed explosion prescription (right). Plots for all stable elements and many isotopes at all metallicities including delayed and rapid explosion prescriptions are available online at `http://nugridstars.org/data-and-software/yields/set-1`.

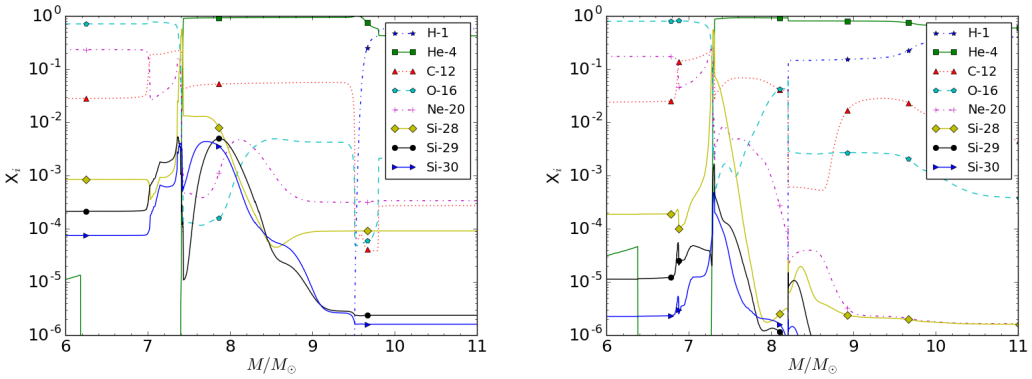

Figure 2.29: Abundance profiles of the C/Si zones after the passage of the SN shock for stellar models with initial mass of $25\,\mathrm{M}_\odot$ at $Z = 0.006$ (left) and $Z = 0.0001$ (right). Shown are the α-chain isotope ^{28}Si and the n-process isotopes ^{29,30}Si.

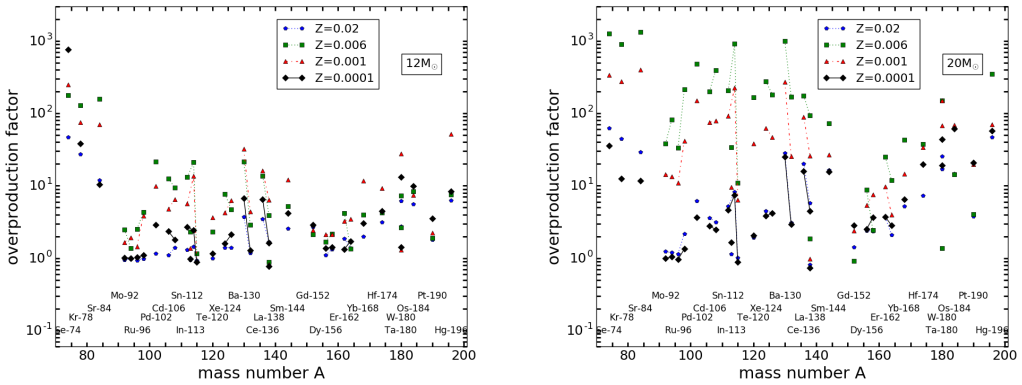

Figure 2.30: Overproduction factors versus mass number of p-process isotopes and their metallicity-dependence of massive star models with initial mass of $12\,\mathrm{M}_\odot$ and $20\,\mathrm{M}_\odot$.

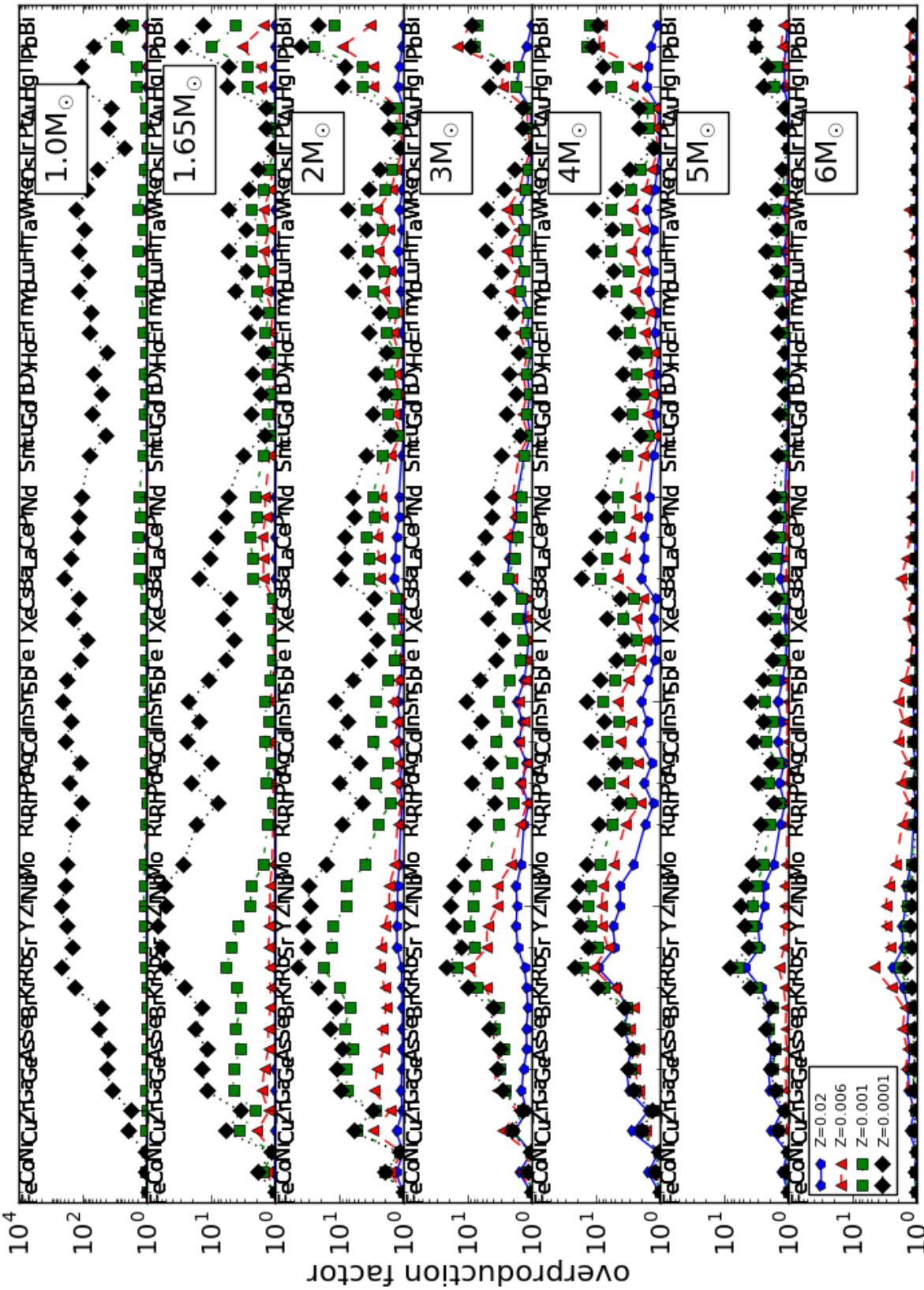

Figure 2.31: Overproduction factors of heavy elements versus charge number of low-mass, massive and SAGB models. Included are AGB models at $Z = 0.02$ of P16.

2.5 Discussion

2.5.1 Resolution of AGB models

In AGB models the H and He shells become hotter and thinner with increasing initial mass and decreasing metallicity. This makes it challenging to model the bottom of the convective envelope and its boundary in massive AGB stars (Siess 2010). To model the effect of HDUP a high time and spatial resolution at the bottom of the convective envelope is required In order to resolve the ^{13}C pocket down to the size of $M_{^{13}C} \approx 10^{-7}\,\mathrm{M}_\odot$ as in these most massive S-AGB models further resolution refinement below the convective boundary is necessary. We achieve a moderate resolution of the envelope boundary and ^{13}C pocket for stellar models with $M_{ini} \geq 4\,\mathrm{M}_\odot$ with the same adaptive mesh refinement as in P16.

To analyze the dependence of the final yields of the stellar model with initial mass of $4\,\mathrm{M}_\odot$ at $Z = 0.0001$ on resolution we compare a high-resolution calculation with up to $\approx 1.8 \times 10^4$ zones with the calculation with moderate resolution of below 2×10^3 zones. The low-resolution model produces two times more elements at Z≈50 than the high-resolution model. The element production increases towards heavier elements up to a factor of 6.7 for Bi and Pb (Fig. 2.32) which is due to the moderate resolution of the convective boundary regions and the ^{13}C pockets.

The heavy element production in the ^{13}C pocket for stellar models with initial mass above $4\,\mathrm{M}_\odot$ decreases strongly due to a rapidly decreasing ^{13}C-pocket size (Fig. 2.17 to Fig. 2.19). For all AGB models with $M_{ini} > 3\,\mathrm{M}_\odot$ we find $T_{PDCZ} > 300$ MK (Table 2.11) which is high enough to activate the ^{22}Ne(α,n) reaction. In these stellar models with initial mass above $4\,\mathrm{M}_\odot$ the PDCZ becomes the main production site of first-peak s-process elements (Fig. 2.17 to Fig. 2.19). The impact of the ^{13}C-pocket resolution on the yields of s-process elements in these stellar models is low.

2.5.2 Resolution of massive star models

The post-processing code does not fully resolve the core He-burning phase in these massive star models. The C/O ratio at the end of the core He-burning differs from stellar evolution calculations by a factor of $\approx$ 30% at $Z = 0.02$ and $\approx$ 50% at $Z = 0.0001$. The largest absolute differences exist at $Z = 0.02$ because the the C/O ratio decreases with metallicity.

To analyze the impact of the C/O ratio difference on the weak s process we have

selected a massive star model with $Z = 0.02$ which shows stronger weak s-process production compared to stars at lower Z. The stellar model with initial mass of $15\,M_\odot$ at $Z = 0.02$ shows the largest relative difference of 32% compared to other massive star models at $Z = 0.02$ and does not show a relevant contribution from the explosive nucleosynthesis to the weak s-process isotopes. Models with higher initial masses which favour weak s process show a strong decrease of the relative C/O ratio difference by about a factor two and three for models with initial mass of $20\,M_\odot$ and $25\,M_\odot$. To converge the C/O ratio of the core He-burning of the stellar model of $15\,M_\odot$ during post-processing we have developed a sub-time step method for the post-processing code.

We compare the final yield ratios of the converged stellar model with the under-resolved stellar model in Fig. 2.33. The largest differences are for weak s-process elements with up to a factor of three. This difference is within the uncertainty which results from the explosion mechanism: the difference between delay and rapid explosion prescription. The difference in yields between the resolved and under-resolved stellar model is similar to the difference between these yields and those of P16 (see Sect. 2.5.3).

To analyze the effect of resolution on the stellar evolution simulation of massive stars we calculate a stellar model with initial mass of $15\,M_\odot$ at $Z = 0.02$ with a factor between about two and ten higher resolved He core-burning phase than the under-resolved model. We find that the He core is smaller at higher resolution as visible in Fig. 2.34. A major O-C shell merger which is present in the under-resolved model disappears at higher resolution. This could indicate that the massive star models are not properly resolved. The late stage of massive star models is affected by larger uncertainties related to the treatment of convection and CBM. Convective burning shells need to be understood with multi-D hydrodynamic simulations since 1-D simulations fail to describe the flow properties of the violent convective motions present in 2D and 3D simulations (Meakin and Arnett 2006b; Herwig et al. 2014; Jones et al. 2016a). We refrain from calculating higher resolution models since physics in the late stage of massive star evolution requires further input from multi-D simulations. We conclude that the effect of the low resolution of these massive star models adds to the large uncertainties already present.

2.5.3 Comparison with stellar yields in literature

Significant efforts have been made over the years to create yield sets of various metallicities of AGB and S-AGB models. Recent works are Karakas (2010), Siess (2010), the FRUITY database (Cristallo et al. 2011; Cristallo et al. 2015), Lugaro et al. (2012), Ventura et al. (2013), Fishlock et al. (2014) and Doherty et al. (2014). Others have published AGB *and* massive star yields such as the Padova group (Portinari, Chiosi, and Bressan 1998; Marigo 2001b).

We compare yields of the AGB model with initial mass of $2\,M_\odot$ at $Z = 0.0001$ of this work with yields of models of the same initial mass and metallicity from Herwig (2004, H04), Karakas (2010, K10) and Straniero, Cristallo, and Piersanti (2014, S14) in Table 2.14. For the isotopes ^{12}C and ^{14}N we find yields between those of K10 and S14 and within a factor two of those of H04. The strong production of ^{16}O compared to K10 and S14 might be due to the choice of the CBM applied in the He intershell (Herwig 2005). H04 get about 2.5 times lower O yield with the application of the same CBM efficiency. In this work s-process isotopes are less produced than in S14. The yield of ^{88}Sr of the AGB model of this work is roughly 50% lower than of S14. The yields of ^{138}Ba and ^{208}Pb are by more than 1 dex and 2 dex lower than those of S14, respectively. We attribute the differences in part to less convective boundary mixing, smaller ^{13}C pockets and less s-process production in our AGB models compared to S14.

Yields of the AGB model with initial mass of $5\,M_\odot$ at $Z = 0.0001$ of this work and yields from models of the same initial mass and metallicity from H04, K10 and Cristallo et al. (2015, p. C15) are shown in Table 2.15. ^{12}C yield of this work lies between those of H04 and K10 while ^{14}N is less than a factor of two lower than yields of H04. The ^{16}O yield presented here is the lowest of all other works with about a factor of three below the yield of K10. The stellar model with initial mass of $5\,M_\odot$ of this work has ^{88}Sr and ^{138}Ba yields more than 1 dex below those of C15. The yield of ^{208}Pb is about a factor 88 lower than the yield of C15.

Groups have published massive star yields of various metallicities, among others Woosley and Weaver (1995), the Geneva group (Hirschi, Meynet, and Maeder 2005b), Chieffi and Limongi (2004) and Heger and Woosley (2010). We choose the yields of Chieffi and Limongi (2004, p. CL04) and Kobayashi et al. (2006, K06) for a comparison with yields of this work. The metallicity dependence of the mass loss has a significant impact on the final yields. K06 apply a metallicity-dependent mass loss

while CL04 do not include any mass loss.

Yields of stellar models with initial mass of $15\,M_\odot$ at $Z = 0.02$ of this work are compared with yields of the same initial mass and metallicity based on the models of P16 in Table 2.16. The yields of ^{12}C and ^{14}N are close to those of P16 while ^{16}O yields are by about a factor three larger than in P16. We find only low sensitivity of the yields on the amount of fallback. For ^{56}Fe the difference in yields to P16 increases and we find a factor of 3.2 and 4.5 lower Fe yields than in P16 which indicate larger Fe cores in the massive star models of P16. ^{88}Sr yields are more sensitive to the amount of fallback then the CNO species as in P16. ^{88}Sr yields of stellar models presented here differ by about a factor two from those of P16.

At low Z we show yields for stellar models with initial mass of $15\,M_\odot$ at $Z = 0.001$ of this work and models of the same initial mass and metallicity of CL04 and K06 in Table 2.17. Yields of ^{12}C and ^{14}N are in between those of CL04 and K06 while ^{16}O yields are larger than both works and roughly a factor of two larger than those of CL04. The range of ^{56}Fe yields given through the delayed and rapid explosion prescriptions includes the yields of CL04 and K06. In contrast to this work CL04 and K06 fix the ejecta of Ni and Fe respectively and amount of fallback is adjusted accordingly. The yields of ^{88}Sr in these massive star models are considerably larger than found in K06. Little fallback due to the rapid explosion prescription leads to about 3 dex more production of ^{88}Sr compared to Cl04 which originates mostly from the innermost layers,

We compare yields of stellar model with initial mass of $25\,M_\odot$ at $Z = 0.001$ with yields of models of the same initial mass and metallicity from CL04 and K06 in Table 2.18. ^{12}C yields agree well with K06 yields and ^{14}N yields with CL04 yields. We find lower ^{16}O yields than CL04 and K06 which might be due to the fallback of larger parts of the O shell in these models. Fallback strongly reduces ^{56}Fe ejection in stellar models presented here while it does not affect ^{56}Fe in CL04 and K06 because of their fixed Ni and Fe ejecta. This leads to more than 2 dex lower ^{56}Fe yields of the presented models than CL04 and K06. ^{88}Sr yields of these massive star models are considerable larger than those of CL04 similar to stellar models with initial mass of $15\,M_\odot$.

Table 2.14: Comparison of the final yields of the stellar models with initial mass of $2\,M_\odot$ at $Z = 0.0001$ from this work with H04, K10 and S14. Units in $M_\odot$.

specie	this work	H04	K10	S14
C-12	2.356E-02	1.834E-02	3.274E-02	1.424E-02
N-14	3.870E-05	2.767E-05	7.458E-05	4.110E-05
O-16	9.951E-03	3.830E-03	1.015E-03	5.031E-04
Sr-88	2.161E-09			3.528E-09
Ba-138	1.678E-10			3.901E-09
Pb-208	6.656E-10			1.084E-07

Table 2.15: Comparison of the final yields of the stellar models with initial mass of $5\,M_\odot$ at $Z = 0.0001$ from this work with H04, K10 and C15. Units in $M_\odot$.

specie	this work	H04	K10	C15
C-12	6.948E-04	1.830E-04	2.787E-03	1.274E-02
N-14	4.692E-03	6.703E-03	2.405E-02	3.405E-04
O-16	1.824E-04	1.200E-03	6.094E-04	9.350E-04
Sr-88	8.969E-10			2.238E-08
Ba-138	1.450E-10			5.523E-09
Pb-208	1.465E-10			1.284E-08

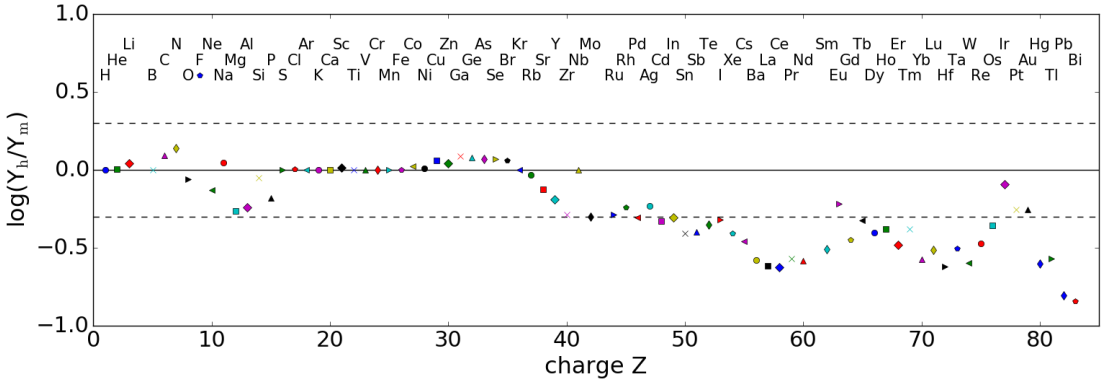

Figure 2.32: Ratio of final yields versus charge number based on a medium resolution (Y_m) and a high resolution (Y_h) AGB model of $4\,M_\odot$ at $Z = 0.0001$. The dashed lines indicate a factor of 0.5 and 2.

Table 2.16: Comparison of the final yields of stellar models with initial mass of 15 $M_\odot$ at $Z = 0.02$ of this work (delay, rapid) with those of P16. Units in $M_\odot$.

specie	delay	rapid	P16 (delay)	P16 (rapid)
C-12	1.543E-01	1.528E-01	1.761E-01	1.785E-01
N-14	4.965E-02	4.989E-02	4.967E-02	4.973E-02
O-16	9.162E-01	8.137E-01	2.986E-01	3.011E-01
Fe-56	4.306E-02	5.395E-02	1.915E-01	1.681E-01
Sr-88	5.537E-06	1.752E-05	2.648E-06	4.056E-05

Table 2.17: Comparison of the final yields of stellar models with initial mass of 15 $M_\odot$ at $Z = 0.001$ from this work (delay, rapid) with CL04 and K06. Units in $M_\odot$.

specie	delay	rapid	CL04	K06
C-12	1.537E-01	1.538E-01	1.840E-01	8.500E-02
N-14	2.675E-03	2.677E-03	2.990E-03	3.580E-03
O-16	1.148E+00	1.022E+00	5.270E-01	2.940E-01
Fe-56	5.280E-02	1.294E-01	1.000E-01	7.080E-02
Sr-88	3.935E-07	5.845E-05	3.230E-08	

Table 2.18: Comparison of the final yields of stellar models with initial mass of 25 $M_\odot$ at $Z = 0.001$ from this work (delay, rapid) with CL04 and K06. Units in $M_\odot$.

specie	delay	rapid	CL04	K06
C-12	2.115E-01	2.242E-01	5.300E-01	2.150E-01
N-14	5.825E-03	5.833E-03	4.560E-03	9.200E-03
O-16	7.878E-01	1.151E+00	2.280E+00	3.820E+00
Fe-56	2.140E-04	2.152E-04	1.010E-01	7.110E-02
Sr-88	4.575E-07	6.784E-07	8.010E-08	

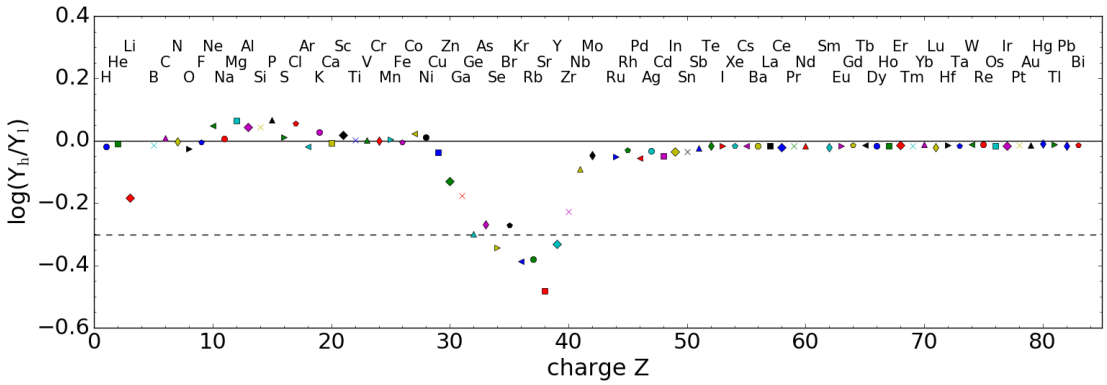

Figure 2.33: Ratios of yields versus charge number based on the massive star model with initial mass of $15\,M_\odot$ at $Z = 0.02$ computed with highly resolved core He-burning (Y_h) and computed with the resolution applied in the Set1 extension model (Y_l). The dashed line indicates a factor of 0.5.

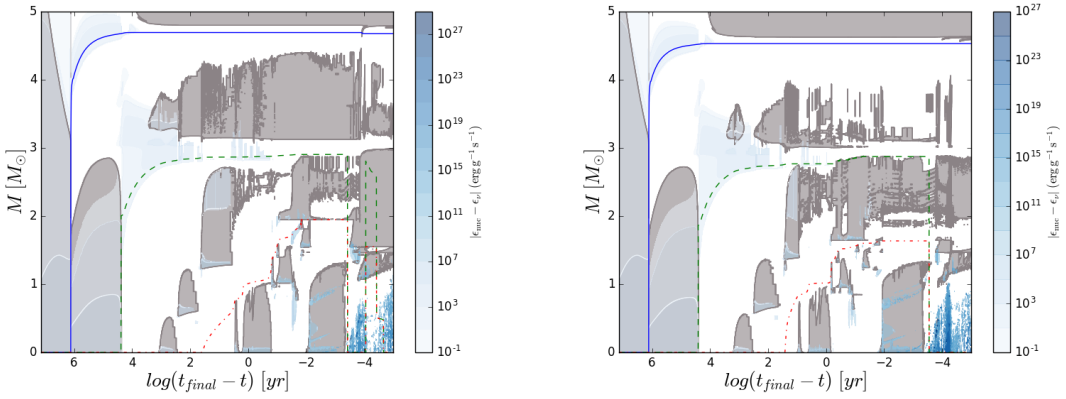

Figure 2.34: Kippenhahn diagrams of two massive star models with initial mass of $15\,M_\odot$ at $Z = 0.02$ with the default resolution (left) and with an increased resolution during core He-burning (right). t_{final} indicates the time when the infall velocity reaches 1000km/s. More details about the Kippenhahn diagram in Fig. 2.7.

2.6 Summary

Stellar models and chemical yields for initial masses of $M/M_{\odot} = 1$, 1.65, 2, 3, 4, 5, 6, 7, 12, 15, 20, 25 at each metallicity $Z = 0.006$, $Z = 0.001$ and $Z = 0.0001$ are calculated. Further stellar evolution tracks with initial masses of $M/M_{\odot} = 1$, 6, 7, 12, 15, 20, 25 for the metallicities $Z = 0.02$ and $Z = 0.01$ are added to complete the NuGrid yield grid Set 1. Set1 includes the same initial masses at all five metallicities and all its stellar evolution and post-processing data is available online at the CADC[3] and can be analyzed interactively through the web interface WENDI at wendi.nugridstars.org.

We provide explosive yields of each massive star model based on two 1D CCSN prescriptions which create the largest mass-metallicity grid of CCSN models with strong shocks currently available. Predictions of elements and isotopes up to Bi are available for all stellar models which make largest number of elements available for the considered mass-metallicity space. These yields are consistent input for chemical evolution simulations because they are based on the same nuclear reaction rates and calculated with the same stellar evolution code MESA and post-processing code MPPNP.

AGB models include the effect of convective boundary mixing at all boundaries which results in hot dredge-up in the most massive models. We predict the strong production of N and Li in the massive AGB and S-AGB stars and heavy elements through the application of a nested network approach which resolves HBB in the post-processing code. All AGB yields show s-process enhancements based on a self-consistent ^{13}C pockets which strongly decrease in massive AGB and S-AGB models. AGB mass loss is reduced towards higher initial masses and lower metallicity based on a mass-and metallicity dependent mass loss prescription. H ingestion events in the AGB model of initial mass of $1\,M_{\odot}$ at $Z = 0.0001$ lead to heavy-element production up to the third s-process peak. S-AGB models at the lowest metallicity experience H ingestion events which are a potential i-process site.

Fallback strongly reduces s-process and p-process production in these most massive star models down to the lowest metallicity. In stellar models with initial mass of $12\,M_{\odot}$ and $15\,M_{\odot}$ α-rich freeze-out layers are ejected which produce most Ni and significant amounts of p nuclei. The non-linear behaviour of the core masses with initial stellar mass together with the mass-and metallicity dependent fallback lead to

[3]The Canadian Astronomical Data Center, http://www.cadc-ccda.hia-iha.nrc-cnrc.gc.ca/vosui/#nugrid

large variations of the yields of Fe-peak elements with initial mass and metallicity. We find convective O-C shell merger in the stellar models with initial mass of $12\,M_\odot$, $15\,M_\odot$, $20\,M_\odot$ at Z=0.01 and $15\,M_\odot$ at Z=0.02 which lead to the strong boost of odd-Z elements P, Cl, K and Sc. The massive star yields of stellar models with initial mass of $20\,M_\odot$ and $25\,M_\odot$ include additional amounts of N and F due to H ingestion events.

To apply the stellar yields presented here in chemical evolution studies chemical evolution frameworks are required. The development of such codes and their applications are presented in the following chapter.

Chapter 3

Applications of yields in chemical evolution studies

3.1 Chemical enrichment and stellar feedback of simple stellar populations for galaxy models

In this section I present and verify the functionality of the SYGMA module for chemical enrichment and stellar feedback of simple stellar populations for galaxy models. The ejecta of simple stellar populations based on stellar yields of Chapter 2 and of previous works are compared. The effect of CCSN fallback on the chemical enrichment of stellar populations is analyzed.

Draft of C. Ritter, B. Côté, F. Herwig, J. F. Navarro, C. Fryer, L. Siemens, to be submitted to ApJS

Abstract

We present the stellar yields for galactic modeling applications module which models the chemical ejecta and feedback of simple stellar populations in hydrodynamic simulations and semi-analytic models. An extensive extendable stellar yields library is available including yields by the NuGrid collaboration which aims to adopt the same nuclear reaction rates in all stellar models. With NuGrid yields the enrichment of all elements and many isotopes up to Bi can be tracked. Our module models the enrichment by r-process sites such as core-collapse supernova and neutron-star mergers. Stellar feedback from the mechanic luminosities and luminosities in various

frequency bands is computed based on stellar model input and is provided for the NuGrid models. Our module offers a variety of input chemical evolution parameters including options such as SNIa delay-time distributions and initial mass functions. We compare the ejecta of simple stellar populations based on NuGrid yields and yields of Portinari, Chiosi, and Bressan (1998) and Marigo (2001a) for C, N, O, Si and Fe. We find up to a factor of 3.5 and 4.8 less C and N enrichment from AGB stars at low metallicity in NuGrid yields which we attribute to complete stellar models, the modeling of the TP-AGB stage and and hot-bottom burning in super-AGB stars. The total amount of Fe enrichment by massive stars differs by up to two at $Z = 0.02$ due to the different CCSN fallback prescriptions. We verify our module in a comparison with Wiersma et al. (2009) by applying the same yield input. We find that the evolution of accumulated ejecta of the majority of elements agree well. We compare the impact of two core-collapse explosion prescriptions and find variations with up to a factor of ten for the accumulated ejecta of C, O and Si in the first 10 Myr at a initial metallicity of $Z = 0.001$ in contrast to ejecta with $Z = 0.02$ which are in good agreement. The module is accessible as an open-source code at http://nugrid.github.io/NuPyCEE and we provide a web interface which allows to perform simulations, analysis and data extraction of the evolution of all stable elements and many isotopes.

3.1.1 Introduction

To understand the chemical evolution of galaxies such as the Milky Way it is necessary to model galaxy dynamics coupled with metal enrichment (Raiteri, Villata, and Navarro 1996). Star particles make it possible to include the metal enrichment and energy feedback via supernovae in multi-dimensional cosmological hydrodynamic simulations (Navarro and White 1993; Steinmetz and Mueller 1994; Raiteri, Villata, and Navarro 1996). The particles represent simple stellar populations (SSPs) which are born in one star burst based on the same chemical evolution assumptions and initial composition.

Presently, simple stellar populations are applied in sophisticated large-scale semi-analytic models based on N-body simulations (e.g. Yates et al. 2013; Côté, Martel, and Drissen 2015; Crosby et al. 2016), hydrodynamic simulations (e.g. EAGLE and Illustris simulations Schaye et al. 2015; Vogelsberger et al. 2014) or chemo-dynamic models (e.g. Kawata and Gibson 2003; Few et al. 2012). In such simulations the ejecta of simple stellar populations is responsible for the metal enrichment and can be pre-calculated and provided as an input. SSPs represent the basic building blocks of simple galactic chemical evolution models (e.g. Prantzos 2008; Matteucci 2014) such as OMEGA (Côté et al. 2016c).

Most SSP models include stellar yields of various compilations produced with different stellar evolution codes, post-processing codes and nuclear-physics input which leads to large uncertainties in yields as shown in Gibson (2002) and Romano et al. (2010). Wiersma et al. (2009), in the following W09, developed a chemical feedback module for hydrodynamic simulations. They found that their SSP ejecta can differ by a factor of two or more for different yields available in literature. For Stellar Yields for Galactic Modeling Applications (SYGMA) we provide yields of AGB and massive star models calculated with consistent nuclear-physics input and explosion prescriptions based on the same codes provided by the NuGrid collaboration[1].

Many codes for chemical enrichment in hydrodynamic simulations of galaxies track only a few elements which are relevant for feedback such as the modification of gas cooling properties (W09, Yates et al. 2013). Other codes use a compilation of yield sets because the latter often comprise different elements (Romano et al. 2010). SYGMA follows *all* elements and many isotopes up to Bi from NuGrid which avoids the mixing of different AGB yield sets or massive star yield sets.

[1] http://nugridstars.org

The widely adopted code starburst99 (Leitherer et al. 1999) models the chemical enrichment by SSPs with focus on the early enrichment by massive stars. Additional data such as stellar continua, luminosities and colors are provided. Currently available AGB yields are provided by the Geneva group (Ekström et al. 2012; Georgy et al. 2013) and are based on models calculated until the early AGB stage or the He flash and without the TP-AGB stage. An alternative are yields by the Padova group which include synthetic TP-AGB models (Girardi et al. 2000). In contrast, AGB yields of NuGrid are based on full stellar evolution tracks computed from the pre-main sequence through the TP-AGB phase, the most important phase of chemical enrichment.

Ejecta enhanced by r-process from CCSNe and neutron-star (NS) mergers can be tracked besides the commonly adopted AGB star, massive star and supernova Ia (SNIa) enrichment (e.g. W09, starburst99). As other SSP codes SYGMA comes with a variety of IMF types to select. To allow the test of exotic IMF types such as for Pop III populations an arbitrary IMF can be defined.

Stellar feedback alters the surrounding medium through winds and radiation and is often included in galaxy simulations. As commonly adopted, W09 include energetic stellar feedback without a dependence on the stellar models from which the yields were derived. They adopt a constant kinetic energy of 10^{51}erg for stars above $6\,M_{\odot}$. We calculate energetic feedback such as mechanical luminosities of winds and SN is calculated based on stellar model data. For the NuGrid yields we supply such tables derived from the stellar models.

SYGMA is the basic building block of NuGrids python chemical evolution framework NuPyCEE. It is essential to trace back element signatures of galactic chemical evolution models to single stellar models which can be subsequently analyzed since stellar and post-processing data is provided online. A first estimate of the impact of stellar model assumptions can be done with simple stellar populations and without applying complex galactic chemical evolution models. The NuPyCEE framework consists of an open-source python code framework which includes examples and analysis tools.

Any yields can be used which allows the analysis of different data sets. We provide a library of commonly adopted yield sets of various sources. Our web interface allows the user to run simulations and to download the evolution of chemical enrichment and feedback. In contrast to starburst99 additional analysis steps can be done within the interface.

In this work we first present the functionality of our code (Sect. 3.1.2). We then analyze the ejecta of SSPs at solar metallicity and low metallicity based on the new NuGrid yields compared to the combined yield set of AGB yields of Marigo (2001a) and massive star yields of Portinari, Chiosi, and Bressan (1998) (Sect. 3.1.3). We will refer to both works as M01 and P98 respectively. Afterwards we aim to reproduce the evolution of key elements ejected by SSP's presented in W09 by applying their yield set (Sect. 3.1.4). Finally, we discuss the effect of core-collapse mass-cut prescriptions on yields from massive star models.

3.1.2 Code details

We discuss the basic assumptions of our simple stellar population model. Results in this section are based on NuGrid yield input and models (Pignatari et al. 2016b, Ritter et al., in prep.).

Population modeling

A simple stellar population consist of stars formed in one star burst out of a gas cloud of a certain initial composition. To follow the gas enrichment of a SSP one need to track only the ejecta of stars since all gas is locked up in stars during the the initial star formation. The composition of the stellar ejecta is based on the yields of stellar models computed with the initial abundance composition of the gas cloud. The total mass of the gas cloud affects the total number of stars formed and the total amount of stellar ejecta. Chemical evolution assumptions describe properties of the stellar population such as the number of stars formed at a certain initial mass. The initial mass and metallicity of the gas cloud, chemical evolution assumptions and stellar yields are required for SSP modeling and determine the chemical enrichment.

SSP ejecta

SYGMA models the enrichment by AGB stars, massive stars, SNIa and neutron-star mergers. due to massive stars. Besides the total enrichment the contribution from AGB stars, massive stars and SNIa is tracked individually as show for a SSP of $10^6\,\mathrm{M}_\odot$ at $Z = 0.02$ in Fig. 3.1. Initial massive stars are the only contributor to the total ejecta due to their short lifetime. Later AGB stars and SNIa start ejecting matter and AGB stars become the dominant source of ejecta. We apply the delayed production approximation which results in the instantaneous ejection of stellar yields

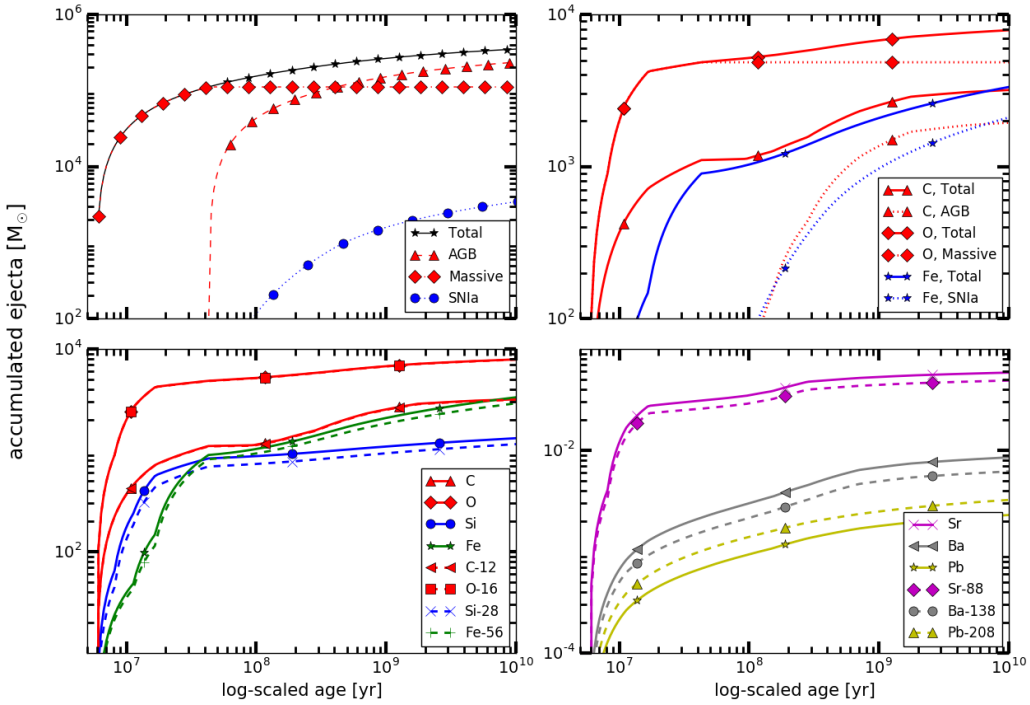

Figure 3.1: Accumulated ejecta from AGB stars, massive stars and SNIa for a SSP of $10^6\,M_\odot$ at $Z = 0.02$ (top, left). Accumulated ejecta of C, O and Fe from all (total) or from distinct sources (top, right). Total accumulated ejecta of elements and isotopes of intermediate mass and from the first, second and third s-process peak (bottom). Online Access.

after a certain time span (Pagel 2009). The times provided with the NuGrid yield tables are for AGB models the stellar lifetime at the end of the computation and excluding evolution beyond the post-AGB stage. For massive star models the time until core collapse is taken. The lifetime τ for a certain initial mass M are derived through a log-log spline fit of the tabulated lifetimes and initial masses. We show $\tau(M)$ for the initial masses in Fig. 3.2[2]. The mass ΔM_{SSP} lost by a SSP over the

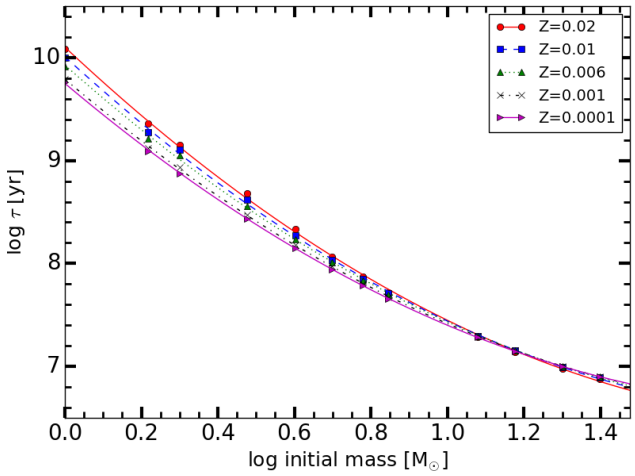

Figure 3.2: Stellar lifetimes τ for initial masses of the NuGrid models. The fits of the lifetimes over the initial mass range are shown for each metallicity. Online Access.

time interval $[t,t+\Delta t]$ is

$$\Delta M_{SSP} = \int_{t}^{t+\Delta t} \xi(M_\tau(t'))\, M_\star(M_\tau(t'), Z)\, dt' \tag{3.1}$$

where $M_\tau(t)$ is the inverse of the lifetime function $\tau(M)$. $\xi(M)$ is the initial mass function normalized to the total gas mass of the SSP. $M_\star(M, Z)$ is the total ejected mass of the star of mass M and metallicity Z. In our 1-zone closed-box approximation the stellar ejecta is homogeneously mixed with available gas.

General input

The choice of initial mass and metallicity for the SSP depend on the yield input. Yields with an arbitrary number of isotopes can be applied. The yield tables need to include the lifetime and final mass for each star which is for massive stars the neutron star (NS) or black hole (BH) remnant. If the CCSN energies for all massive stars are

[2]For all figures in this work we provide figures online accessible via ipython notebooks.

provided, SYGMA can track the total energy release. Other input parameters are discussed in the next sections.

Initial mass function

The initial mass function ξ gives the number of stars N within an initial mass interval [m_1,m_2] via

$$N = A \int_{m_1}^{m_2} \xi(m')\, dm' \tag{3.2}$$

where the normalization constant A is derived from the total gas mass. SYGMA provides the Salpeter IMF (Salpeter 1955) given as

$$\xi(m) = A_S\, m^{-\alpha} \tag{3.3}$$

where $\alpha = 2.35$. A single power law with an exponent α of choice can also be selected. We provide the Chabrier IMF (Chabrier 2003) which is defined as

$$\begin{aligned} \xi(m) =& A_C\, m^{-1} e^{-\frac{(\log m - \log m_c)^2}{2\sigma^2}} && \text{for } m \leq 1\,\mathrm{M}_\odot, \\ \xi(m) =& A_C\, m^{-2.3} && \text{for } m > 1\,\mathrm{M}_\odot, \end{aligned} \tag{3.4}$$

where $m_c = 0.079$ and $\sigma = 0.69$. The Kroupa IMF (Kroupa 2001) is provided and calculated via

$$\begin{aligned} \xi(m) =& A_K\, m^{-0.3} && \text{for } 0.01\,\mathrm{M}_\odot \leq m \leq 0.08\,\mathrm{M}_\odot, \\ \xi(m) =& A_K\, m^{-1.3} && \text{for } 0.08\,\mathrm{M}_\odot \leq m \leq 0.50\,\mathrm{M}_\odot, \\ \xi(m) =& A_K\, m^{-2.3} && \text{for } m \geq 0.50\,\mathrm{M}_\odot. \end{aligned} \tag{3.5}$$

IMF types are discussed in more in detail in Kroupa et al. (2013). A custom IMF can also be defined and applied in the code. The lower and upper boundaries of the IMF can be set and are related to the onset of H-burning and the occurrence of the most massive stars respectively (see discussion in Côté et al. 2016b).

SNIa rates

The number of SNe Ia N_{Ia} per $\mathrm{M}_\odot$ in the time interval [t,t+Δt] is given by

$$N_{Ia} = A_{Ia} \int_{t}^{t+\Delta t} f_{WD}(t')\ \Psi_{Ia}(t')\, dt' \tag{3.6}$$

where A_{Ia} is the normalization constant, $f_{WD}(t)$ the fraction of white dwarfs and $\Psi_{Ia}(t)$ the delay-time distribution (DTD) at time t (W09). In SYGMA only white dwarfs with initial masses between $3\,M_\odot$ and $8\,M_\odot$ are potential SNIa progenitors as commonly adopted (e.g. Dahlen et al. 2004; Mannucci, Della Valle, and Panagia 2006, W09). The boundaries approximate the lowest mass of a CO white dwarf which can form in a binary system and the maximum white dwarf mass (Yungelson 2005). Either A_{Ia} or the total number of SNe Ia per $M_\odot$ has to be provided as an input. The power-law DTD of Maoz and Mannucci (2012) given as

$$\Psi_{Ia}(t) = t^{-1} \tag{3.7}$$

can be selected. The power-law exponent can varied separately. We provide a Gaussian in the form of

$$\Psi_{Ia}(t) = \frac{e^{-t/\tau_{Ia}}}{\tau_{Ia}} \tag{3.8}$$

and an exponential DTD as

$$\Psi_{Ia}(t) = \frac{1}{\sqrt{2\pi\sigma^2}} e^{-\frac{(t-\tau_{Ia})^2}{2\sigma^2}} \tag{3.9}$$

as in W09. τ_{Ia} is the characteristic delay time and σ defines the width of the Gaussian distribution. For a discussion of the parameters see W09 and references within.

NS merger rates

The number of NS mergers N_{NS} in the time interval $[t,t+\Delta t]$ is given as

$$N_{NS} = A_{NS} \int_t^{t+\Delta t} \Psi_{NS}(t', Z)\, dt' \tag{3.10}$$

where A_{NS} is the normalization constant. $\Psi_{NS}(t, Z)$ is the NS DTD. The user can choose between a power law DTD, the DTD of Dominik et al. (2012), or a constant coalescence time. For our DTD based on Dominik et al. (2012) we adopt for $Z \geq 0.019$ their DTD at solar metallicity and for $Z \leq 0.002$ their DTD at a tenth of solar Z. We interpolate the distribution between the two metallicities. The normalization constant A_{NS} is derived from the total number of merger systems $N_{NS,tot}$ via

$$A_{NS} = N_{NS,tot} \,/ \int \Psi_{NS}(t, Z)\, dt'. \tag{3.11}$$

$N_{NS,tot}$ is calculated as

$$N_{NS,tot} = 0.5\, f_m\, f_b \int_{m_1}^{m_2} \xi(m')\, dm' \tag{3.12}$$

where f_m is the fraction of merger of massive-star binary systems and f_b is the binary fraction of all massive stars. f_m and f_b as well as the initial mass range for potential merger progenitors [m_1,m_2] are free parameters to be set.

Stellar yields

Yield implementation

The yield tables with total yields $y_{tot,i}$ defined as the total mass of isotope or element i ejected over the stars lifetime $y_{tot,i}$ (Pignatari et al. 2016b) are applied by default. For the comparison with W09 (Sec. 3.1.4) tabulated net yields can be applied instead. Net yields $y_{p,i}$ are defined as $y_{p,i} = y_{tot,i} - y_{p,i}$ where $y_{p,i}$ refers to the mass of isotope or element i initially available in the star. SYGMA calculates from tabulated net yields $y_{p,i}$ the total yields $y_{tot,i}$ of isotope i via $y_{tot,i} = y_{0,sim,i} + y_{p,i}$ where $y_{0,sim,i}$ refers to the current abundance of isotope i in the simulation. Yields are only applied in an initial mass interval which allows to take into account material locked away for example through black hole formation. This IMF yield range is by default from $1\,\mathrm{M}_\odot$ to $30\,\mathrm{M}_\odot$. The IMF yield range and the IMF range can both be set separately for stars of $Z > 0$ and Pop III stars to take into account different types of star formation. The yields of a specific tabulated stellar model are applied in an initial mass interval with boundaries given as half the distance to the next available tabulated entries of lower and higher initial mass. If those are either not available or outside of the IMF yield range the boundaries of the latter are applied. The total stellar ejecta $y_{tot,i}$ is fitted over the whole initial mass range which includes the transition between AGB stars and massive star models.

Extra sources for massive stars

SYGMA allows to attach additional yields to massive stars to follow the enrichment via neutrino-driven winds or other sources. Yields are specified as an extra yield table input and can be applied in fractions of the total ejected mass.

Yield tables

The default yields of AGB models, massive star models and core-collapse supernova approximations are from the NuGrid collaboration. Stellar yields for $Z = 0.02$,

0.01, 0.006, 0.001 and 0.0001 are available. For each metallicity twelve stellar masses are provided from $1\,M_\odot$ to $25\,M_\odot$, including super-AGB stars. Low- and intermediate-mass stars are followed through the thermal pulse (TP) AGB stage and massive stars through all burning phases until collapse. Each simulation includes about 1000 isotopes in nearly 2000 grid zones and contains about 10^5 time steps. All stable elements and many isotopes up to Bi are provided in the yield tables.

SYGMA provides analytic tools to distinguish which source is responsible for the most element production. For the SSP of $10^6\,M_\odot$ at $Z = 0.02$ we verify and confirm previous results that AGB stars are important producer of C, massive stars produce the most O and SNIa produce the most Fe in Fig. 3.1 (e.g Schneider et al. 2014; Woosley, Heger, and Weaver 2002; Thielemann, Nomoto, and Yokoi 1986). We track all the stable elements and many isotopes up to Bi in SYGMA, as shown for some intermediate elements and heavy elements.

In AGB and massive star models a mass and metallicity dependent mass loss is used. Convective boundary mixing is applied at all convective boundaries of AGB stars. The boundary mixing leads self-consistently to the creation of a ^{13}C pocket and an efficient s process in AGB models. A new hybrid post-processing method allows to resolve hot-bottom burning and predict isotopes of the CNO cycle and s process isotopes. Models at low Z experience hot dredge-up which impacts core-growth and length of the AGB phase. The semi-analytic explosion prescription takes into account a mass- and metallicity dependent fallback which lead at high mass to efficient black hole formation. Explosive nucleosynthesis includes α-rich freeze-out which is present in stars of $12\,M_\odot$ and $15\,M_\odot$ and the p process. The NuGrid data applied in this work is available online as tables and through the WENDI interface (Section 3.1.5). A sub-set consisting of AGB yields at solar and half-solar metallicity is published (Pignatari et al. 2016b).

SNIa yields are from Thielemann et al. (2003) or (default) from Thielemann, Nomoto, and Yokoi (1986). SNIa yields of a particular metallicity are applied only until the next higher available metallicity. At zero metallicity we use the yields of massive star models by Heger and Woosley (2010). The NS merger yields are from Arnould, Goriely, and Takahashi (2007) and (default) from Rosswog et al. (2014). The (default) yields for the extra yield input stem from pseudo neutrino-driven winds of a proto-neutron star model.

Stellar feedback

Wind properties and mechanical luminosities, including massive star explosion energies, of SSPs can be followed with additional input tables. These contain the time dependence of stellar quantities which can be derived from stellar models. Parameters for a specific tabulated model are applied in the same initial mass range as the yields.

Stellar winds

The properties of stellar winds are of importance since they can contribute to the production of galactic winds which distribute metals and enrich the intergalactic medium (Hopkins, Quataert, and Murray 2012). We provide the time evolution of the mass ejection rates of each stellar model of NuGrid as an input for SYGMA. We show the combined mass loss rates of AGB and massive star models for a population of $10^6\,\mathrm{M}_\odot$ at $Z = 0.02$ in the upper panel of Fig. 3.3. The AGB stellar mass loss rates decrease towards lower initial masses which is visible in the decreasing trend with time. The values are similar to Côté, Martel, and Drissen (2015) (Fig. 3, 4). The steps in the evolution of the ejected mass (Fig. 3.3) origin from the transition from one tabulated stellar model to the following model. The strongest AGB mass loss found in the $5\,\mathrm{M}_\odot$ model and visible in the peak shortly after 10^8 yr. To calculate the mechanical luminosity of stellar winds L_{mech} we get for each stellar model the time-dependent escape velocities v_{esc} via

$$v_{esc}(t) = \sqrt{\frac{2GM(t)}{R(t)}} \tag{3.13}$$

where $M(t)$ and $R(t)$ are total mass and radius of a stellar model at time t. By deriving the terminal velocity v_∞ from v_{esc} one gets

$$L_{mech}(t) = \frac{1}{2}\dot{m}(t)v_\infty(t)^2 \tag{3.14}$$

Abbott (1978) found the relation $v_\infty = 3v_{esc}$ for observed O, B, A and Wolf-Rayet stars based on radiation-driven wind theory. We adopt this relation because our massive star models indicate efficient radiative momentum transfer with $T_{eff} > 15000$K on the main sequence (Leitherer, Robert, and Drissen 1992). For AGB models we approximate $v_\infty = v_{esc}$ which might overestimate the kinetic energy contribution of the AGB phase as indicated by observations (Bolton 2000). The AGB stars are often not considered since their contribution is negligible compared to massive stars (Leitherer

et al. 1999; Côté, Martel, and Drissen 2015).

We find that the largest mechanical wind luminosities originate from massive star models while AGB models drop off by orders of magnitude (Fig. 3.3). Since the stellar grid includes stellar models up to $25\,M_\odot$ we do not consider stellar models above $30\,M_\odot$ which would be major contributors. Considering this threshold, the massive star model luminosities are similar to a SSP of same mass and metallicity derived with the population synthesis code starburst99 (Fig. 111, Leitherer et al. 1999).

SN luminosities

The CCSN luminositiy is canonically taken as 10^{51}erg which matches the observed explosion energy of SN such as SN 1987A. We apply CCSN energies based on the CCSN explosion prescription used for NuGrid stellar models. We derive from Fryer et al. (2012, their Fig. 2) mass- and metallicity-dependent mechanical luminosities. For SYGMA, CCSN luminosities are provided for each massive star model in the yield tables. Since yields are provided for stellar models up to $25\,M_\odot$ luminosities from more massive models are presently not taken into account. The mechanical luminositiy of a SNe Ia is an input parameter of SYGMA and is set to 10^{51}erg. For a SSP of $10^6\,M_\odot$ at solar Z we find the mechanical luminosity from CCSN SN explosions of $\approx 10^{40}$erg/s which is similar to starburst99 (Fig. 113, Leitherer et al. 1999). In comparison the SNe Ia contribution is more than 1 dex lower as shown in Fig. 3.3 and very similar to Côté, Martel, and Drissen (2015) (Fig. 4). The mechanical luminosity of the winds is at all times low than the SN contributions.

Stellar Luminosities

Stellar radiation alters the surrounding medium through ionization and its momentum flux due to radiation pressure. SYGMA can read in tables containing time-dependent luminosities. To follow the energy release of our SSPs we include the bolometric luminosities. To derive the lumminosities in specific wavelength bands such as the H-ionizing band (13.6 - 24.6 eV) we use the synthetic spectra libraries PHOENIX (Husser et al. 2013) and ATLAS9 (Castelli and Kurucz 2004). We calculate the time-dependent luminosities of spectral bands based on the spectra of the stellar evolution models. Spectra are derived from the best match of effective temperature T_{eff}, the gravity g, [Fe/H] and α-enhancement of a stellar model. The α-enhancement at low Z is based on observations of individual elements and each element has its own enhancement. We derive [α/Fe]=0.8 by taking into account the initial abundance of each element. The bolometric luminosity as well as the luminosity in two wavelength

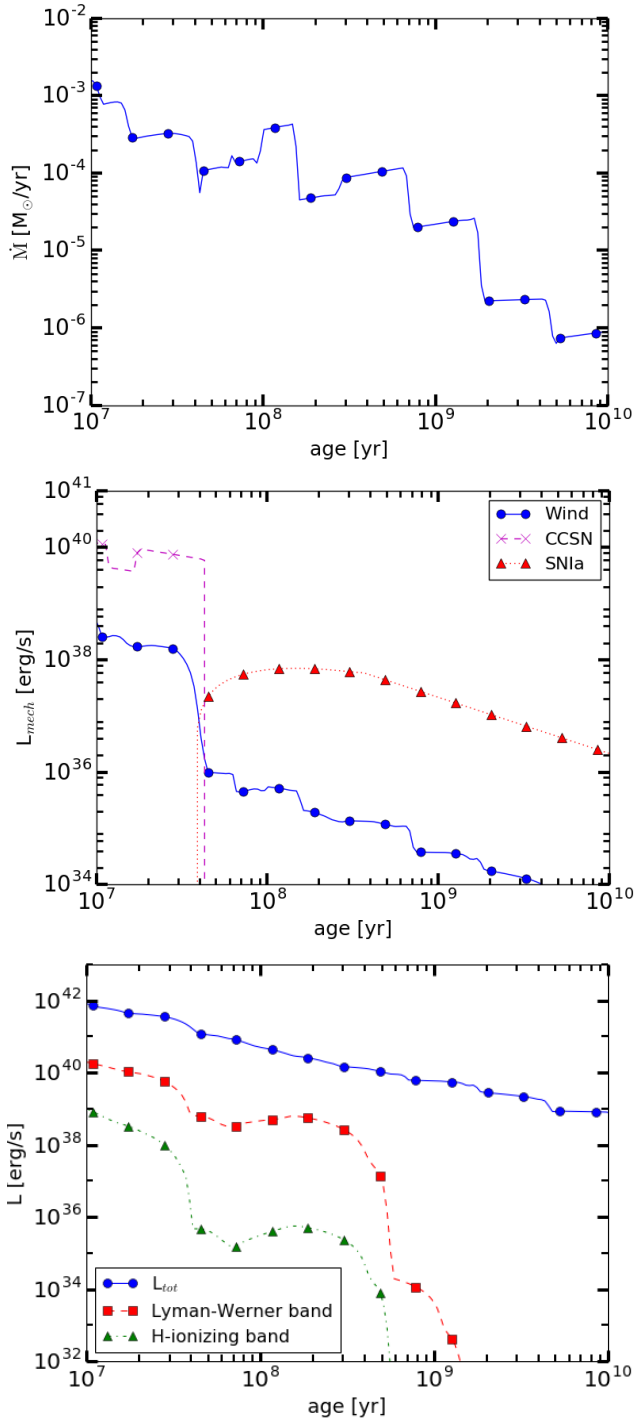

Figure 3.3: Evolution of mass ejection of a SSP of 10^6 $M_\odot$ at solar Z (top). Mechanical luminosities of stellar winds, CCSNe and SNe Ia (middle). Time dependence of the total luminosity and luminosities in the Lyman-Werner and H-ionizing bands emitted by the SSP (bottom). Online Access.

bands of a SSP of $10^6\,M_\odot$ at $Z = 0.02$ are shown the lower panel of Fig. 3.3.

3.1.3 Results

Simple stellar populations at solar Z

We compare the ejecta of two SSPs based on yields from NuGrid and the yield set of P98+M01. NuGrid yields at Z=0.02, P98 yields at Z=0.02 and M01 yields at Z=0.019 are used and we will refer to all as yields at solar Z. As the initial abundance those of the NuGrid yield calculations are chosen (Pignatari et al. 2016b). We calculate the total yields y_{tot} from the net yields of P98+M01 (Sec. 3.1.2). For C, Mg and Fe yields of P98 the factors of 0.5, 2 and 0.5 are applied as in W09. We use identical SSP parameters for P98+M01 yields and NuGrid yields to analyze only the differences due to the yield sets. A Chabrier (2003) IMF with a initial mass range from $0.1\,M_\odot$ to $100\,M_\odot$ is selected and yields are applied in the range from $1\,M_\odot$ to $30\,M_\odot$. The DTD for SNe Ia is exponential and has a characteristic delay time τ of $\tau = 2 \times 10^9$ yr and a normalization parameter A_{Ia} of $A_{Ia} = 0.02$ as W09. We choose the transition mass M_{mass} from AGB stars to massive stars as $M_{mass} = 8\,M_\odot$ which is in agreement with the upper limit of the progenitors of SNIa of this work. All parameters are listed in Table 3.1. We compare the accumulated ejecta of SSPs of $10^4\,M_\odot$ based

IMF type	Chabrier
IMF range	0.1 - 100 $M_\odot$
IMF yield range	1 - 30 $M_\odot$
τ_{Ia}	2×10^9 yr
A_{Ia}	0.02
M_{mass}	$8\,M_\odot$

Table 3.1: Chemical evolution parameters of a SSP according to the model described in Sec. 3.1.2.

on NuGrid yields and based on yields of P98+M01 (Fig. 3.4). The evolution of the total accumulated mass of AGB stars and massive stars is about the same for NuGrid yields and P98+M01 yields due similar amounts of total ejecta of both yield sets.

C, N — AGB stars are important dust producer (Ferrarotti and Gail 2006; Schneider et al. 2014) and feature the primary production of of C (Herwig 2005). In massive and super-AGB stars C is destroyed in hot-bottom burning (HBB) in the TP-AGB

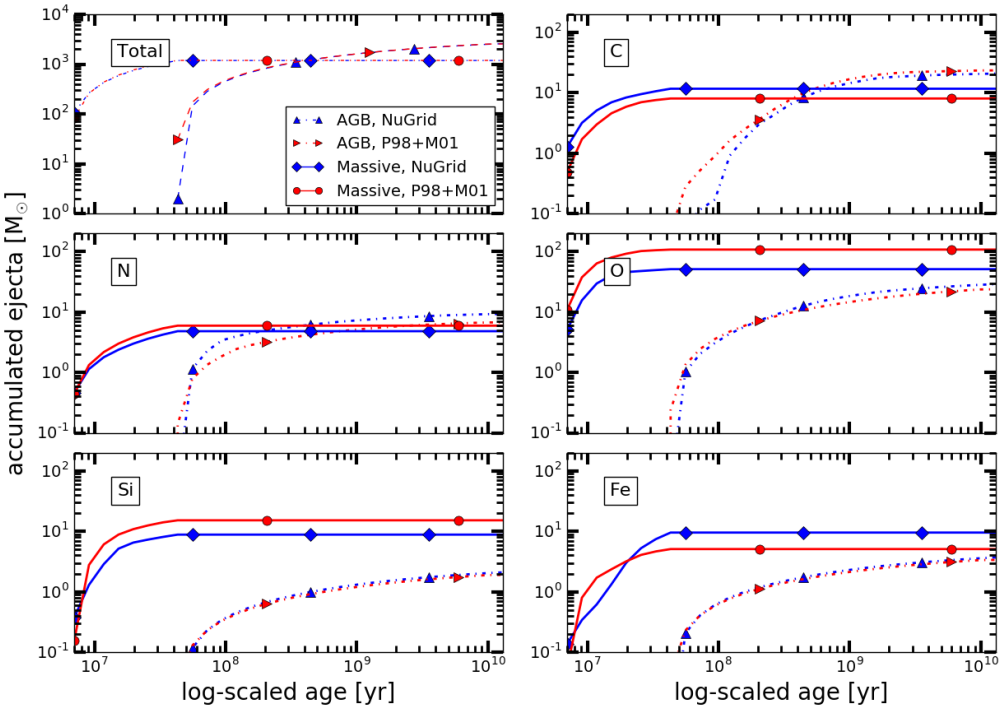

Figure 3.4: Accumulated ejecta of AGB stars and massive stars at solar Z based on NuGrid yields and P98+M01 yields. Online Access.

stage (Lattanzio et al. 1996). Lower C yields in the NuGrid stellar models of $6\,M_\odot$ and $7\,M_\odot$ than in stellar models of lower initial mass is due to more efficient HBB in the TP-AGB phase. The stellar models with initial mass of $6\,M_\odot$ and $7\,M_\odot$ provided by P98 do not include the TP-AGB phase and the third dredge-up (TDUP). Hence the accumulated ejecta of C of the SSP is lower with NuGrid yields than with P98+M01 yields before $\approx 2 \times 10^8$ yr (Fig. 3.4). The TP-AGB phase changes dramatically the structure and chemistry of intermediate mass models. The SSP produce overall more C with NuGrid yields while we would get the opposite without the decrease of massive star yields by 0.5 as suggested in W09. In the former case AGB stars would start to dominate the total production of C at 3.6×10^8 yr and in the latter case at 9×10^8 yr.

HBB transforms C into N which leads to larger N yields in the NuGrid tables (Fig. 3.5). The result is a bump in the IMF-weighted ejecta of models with initial mass of $6\,M_\odot$ and $7\,M_\odot$ (Fig. 3.5).

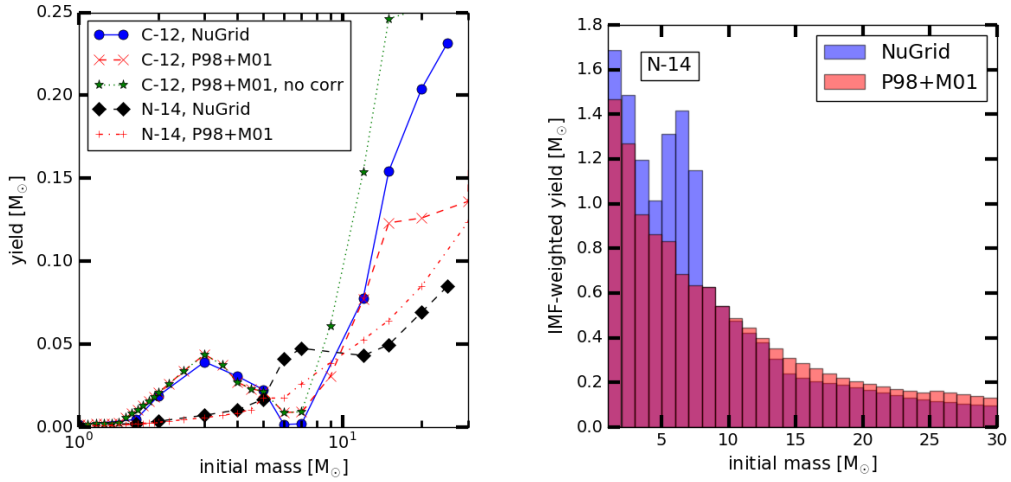

Figure 3.5: ^{12}C and ^{14}N yields at solar metallicity versus initial mass of NuGrid, P98+M01 and P98+M01 without correction factor (no corr) of 0.5 (left). IMF-weighted yields of ^{14}N of stars of different initial mass (right). Online Access.

O, Si — O is mostly produced in massive stars (Timmes, Woosley, and Weaver 1995; Woosley, Heger, and Weaver 2002). The size of the O shell increases with initial mass but fallback and BH formation prevent a continuous increase of O yield with initial mass. Stellar models with initial mass of $20\,M_\odot$ and $25\,M_\odot$ from NuGrid experience strong fallback of large parts of the O shell which leads to higher remnant

masses at high initial mass compared to P98 (Fig. 3.6). NuGrid yields feature less O which results in less accumulated O by the SSP (Fig. 3.6, Fig. 3.4). AGB models of NuGrid include convective boundary mixing which leads to a larger enrichment of O of about 15% in the He intershell of low-mass TP-AGB models compared to 2% without any convective boundary mixing (Herwig 2005). M01 does not include any convective boundary mixing which is why the mass of O released by AGB stars in our SSP is higher with NuGrid yields than with M01 yields.

Si is mostly ejected in massive stars with a contribution from SNe Ia. Due to its closer proximity to the core it is stronger affected by fallback than lighter elements but it does not vary much with initial mass. We find that the difference in chemical evolution of Si based on NuGrid and P09+M01 yields are smaller than for O. AGB stars eject mostly unprocessed Si and the SSP ejecta is about the same for both yield sets.

Fe — SNe Ia produce most of the Fe (e.g. Thielemann, Nomoto, and Yokoi 1986) are not discussed here. The SSP ejecta of Fe of massive stars are qualitative different (Fig. 3.4) due to the variation of Fe yields with initial stellar mass (Fig. 3.6). Most Fe of NuGrid yields comes from massive star models at the lowest initial mass. P98+M01 yields contain the most yields at the initial mass of $20\,M_{\odot}$. Within the first 20 Myr the SSP ejecta of Fe from massive stars is up to a factor of three larger for yields of P98 compared to NuGrid yields. At later times the Fe yields from NuGrid dominate. SSP ejecta of Fe of AGB stars is unprocessed and does not differ much between yield sets.

Simple stellar populations at low Z

To analyze the SSP ejecta at lower metallicity we compare the NuGrid yields at $Z = 0.001$ with the yields of P98+M01 at $Z = 0.004$. We take a initial abundance of $Z = 0.004$ to calculate total yields which is scaled from the initial abundance applied previously. Yields of both sets at the same sub-solar metallicity are not available. The initial abundance of NuGrid yields at $Z = 0.001$ is α enhanced opposite to P98 and M01. We compare the total accumulated ejecta of AGB stars and massive stars based on yields from P98+M01 with those based on NuGrid yields (Fig. 3.7).

C, N — SSP eject of C of AGB stars is a factor of 3.5 larger with yields of P98 than with NuGrid yields (Fig. 3.7). This is due to the low-mass AGB models of P98

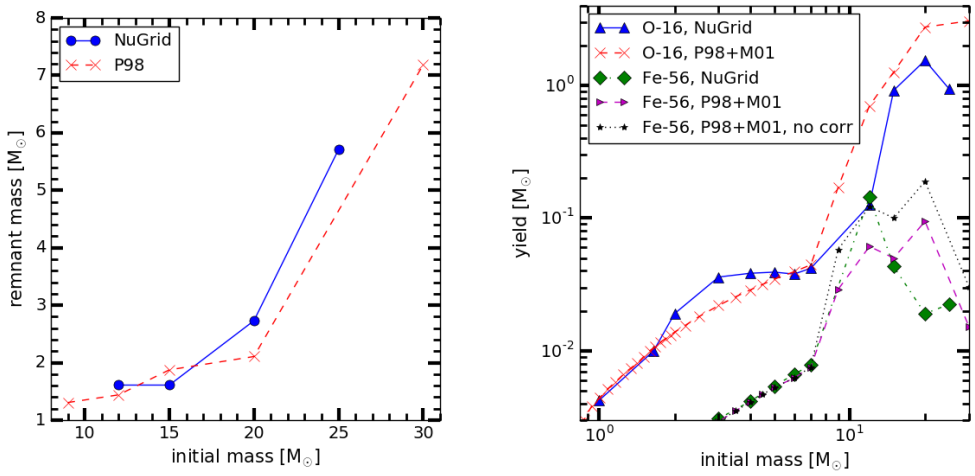

Figure 3.6: Remnant masses versus initial mass of NuGrid and P98 models at solar Z (left). Yields of ^{16}O and ^{56}Fe at solar Z versus initial mass (right). Online Access.

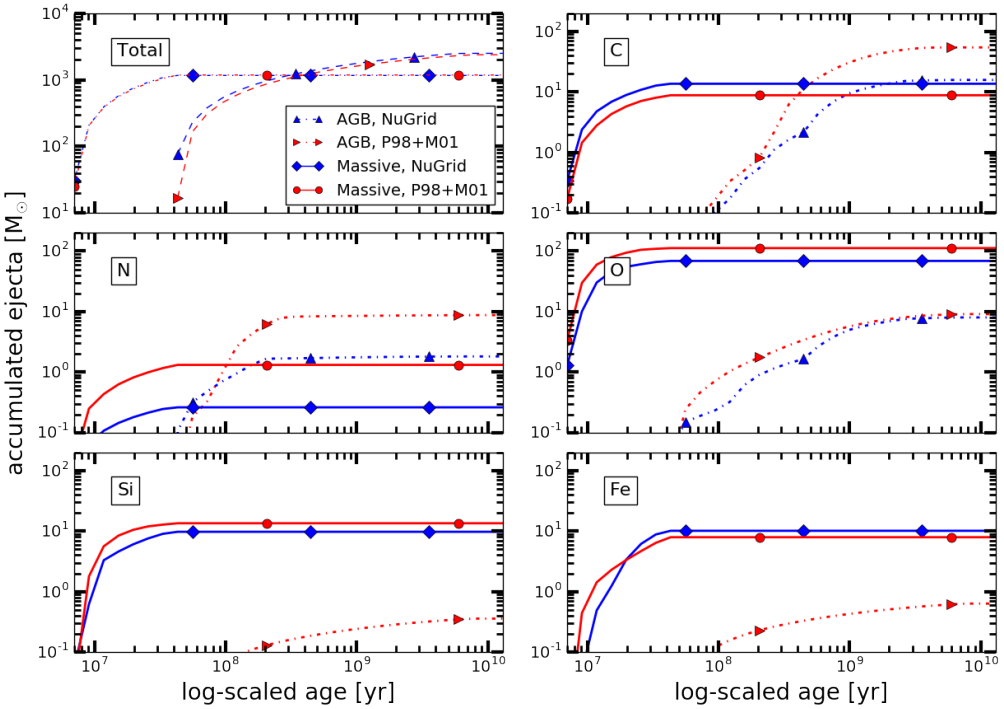

Figure 3.7: Accumulated ejecta of AGB stars and massive stars based on NuGrid yields at Z=0.001 and P98+M01 yields at Z=0.004. Online Access.

which eject larger amounts of C compared to NuGrid models (Fig. 3.8). M01 uses synthetic models which do not model the TDUP self-consistently as NuGrid models. The synthetic models might dredge up larger amount of C into the envelope since the dredge-up strength and minimum core mass of TDUP occurrence are calibrated through the observed carbon star luminosity distribution. At solar Z more C is produced in NuGrid massive star models.

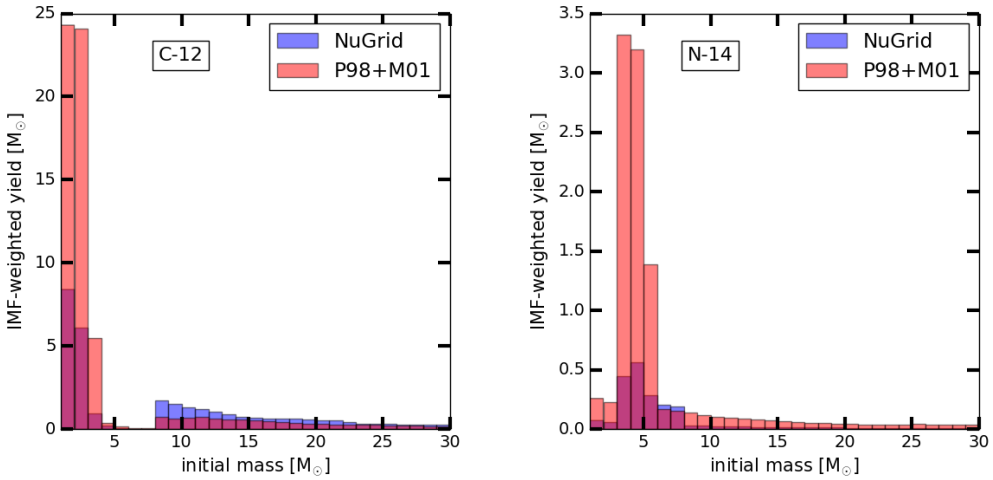

Figure 3.8: IMF-weighted yields of ^{12}C and ^{14}N versus initial mass based on NuGrid yields with $Z = 0.001$ and P98+M01 yields with $Z = 0.004$. Online Access

.

The AGB ejecta of N of the SSP based on M01 yields are a factor of 4.8 larger than those based on NuGrid yields. More massive AGB models which are responsible for N production via HBB show large discrepancies in yields between NuGrid and M01 (Fig. 3.8). The amount of N produced in these stellar models depend on the length of the TP-AGB phase which is based on free parameters of the synthetic models of M01. Through most of the evolution the SSP ejecta of N from massive stars is about a factor of five lower for NuGrid yields than for yields by P98+M01.

O, Si — The stellar yields of O of AGB models differs more between yield sets at lower Z than at solar Z. At low Z this difference is the largest for the most massive AGB models which results early on in the largest difference in the SSP ejecta of AGB stars (Fig. 3.7). The evolution of SSP ejecta of O from massive stars is in slightly better agreement between the yield sets at low Z than at solar Z.

The SSP ejecta of Si from AGB stars is low with P98+M01 yields and below figure

boundaries with NuGrid yields. Si is only sensitive to the initial abundance which differs between yield sets since NuGrid applies an α-enhanced initial abundance for models of $Z = 0.001$. AGB ejecta of both sets are in good agreement when we apply the same initial abundance. The SSP ejecta of Si from massive stars shows a good agreement between yield sets as at solar Z.

Fe — Fe ejecta from AGB stars do not agree between yield sets of M01 and NuGrid due to the difference in initial abundance. Accumulated Fe ejecta of massive stars based on NuGrid yields starts below and then increases above the ejecta based on of P98+M01 yields as at solar Z. The strong fallback in NuGrid models of high initial mass limits the Fe ejecta at early times in the SSP evolution.

3.1.4 Discussion

Comparison with Wiersma et al.

We compare the SSP ejecta calculated with SYGMA with the results presented in W09, using the same set of stellar yields as in W09. We apply the net yields of AGB star models by M01 and net yields of massive star models by P98. We modify C, Mg and Fe yields of massive star models by a factor of 0.5, 2 and 0.5 as W09. The yields of Thielemann et al. (2003) are applied for SNe Ia as W09. The initial abundance of elements is taken from Table 1 of the latter work. We apply the same chemical evolution parameter as in W09: The Chabrier (2003) IMF which spans the initial mass range from $0.1\,\mathrm{M}_\odot$ to $100\,\mathrm{M}_\odot$ and an exponential DTD for SNe Ia with a characteristic delay time τ of 2×10^9 yr. The initial mass range for which yields were ejected is not known and we choose the range from $0.8\,\mathrm{M}_\odot$ to $100\,\mathrm{M}_\odot$ to match best Fig. 2 in W09. The lower limit is the lowest initial mass of stellar models to ignite He in the center and to enter the AGB stage (Karakas 2011). Stars of lower initial mass are not of relevance due to their long lifetime beyond the Hubble time.

The initial mass M_{mass} which marks the transition from AGB stars to massive stars depends on the upper limit of super-AGB stars and their electron-capture SN channel. Poelarends et al. (2008) estimated $M_{mass} = 9.25\,\mathrm{M}_\odot$ based on their models of solar metallicity but this value might vary with metallicity (Doherty et al. 2015). Note that M_{mass} depends sensitively on the core growth which in turn depends on the choice of mass loss and efficiency of TDUP in the AGB stage. Jones et al. (2016a) found that an increasing convective boundary mixing efficiency increases the TDUP

efficiency in super-AGB stars and impedes core growth which might influence M_{mass}. We choose a value of $M_{mass} = 8\,M_{\odot}$ as the transition from AGB to massive star models since this value agrees best with the accumulated fraction of ejecta of AGB stars, massive stars and SNe Ia of Fig. 2 in W09. We do not know M_{mass} chosen to derive the results of their Fig. 2 but it might lay in the transition from the largest AGB star model of $7\,M_{\odot}$ to the smallest massive star model of $9\,M_{\odot}$ of the P98+M01 set. All parameter choices are as in Table 3.1 except for the IMF yield range which extends from $0.8\,M_{\odot}$ to $100\,M_{\odot}$.

We compare the accumulated fraction of total ejecta of AGB stars, massive stars and SNe Ia of our SSP model at solar Z with W09 (Fig. 3.9). The uncertainty related

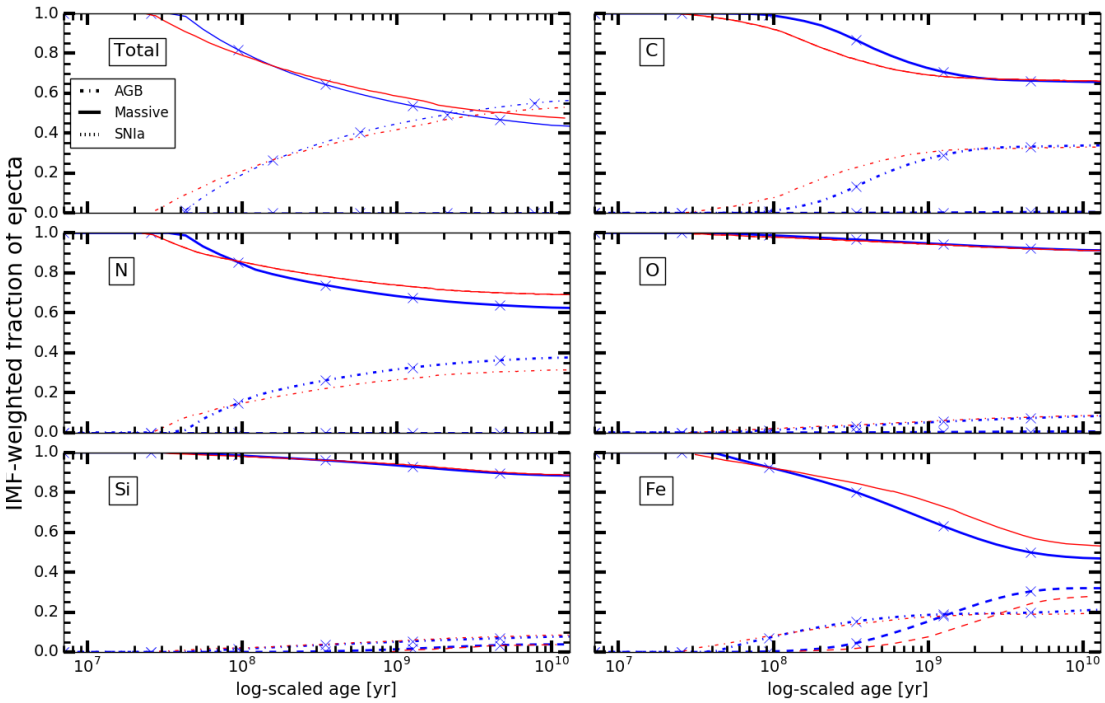

Figure 3.9: Fraction of total mass ejected from AGB, massive star and SNe Ia for a SSP at solar metallicity with yield input from P98+M01 (blue, triangles) compared to results extracted from Fig. 2 in W09 (red, crosses). Online Access.

to the value of the transition mass M_{mass} affects the appearance of the AGB star ejecta and the drop in total massive star ejecta. Fig. 3.10 demonstrates the sensitivity of accumulated AGB and massive star ejecta for choices of $M_{mass} = 7.5\,M_{\odot}$, $8\,M_{\odot}$ and

8.5 $M_\odot$.

The evolution of C indicates up to 10% less ejecta from intermediate-mass stars in our model but agrees very well above 10^9 yr when stars with initial mass below

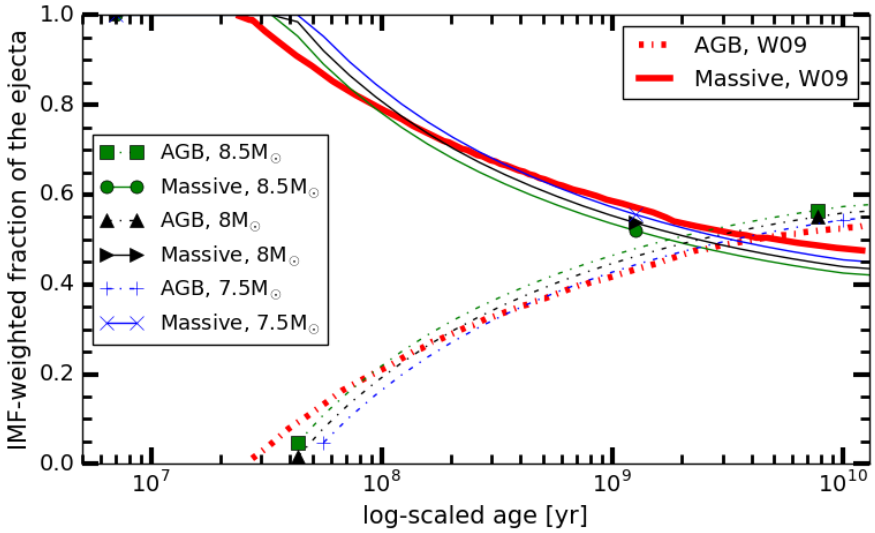

Figure 3.10: Evolution of fraction of total ejecta for transition masses of 7.5 $M_\odot$, 8 $M_\odot$ and 8.5 $M_\odot$. Online Access.

2 $M_\odot$ start ejecting their material. N yields increase smoothly with initial mass which leads to a smooth increase of the SSP ejecta similar to W09. C and N evolution in the transition region from AGB to massive stars depends on the way the yields are treated over the initial mass range. We fit the total ejected yields over the whole initial mass range while we do not know the treatment in W09. The total ejecta over the initial mass range where the range for potential values of M_{mass} between the AGB star model of 7 $M_\odot$ and the massive star model at 9 $M_\odot$ is highlighted in yellow in Fig. 3.11. In this yellow uncertainty band the total ejecta increases by about one third and the stellar lifetime decreases by more than 50% towards higher initial mass.

Another uncertainty is variation of elements with initial mass. Different methods have been used in literature such as an interpolation of single elements over the initial mass range (Côté et al. 2012). In SYGMA, yields of a specific stellar model are applied in an initial mass interval given by half the distance to the neighbouring stellar models. Since we do not know about the approach of W09 one might expect differences due the yield interpolation methods. The strong variation of C and N yields of massive AGB models combined with different model assumptions might explain the deviation

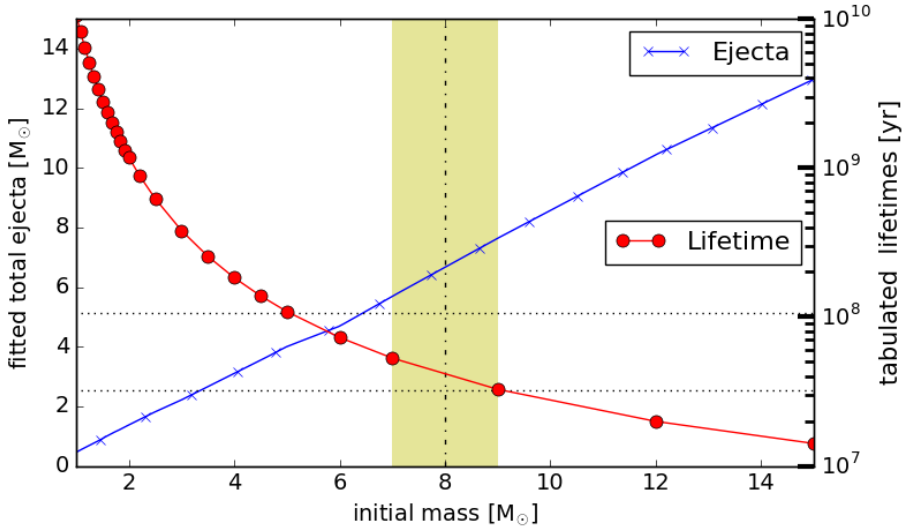

Figure 3.11: Stellar lifetime and total ejected mass versus initial mass for P09+M01. The shaded region indicates the transition from the yield set of M01 to the yield set of P98, when the stellar models of $6\,M_\odot$ and $7\,M_\odot$ of P98 are excluded. The dashed-dotted line represents the transition mass of $8\,M_\odot$ for our best model matching results of W09. Online Access.

between our results and W09.

The α-elements O and Si agree very well with W09 (Fig. 3.9). They are dominantly produced in massive stars within the first 30 Myr and the dependence of the massive star ejecta on initial mass cannot be compared. The evolution of Fe ejecta of massive stars and SNe Ia are qualitative similar but show differences of similar magnitude as C. As for O and Si the contribution from AGB stars stems from the initial, unprocessed material with good agreement between our result and W09.

We compare the evolution of [C/Fe], [N/Fe], [O/Fe] and [Si/Fe] in comparison with W09 (Fig. 3.12). The overall largest differences are found within the first ≈ 20

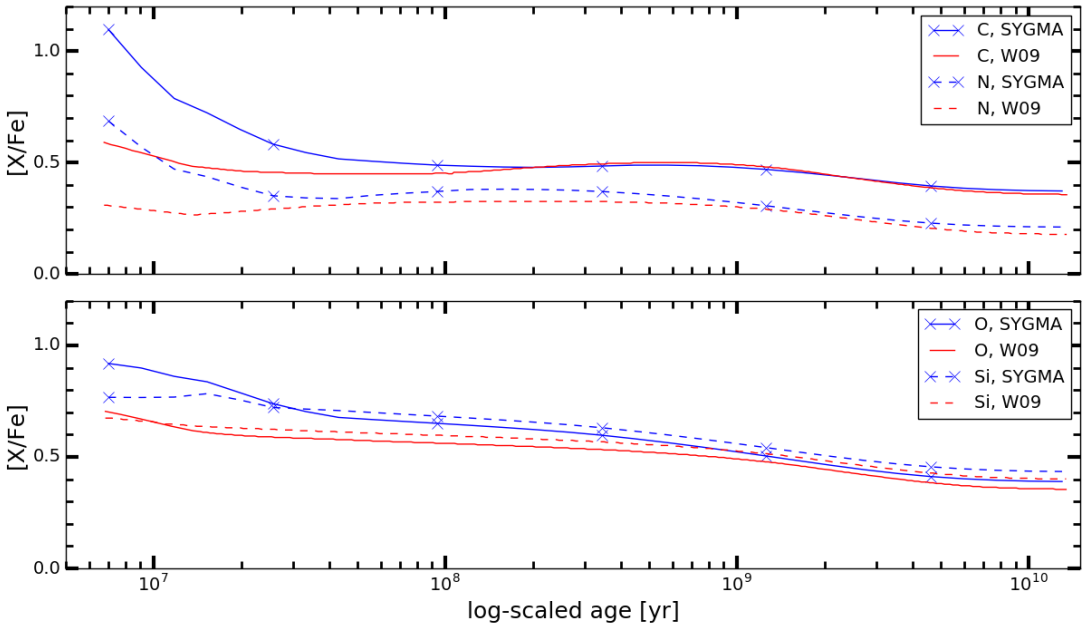

Figure 3.12: Elemental ratios of the total ejecta of a SSP at solar Z simulated with SYGMA and with yields from P98+M01 compared to results by W09. Online Access.

Myr where [C/Fe] in our model differs from W09 by over 0.4 dex. During this time enrichment takes place only by massive stars (Fig. 3.11) which stellar yields span 1.7 dex in [C/Fe] over the whole initial mass range. [C/Fe] in the SSP ejecta is very sensitive to the upper limit of the IMF yield range. A decrease of the upper IMF yield limit from our best fit value of $100\,M_\odot$ down to $30\,M_\odot$ leads to a better agreement with the first value of [C/Fe] of 0.7 in W09 (Fig. 3.13). Later in the evolution [C/Fe] drops by about 0.5 dex below the results of W09. The choice of the upper limit of

the IMF as W09 together with the same interpolation of C and Fe with initial mass of the massive stars as W09 could result in a better agreement of our results with W09. [N/Fe], [O/Fe] and in particular [Si/Fe] of the yields vary less strongly with

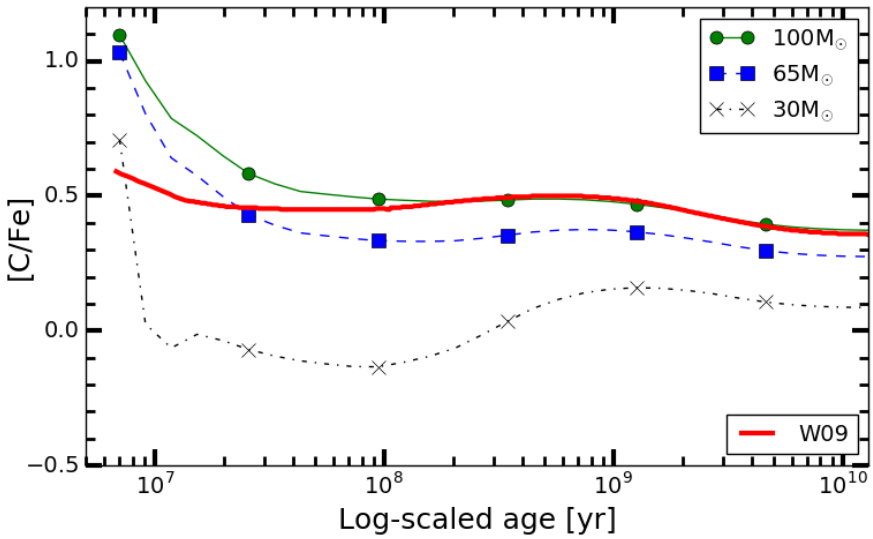

Figure 3.13: Evolution of [C/Fe] for upper boundaries of 30 $M_\odot$, 65 $M_\odot$ and 100 $M_\odot$ up to which yields are applied. Online Access.

initial mass which might explain the better agreement with W09 (Fig. 3.12).

We distinguish between the same chemical evolution assumptions but different yield input (Fig. 3.14) and different chemical evolution assumptions with same yield input (Fig. 3.9). We find that the total ejecta of AGB stars and massive stars are in better agreement when applying the same chemical evolution assumptions. During the early AGB contribution there is a larger disagreement in the evolution of C due to different chemical evolution assumptions while at later times is is due to different yield input. The evolution of N, O and Si differ the most for different yield input likely due to the fallback prescriptions. Fe differs stronger with varying chemical evolution assumptions. The same SNIa yields are applied in both sets which results in a good agreement when the same chemical evolution assumptions are applied. Overall we find that differences in SSP implementation can play a more important role than the input yields which emphasizes to use the same SSP implementation for different yield sets.

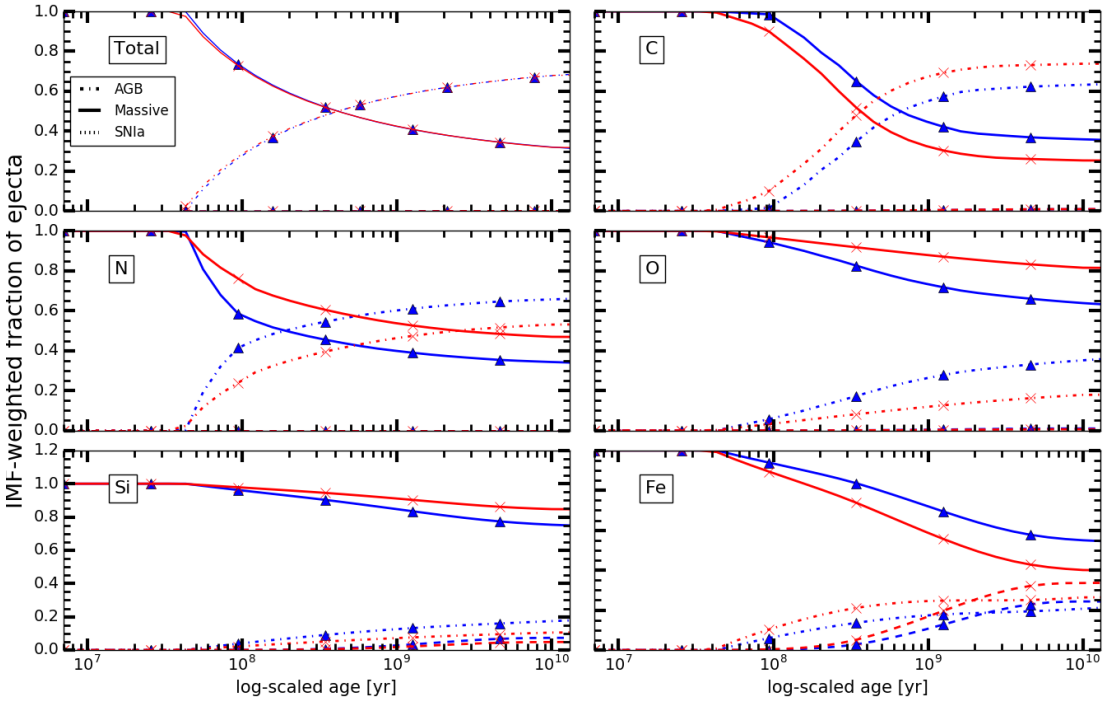

Figure 3.14: Fraction of total mass ejected from AGB, massive star and SNe Ia for a SSP at solar metallicity with NuGrid yield (blue, crosses) and yields from P98+M01 (red). Online Access.

Impact of mass-cut prescriptions

The composition of SSP ejecta depends on the choice of the mass-cut prescription and fallback of the underlying stellar models. NuGrid provides two different explosion prescriptions based on the convective-enhanced neutrino-driven engine (e.g. Fryer and Young 2007; Fryer et al. 2012, F12). On a short timescale the rapid-convection explosion provides enough energy for a successful explosion. The delayed-convection explosion requires longer times to deposit enough energy to explode which results in more fallback and larger remnants for stellar models of $Z = 0.02$ and $Z = 0.001$ (Fig. 3.15). The remnant mass in the delayed explosion increases with initial mass while the remnant mass for the rapid explosion peaks strongly around $24\,M_\odot$ which results in the large remnant mass of $15.5\,M_\odot$ for the stellar model with initial mass of $25\,M_\odot$. The latter model collapses directly into a BH and the remnant mass becomes the total mass at collapse (Fig. 3.15).

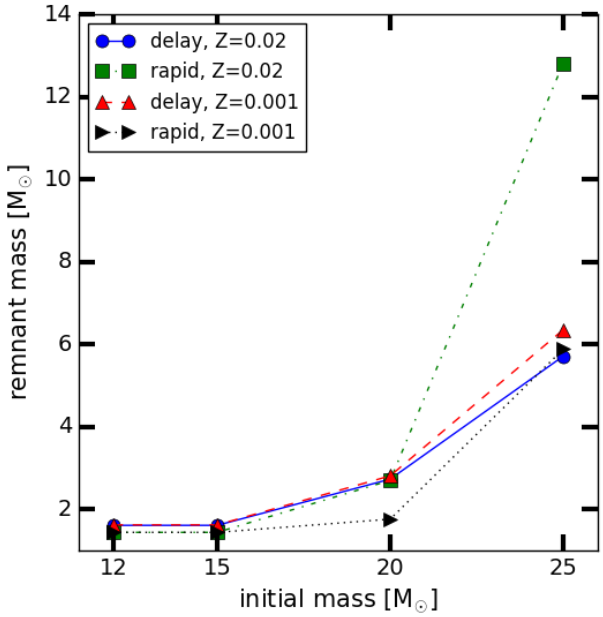

Figure 3.15: Remnant masses based on stellar models of $Z = 0.02$ and $Z = 0.001$ of NuGrid with the delayed and rapid explosion prescription. Online Access.

We compare the impact of the two fallback prescriptions on the massive-star ejecta of SSPs of $10^4\,M_\odot$ for $Z = 0.02$ and $Z = 0.001$ (Fig. 3.16). The SSP ejecta of C, O and Si differ more between the fallback prescriptions at $Z = 0.02$ than at $Z = 0.001$

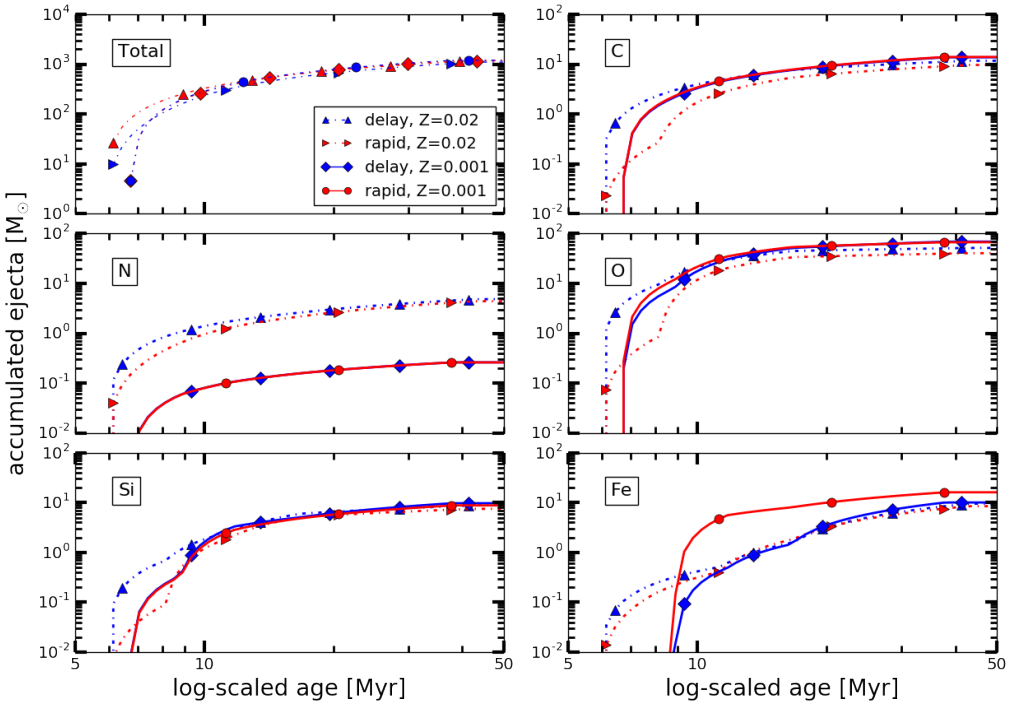

Figure 3.16: Accumulated ejecta of massive stars of NuGrid yields at $Z = 0.02$ and $Z = 0.001$ computed with the delayed and rapid fallback prescription. Online Access.

due to the BH formation in the rapid explosion of the stellar model with initial mass of $25\,M_\odot$ at $Z = 0.001$. This prevents the ejection of the Si, O and C shell. Similar amounts of Fe fall back onto the remnant with both explosion prescriptions due to the deep location of the Fe core and the SSP ejecta of Fe show smaller differences.. The ejection of elements of the SSP at $Z = 0.001$ agree well except for Fe. Little fallback in the rapid explosion of the stellar model with initial mass of $20\,M_\odot$ and a sufficient large Fe core allows the ejection of a thin layer of the Fe core which boosts the amount of SSP ejecta.

The yield sets with the delayed and rapid prescription are available online (Section 3.1.5, 3.1.6). The rapid explosion models match better the observed gap between NS and BH remnants than the delayed models even though the gap might be sparsely populated (references in F12). Delayed explosions produce more fallback BHs, in particular at low mass and yield a larger fraction of low-mass BHs formed with a SN explosion. The latter can explain the observed BH systems which indicate a natal kick (F12). Fallback is also relevant to produced the observed weak supernova which are believed to be observed (F12). While both sets are valid to use we recommend yields with the delayed explosion prescription in chemical evolution models. F12 argues that both extremes might be necessary to explain the SN. We combine yields of the delayed and rapid explosions to take into account explosions on short and long timescale and provide a yield table in which we add half of the yields of each prescription.

3.1.5 Online availability

The SYGMA web interface allows to simulate, analyze, and extract SSP ejecta which includes all stable elements and many isotopes up to Bi. The web page with documentation can be found at `http://nugrid.github.io/NuPyCEE`. We introduce the yield sets and parameters which are available within the web interface. The yield input are the NuGrid yields, with delayed and rapid explosion prescription as well as a mix of both, and SNIa yields by Thielemann, Nomoto, and Yokoi (1986) and Pop III yields by Heger and Woosley (2010). The available metallicities are $Z = 0.02$, 0.01, 0.006, 0.001 and 0.0001, 0. Yields are applied in the initial mass range from $1\,M_\odot$ to $30\,M_\odot$. Different chemical evolution parameters such as IMF and SNIa DTD can be set.

SSP ejecta can be extracted in the form of tables which contain for each time step

the fraction of elements and isotopes of choice. The ejecta of each element or isotope is normalized to the total mass of the SSP. Parts of a table which contains the amount of elements ejected over 10^{10} yr by a SSP of $10^4\,M_\odot$ at $Z = 0.02$ is presented in Table 3.2.

Age [yr]	C	N	O	Fe	Sr	Ba	M_tot [Msun]
0.000E+00	3.466E-03	1.063E-03	9.650E-03	1.438E-03	6.072E-08	1.813E-08	1.000E+04
1.000E+07	7.848E-04	2.770E-04	4.412E-03	8.351E-05	2.715E-08	1.425E-09	6.557E+02
1.269E+07	1.120E-03	3.859E-04	6.546E-03	1.866E-04	4.197E-08	2.014E-09	9.426E+02
				.....			
7.880E+09	6.301E-03	2.697E-03	1.508E-02	2.505E-03	1.391E-05	3.973E-06	7.067E+03
1.000E+10	6.304E-03	2.697E-03	1.509E-02	2.552E-03	1.391E-05	3.973E-06	7.068E+03

Table 3.2: Table of elements extracted with the SYGMA interface.

The SYGMA code is open-source and available to download at `http://nugrid.github.io/NuPyCEE`. We provide an online documentation based on SPHINX[3], guides and teaching material in form of ipython notebooks. NuGrid's stellar and nucleosynthesis data sets are available at `http://nugridstars.org/data-and-software/yields/set-1` and can be analyzed with NuGrid's WENDI interface at `http://wendi.nugridstars.org`.

3.1.6 Yield set database

We provide a comprehensive set of yield tables for SYGMA which includes all yield tables applied in this work. Yields of massive star simulations with modeled CCSN, hypernova and pair-instability SN of Nomoto, Kobayashi, and Tominaga (2013) are included. SNIa yields by Thielemann et al. (2003) and by Seitenzahl et al. (2013) can be used. Included are yield tables of neutron star merger ejecta by Rosswog et al. (2014) and Arnould, Goriely, and Takahashi (2007). Ejecta of magneto-hydrodynamic simulations by Nishimura, Takiwaki, and Thielemann (2015) and Pseudo-proto-neutron star wind ejecta based on analytic models are also available. Abundances from primordial nucleosynthesis are taken from Timmes, Woosley, and Weaver (1995) based on Walker et al. (1991) and from Coc, Uzan, and Vangioni (2013). Other yield tables will be added on request.

[3]http://www.sphinx-doc.org

3.1.7 Summary and Conclusions

We have introduced the SYGMA module which provides the chemical ejecta and stellar feedback of simple stellar populations for hydrodynamical simulations and semi-analytical models of galaxies. We presented the model assumptions and capabilities such as a variety of SNIa delay-time distributions and initial mass functions. The contributions from AGB stars, massive stars, SNe Ia and r-process sites such as NS mergers and CCSN can be analysed. Arbitrary yields can be applied and available in a large yield library which include yields from the NuGrid collaboration for all stable elements and many isotopes up to Bi.

An online interface can be used to simulate, analyze and extract the ejecta SSP ejecta in tabulated form for choices of chemical evolution parameters (Appendix 3.1.5). Access to the web interface, documentation, interactive examples are available at http://nugrid.github.io/NuPyCEE. where the mdule is the basic building block of NuGrids chemical evolution framework NuPyCEE.

The SSP ejecta based on the NuGrid yields and the combined yields of P98 and M01 are compared at solar Z and low Z. We find at both metallicities differences in C and N due to massive and super-AGB stars which are a factor of 3.5 and 4.8 at low Z. This is due to the complete stellar models of NuGrid which include the TP-AGB stage and HBB in the most massive models. O, Si and Fe in the SSP ejecta vary by up to a factor in case of the total ejecta of O and Fe at solar Z due to the amount of CCSN fallback in both yield sets.

The functionality of the module was verified through a comparison with W09 in which we apply their yields. The final accumulated ejecta are well in agreement in both works with the largest differences in the fraction of ejecta of N and Fe from massive stars of 10%.

We have analyzed the impact of CCSN fallback prescriptions of massive stellar models on the ejecta composition of SSPs at $Z = 0.02$ and $Z = 0.001$. At the latter metallicity we find the largest variations of about a factor of ten in C, O and Si in the first 10 Myr which decreases to less than a factor two in the total ejecta. The total ejecta of Fe at $Z = 0.02$ shows with a factor of 1.6 the largest difference between the fallback prescriptions at both metallicities.

3.2 Effect of convective boundary mixing on O production and [O/Fe] in SSPs

In this section I summarize my work about the impact of convective boundary mixing in AGB models, as applied in Chapter 2, on the chemical enrichment of simple stellar populations.

Discontinuities at boundaries, an outcome of theory of mixing length, are in disagreement with Newton's laws (Canuto 1998; Herwig 2000). Many efforts have been made to study convection in stars through multi-D hydro simulations (e.g. Freytag, Ludwig, and Steffen 1996; Porter and Woodward 2000; Stancliffe et al. 2011; Herwig et al. 2014) Applying prescriptions for convective boundaries derived from multi-D simulations are common (Miller Bertolami and Althaus 2006; Weiss and Ferguson 2009). Core-overshooting, additional mixing at the upper boundary of the convective core, is needed to match the morphology of cluster turnoffs (VandenBerg and Stetson 2004, and references in it).

CBM at all convective boundaries is applied in my stellar models (Chapter 2) through a exponential declining velocity field beyond the boundary (Freytag, Ludwig, and Steffen 1996; Herwig et al. 1997; Herwig 2000). Special boundary mixing parameter are applied in the TP-AGB phase for the pulse-driven convective zone as motivated by Herwig et al. (2007)'s 2D and 3D simulations. Also an increased mixing efficiency is applied during TDUP (Herwig, Langer, and Lugaro 2003). The boundary mixing at the bottom of the pulse-driven convective zone has strong implications for the He intershell abundance and structure. Convective boundary mixing leads to effective O production of about 15% in mass fraction while without CBM only about 2% is reached in the intershell (Herwig 2005).

The O enrichment is in agreement with surface abundance of post-AGB PG1159 stars which reveal the He intershell (Werner and Herwig 2006). Recently Delgado-Inglada et al. (2015) found O enrichment in the successor of AGB stars, in planetary nebula, at different metallicity supporting the idea of O production in AGB stars. The impact of the boost of O production due to CBM has not been estimated. Stellar abundance could serve as constrains for the CBM efficiency in AGB models.

With simple stellar populations the relevance of O production due to CBM for the chemical evolution is estimated. Applied are the AGB yields enriched based on stellar models with CBM (Chapter 2) and AGB yields by Karakas (2010, K10) who

do not include CBM. The yields of massive star models are those of Chapter 2 and SNIa yields are from Thielemann, Nomoto, and Yokoi (1986).

We compare SSPs of $10^4\,M_\odot$ at $Z = 0.02$ and $Z = 0.0001$. We find at $Z = 0.0001$ 1 dex more total O ejecta with yields of this work than with K10 while the difference is small at $Z = 0.02$ (Fig. 3.17). The total amount of O ejected by AGB stars is only about 12% of the O ejected by massive stars at $Z = 0.0001$ and not relevant for Galactic production.

SSPs of both metallicities show early on a drop in [O/Fe] down to about -0.1 due to the contribution of massive stars. At 5×10^7 yr the SSPs show the beginning of a 'knee' in [O/Fe] which indicates the onset of SNIa contributions (Fig. 3.17). This [O/Fe] drop is increased at $Z = 0.0001$ by up to 0.05 when yields with CBM are applied while at $Z = 0.02$ the increase is below 0.05.

These estimates indicate no relevance of CBM for Galactic production. With the galaxy code OMEGA presented in the next section the impact on the Milky Way can be estimated.

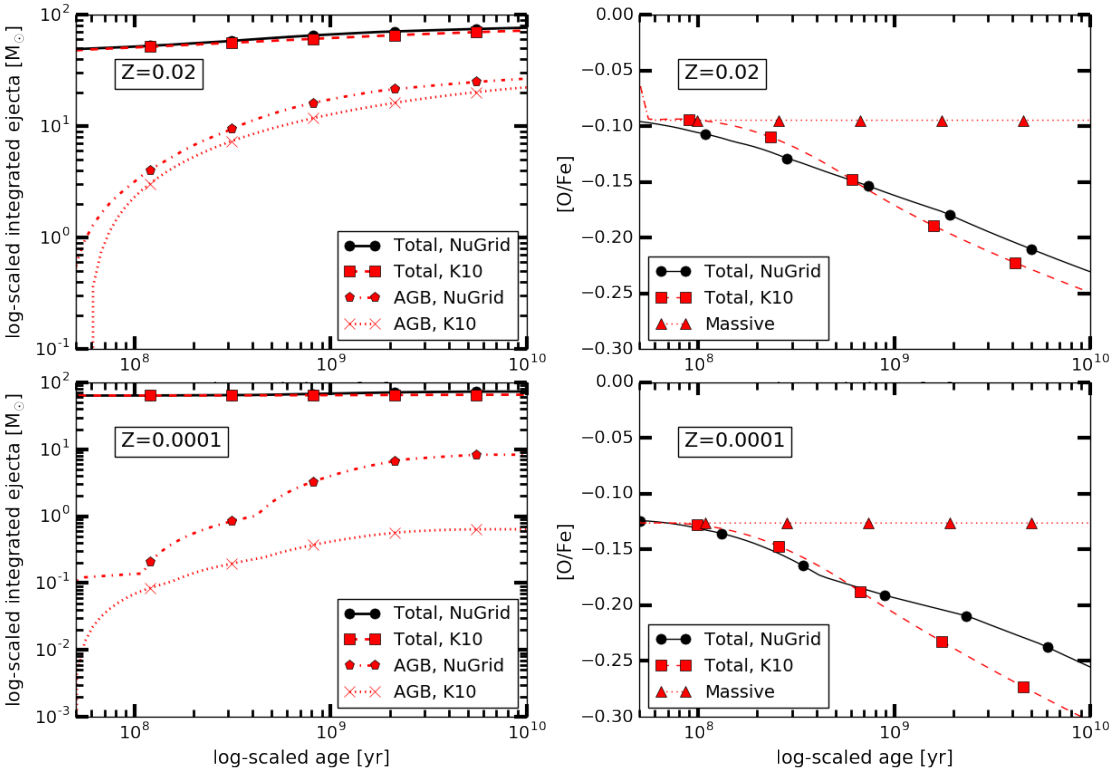

Figure 3.17: Comparison of the evolution of [O/Fe] in the ejecta of different (combined) contributors, namely AGB stars, massive stars and SNIa for $Z = 0.0001$ (top) and $Z = 0.02$ (bottom).

3.3 Galactic chemical evolution with the NuPyCEE framework

For galactic chemical evolution studies I have built with Dr. Côté the one-zone model for the evolution of galaxies (OMEGA) which utilized SSPs of SYGMA (Côté et al. 2016b; Côté et al. 2016c). OMEGA models the gas content and takes into account dark matter as well as galactic infall and outflows of matter (Côté et al. 2016c). I have developed the framework which models multiple stellar populations and allows to apply continuous star formation rates and Dr. Côté have developed different inflow and outflow models. Available is also a stellar abundance database (STELLAB) for comparisons with observations which was mainly build by Dr. Côté and I contributed

features which allowed the easy addition of stellar abundance datasets.

SYGMA, OMEGA and STELLAB are the NuGrid chemical evolution framework. All code is available through a website at http://nugrid.github.io/NuPyCEE which I created (Fig. 3.18). With NuPyCEE the impact of new stellar yield sets provided by NuGrid on chemical evolution can be explored. The NuPyCEE framework was utilized in a variety of studies to which I have contributed mostly through the development of OMEGA and my stellar yields and which are summarized below.

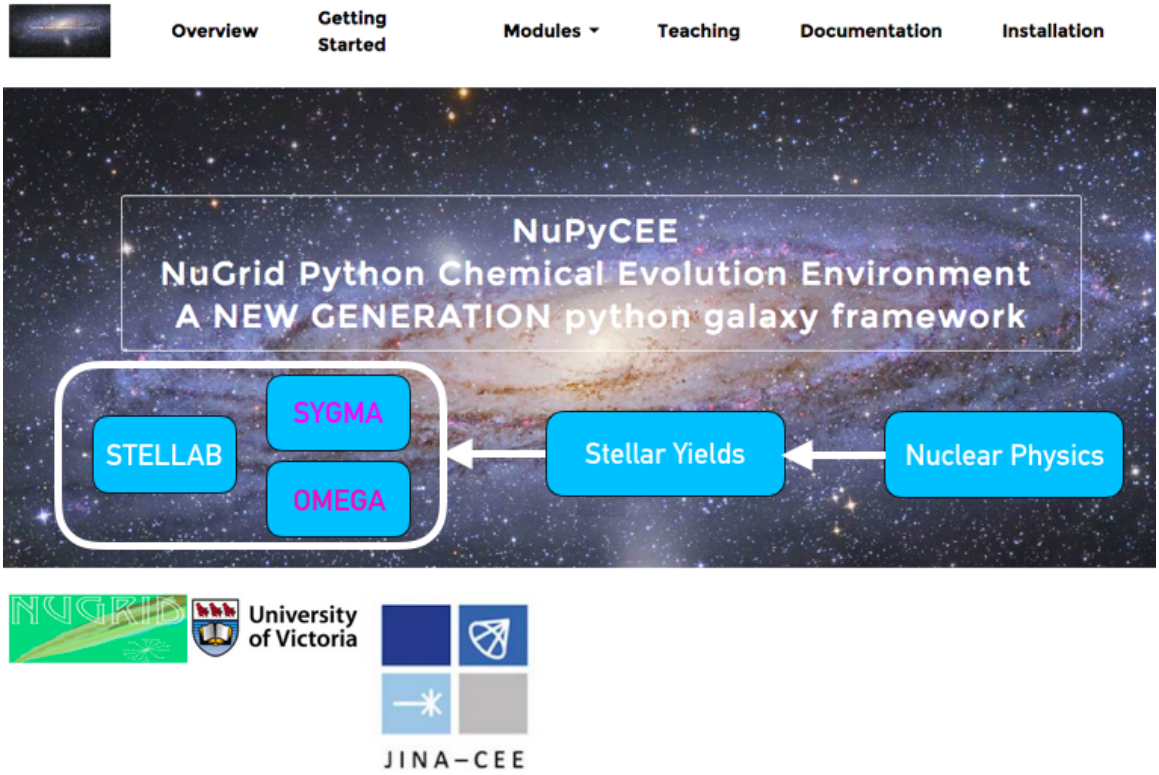

Figure 3.18: Website of the NuPyCEE framework. On top a pipeline with the NuPYCEE modules SYGMA, OMEGA and STELLAB is shown.

With a Monte Carlo method the influence of uncertainties of chemical evolution parameters on the chemical evolution of 16 elements of a Milky Way model were estimated Côté et al. (2016d). Bands of uncertainty were derived for the evolution of each element. The slope of the IMF and the total number of SNIae were identified as the main sources of uncertainties.

A first investigation into the impact of the yield input grid size on chemical evolution is done in Côté et al. (2016b). The number of massive star models included in the yield set was varied and the impact on nine elements analyzed. The chemical

evolution of elements is more sensitive to the metallicity range of the yield grid rather than the number of metallicities within that range. Also stressed is the importance of the remnant mass prescription which can lead to variations of up to 0.7 dex in chemical evolution predictions.

In Côté et al. (2016c) different galactic inflows and outflow models and their impact on the chemical evolution of elements of the dwarf galaxy Sculptor is analyzed. The best parameter values to match the observed abundance distribution for each inflow- and outflow model is derived with a Markov-Chain Monte-Carlo method. Similar matches to the observed element distributions are obtained with each prescription while fundamental parameters such as the number of SNIa and the strength of the outflows differ. Hence the evolution of galaxies cannot be constrained by matching the observed element abundances.

3.4 Outreach

The aim is to provide the chemical evolution code NuPyCEE to the scientific community since GCE codes are often either not publicly available (e.g. Kobayashi et al.) or not well documented (e.g. code of Timmes, Woosley, and Weaver 1995). We develop our framework online on GitHub[4] and include an extensive documentation inside and outside of the code.

To give students insight into chemical evolution I have created interactive tutorials available online (Fig. 3.18). NuPyCEE is written in the common programming language python which allows an easy start with the code. I have taught an introduction into chemical evolution and NuPyCEE in the ASTR501 and ASTR404 Astronomy class for graduate students at the University of Victoria. I have created teaching notebooks and supervised students with projects about the impact of different r-process sources on the solar-system distribution and the investigation into the chemical evolution of the ultra-faint dwarf galaxy Hercules.

3.5 Summary

To model the chemical ejecta and feedback of simple stellar populations in hydrodynamic simulations and semi-analytic models the SYGMA module is presented. Its

[4]http://nugrid.github.io/NuPyCEE

functionality was verified in a comparison with work by Wiersma et al. (2009). The SSP ejecta of different elements based on the yield set presented in Chapter 2 was compared with a widely used yield set.

Convective boundary mixing in AGB models which is required to explain observed features leads to an increase of the amount of O ejected. Its impact on the chemical evolution was estimated through a comparison of SSP ejecta based on yields with and without CBM. The impact was found to be small for metallicities of $Z = 0.02$ and $Z = 0.0001$.

To model the evolution of galaxies the chemical evolution framework NuPyCEE is presented and applications are summarized. Such studies require ejecta of stellar models at very low metallicity which experience H ingestion events. H-ingestion events are investigated in the following chapter.

Chapter 4

H-ingestion flashes and i process

4.1 Introduction

Observation of stars at lower and lower metallicity in the galactic halo (e.g. Keller et al. 2014, recently with [Fe/H] below -7) motivate to investigate stellar models down to extreme low and zero metallicity. Such stellar evolution simulations reveal strong H-ingestion episodes in different phases of evolution for example in low and zero-metallicity AGB stars (Fujimoto, Ikeda, and Iben 2000), in very late thermal pulses (VLTP) in post-AGB starsH- (Herwig et al. 2011) and in the He-core flash in low-Z low mass stars (Campbell, Lugaro, and Karakas 2010).

In an ingestion event H is mixed from a H-rich stellar envelope, down into a C-rich convective layer where high enough temperatures exist to allow C to capture a proton. ^{13}N is produced which decays to ^{13}C while under the influence of convective motions as shown in the sketch in Fig. 4.1. If ^{13}C reaches deep enough layers, available alpha particle lead to the reaction ^{13}C(α,n)^{16}O) which releases neutrons. The latter can lead to the build-up of heavy elements. This process is called intermediate neutron-capture process (Cowan and Rose 1977) and operates at neutron densities between s- and r-process of $N_n \approx 10^{15}\mathrm{cm}^{-3}$.

The stellar evolution tracks of the lowest metallicities which I calculated reveal ingestion episodes in low-mass AGB stars, super AGB stars and massive stars. The ingested H burns on the same timescale as it is mixed and its burning affects the fluid flow. Such a convective-reactive regime cannot be properly described with the mixing length theory applied in stellar evolution models (Herwig et al. 2011; Jones et al. 2016b). Results of 3D hydrodynamic simulations of Sakurai's object by Herwig

et al. (2011), Herwig et al. (2014), and Woodward, Herwig, and Lin (2015) reveal that ingestion events cannot be properly treated in 1D.

These results have to be understood in context of observations. For example the i process in VLTP of the post-AGB star Sakurai's object is motivated by its light curve and surface abundances (Herwig et al. 2011). Also certain grains can be explained by the i process (Fujiya et al. 2013; Jadhav et al. 2013). To model yields of stars below the current lower limit of [Fe/H] = -2.3 3D investigations are required and a proper prescription of these 3D processes in 1D have to be found. In the following sections I lay out my work about such ingestion events.

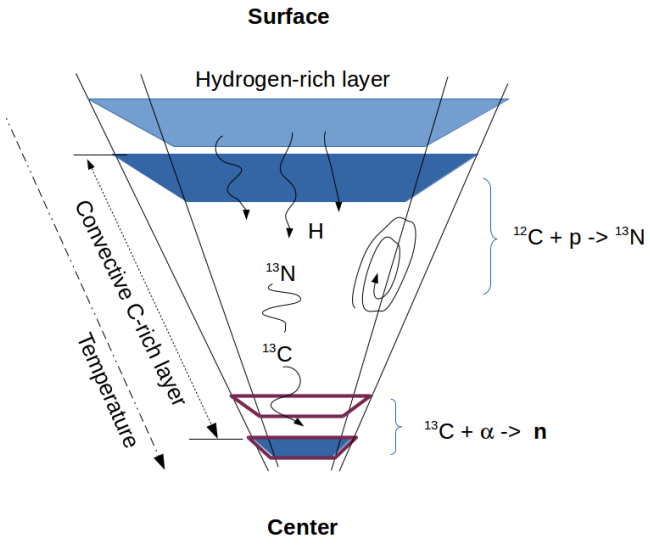

Figure 4.1: Sketch of a slice of a sphere showing H ingestion with relevant processes for the nucleosynthesis of heavy elements.

4.2 H ingestion in super-AGB stars

In this section I summarize my contributions to and the results of the investigation of H ingestion and convective boundary mixing in S-AGB models which are reported in Jones et al. (2016b).

Included in S. Jones, C. Ritter, F. Herwig, C. Fryer, M. Pignatari, M. G. Bertolli, B. Paxton, 2016, MNRAS, 455, 3848

The Super-AGB stars are the most massive AGB stars in the initial mass range from $\approx 7.5\,M_\odot$ to $\approx 9.75\,M_\odot$ (Poelarends et al. 2008). Those models ignite C due to their degenerate conditions and neutrino cooling (Jones et al. 2016b) which leads to the formation of a O/Ne/Mg core under the He-burning shell of the TP-AGB phase (García-Berro and Iben 1994; García-Berro, Ritossa, and Iben 1997; Siess 2010).

In Super-AGB models presented in Chapter 2 convective boundary mixing (CBM) is applied at all boundaries in the form of an exponential decreasing mixing diffusion coefficient (Herwig 2000). CBM in low-mass stellar models can match the abundance observed in post-AGB stars (Werner and Herwig 2006) and produce ^{13}C pockets and the observed s process signatures (Herwig 2000). In intermediate mass models the protons mixed through the boundaries due to CBM are burned at high temperatures which can alter the stellar evolution and chemical enrichment (Herwig 2004; Herwig 2004). To take into account feedback of very energetic proton burning the efficiency of CBM was reduced in S-AGB models presented in Chapter 2 while systematic studies are required to analyze the impact of different CBM efficiencies in detail.

In the S-AGB models at $Z = 0.0001$ (Chapter 2) I found repeating H ingestion in the pulse-driven convective zone (PDCZ) during third dredge-up in the TP-AGB stage. The occurrence of H ingestion events in these S-AGB models depends on the initial mass and metallicity.

I estimated that the energy release due to the burning of ingested H can become close to the internal energy which could lead to the unbinding of the layers above. Such conditions violate the assumption of hydrostatic equilibrium of stellar evolution models. The energy release due to H burning splits the PDCZ and stops further transport of H into deeper layers. Herwig et al. (2011) showed with 3D hydrodynamic simulations that such a split is a feature of the spherical approximation of the stellar model.

We performed a systematic study of different CBM efficiencies applied at the bottom of the pulse-driven convective zone and the convective envelope during the TP-AGB phase of S-AGB models of a range of metallicities. High CBM efficiencies at the bottom of the convective envelope can prevent growth of the He-free core and prevent the appearance of electron-capture SN. H ingestion in these stellar models could lead to i-process nucleosynthesis of second-peak elements as observed in C-Enhanced Metal Poor stars and introduced in the following section.

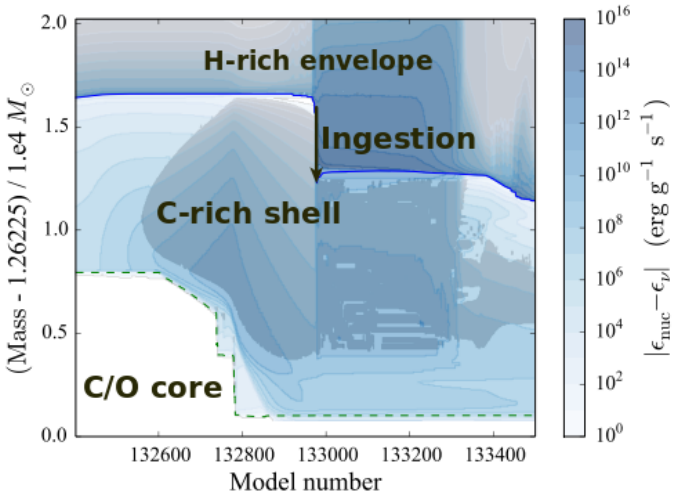

Figure 4.2: H ingestion into the convective He shell during a thermal pulse in the AGB phase of a 7 $M_\odot$ model of $Z = 0.0001$. Figure adopted from Jones et al. (2016b).

4.3 CEMP-r/s stars reveal i process signature

In this section I present results which were created in collaboration with Laurent Dardelet. We compared the prediction of simple i-process models based on the assumption of H ingestion found in AGB models (Chapter 2, Section 4.2) with the peculiar abundance of CEMP-r/s stars.

Included in L. Dardelet, C. Ritter, P. Prado, E. Heringer, C. Higgs, S. Sandalski, S. Jones , P. Denissenkov, K.Venn, M. Bertolli, M. Pignatari, P. Woodward, F. Herwig, 2014, XIII Nuclei in the Cosmos (NIC XIII), 145

4.3.1 CEMP-r/s stars

C-Enhanced Metal Poor (CEMP) stars are a class of metal poor stars with surface abundance of [C/Fe]>1. Their fraction increases towards lower metallicity and reaches 20% at [Fe/H]=-2 (Allen et al. 2012; Beers and Christlieb 2005). A subclass are CEMP-r/s stars which are characterized by large enhancement of s-process and r-process elements (Jonsell et al. 2006; Lugaro et al. 2012; Masseron et al. 2010).

The established theory to explain these enhancements assumes pre-enrichment with r-process material and s-process material accretion from a heavier companion AGB star (Jonsell et al. 2006). This theory is unable to explain the large [hs/ls][1] and low [La/Eu] ratios of CEMP-r/s stars such as the star CS 31062-050 (Fig. 26 in Bisterzo et al. 2012, Fig. 4.3).

4.3.2 A simple i-proces model for the CEMP-r/s stars

We build a 1-zone i-process model based on the physical conditions in a PDCZ of a AGB stellar evolution model. Adopted are temperature of 2×10^8 K, a density of $10^4\,\mathrm{g\,cm^{-3}}$ and a solar-scaled initial abundance of $Z = 10^{-3}$ with enhancements of O and C according to the abundances in the PDCZ. H is enhanced to mimic the H ingestion and the nucleosynthesis is modeled with the NuGrid single-zone PPN code (Herwig et al. 2008).

[1] ls and hs represent the total abundances of elements from the first and second s-process peaks of the solar system abundance distribution.

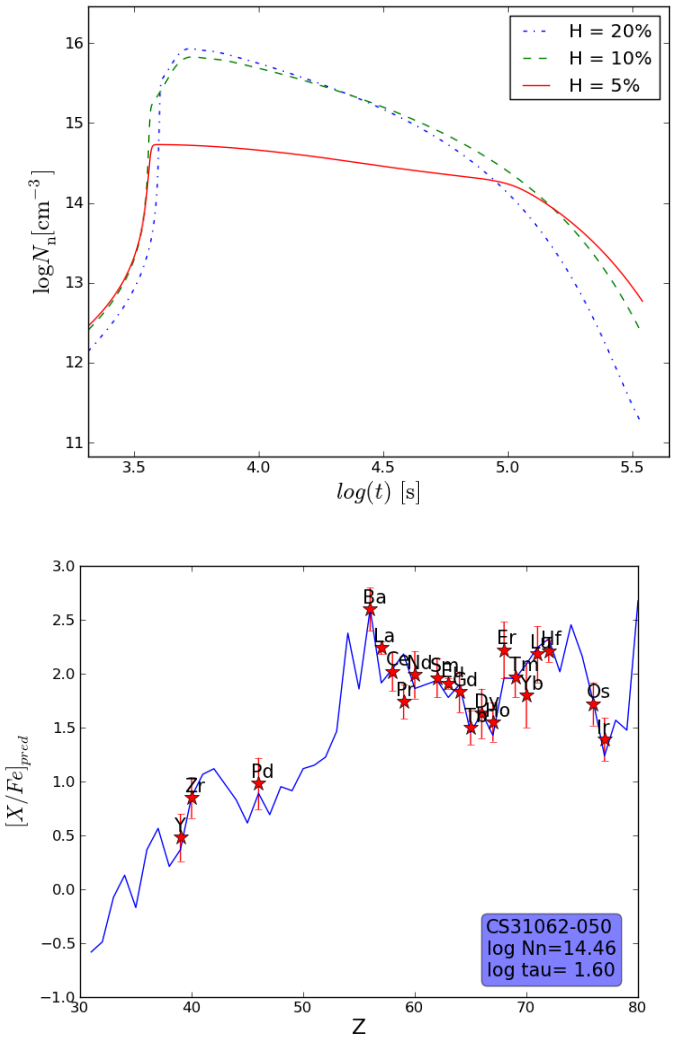

Figure 4.3: Change of neutron density N_n with time for the initial mass fractions of H of 0.2, 0.1 and 0.05 (top). Best match of the i-process model with the abundance pattern of the CEMP-r/s star CS 31062-050 Johnson and Bolte (bottom, abundance data from 2004). In the bottom-right corner the values of the neutron density N_n and exposure (tau) are shown.

Within the first second ^{13}N is produced out of most ^{12}C and decays into ^{13}C on the timescale of 9.97 min. This enables the ^{13}C(α,n)^{16}O neutron source which can produce neutron densities of $N_{\rm n} \sim 10^{15}{\rm cm}^{-3}$ depending on the amount of H initially available (Fig. 4.3). Over time the neutron exposure $\tau = \int_0^t N_{\rm n} v_T \, dt'$ (v_T is the neutron thermal velocity) increases which shifts the production from lighter to heavier elements. We find a good match of the i-process 1-zone model to the abundance of CS 31062-050 from Y to Ir (within the observational errors) for a given amount of H initially available and a given neutron exposure (Fig. 4.3).

When the energy release of burning of ingested H results in extreme perturbation of the spherical symmetry as in 3D hydrodynamic simulations (Herwig et al. 2014) these perturbations might terminate i-process nucleosynthesis. Such a self-quenching might depend on the physical conditions of the convective zone and stellar structure and a range of i-process termination times are expected. We treat the neutron exposure as a free parameter and find the best match for $log\tau = 1.6$ (Fig. 4.3).

Our predictions match the large ratio of [hs/ls] ≈ 1, the [La/Eu] ratios between 0.0 and 0.5 and the ratio of the Er-W region compared to those in the Os-Ir region of CS 31062-050. We identify these i-process signatures in other CEMP-r/s stars. Fe-group elements and Pb are not properly described due to the depletion of n-capture seed elements.

4.4 Summary and Outlook

In this chapter we investigated H ingestion and the i process in AGB models. We identify H-ingestion events in S-AGB models, which are stronger at low metallicity. They are sensitive to the choice convective boundary mixing and could lead to i-process nucleosynthesis. It has been found that ingestion events are not properly treated in 1D stellar models and require 3D hydrodynamic simulations.

We have shown that the observed heavy-element abundance of some CEMP-r/s stars can be matched with simple 1-zone i process models based on conditions derived from AGB model. These observations cannot be described with classical r-process and/or s-process predictions.

Realistic i-process predictions are required to connect observations with potential i-process sites. Herwig et al. (2011) has first shown that 3D hydrodynamic simulations are required to model H ingestion in Sakurai's object. For example only the 3D hydrodynamic simulations were able to identify the Global Oscillation of Shell H-

ingestion which appeared during H entrainment (GOSH, Herwig et al. 2014). But it is currently not computationally feasible to include hundreds or thousands of species for i process nucleosynthesis in such simulations.

As a first step towards overcoming those limitations I am working on a method to perform the comprehensive nucleosynthesis by post-processing the output of 3D hydrodynamic simulations generated by the PPMstar code (Woodward, Herwig, and Lin 2015). At each time step of this post-processing approach isotopes would be advected on a reduced grid and then comprehensive nucleosynthesis performed. I have developed a post-processing framework which processes the low-resolution output of the 3D hydrodynamical simulations with a time step size and network size of choice. The nucleosynthesis network of each cell is constructed with code of the NuGrid collaboration. The advection routines are not fully implemented and mixing does not take place yet. As an application I have post-processed an event of strong H ingestion in the 3D hydrodynamic simulation of a low-Z AGB model of Woodward et al. (in prep.) and find the production of large amounts of ^{13}N of up to 14% (Fig. 4.4). This hints towards strong i-process production under the assumption that ^{13}N is effectively transported into the deepest layers.

The extreme cost of the post-processing nucleosynthesis is estimated to be up to 10% of the 3D hydrodynamic simulation which motivates an inline processing in the PPMstar code to take advantage of the available scaling ability and routines. For this purpose I have provided Prof. Paul Woodward with the nucleosynthesis modules to be included in the PPMstar code.

The convective-reactive nucleosynthesis as during H ingestion is also found in O-C shell mergers presented in the next chapter. Post-processing or co-processing as introduced in this chapter might be needed to explore nucleosynthesis in such events.

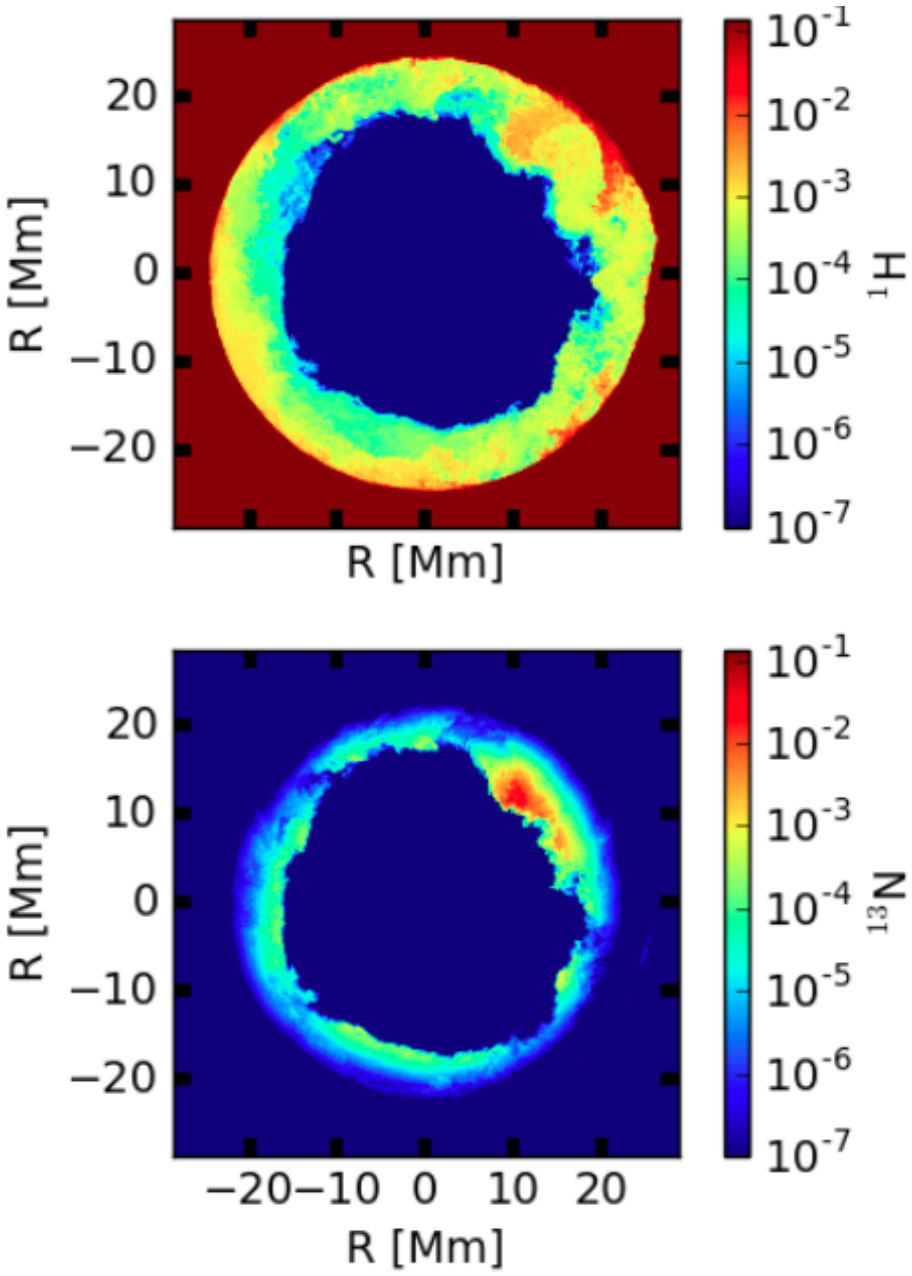

Figure 4.4: Mass fractions of the ingested ^{1}H and the ^{13}N produced after about 3 min in a sphere slice based on the post -processed 3D hydrodynamic simulation.

Chapter 5

O-C shell merger in massive stars

In this section I present my investigation into the nucleosynthesis of interacting convective O and C shells of massive star models. Comprehensive nucleosynthesis in a 1D model based on 3D hydrodynamic simulations is analyzed and compared with O-C shell mergers found in 1D stellar evolution models. The relevance of Cl, K and Sc produced in O-C shell mergers for the Galactic production is estimated.

Draft of C. Ritter, B. Côté, F. Herwig, J. F. Navarro, C. Fryer, L. Siemens, to be submitted to MNRAS

Abstract We investigate the nucleosynthesis in mergers of O- and C-shell convection in massive stars or when large amounts of C-shell material is ingested into the O-shell convection zone. An initial attempt to perform a 3D hydrodynamic simulation of O-shell convection with a moderate C-ingestion shows no dramatic deviation from spherical symmetry and provides an estimate for the convective mixing efficiency in this situation. With the application of the derived mixing in comprehensive 1D multi-zone nucleosynthesis simulations we find that combined convective-reactive O- and C-shell burning can be a production site for the odd-Z elements P, Cl, K and Sc. But very large overproduction factors of ≈ 5 can be achieved only when the entrainment rate is enhanced to $\approx 10^{-3}\,M_\odot/s$ which can be associated with O-C shell mergers. We identify such production in a number of our 1D stellar evolution models of massive stars that are part of the NuGrid yields with overproduction factors beyond 1 dex. In addition we report that p-process species are produced in this environment with strongly mass-and metallicity dependent overproduction factors of more than 1 dex for ^{130,132}Ba and heavier isotopes. We find that the merger of the O shell with the Si

shell produces Fe peak elements which are effectively mixed out of the shells which fall back on the remnant during the core-collapse explosion, similar to the mixing-fallback mechanism. Under the assumption that merger or entrainment convective-reactive events involving O- and C-burning shells occur not always but in more than 50% of all massive stars chemical evolution models are able to reproduce the observed trends of the odd-Z elements in the Milky Way.

5.1 Introduction

Massive stars are the main producer of intermediate elements below the Fe peak with a contribution to heavy elements(e.g. Woosley, Heger, and Weaver 2002). However, the odd-Z elements K and Sc in galactic chemical evolution models of the Milky Way based on yields of NuGrid (Pignatari et al. 2016b; Ritter et al. 2016, in prep.), Kobayashi et al. (2006, K06) or Nomoto, Kobayashi, and Tominaga (2013, N13) are up to 1 dex lower compared to halo and disk stars (Fig. 5.1).

Several production mechanisms have been considered for Sc, such as the ejecta of proton-rich neutrino winds (Fröhlich et al. 2006), jet-induced core-collapse supernova explosions (e.g. Tominaga 2009) and hypernovae (e.g. Sneden et al. 2016). However the quantitative impact of these mechanisms on chemical evolution models has not yet been demonstrated.

Another group of species with still essentially unknown nuclear production are the p-process isotopes. For decades massive stars have been considered the main source of rare proton-rich stable isotopes beyond iron[1]. This scenario was never consistently tested by GCE simulations but the underproduction of p-process yields within this scenario has always been recognized compared to the solar abundances (see Pignatari et al. 2016c, and references therein).

Uncertainty of the nuclear C-burning reactions (Pignatari et al. 2013b) and neutrino-induced reactions (e.g. Fröhlich et al. 2006) supported by multi-D simulations (e.g. Arcones and Montes 2011) enhance the p-nuclei production in massive star models. Rapidly rotating, strongly magnetic collapsing stars (Fujimoto et al. 2007) are further candidates for p-nuclei synthesis. Low mass retention efficiencies of rapidly accreting C/O white dwarfs question the single degenerate SNIa channel as proposed source of

[1] ^{74}Se, ^{78}Kr, ^{84}Sr, ^{92,94}Mo, ^{96,98}Ru, ^{102}Pd, ^{106,108}Cd, ^{112,114,115}Sn, ^{113}In, ^{120}Te, ^{124,126}Xe, ^{130,132}Ba, ^{136,138}Ce, ^{138}La, ^{144}Sm, ^{152}Gd, ^{156,158}Dy, ^{162,164}Er, ^{168}Yb, ^{174}Hf, ^{180}Ta, ^{180}W, ^{184}Os, ^{190}Pt, and ^{196}Hg

p nuclei (Denissenkov et al. 2017).

While previous attempts to explain the sufficient production of odd-Z elements focussed on explosive nucleosynthesis environments we are here proposing that odd-Z elements are forming in convective-reactive pre-supernova stellar evolution. Convection is described by the mixing-length theory (Cox and Giuli 1968) in 1D stellar models. This theory is highly effective and works very well in many phases of stellar evolution. However, it fails to describe accurately the evolution of convection zone in the late phases of stellar evolution of stars.

In recent years multi-dimensional stellar hydrodynamic simulations have been constructed that start to elucidate the complex behaviours that can be encountered in shell convection with fuel ingestion. For example, (Herwig et al. 2014) showed that the convective-reactive combustion of H-rich material ingested into He-shell flash convection can lead to violent global, non-radial oscillations that severely compromise the assumption of spherical symmetry. This particular type of convective-reactive event has been shown to lead to the unique intermediate neutron-capture process, or i process.

Just as the i-process nucleosynthesis pathway is only possible in convective-reactive H-He burning, we are now generalizing on this example, and consider what other unusual nucleosynthesis could be possible in other types of convective-reactive nucleosynthesis. One such interaction can occur between convective C- and O-shell burning when C-shell material is ingested into the O shell. Based on 2D hydrodynamic simulations Meakin and Arnett (2006a) suggested that such ingestion could rapidly transition into a situation with accreting entrainment rates. Mergers of O- and C-shell convection zones have been mentioned in passing in the literature (Rauscher et al. 2002; Tur, Heger, and Austin 2007). But neither the nucleosynthesis nor the hydrodynamic processes of such shell mergers have been investigated in detail.

In this work the convective-reactive C ingestion into O-shell convection in full 3D is explored, followed by comprehensive multi-zone nucleosynthesis simulations and analysis of shell mergers in stellar evolution models. The result are preliminary estimates of odd-Z element production the impact of which we analyze in galactic chemical evolution models of the Milky Way.

We introduce our simulation tools in Section 5.2. The results are presented in Section 5.3 followed by a discussion of current model limitations in Section 5.4. In Section 5.5 we present a summary and the conclusion.

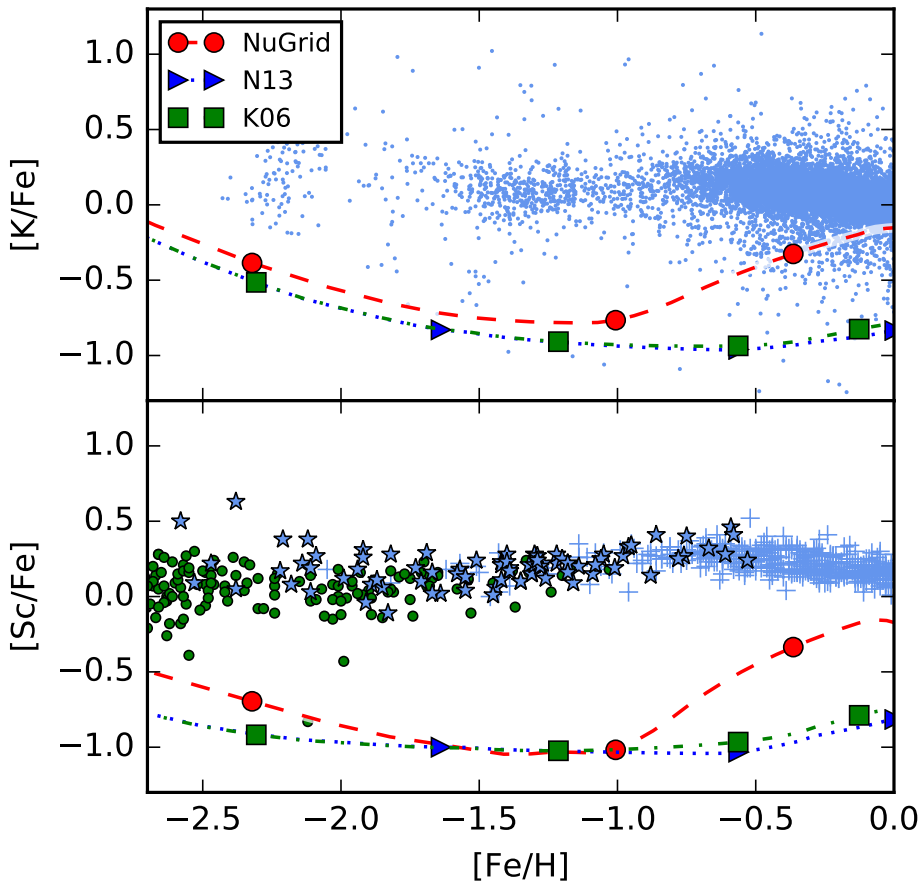

Figure 5.1: K and Sc predictions of our GCE model based on NuGrid yields (R16) in comparison with disk and halo stars of the Milky Way. For comparison we show GCE predictions based on yields from K06 and N13. Data of K are from the APOGEE survey (Wilson et al. 2010; SDSS Collaboration et al. 2016), and Sc data from Ishigaki, Chiba, and Aoki (2012) and Ishigaki, Aoki, and Chiba (2013, crosses), Roederer et al. (2014, dots) and Battistini and Bensby (2015, stars).

5.2 Methods

We perform 3D simulations of a convective O shell with C ingestion in a stellar model with an intially mass of $25\,M_\odot$ and metallicity $Z = 0.02$ with the explicit hydrodynamics code PPMstar (Woodward, Herwig, and Lin 2015). The overall approach is the same as in Jones et al. (2016a), including 4π geometry and a 768^3 grid. However, instead of driving the convection with a constant volume heating the O-shell fluid burns via the ^{16}O-^{16}O rate according to Eq. 18.74 in Kippenhahn and Weigert (1990).

To model the burning of C fluid in our hydrodynamic simulation we have computed the nucleosynthesis of C-shell material on a trajectory through the O shell. We find the ^{12}C-^{12}C and the ^{16}O(α,g)^{20}Ne reactions to produce the most energy over most of the O shell. It is assumed that each α particle liberated by the former reaction triggers the latter reaction as plenty of O is available and C fluid is burned according to the ^{12}C-^{12}C rate (Eq. 18.72 in Kippenhahn and Weigert 1990). The energy release of C-fluid burning is the sum of Q values of both reactions.

The detailed nucleosynthesis is computed with the 1D multi-zone post-processing code mppnp that includes all relevant isotopes (Pignatari et al. 2016b). Similar to Herwig et al. (2011) we ingest unprocessed fuel from the layer above the convection zone, in this case C-shell material into the O-shell convective zone, at a prescribed rate.

We model the chemical evolution of the Milky Way with a one-zone open-box model with galactic inflows and outflows in OMEGA (Côté et al. 2016c; Côté et al. 2017) that is part of the NuGrid chemical evolution framework NuPyCEE[2]. Yields of AGB and massive star models are taken from NuGrid. Alternatively, massive star yields are from K06 and N13. Yields of PopIII stars are from Heger and Woosley (2010) and SNIa yields are from (Thielemann, Nomoto, and Yokoi 1986). The initial mass function of Kroupa (2001) is adopted over the initial mass range from $0.1\,M_\odot$ to $100\,M_\odot$, and we assume the ejection of stellar yields between the initial masses of $1\,M_\odot$ and $30\,M_\odot$.

[2]http://nugrid.github.io/NuPyCEE

5.3 Results

5.3.1 Convection and feedback in 3D

3D hydrodynamic simulations of the O shell of Jones et al. (2016a) indicate a entrainment rate of $1.3 \times 10^{-6}\,\mathrm{M}_\odot/\mathrm{s}$. If the O shell of that underlying stellar model grows in mass with this entrainment rate at the upper boundary it can reach the C shell in 1.91 days. This is before the end of O shell convection in 9.7 days which would allow a convective O-C shell merger. The shell merger would likely boost the entrainment rate by many orders of magnitude.

In our simulation C-shell material is entrained into the O shell over 110 convective turn-over times of $\Delta r_{\mathrm{shell}}/v_{\mathrm{radial}} \approx 2.2\mathrm{min}$. The entrained fluid reaches to the bottom of the convective O shell (Fig. 5.2) where its spherically averaged abundance develops towards a stationary state.

The energy release by C burning does not strongly affect the flow properties in contrast to global oscillation of shell-H ingestion (GOSH) events found with H entrainment into a convective He shell in low-mass stellar models (Herwig et al. 2014).

This motivates to calculate a diffusion coefficient in a spherically symmetric approximation of the mixing as in Jones et al. (2016a). We find an average entrainment rate of $3.13 \times 10^{-7}\,\mathrm{M}_\odot/\mathrm{s}$ over 60 min during which the fluid interface shows little variation. This entrainment rate is lower than of Jones et al. (2016a) due to our lower O shell luminosity.

5.3.2 Nucleosynthesis in 1D

The large processing power required does not allow to include large networks of C burning, O burning and p-process nucleosynthesis in 3D hydrodynamic simulations. We construct a 1D setup of the 3D hydrodynamic simulation based on a time-averaged diffusion coefficient and the temperature and density profile of the stellar evolution simulation (Fig. 5.3). We ingest C-shell material at the radial position at which the entrainment rate from the hydrodynamic simulation was derived. A possible O-C shell interaction leads to higher entrainment rates (Meakin and Arnett 2006a) and we expect an increase by some undetermined orders of magnitude higher than what is derived from our hydrodynamic simulation.

We investigate entrainment rates of C-shell material from $1.2 \times 10^{-7}\,\mathrm{M}_\odot/\mathrm{s}$ to

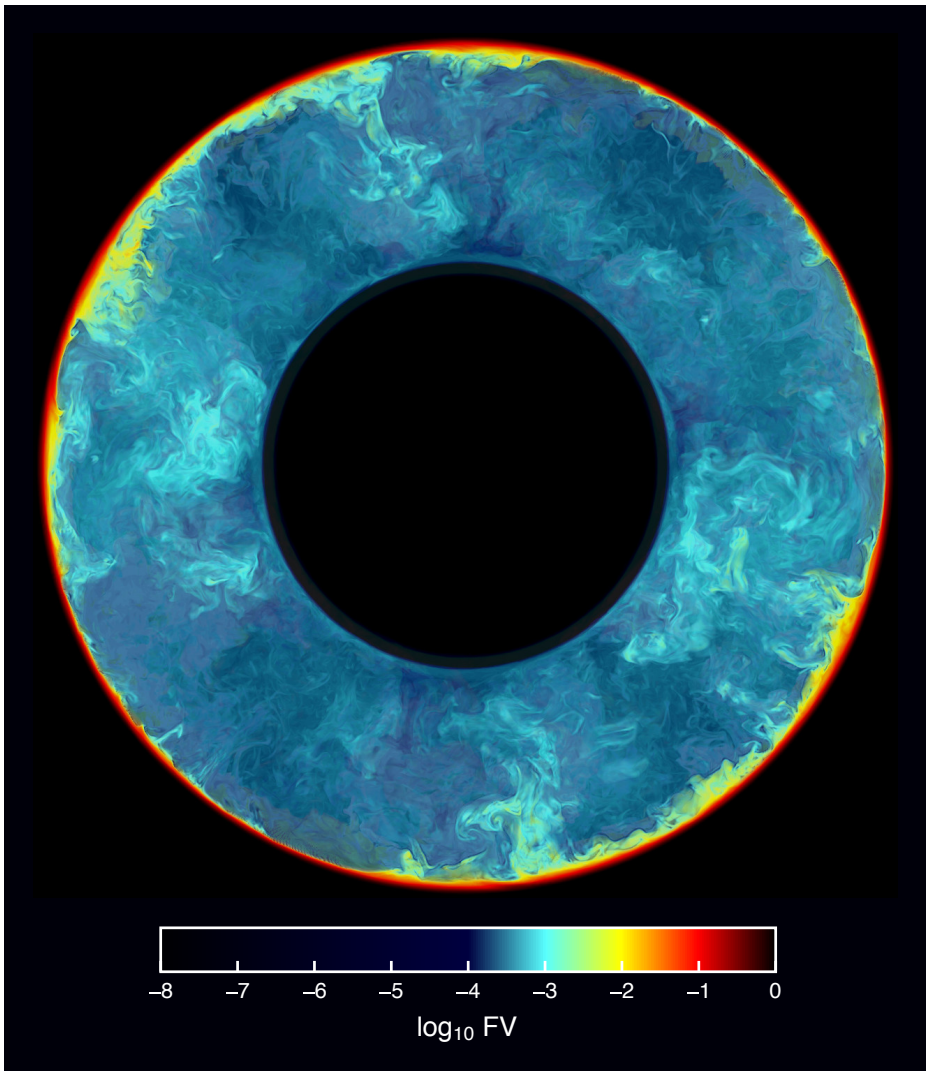

Figure 5.2: Volume fraction of C-shell fluid after 148 min of entrainment in a sphere slice of the convective O shell.

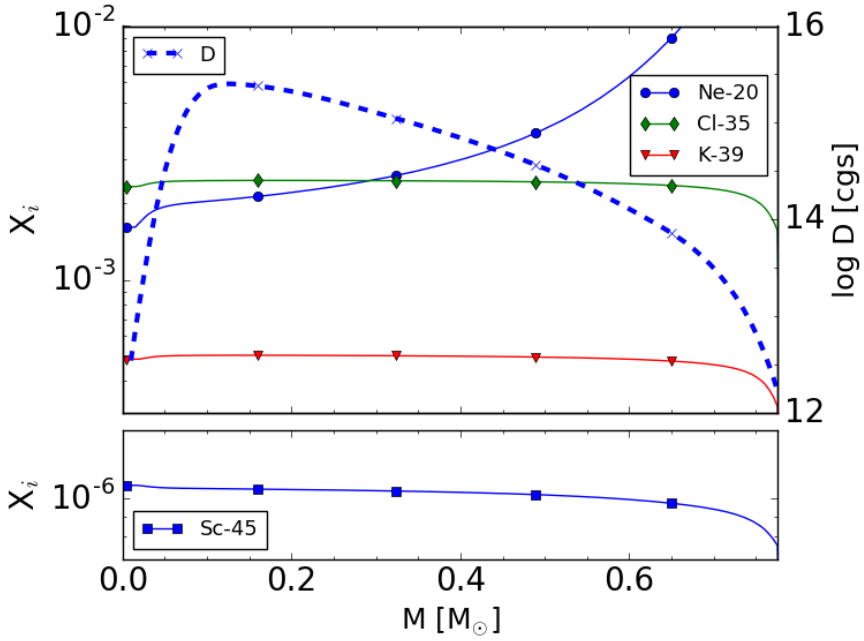

Figure 5.3: Abundance profile of the MPPNP simulation of the O-shell after 16.5 min of ingested C-shell material at a rate of $10^3 \dot{M}_e$. The diffusion coefficient D is extracted from our 3D hydrodynamic simulation.

$1.2 \times 10^{-2}\,M_\odot$/s. At $1.2 \times 10^{-2}\,M_\odot$/s the whole C shell would be entrained in 100 s which is the overturning timescale of the hydrodynamic simulation of the O shell in Meakin and Arnett (2007b). This entrainment time is small compared to the sound crossing time of our O shell of the order of seconds. In a catastrophic scenario of a transsonic mass exchange, the mass exchange rate could event reach $1\,M_\odot$/s.

Intermediate elements

At an entrainment rate of $1.2 \times 10^{-4}\,M_\odot$/s we find considerable production of ^{35}Cl, ^{39}K and ^{45}Sc after 16.5 min (Fig. 5.3).

^{31}P, ^{35}Cl, ^{39}K and ^{45}Sc are produced in the lower part of the O shell through entrainment of large amounts of ^{20}Ne under convective-reactive conditions.

We investigate the nucleosynthesis through repeated multi-zone simulations by turning on and off individual rates aided by flux analysis of 1-zone simulations. The protons released by ^{20}Ne burning produce ^{31}P. The latter is transported into deeper layers where it is destroyed with ^{31}P(γ,p). The resulting protons are captured by plenty available ^{34}S and produce ^{35}Cl via ^{34}S(p,γ)^{35}Cl. ^{39}K is synthesized via ^{38}Ar(p,γ)^{39}K and to a less extent ^{39}Ar(p,n)^{39}K at about the same depth as ^{35}Cl. ^{35}Cl is disintegrated in deeper layers and produces ^{45}Sc via ^{44}Ca(p,γ)^{45}Sc. Neutron-capture on other Ca isotopes lead to the production of ^{44}Ca in the highly neutron-rich environment of the O shell.

To analyze the impact of the nucleosynthesis on the total stellar production we calculate the elemental overproduction factors as $OP = (Y_i + Y_{tot})/(Y_{ni} + Y_{tot})$. Y_i is the amount of material produced after 16.5 min and Y_{ni} is the amount produced over the same time without ingestion of C-shell material. We compare the amounts relative to the total yields Y_{tot} produced in the stellar model with initial mass $25\,M_\odot$ at $Z = 0.02$ of NuGrid (Fig. 5.5). The overproduction factors of P, Cl, K and Sc increase with the entrainment rate in most cases while the relative production can differ.

The stellar model with initial mass of $15\,M_\odot$ at $Z = 0.02$ experiences a O-C shell merger about 4 min after the end of convective Si core burning (Ritter et al. 2016, in prep.). During the initial phase large amounts of material are entrained while most parts of both convective shells are still separated (Fig. 5.4). Shortly afterwards both convective shells merge. We find the production of ^{35}Cl, ^{39}K and ^{45}Sc under convective-reactive conditions.

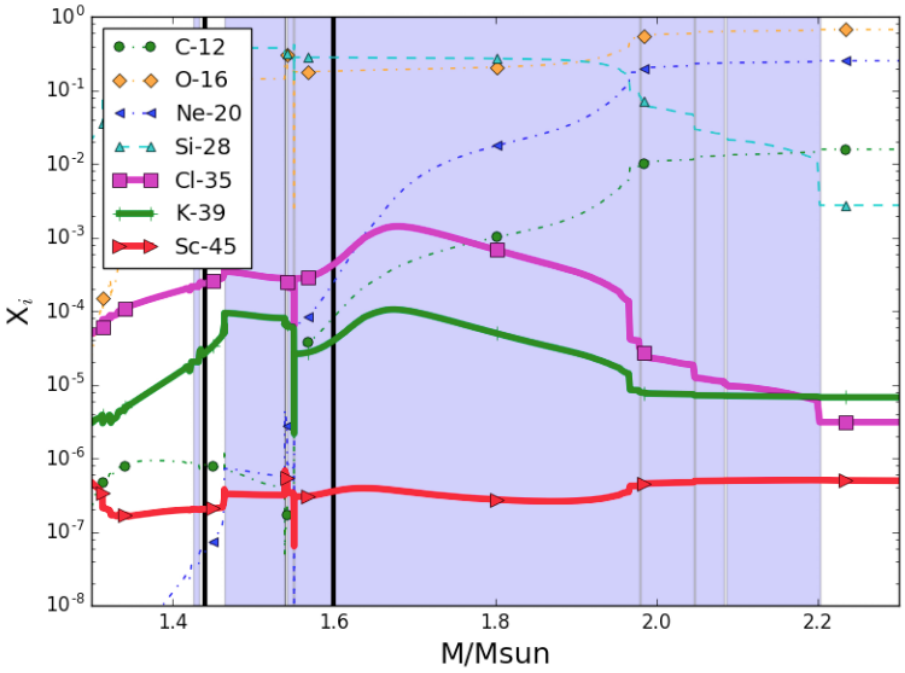

Figure 5.4: Abundance profile during entrainment of C-shell material into the O shell about 4 min after the end of convective Fe core burning of the stellar model of 15 $M_\odot$ at $Z = 0.02$. The blue shades indicate convective regions. The two black vertical lines show the position of the remnant mass of the CCSN explosion model.

The overproduction factors due to the O-C shell merger in the stellar model are qualitatively similar to what we found in our 1D ingestion setup with the variation of the maximum overproduction factor between Cl and K (Fig. 5.5). For stellar models the overproduction factors are calculated as $OP = Y_f/Y_{ini}$ where Y_{ini} and Y_f are the total amounts at onset and after inter-shell mixing, respectively. We identify further O-C shell merger in the massive star models of NuGrid with initial masses of $12\,M_\odot$, $15\,M_\odot$ and $20\,M_\odot$ at $Z = 0.01$. The overproduction factors of P, Cl, K and Sc vary with the initial mass and metallicity (Fig. 5.5).

Due to its deep location the O shell is significantly modified by the core-collapse SN explosion and affected by fallback. The CCSN prescription for the stellar model of $15\,M_\odot$ at $Z = 0.02$ includes two neutron-star remnant coordinates based on the delayed and rapid explosion prescription of Fryer et al. (2012). Both remnant coordinates are below the peak production of ^{31}P, ^{35}Cl, ^{39}K and ^{45}Sc (Fig. 5.4). The overproduction factors based solely on the explosive nucleosynthesis indicate that P, Cl, K and Sc are little affected by the explosion (Fig. 5.5).

Fe-peak elements

The convective Si-burning shell in the stellar model of $20\,M_\odot$ at $Z = 0.01$ grows into O-shell layers. The convective Si-O shell transports Fe peak elements into regions which will be ejected during CCSN based on the rapid explosion prescription (Fryer et al. 2012). The convective Si-O shell expands further in mass and its bottom layers cool significantly which shuts off Si burning. The shell merges with the convective C-burning shell. With the delayed explosion prescription (Fryer et al. 2012) O-shell and Si-shell material would fall back onto the remnant but the extended convective Si-O-C shell allows the ejection. The Si-O-C shell merger results in the efficient production of Fe peak elements (Fig. 5.5). These mergers allow the transport of Fe peak elements outside of the core which is similar to the core-collapse SN mixing-fallback mechanism which has been suggested to explain the abundance of extreme and ultra-metal poor stars Umeda and Nomoto (e.g. 2005) and Iwamoto et al. (2005).

p-process isotopes

The p process occurs in Ne and O shell burning in the CCSN explosion of massive star models through photo-disintegration reactions on heavy elements (Woosley and Howard 1978; Pignatari et al. 2016c).

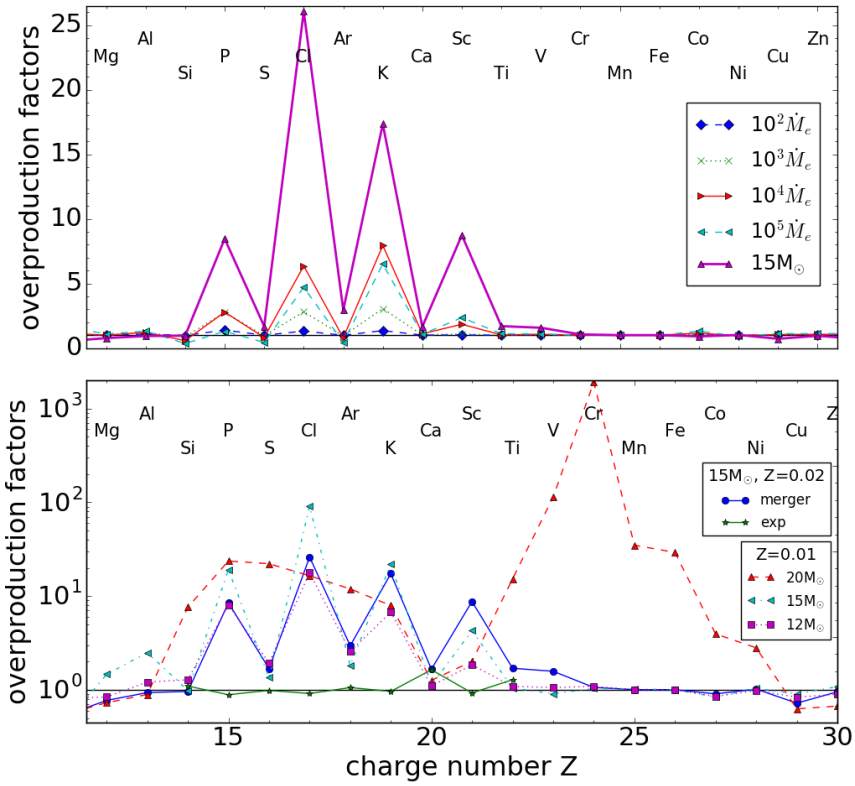

Figure 5.5: Top: Overproduction factors due to C-shell ingestion for different entrainment rates of C-shell material in comparison with the production in the O-C shell merger of the stellar model with initial mass of $15\,M_\odot$ at $Z = 0.02$. Bottom: Overproduction factors of the stellar model with initial mass of $15\,M_\odot$ at $Z = 0.02$ during merger (merger) and due to explosive nucleosynthesis (exp) for species between Si and Ti. In comparison the overproduction factors of O-C shell mergers of NuGrid models with initial masses of $20\,M_\odot$, $15\,M_\odot$ and $12\,M_\odot$ at $Z = 0.01$.

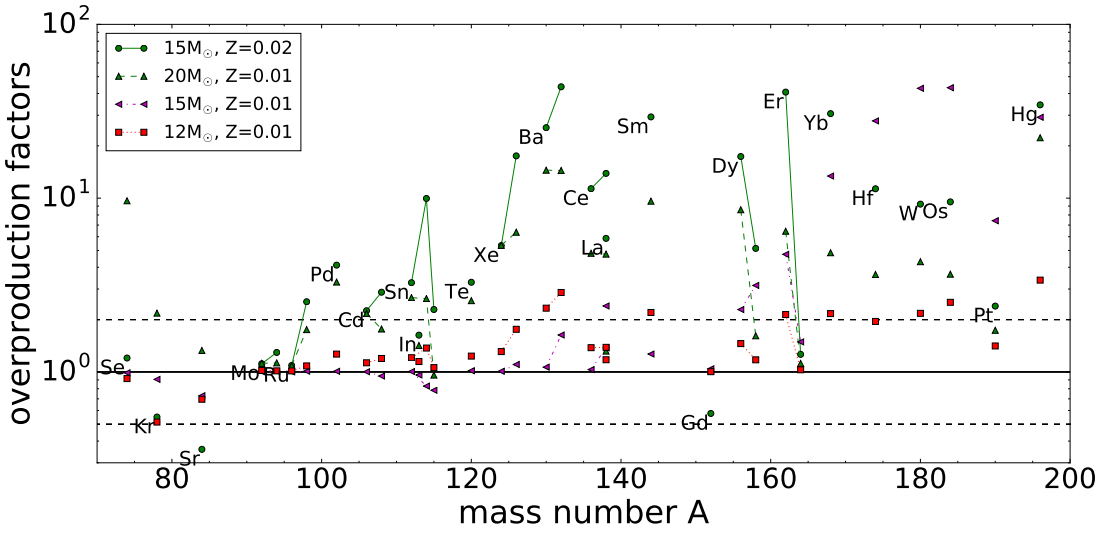

Figure 5.6: Overproduction factors of p-process isotopes in O-C shell mergers of stellar models of NuGrid. ^{180}Ta values are omitted for clarity and are 2.95, 0.7, 5.61 and 0.64 in legend order, starting from the top. The dashed horizontal lines show an overproduction factor of 0.5 and 2.

During O-C shell merger, "fresh" heavy elements are constantly transported down to the O-burning shell, providing new seeds for photo-disintegration. We compare the overproduction factors of the classical 35 isotopes of the O-C shell merger of the stellar models of NuGrid (Fig. 5.6).

In these models we find strong variations in the overproduction factors with stellar mass and metallicity. Light p nuclei are destroyed while heavier species are effectively produced. Most of those species have the largest overproduction factors in the stellar model with initial mass of $15\,M_\odot$ at $Z = 0.02$. We confirm the results of Rauscher et al. (2002) that p nuclei can be made in O-C shell merger. At this level of production, the impact of O-C shell merger may change the GCE scenario of at least some of the p-process nuclei.

5.3.3 Relevance for galactic chemical evolution

With Milky Way models the impact of the element production in O-C shell mergers on the galactic scale is estimated. Stellar models of NuGrid with initial masses of $15\,M_\odot$ at $Z = 0.02$ and $12\,M_\odot$, $15\,M_\odot$ and $20\,M_\odot$ at $Z = 0.01$ show O-C shell merger. This results in the rise in in [Cl,K,Sc/Fe] above [Fe/H] ¿ -1 (Fig. 5.7).

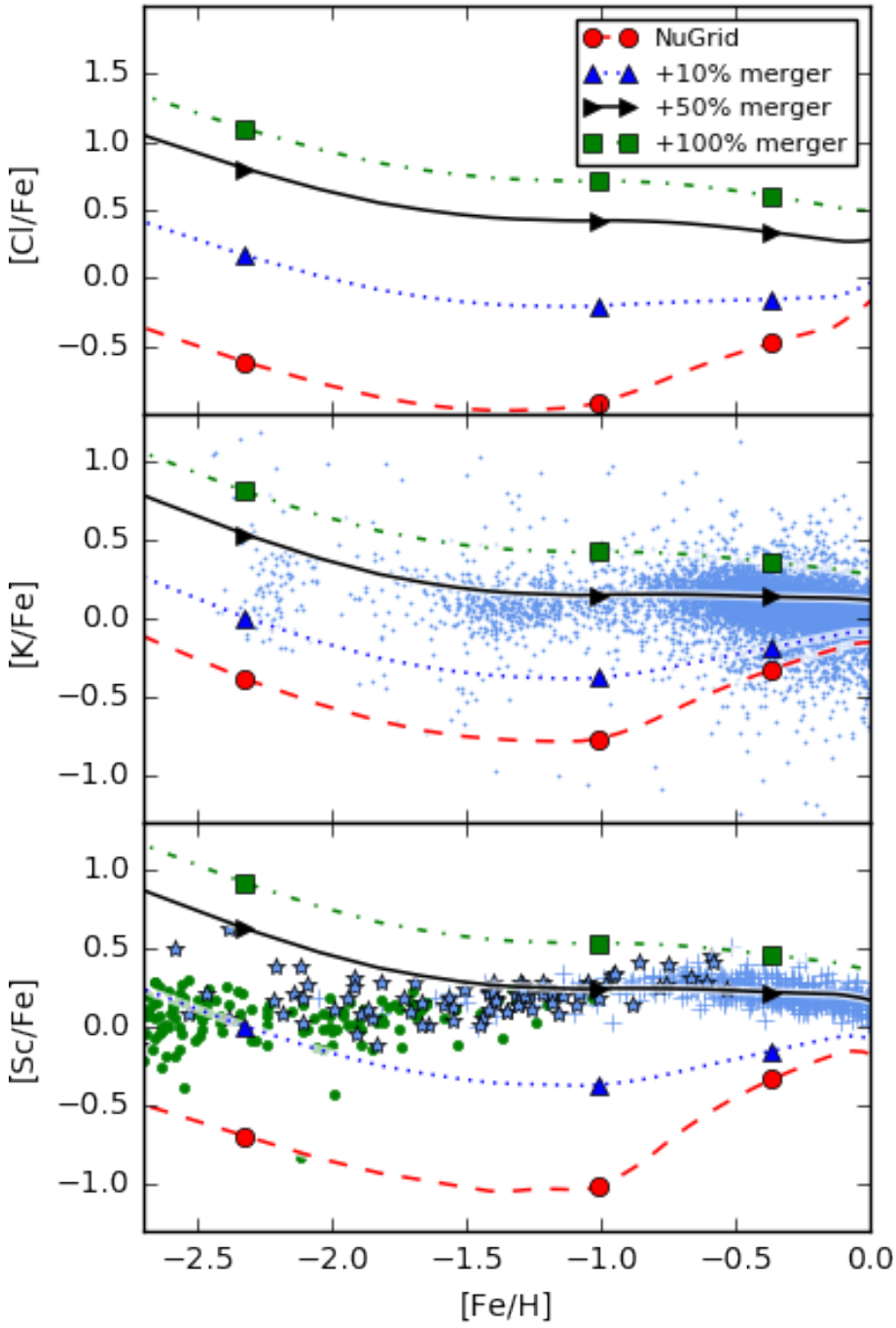

Figure 5.7: Comparison of the predictions of Cl, K and Sc of our Milky Way model with observational data. Predictions with 10%, 50% and 100% addition of material produced in the O-C shell merger of the stellar model of $15\,M_\odot$ at $Z = 0.02$ to all massive stars without O-C shell merger. References of observational data in Fig. 5.1.

Massive star models at $Z < 0.01$ of NuGrid show convective O and C shells separated only by a thin convective boundary which might be overcome if convective boundary mixing is taken into account as motivated by 3D hydrodynamic simulations (Jones et al. 2016a). The metallicity effect on the O-C shell merger occurrence in our 1D simulations is due to modelling limitations.

Under the assumption of shell mergers at all Z we apply amounts of material produced in the O-C shell merger of our stellar model of $15\,M_\odot$ at $Z = 0.02$ to all massive star models which do not experience O-C shell mergers. We add the material to 10%, 50% and 100% of these stars and find that if between 10% and 50% of the O-C shell ejecta is affected by entrainment events the missing amounts from K and Sc observations can be reproduced. We cannot confirm the same results for Cl, since there are no observations available at different metallicities to compare with. However, within this scenario Sc and K can be used to trace the production of Cl in the Milky Way.

An increased p-process production via O-C shell merger might also boost the Galactic p-process contribution of massive stars. Rayet et al. (1995) find a global underproduction of p nuclides produced in massive stars compared to what is necessary to explain the solar-system distribution. We speculate that the shell merger production could allow to match the solar distribution when assuming a wide spectrum of entrainment rates, convective motions and stellar structures. To analyze the impact of p-process nucleosynthesis in shell mergers on the Galactic production the secondary nature of the p process has to be taken into account.

5.4 Discussion

5.4.1 Towards full shell merger

Only ingestion rates of C-shell fluid many orders of magnitude higher than $3.13 \times 10^{-7}\,M_\odot/s$ of our hydrodynamic simulation produce amounts of Cl, K and Sc relevant for galactic chemical evolution. Such ingestion rates might occur in the second O shell due to its higher luminosity (Jones et al. 2016a). In this phase our stellar models show O-C shell merger. We artificially increase the O-burning luminosity in our hydrodynamic simulation by 2 dex to $7 \times 10^{12}\,L_\odot$ similar to the increase between the first and second O shell of the stellar model with initial mass of $15\,M_\odot$ at $Z = 0.02$. The luminosity increase is gained through a 67.5 times larger Q value of the O-burning

reaction.

We run over 11 convective turn-over times of 50 s during which substantial more material is entrained than at lower luminosity (Fig. 5.8). We derive an average entrainment rate of $1.07 \times 10^{-4}\,\mathrm{M}_{\odot}/\mathrm{s}$ in agreement with the entrainment-luminosity law of Jones et al. (2016a). Such entrainment leads to three times more Cl and K production than in the reference stellar model with initial mass of $25\,\mathrm{M}_{\odot}$ at $Z = 0.02$ (Fig. 5.5).

To explain the Galactic underproduction of K and Sc much higher overproduction factors are needed as they could appear in full shell mergers. But the extensive mass exchange between shells could be hindered by the different entropy gradients of the shells or the appearance of strong non-spherical instability similar to the GOSH. Such an instability appears when the energy release due to burning of C fluid and O-shell fluid is artificially increased by 1 dex and a factor of 13.5 respectively. Further investigations are required to analyze if this Global Oscillation of Shell C-ingestion (GOSC) boosts the entrainment rate or choke off any further nucleosynthesis.

5.4.2 Model dependence of shell merger nucleosynthesis

With the assumption of applying material produced in a O-C shell merger in our GCE model we neglect that the element synthesis in O-C shell merger has a complex dependence on initial mass and metallicity. While more massive stars are affected by larger fallback (Fryer et al. 2012) they also inhibit larger O and C shells which boost the p-process production. A larger convective C shell allows to entrain more material which boosts the production of elements such as P, Cl, and K (Fig. 5.5). The produced material can be transported further outwards and will be less affected by fallback. Higher temperatures in the O shells of lower mass stars might lead to a stronger production of lighter p nuclei which are transported into the upper part of the C shell. The time between onset of O-C shell merger and core-collapse is also crucial to enable effective element production. In all stellar models of NuGrid the O-C shell merger production reaches a production equilibrium before the stellar collapse.

With convective boundary mixing in all massive star models of NuGrid we expect O-C shell mergers in a wide range of models from $Z = 0.02$ down to $Z = 0.0001$. We find that stellar models with initial mass of $25\,\mathrm{M}_{\odot}$ do not have fully convective C shells and below $Z < 6 \times 10^{-3}$ convective C shells are absent in layers of $1\,\mathrm{M}_{\odot}$ above the convective O shell. This might indicate that O-C shell mergers are less likely at

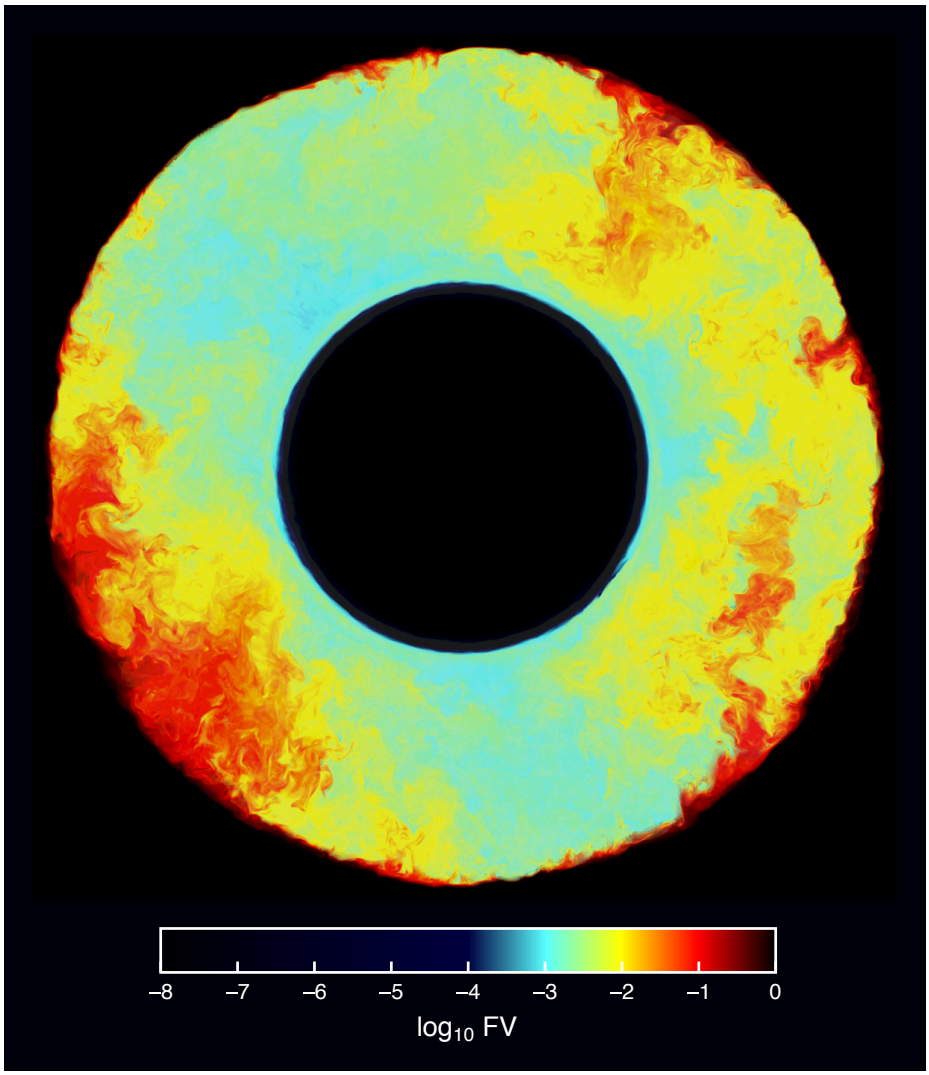

Figure 5.8: Volume fraction of C-shell fluid after 10.5 min of entrainment in a sphere slice of the convective O shell. The entrainment rate is 1000 times higher than the simulation shown in Fig. 5.2.

higher initial mass and lower metallicity.

The production of p nuclei in massive star models is affected by large uncertainties such as the C-burning rate (Pignatari et al. 2013b) and fallback during the CCSN explosion (Pignatari et al. 2016b; Ritter et al. 2016, in prep.). Further studies with Galactic chemical evolution models have to asses the impact of O-C shell mergers on the galactic production.

5.5 Summary and Conclusions

To investigate the interaction of O and C shell in massive stars we perform 3D hydrodynamic simulations of the entrainment and burning of C-shell fluid in the first O shell of a stellar model with initial mass of $25\,M_\odot$ at $Z = 0.02$. We do not find strong aspherical feedback, similar to the GOSH, and instead the development of a spherically averaged equilibrium of the entrained material. The comprehensive nucleosynthesis in such as shell interaction is calculated with a 1D setup based on a diffusion coefficient derived from the hydrodynamic simulation.

We find the strong production of odd-Z elements P, Cl, K and Sc under convective-reaction conditions when we increase the entrainment rates by many orders more than in the hydrodynamic simulation. The production of these elements is by many factors more than in a reference stellar model. It is qualitative similar, but of less amount, than in the merger of the second O shell with the C shell in massive star models of NuGrid. In the latter models full O-C shell mergers occur in the second O shells and the odd-Z production depend crucially on the initial mass and metallicity. With the increase of the luminosity similar to the second O shell in our hydrodynamic simulation we find 3 dex more entrainment which produce up to a factor three more odd-Z elements according to our entrainment tests.

We have performed GCE simulations with the assumption that different numbers of stars eject material produced in the O-C shell merger of the stellar model with initial mass of $15\,M_\odot$ at $Z = 0.02$. If shell mergers occur in more than 50% of all stars they can explain the underproduction of K and Sc in Milky Way models compared to disk and halo stars. Inhomogeneous mixing in systems such as ultra-faint dwarfs could allow to trace the occurrence of shell mergers through their observed abundance signatures.

With the entrainment of C-shell material heavy-element seeds are swept into the O shell and serve as a boost for the p-process production. In 1D stellar models we

find a variety of production efficiencies which vary with initial mass and metallicity and can be more than 1 dex for many isotopes beyond Ba. Such strong production might influence the Galactic production and further investigations require galactic chemical evolution models.

In recent years efforts have started to model the interaction in 3D hydrodynamics (Meakin and Arnett 2006a) but predictions of intermediate and heavy elements require large networks to model the reactive-convective nucleosynthesis of advanced burning stages. Currently 3D to 1D approximations remain the only way for qualitative predictions and new approaches in multi-D are required to give a definitive answer.

Chapter 6

Summary and Conclusion

6.1 Advances in theory of element production

The question about the origin of elements and their production emerged with the theoretical predictions of element production in stars in the first half of the last century (e.g. Bethe 1939). These theories were complemented by the observations of varying composition of stars in the second half of the century (e.g. Chamberlain and Aller 1951). Since then our understanding has been improved through individual observations, large surveys and theoretical modeling but many questions about the nucleosynthesis at low metallicity remain. In the following I present in short my contributions to the theory of element production.

One of the largest uncertainties in chemical evolution models is the stellar yield input. This uncertainty is related to the nuclear physics, model assumptions and the provided elements which differ between yield grids. I have partly solved this problem by producing a large yield grid of AGB stars, massive stars and CCSN models with consistent nuclear reaction rates and physics assumptions which covers all stable elements up to Bi. In a novel approach I made all stellar evolution data and post-processing nucleosynthesis data available online. The yield grid has been applied in chemical evolution studies.

To connect stellar yields with observations over a wide metallicity range chemical evolution models are necessary. To follow the chemical enrichment in dark matter plus gas simulations stellar yields need to be folded into simple stellar populations. I have created the SYGMA module to model the ejecta of SSPs. I have applied SYGMA to estimate the impact of convective boundary mixing in AGB stars on the Galactic

production of O and found it to be negligible. To follow the chemical evolution of galaxy I have created with Dr. Cote the NuPyCEE galaxy framework which includes a 1-zone galaxy model and a stellar abundance database. The framework has successfully been applied in different works and I have made efforts to provide it to the scientific community, for research and teaching.

There is mounting evidence in recent years for an intermediate nucleosynthesis process, the i process, between the s process and r process. I contributed to the investigation of H ingestion and i process in S-AGB models of Jones et al. (2016b). In Dardelet et al. (2015) we have shown that simple 1-zone i-process models can explain the abundance signature of some CEMP-r/s stars while previous efforts to describe the abundance distribution with a combination of s-process and r-process production have failed.

I have investigated the comprehensive nucleosynthesis during the interaction of the convective O shell and C shell informed by 3D hydrodynamic simulations. I found the effective production of odd-Z elements P, Cl, K and Sc under the assumption of entrainment of large amounts of C-shell material as expected in a O-C shell merger. Such shell merger can explain the underproduction of K and Sc in Milky Way models compared to the observation of disk and halo stars.

6.2 Prospects

Recent studies about convective boundary mixing in AGB stars (Battino et al. 2016) and ongoing studies of rotation in AGB models motivate the production of a new yield grid with updated physics input. Such an effort was initiated by the NuGrid collaboration and will allow to improve the predictions of element production of Chapter 2.

The ejecta of SSPs generated by SYGMA and based on my yields can be adopted in studies with hydrodynamic simulations and semi-analytic models of galaxies. Currently only a small number of elements are tracked individually in those simulations (e.g. 11 elements in the EAGLE simulations Schaye et al. 2015) while future studies will be able to include elements up to Bi with the yield grid of Chapter 2.

With the Advanced Laser Interferometer Gravitational-Wave Observatory (LIGO) and its detection of gravitational waves from compact objects (Abbott et al. 2016) neutron star merger rates can be constrained which help to estimate the impact of neutron-star mergers on the Galactic r-process production (Côté et al. 2016a). The

capabilities of NuPyCEE can be used to test the impact of the various r-process sources in combination with the constraints from LIGO.

Our finding that 1-zone i-process models match the abundance of some CEMP-r/s stars has been recently confirmed in Hampel et al. (2016). Studies use this i-process model to explain peculiar abundance patterns (e.g. Roederer et al. 2016). Very recently a new site for i process, the rapidly accreting white dwarfs, was found (Denissenkov et al. 2016). In these studies nucleosynthesis predictions are based on 1-zone and 1D models. Realistic predictions of i-process nucleosynthesis require the modeling of large networks in 3D hydrodynamic simulations which is currently not feasible due to the computational cost. I have made first efforts to solve this problem through post-processing and co-processing approaches in collaboration with Prof. Woodward (MSU).

The reactive-convective nucleosynthesis of H ingestion can produce the odd-Z elements Li, N and F while the reactive-convective nucleosynthesis of C ingestion in the O shell can produce the odd-Z elements P, Cl, K, Sc. If odd-Z elements are dominantly produced under reactive-convective conditions then understanding their origin requires predictions of nucleosynthesis based on 3D hydrodynamic simulations of AGB stars and massive stars.

Bibliography

[1] B. P. Abbott et al. "GW150914: First results from the search for binary black hole coalescence with Advanced LIGO". In: *Physical Review D* 93.12, 122003 (June 2016), p. 122003. DOI: 10.1103/PhysRevD.93.122003. arXiv: 1602.03839 [gr-qc].

[2] D. C. Abbott. "The terminal velocities of stellar winds from early-type stars". In: *ApJ* 225 (Nov. 1978), pp. 893–901. DOI: 10.1086/156554.

[3] C. J. Akerman et al. "The evolution of the C/O ratio in metal-poor halo stars". In: *Astronomy and Astrophysics* 414 (Feb. 2004), pp. 931–942. DOI: 10.1051/0004-6361:20034188.

[4] D. M. Allen et al. "Elemental abundances and classification of carbon-enhanced metal-poor stars". In: *A&A* 548, A34 (Dec. 2012), A34. DOI: 10.1051/0004-6361/201015615. arXiv: 1210.5009 [astro-ph.SR].

[5] A. Arcones and F. Montes. "Production of Light-element Primary Process Nuclei in Neutrino-driven Winds". In: *ApJ* 731 (Apr. 2011), pp. 5–+. DOI: 10.1088/0004-637X/731/1/5. arXiv: 1007.1275 [astro-ph.GA].

[6] D. Arnett. *Supernovae and Nucleosynthesis: An Investigation of the History of Matter from the Big Bang to the Present*. 1996.

[7] W. D. Arnett and C. Meakin. "Toward Realistic Progenitors of Core-collapse Supernovae". In: *ApJ* 733, 78 (June 2011), p. 78. DOI: 10.1088/0004-637X/733/2/78. arXiv: 1101.5646 [astro-ph.SR].

[8] M. Arnould and S. Goriely. "The p-process of stellar nucleosynthesis: astrophysics and nuclear physics status". In: *Phys. Rep.* 384 (Sept. 2003), pp. 1–84. DOI: 10.1016/S0370-1573(03)00242-4.

[9] M. Arnould, S. Goriely, and K. Takahashi. "The r-process of stellar nucleosynthesis: Astrophysics and nuclear physics achievements and mysteries". In: *Phys. Rep.* 450 (Sept. 2007), pp. 97–213. DOI: 10.1016/j.physrep.2007.06.002. arXiv: 0705.4512.

[10] I. Baraffe, M. F. El Eid, and N. Prantzos. "The s-process in massive stars of variable composition". In: *Astronomy and Astrophysics* 258 (May 1992), pp. 357–367.

[11] U. Battino et al. "Application of a Theory and Simulation-based Convective Boundary Mixing Model for AGB Star Evolution and Nucleosynthesis". In: *ApJ* 827, 30 (Aug. 2016), p. 30. DOI: 10.3847/0004-637X/827/1/30. arXiv: 1605.06159 [astro-ph.SR].

[12] C. Battistini and T. Bensby. "VizieR Online Data Catalog: Sc, V, Mn, and Co in Milky Way stars (Battistini+, 2015)". In: *VizieR Online Data Catalog* 357 (Feb. 2015).

[13] G. Bazan and D. Arnett. "Convection, nucleosynthesis, and core collapse". In: *ApJL* 433 (Sept. 1994), pp. L41–L43. DOI: 10.1086/187543.

[14] S. A. Becker and I. Iben Jr. "The asymptotic giant branch evolution of intermediate-mass stars as a function of mass and composition. II - Through the first major thermal pulse and the consequences of convective dredge-up". In: *ApJ* 237 (Apr. 1980), pp. 111–129. DOI: 10.1086/157850.

[15] T. C. Beers and N. Christlieb. "The Discovery and Analysis of Very Metal-Poor Stars in the Galaxy". In: *Annual Review of Astronomy and Astrophysics* 43 (Sept. 2005), pp. 531–580. DOI: 10.1146/annurev.astro.42.053102.134057.

[16] T. C. Beers, G. W. Preston, and S. A. Shectman. "A search for stars of very low metal abundance. I". In: *AJ* 90 (Oct. 1985), pp. 2089–2102. DOI: 10.1086/113917.

[17] K. Belczynski et al. "Missing Black Holes Unveil the Supernova Explosion Mechanism". In: *ApJ* 757, 91 (Sept. 2012), p. 91. DOI: 10.1088/0004-637X/757/1/91. arXiv: 1110.1635.

[18] H. A. Bethe. "Energy Production in Stars". In: *Physical Review* 55 (Mar. 1939), pp. 434–456. DOI: 10.1103/PhysRev.55.434.

[19] S. Bisterzo et al. "The s-process in low-metallicity stars - III. Individual analysis of CEMP-s and CEMP-s/r with asymptotic giant branch models". In: *MNRAS* 422 (May 2012), pp. 849–884. DOI: 10.1111/j.1365-2966.2012.20670.x. arXiv: 1201.6198 [astro-ph.SR].

[20] T. Blöcker. PhD thesis. Universität Kiel, Germany, (1993), 1993.

[21] T. Blöcker and D. Schönberner. "On the Evolution and Mass of FG Sge." In: *2nd Int. Coll. on Hydrogen-Deficient Stars*. preprint. 1995.

[22] E. Böhm-Vitense. In: *Z. Astrophys.* 46 (1958), p. 108.

[23] C. T. Bolton. "Introduction to Stellar Winds, by Henny J. G. L. M. Lamers and Joseph P. Cassinelli". In: *Physics Today* 53.8 (Aug. 2000), p. 48.

[24] E. M. Burbidge et al. "Synthesis of the elements in stars". In: *Rev. Mod. Phys.* 29 (1957), p. 547.

[25] M. Busso, R. Gallino, and G. J. Wasserburg. "Nucleosynthesis in Asymptotic Giant Branch Stars: Relevance for Galactic Enrichment and Solar System Formation". In: *Annual Review of Astronomy and Astrophysics* 37 (1999), pp. 239–309.

[26] A. G. W. Cameron and W. A. Fowler. "Lithium and the s-PROCESS in Red-Giant Stars". In: *ApJ* 164 (Feb. 1971), pp. 111–+.

[27] S. W. Campbell, M. Lugaro, and A. I. Karakas. "Evolution and nucleosynthesis of extremely metal-poor and metal-free low- and intermediate-mass stars. II. s-process nucleosynthesis during the core He flash". In: *AAP* 522, L6 (Nov. 2010), p. L6. DOI: 10.1051/0004-6361/201015428. arXiv: 1010.1987 [astro-ph.SR].

[28] V. M. Canuto. "Overshooting and the mu-barrier". In: *ApJ* 508 (1998), p. L103.

[29] F. Castelli and R. L. Kurucz. "New Grids of ATLAS9 Model Atmospheres". In: *ArXiv Astrophysics e-prints* (May 2004). eprint: astro-ph/0405087.

[30] G. Chabrier. "Galactic Stellar and Substellar Initial Mass Function". In: *PASP* 115 (July 2003), pp. 763–795. DOI: 10.1086/376392. eprint: astro-ph/0304382.

[31] JW Chamberlain and LH Aller. "The Atmospheres of A-Type Subdwarfs and 95 Leonis." In: *The Astrophysical Journal* (1951). URL: http://adsabs.harvard.edu/full/1951ApJ...114...52C.

[32] A. Chieffi and M. Limongi. "Explosive Yields of Massive Stars from Z = 0 to Z = Z_{solar}". In: *ApJ* 608 (June 2004), pp. 405–410. DOI: 10.1086/392523. eprint: astro-ph/0402625.

[33] N. Christlieb et al. "The stellar content of the Hamburg/ESO survey. IV. Selection of candidate metal-poor stars". In: *AAP* 484 (June 2008), pp. 721–732. DOI: 10.1051/0004-6361:20078748. arXiv: 0804.1520.

[34] A. Coc, J.-P. Uzan, and E. Vangioni. "Standard Big-Bang Nucleosynthesis after Planck". In: *ArXiv e-prints* (July 2013). arXiv: 1307.6955 [astro-ph.CO].

[35] B. Côté, H. Martel, and L. Drissen. "Cosmological Simulations of Intergalactic Medium Evolution. I. Test of the Subgrid Chemical Enrichment Model". In: *ApJ* 777, 107 (Nov. 2013), p. 107. DOI: 10.1088/0004-637X/777/2/107.

[36] B. Côté, H. Martel, and L. Drissen. "Cosmological Simulations of the Intergalactic Medium Evolution. II. Galaxy Model and Feedback". In: *ApJ* 802, 123 (Apr. 2015), p. 123. DOI: 10.1088/0004-637X/802/2/123.

[37] B. Côté et al. "Advanced LIGO Constraints on Neutron Star Mergers and R-Process Sites". In: *ArXiv e-prints* (Oct. 2016). arXiv: 1610.02405.

[38] B. Côté et al. "Galactic outflows and evolution of the interstellar medium". In: *MNRAS* 421 (Mar. 2012), pp. 847–861. DOI: 10.1111/j.1365-2966.2011.20362.x. arXiv: 1112.2182.

[39] B. Côté et al. "Mass and Metallicity Requirement in Stellar Models for Galactic Chemical Evolution Applications". In: *ArXiv e-prints* (Feb. 2016). arXiv: 1602.04824.

[40] B. Côté et al. "The Impact of Modeling Assumptions in Galactic Chemical Evolution Models". In: *ArXiv e-prints* (Apr. 2016). arXiv: 1604.07824.

[41] B. Côté et al. "The Impact of Modeling Assumptions in Galactic Chemical Evolution Models". In: *ApJ* 835, 128 (Feb. 2017), p. 128. DOI: 10.3847/1538-4357/835/2/128. arXiv: 1604.07824.

[42] B. Côté et al. "Uncertainties in Galactic Chemical Evolution Models". In: *ApJ* 824, 82 (June 2016), p. 82. DOI: 10.3847/0004-637X/824/2/82. arXiv: 1509.06270.

[43] J. J. Cowan and W. K. Rose. "Production of C-14 and neutrons in red giants". In: *ApJ* 212 (Feb. 1977), pp. 149–158. DOI: 10.1086/155030.

[44] J. P. Cox and R. T. Giuli. *Principles of stellar structure*. New York, Gordon and Breach [1968], 1968.

[45] S. Cristallo et al. "Asymptotic-Giant-Branch Models at Very Low Metallicity". In: *PASA* 26 (Aug. 2009), pp. 139–144. DOI: 10.1071/AS09003. arXiv: 0904.4173 [astro-ph.SR].

[46] S. Cristallo et al. "Evolution, nucleosynthesis and yields of AGB stars at different metallicities (III): intermediate mass models, revised low mass models and the ph-FRUITY interface". In: *ArXiv e-prints* (July 2015). arXiv: 1507.07338 [astro-ph.SR].

[47] S. Cristallo et al. "Evolution, Nucleosynthesis, and Yields of Low-mass Asymptotic Giant Branch Stars at Different Metallicities. II. The FRUITY Database". In: *ApJs* 197, 17 (Dec. 2011), p. 17. DOI: 10.1088/0067-0049/197/2/17. arXiv: 1109.1176 [astro-ph.SR].

[48] B. D. Crosby et al. "Population III Star Formation in Large Cosmological Volumes. I. Halo Temporal and Physical Environment". In: *ApJ* 773, 108 (Aug. 2013), p. 108. DOI: 10.1088/0004-637X/773/2/108. arXiv: 1306.4679.

[49] B. D. Crosby et al. "Tracing the Evolution of High-redshift Galaxies Using Stellar Abundances". In: *ApJ* 820, 71 (Mar. 2016), p. 71. DOI: 10.3847/0004-637X/820/1/71.

[50] T. Dahlen et al. "High-Redshift Supernova Rates". In: *ApJ* 613 (Sept. 2004), pp. 189–199. DOI: 10.1086/422899. eprint: astro-ph/0406547.

[51] L. Dardelet et al. "The i-process and CEMP-r/s stars". In: *ArXiv e-prints* (May 2015). arXiv: 1505.05500 [astro-ph.SR].

[52] C. de Jager, H. Nieuwenhuijzen, and K. A. van der Hucht. "Mass loss rates in the Hertzsprung-Russell diagram". In: *Astronomy and Astrophysics, Supplement* 72 (Feb. 1988), pp. 259–289.

[53] G. Delgado-Inglada et al. "Oxygen enrichment in carbon-rich planetary nebulae". In: *MNRAS* 449 (May 2015), pp. 1797–1810. DOI: 10.1093/mnras/stv388. arXiv: 1502.06043 [astro-ph.SR].

[54] P. Denissenkov et al. "i-process nucleosynthesis and mass retention efficiency in He-shell flash evolution of rapidly accreting white dwarfs". In: *ArXiv e-prints* (Oct. 2016). arXiv: 1610.08541 [astro-ph.SR].

[55] P. A. Denissenkov et al. "i-process Nucleosynthesis and Mass Retention Efficiency in He-shell Flash Evolution of Rapidly Accreting White Dwarfs". In: *ApJL* 834, L10 (Jan. 2017), p. L10. DOI: 10.3847/2041-8213/834/2/L10. arXiv: 1610.08541 [astro-ph.SR].

[56] P A Denissenkov et al. "The C-flame Quenching by Convective Boundary Mixing in Super-AGB Stars and the Formation of Hybrid C/O/Ne White Dwarfs and SN Progenitors". In: (2013), pp. 1–26. arXiv: arXiv:1305.2649v2.

[57] Pavel Denissenkov et al. "Constraining (n,) cross sections for the i-process in Sakurais object". In: (2015). in prep.

[58] C. L. Doherty et al. "Super- and massive AGB stars - IV. Final fates - initial-to-final mass relation". In: *MNRAS* 446 (Jan. 2015), pp. 2599–2612. DOI: 10.1093/mnras/stu2180. arXiv: 1410.5431 [astro-ph.SR].

[59] C. L. Doherty et al. "Super and massive AGB stars - III. Nucleosynthesis in metal-poor and very metal-poor stars - Z = 0.001 and 0.0001". In: *MNRAS* 441 (June 2014), pp. 582–598. DOI: 10.1093/mnras/stu571. arXiv: 1403.5054 [astro-ph.SR].

[60] C. L. Doherty et al. "Super asymptotic giant branch stars. I - Evolution code comparison". In: *Monthly Notices of the Royal Astronomical Society* 401 (Jan. 2010), pp. 1453–1464. DOI: 10.1111/j.1365-2966.2009.15772.x.

[61] M. Dominik et al. "Double Compact Objects. I. The Significance of the Common Envelope on Merger Rates". In: *ApJ* 759, 52 (Nov. 2012), p. 52. DOI: 10.1088/0004-637X/759/1/52. arXiv: 1202.4901 [astro-ph.HE].

[62] O. J. Eggen, D. Lynden-Bell, and A. R. Sandage. "Evidence from the motions of old stars that the Galaxy collapsed." In: *ApJ* 136 (Nov. 1962), p. 748. DOI: 10.1086/147433.

[63] P. Eggenberger et al. "The Geneva stellar evolution code". In: *Ap&SS* 316 (Aug. 2008), pp. 43–54. DOI: 10.1007/s10509-007-9511-y.

[64] S. Ekström et al. "Grids of stellar models with rotation. I. Models from 0.8 to 120 M at solar metallicity (Z = 0.014)". In: *A&A* 537, A146 (Jan. 2012), A146. DOI: 10.1051/0004-6361/201117751. arXiv: 1110.5049 [astro-ph.SR].

[65] T. Ertl et al. "A Two-parameter Criterion for Classifying the Explodability of Massive Stars by the Neutrino-driven Mechanism". In: *ApJ* 818, 124 (Feb. 2016), p. 124. DOI: 10.3847/0004-637X/818/2/124. arXiv: 1503.07522 [astro-ph.SR].

[66] D. Ezer. "Models of Massive Pure Hydrogen Stars." In: *ApJ* 133 (Jan. 1961), p. 159. DOI: 10.1086/147012.

[67] D. Fabbian et al. "The C/O ratio at low metallicity: constraints on early chemical evolution from observations of Galactic halo stars". In: *AAP* 500 (June 2009), pp. 1143–1155. DOI: 10.1051/0004-6361/200810095. arXiv: 0810.0281.

[68] R. Farmer, C. E. Fields, and F. X. Timmes. "On Carbon Burning in Super Asymptotic Giant Branch Stars". In: *ApJ* 807, 184 (July 2015), p. 184. DOI: 10.1088/0004-637X/807/2/184. arXiv: 1506.01093 [astro-ph.SR].

[69] A. Fattahi et al. "The APOSTLE project: Local Group kinematic mass constraints and simulation candidate selection". In: *MNRAS* 457 (Mar. 2016), pp. 844–856. DOI: 10.1093/mnras/stv2970. arXiv: 1507.03643.

[70] A. S. Ferrarotti and H.-P. Gail. "Composition and quantities of dust produced by AGB-stars and returned to the interstellar medium". In: *A&A* 447 (Feb. 2006), pp. 553–576. DOI: 10.1051/0004-6361:20041198.

[71] C. G. Few et al. "RAMSES-CH: a new chemodynamical code for cosmological simulations". In: *MNRAS* 424 (July 2012), pp. L11–L15. DOI: 10.1111/j.1745-3933.2012.01275.x. arXiv: 1202.6400.

[72] C. K. Fishlock et al. "Evolution and Nucleosynthesis of Asymptotic Giant Branch Stellar Models of Low Metallicity". In: *ApJ* 797, 44 (Dec. 2014), p. 44. DOI: 10.1088/0004-637X/797/1/44. arXiv: 1410.7457 [astro-ph.SR].

[73] B. Freytag, H.-G. Ludwig, and M. Steffen. "Hydrodynamical models of stellar convection. The role of overshoot in DA white dwarfs, A-type stars, and the sun". In: *A&A* 313 (1996), p. 497.

[74] C. Fröhlich et al. "Nucleosynthesis in neutrino-driven supernovae". In: *New Astronomy Review* 50 (Oct. 2006), pp. 496–499. DOI: 10.1016/j.newar.2006.06.003. eprint: arXiv:astro-ph/0511584.

[75] C. A. Frost et al. "The brightest carbon stars". In: *A&A* 332 (Apr. 1998), pp. L17–L20.

[76] C. L. Fryer and P. A. Young. "Late-Time Convection in the Collapse of a 23 M_{solar} Star". In: *ApJ* 659 (Apr. 2007), pp. 1438–1448. DOI: 10.1086/513003. eprint: astro-ph/0612154.

[77] C. L. Fryer et al. "Compact Remnant Mass Function: Dependence on the Explosion Mechanism and Metallicity". In: *ApJ* 749, 91 (Apr. 2012), p. 91. DOI: 10.1088/0004-637X/749/1/91. arXiv: 1110.1726 [astro-ph.SR].

[78] M. Y. Fujimoto, Y. Ikeda, and Jr. Iben I. "The Origin of Extremely Metal-poor Carbon Stars and the Search for Population III". In: *ApJ Lett.* 529 (2000), p. L25.

[79] S.-i. Fujimoto et al. "Heavy-Element Nucleosynthesis in a Collapsar". In: *ApJ* 656 (Feb. 2007), pp. 382–392. DOI: 10.1086/509908. eprint: astro-ph/0602460.

[80] W. Fujiya et al. "Evidence for Radiogenic Sulfur-32 in Type AB Presolar Silicon Carbide Grains?" In: *ApJl* 776, L29 (Oct. 2013), p. L29. DOI: 10.1088/2041-8205/776/2/L29. arXiv: 1310.0485 [astro-ph.SR].

[81] R. Gallino et al. "Evolution and Nucleosynthesis in Low-Mass Asymptotic Giant Branch Stars. II. Neutron Capture and the s-Process". In: *ApJ* 497 (Apr. 1998), pp. 388–+. DOI: 10.1086/305437.

[82] E. García-Berro and I. Iben Jr. "On the Formation and Evolution of Super-Asymptotic Giant Branch Stars with Cores Processed by Carbon Burnung. I. Spica to Antares". In: *ApJ* 434 (1994), p. 306.

[83] E. García-Berro, C. Ritossa, and I. Iben Jr. "On the Evolution of Stars that Form Electron-Degenerate Cores Processed by Carbon Burning. III. The Inward Propagation of a Carbon-Burning Flame and Other Properties of a 9 M Model Star". In: *ApJ* 485 (Aug. 1997), pp. 765–784.

[84] D. A. García-Hernández et al. "Hot bottom burning and s-process nucleosynthesis in massive AGB stars at the beginning of the thermally-pulsing phase". In: *A&A* ().

[85] C. Georgy et al. "Grids of stellar models with rotation. III. Models from 0.8 to 120 M at a metallicity Z = 0.002". In: *A&A* 558, A103 (Oct. 2013), A103. DOI: 10.1051/0004-6361/201322178. arXiv: 1308.2914 [astro-ph.SR].

[86] B. K. Gibson. "Stellar yields and chemical evolution". In: *Cosmic Chemical Evolution*. Ed. by K. Nomoto and J. W. Truran. Vol. 187. IAU Symposium. 2002, pp. 159–163.

[87] P. Gil-Pons and C. L. Doherty. "The upper mass limit for the formation of TP-SAGB stars and the dredge-out phenomenon ." In: *Mem. Soc. Astron. Italiana* 81 (2010), p. 974.

[88] P. Gil-Pons et al. "Evolution and CNO yields of Z = 10^{-5} stars and possible effects on carbon-enhanced metal-poor production". In: *A&A* 557, A106 (Sept. 2013), A106. DOI: 10.1051/0004-6361/201321127. arXiv: 1309.0600 [astro-ph.SR].

[89] L. Girardi et al. "Evolutionary tracks and isochrones for low- and intermediate-mass stars: From 0.15 to 7 M_{sun}, and from Z=0.0004 to 0.03". In: *A&AS* 141 (Feb. 2000), pp. 371–383. DOI: 10.1051/aas:2000126. eprint: astro-ph/9910164.

[90] E. Glebbeek et al. "The evolution of runaway stellar collision products". In: *Astronomy and Astrophysics* 497 (Apr. 2009), pp. 255–264. DOI: 10.1051/0004-6361/200810425. arXiv: 0902.1753 [astro-ph.SR].

[91] S. Goriely and L. Siess. "S-process in hot AGB stars: A complex interplay between diffusive mixing and nuclear burning". In: *A&A* 421 (July 2004), pp. L25–L28.

[92] N. Grevesse and A. Noels. "Cosmic abundances of the elements." In: *Origin and Evolution of the Elements*. Ed. by N. Prantzos, E. Vangioni-Flam, & M. Casse. Jan. 1993, pp. 15–25.

[93] M. Hampel et al. "The Intermediate Neutron-capture Process and Carbon-enhanced Metal-poor Stars". In: *ApJ* 831, 171 (Nov. 2016), p. 171. DOI: 10.3847/0004-637X/831/2/171. arXiv: 1608.08634 [astro-ph.SR].

[94] Walter Hauser and Herman Feshbach. "The Inelastic Scattering of Neutrons". In: *Phys. Rev.* 87 (2 1952), pp. 366–373. DOI: 10.1103/PhysRev.87.366. URL: http://link.aps.org/doi/10.1103/PhysRev.87.366.

[95] A. Heger and S. E. Woosley. "Nucleosynthesis and Evolution of Massive Metal-free Stars". In: *ApJ* 724 (Nov. 2010), pp. 341–373. DOI: 10.1088/0004-637X/724/1/341. arXiv: 0803.3161.

[96] M. Heil et al. "The s process in massive stars". In: *Progress in Particle and Nuclear Physics* 59 (July 2007), pp. 174–182. DOI: 10.1016/j.ppnp.2006.12.013.

[97] LG Henyey, JE Forbes, and NL Gould. "A New Method of Automatic Computation of Stellar Evolution." In: *The Astrophysical Journal* (1964). URL: http://adsabs.harvard.edu/full/1964ApJ...139..306H.

[98] M. Herant and S. E. Woosley. "Postexplosion hydrodynamics of supernovae in red supergiants". In: *ApJ* 425 (Apr. 1994), pp. 814–828. DOI: 10.1086/174026.

[99] F. Herwig. "Dredge-up and envelope burning in intermediate mass giants of very low metallicity". In: *ApJ* 605 (2004), pp. 425–435.

[100] F. Herwig. "Evolution and Yields of Extremely Metal-poor Intermediate-Mass Stars". In: *ApJS* 155 (Dec. 2004), pp. 651–666.

[101] F. Herwig. "Evolution of Asymptotic Giant Branch Stars". In: *Annual Review of Astronomy and Astrophysics* 43 (Sept. 2005), pp. 435–479. DOI: 10.1146/annurev.astro.43.072103.150600.

[102] F. Herwig. "Evolution of Solar and Intermediate-Mass Stars". In: *Planets, Stars and Stellar Systems. Volume 4: Stellar Structure and Evolution*. Ed. by T. D. Oswalt and M. A. Barstow. 2013, p. 397. DOI: 10.1007/978-94-007-5615-1_8.

[103] F. Herwig. "Stellar Evolution and Nucleosynthesis of Post-AGB Stars". In: *Post-AGB Objects as a Phase of Stellar Evolution*. astro-ph/0103004. Aug. 2001, pp. 249+.

[104] F. Herwig. "The evolution of AGB stars with convective overshoot". In: *Astronomy and Astrophysics* 360 (Aug. 2000), pp. 952–968. eprint: arXiv:astro-ph/0007139.

[105] F. Herwig. "The evolutionary time scale of Sakurais object: A test for convection theory". In: *ApJ Lett.* 554 (June 2001), pp. L71–L74. URL: http://adsabs.harvard.edu/cgi-bin/nph-bib_query?bibcode=2001ApJ...554L..71H&db_key=AST.

[106] F. Herwig and S. M. Austin. "Nuclear Reaction Rates and Carbon Star Formation". In: *ApJ Lett.* 613 (Sept. 2004), pp. L73–L76.

[107] F. Herwig, N. Langer, and M. Lugaro. "The s-Process in Rotating Asymptotic Giant Branch Stars". In: *ApJ* 593 (Aug. 2003), pp. 1056–1073. DOI: 10.1086/376726. eprint: arXiv:astro-ph/0305491.

[108] F. Herwig et al. "Convective and Non-Convective Mixing in AGB Stars". In: *Why Galaxies Care About AGB Stars: Their Importance as Actors and Probes*. Ed. by F. Kerschbaum, C. Charbonnel, and R. F. Wing. Vol. 378. Astronomical Society of the Pacific Conference Series. Nov. 2007, p. 43. eprint: arXiv:0709.0197.

[109] F. Herwig et al. "Convective-reactive Proton-^{12}C Combustion in Sakurai's Object (V4334 Sagittarii) and Implications for the Evolution and Yields from the First Generations of Stars". In: *ApJ* 727 (Feb. 2011).

[110] F. Herwig et al. "Global Non-spherical Oscillations in Three-dimensional 4π Simulations of the H-ingestion Flash". In: *ApJl* 792, L3 (Sept. 2014), p. L3. DOI: 10.1088/2041-8205/792/1/L3. arXiv: 1310.4584 [astro-ph.SR].

[111] F. Herwig et al. "Nucleosynthesis simulations for a wide range of nuclear production sites from NuGrid". In: *Nuclei in the Cosmos (NIC X)*. 2008. arXiv: 0811.4653.

[112] F. Herwig et al. "Stellar evolution of low and intermediate-mass stars. IV. Hydrodynamically-based overshoot and nucleosynthesis in AGB stars." In: *A&A* 324 (1997), pp. L81–L84. URL: http://adsabs.harvard.edu/cgi-bin/nph-bib_query?bibcode=1997A\verb$%$26A...324L..81H&db_key=AST.

[113] Falk Herwig et al. "Global Non-spherical Oscillations in Three-dimensional 4π Simulations of the H-ingestion Flash". In: *ApJ* 792.1 (Sept. 2014), p. L3.

[114] R. Hirschi. "Very low-metallicity massive stars:. Pre-SN evolution models and primary nitrogen production". In: *A&A* 461 (Jan. 2007), pp. 571–583. DOI: 10.1051/0004-6361:20065356. eprint: arXiv:astro-ph/0608170.

[115] R. Hirschi, G. Meynet, and A. Maeder. "Stellar evolution with rotation. XIII. Predicted GRB rates at various Z". In: *A&A* 443 (Nov. 2005), pp. 581–591. DOI: 10.1051/0004-6361:20053329. eprint: arXiv:astro-ph/0507343.

[116] R. Hirschi, G. Meynet, and A. Maeder. "Yields of rotating stars at solar metallicity". In: *AAP* 433 (Apr. 2005), pp. 1013–1022. DOI: 10.1051/0004-6361:20041554. eprint: astro-ph/0412454.

[117] P. F. Hopkins, E. Quataert, and N. Murray. "Stellar feedback in galaxies and the origin of galaxy-scale winds". In: *MNRAS* 421 (Apr. 2012), pp. 3522–3537. DOI: 10.1111/j.1365-2966.2012.20593.x. arXiv: 1110.4638 [astro-ph.CO].

[118] F Hoyle. "On Nuclear Reactions Occuring in Very Hot STARS. I. the Synthesis of Elements from Carbon to Nickel." In: *The Astrophysical Journal Supplement Series* (1954). URL: http://adsabs.harvard.edu/full/1954ApJS....1..121H.

[119] T.-O. Husser et al. "A new extensive library of PHOENIX stellar atmospheres and synthetic spectra". In: *A&A* 553, A6 (May 2013), A6. DOI: 10.1051/0004-6361/201219058. arXiv: 1303.5632 [astro-ph.SR].

[120] C. Iliadis. *Nuclear Physics of Stars*. Wiley-VCH Verlag, 2007.

[121] M. N. Ishigaki, W. Aoki, and M. Chiba. "Chemical Abundances of the Milky Way Thick Disk and Stellar Halo. II. Sodium, Iron-peak, and Neutron-capture Elements". In: *ApJ* 771, 67 (July 2013), p. 67. DOI: 10.1088/0004-637X/771/1/67. arXiv: 1306.0954.

[122] M. N. Ishigaki, M. Chiba, and W. Aoki. "Chemical Abundances of the Milky Way Thick Disk and Stellar Halo. I. Implications of [α/Fe] for Star Formation Histories in Their Progenitors". In: *ApJ* 753, 64 (July 2012), p. 64. DOI: 10.1088/0004-637X/753/1/64. arXiv: 1205.2406.

[123] N. Iwamoto et al. "Flash-Driven Convective Mixing in Low-Mass, Metal-deficient Asymptotic Giant Branch Stars: A New Paradigm for Lithium Enrichment and a Possible s-Process". In: *ApJ* 602 (Feb. 2004), pp. 378–388.

[124] N. Iwamoto et al. "The First Chemical Enrichment in the Universe and the Formation of Hyper Metal-Poor Stars". In: *Science* 309 (July 2005), pp. 451–453. DOI: 10.1126/science.1112997. eprint: astro-ph/0505524.

[125] M. Jadhav et al. "Relics of Ancient Post-AGB Stars in a Primitive Meteorite". In: *ApJl* 777, L27 (Nov. 2013), p. L27. DOI: 10.1088/2041-8205/777/2/L27. arXiv: 1310.2679 [astro-ph.EP].

[126] J. A. Johnson and M. Bolte. "The s-Process in Metal-Poor Stars: Abundances for 22 Neutron-Capture Elements in CS 31062-050". In: *ApJ* 605 (Apr. 2004), pp. 462–471. DOI: 10.1086/382147. eprint: arXiv:astro-ph/0402003.

[127] S. Jones et al. "H ingestion into He-burning convection zones in super-AGB stellar models as a potential site for intermediate neutron-density nucleosynthesis". In: *MNRAS* 455 (Feb. 2016), pp. 3848–3863. DOI: 10.1093/mnras/stv2488. arXiv: 1510.07417 [astro-ph.SR].

[128] S. Jones et al. "H ingestion into He-burning convection zones in super-AGB stellar models as a potential site for intermediate neutron-density nucleosynthesis". In: *MNRAS* 455 (Feb. 2016), pp. 3848–3863. DOI: 10.1093/mnras/stv2488. arXiv: 1510.07417 [astro-ph.SR].

[129] S. Jones et al. "Idealised hydrodynamic simulations of turbulent oxygen-burning shell convection in 4π geometry". In: *ArXiv e-prints* (May 2016). arXiv: 1605.03766 [astro-ph.SR].

[130] Sam Jones et al. "H-ingestion into He-burning convection zones in super-AGB stellar models as a potential site for intermediate neutron-density nucleosynthesis". In: (2015). in prep.

[131] K. Jonsell et al. "The Hamburg/ESO R-process enhanced star survey (HERES). III. HE 0338-3945 and the formation of the r + s stars". In: *AAP* 451 (May 2006), pp. 651–670. DOI: 10.1051/0004-6361:20054470. eprint: astro-ph/0601476.

[132] F. Käppeler, H. Beer, and K. Wisshak. "s-process nucleosynthesis and the classical model." In: *Reports on Progress in Physics* 52 (Aug. 1989), pp. 945–1013.

[133] F. Käppeler et al. "The s process: Nuclear physics, stellar models, and observations". In: *Reviews of Modern Physics* 83 (Jan. 2011), pp. 157–194. DOI: 10.1103/RevModPhys.83.157. arXiv: 1012.5218 [astro-ph.SR].

[134] A. I. Karakas. "Current Status of Stellar Evolutionary Models for AGB Stars". In: *Why Galaxies Care about AGB Stars II: Shining Examples and Common Inhabitants*. Ed. by F. Kerschbaum, T. Lebzelter, and R. F. Wing. Vol. 445. Astronomical Society of the Pacific Conference Series. Sept. 2011, p. 3.

[135] A. I. Karakas. "Updated stellar yields from AGB models (Karakas, 2010)". In: *VizieR Online Data Catalog* 740 (Oct. 2010), p. 31413.

[136] A. I. Karakas, D. A. García-Hernández, and M. Lugaro. "Heavy Element Nucleosynthesis in the Brightest Galactic Asymptotic Giant Branch Stars". In: *ApJ* 751, 8 (May 2012), p. 8. DOI: 10.1088/0004-637X/751/1/8. arXiv: 1203.2931 [astro-ph.SR].

[137] D. Kawata and B. K. Gibson. "GCD+: a new chemodynamical approach to modelling supernovae and chemical enrichment in elliptical galaxies". In: *MNRAS* 340 (Apr. 2003), pp. 908–922. DOI: 10.1046/j.1365-8711.2003.06356.x. eprint: astro-ph/0212401.

[138] S. C. Keller et al. "A single low-energy, iron-poor supernova as the source of metals in the star SMSS J031300.36-670839.3". In: *Nature* 506 (Feb. 2014), pp. 463–466. DOI: 10.1038/nature12990. arXiv: 1402.1517 [astro-ph.SR].

[139] R. Kippenhahn and A. Weigert. *Stellar structure and evolution*. Berlin: Springer, 1990.

[140] C. Kobayashi et al. "Galactic Chemical Evolution: Carbon through Zinc". In: *ApJ* 653 (Dec. 2006), pp. 1145–1171. DOI: 10.1086/508914. eprint: arXiv:astro-ph/0608688.

[141] P. Kroupa. "On the variation of the initial mass function". In: *MNRAS* 322 (Apr. 2001), pp. 231–246. DOI: 10.1046/j.1365-8711.2001.04022.x. eprint: astro-ph/0009005.

[142] P. Kroupa et al. "The Stellar and Sub-Stellar Initial Mass Function of Simple and Composite Populations". In: *Planets, Stars and Stellar Systems. Volume 5: Galactic Structure and Stellar Populations*. Ed. by T. D. Oswalt and G. Gilmore. 2013, p. 115. DOI: 10.1007/978-94-007-5612-0_4.

[143] J. C. Lattanzio and A. I. Boothroyd. "Nucleosynthesis of Elements in Low to Intermediate Mass Stars through the AGB Phase". In: *Astrophysical Implications of the Laboratory Study of Presolar Materials*. Ed. by T. Bernatowitz and E. Zinner. AIP Conf. Ser., 1997, p. 85.

[144] J. C. Lattanzio et al. "Hot Bottom Burning Nucleosynthesis in $6M_{solar}$ Stellar Models". In: *Nuclear Physics A* 621 (Feb. 1997), pp. 435–438. DOI: 10.1016/S0375-9474(97)00286-8.

[145] John Lattanzio et al. In: Mem. Soc. Astron. Ital. 67 (1996), p. 729.

[146] C. Leitherer, C. Robert, and L. Drissen. "Deposition of mass, momentum, and energy by massive stars into the interstellar medium". In: *ApJ* 401 (Dec. 1992), pp. 596–617. DOI: 10.1086/172089.

[147] C. Leitherer et al. "Starburst99: Synthesis Models for Galaxies with Active Star Formation". In: *ApJS* 123 (July 1999), pp. 3–40. DOI: 10.1086/313233. eprint: astro-ph/9902334.

[148] M. Limongi and A. Chieffi. "The Nucleosynthesis of ^{26}Al and ^{60}Fe in Solar Metallicity Stars Extending in Mass from 11 to 120 M_{solar}: The Hydrostatic and Explosive Contributions". In: *ApJ* 647 (Aug. 2006), pp. 483–500. DOI: 10.1086/505164. eprint: arXiv:astro-ph/0604297.

[149] K. Lodders. "Solar system abundances and condensation temperatures of the elements". In: *ApJ* (2003). submitted.

[150] M. Lugaro et al. "Post-AGB stars in the Magellanic Clouds and neutron-capture processes in AGB stars". In: *AAP* 583, A77 (Nov. 2015), A77. DOI: 10.1051/0004-6361/201526690. arXiv: 1509.03518 [astro-ph.SR].

[151] M. Lugaro et al. "s-Process Nucleosynthesis in Asymptotic Giant Branch Stars: A Test for Stellar Evolution". In: *ApJ* 586 (Apr. 2003), pp. 1305–1319. DOI: 10.1086/367887. eprint: arXiv:astro-ph/0212364.

[152] M. Lugaro et al. "The s-process in Asymptotic Giant Branch Stars of Low Metallicity and the Composition of Carbon-enhanced Metal-poor Stars". In: *ApJ* 747, 2 (Mar. 2012), p. 2. DOI: 10.1088/0004-637X/747/1/2. arXiv: 1112.2757 [astro-ph.SR].

[153] A. Maeder and G. Meynet. "Stellar evolution with rotation. VII. . Low metallicity models and the blue to red supergiant ratio in the SMC". In: *Astronomy and Astrophysics* 373 (July 2001), pp. 555–571. DOI: 10.1051/0004-6361:20010596. eprint: astro-ph/0105051.

[154] G. Magkotsios et al. "Trends in ˆ44Ti and ˆ56Ni from Core-Collapse Supernovae". In: *APS Division of Nuclear Physics Meeting Abstracts*. Nov. 2010, H5.

[155] F. Mannucci, M. Della Valle, and N. Panagia. "Two populations of progenitors for Type Ia supernovae?" In: *MNRAS* 370 (Aug. 2006), pp. 773–783. DOI: 10.1111/j.1365-2966.2006.10501.x. eprint: astro-ph/0510315.

[156] D. Maoz and F. Mannucci. "Type-Ia Supernova Rates and the Progenitor Problem: A Review". In: *PASA* 29 (Jan. 2012), pp. 447–465. DOI: 10.1071/AS11052. arXiv: 1111.4492.

[157] P. Marigo. "Chemical yields from low- and intermediate-mass stars: Model predictions and basic observational constraints". In: *A&A* 370 (Apr. 2001), pp. 194–217. DOI: 10.1051/0004-6361:20000247. eprint: astro-ph/0012181.

[158] P. Marigo. "Chemical yields from low- and intermediate-mass stars: Model predictions and basic observational constraints". In: *A&A* 370 (Apr. 2001), pp. 194–217.

[159] T. Masseron et al. "A holistic approach to carbon-enhanced metal-poor stars". In: *Astronomy and Astrophysics* 509 (Jan. 2010), A93+. DOI: 10.1051/0004-6361/200911744. arXiv: 0901.4737 [astro-ph.SR].

[160] F. Matteucci. "Chemical Evolution of the Milky Way and Its Satellites". In: *The Origin of the Galaxy and Local Group, Saas-Fee Advanced Course, Volume 37. ISBN 978-3-642-41719-1. Springer-Verlag Berlin Heidelberg, 2014, p. 145* 37 (2014), p. 145. DOI: 10.1007/978-3-642-41720-7_2. arXiv: 0804.1492.

[161] A. McWilliam. "Abundance Ratios and Galactic Chemical Evolution". In: *Annual Review of Astronomy and Astrophysics* 35 (1997), pp. 503–556.

[162] C. A. Meakin and D. Arnett. "Active Carbon and Oxygen Shell Burning Hydrodynamics". In: *ApJL* 637 (Jan. 2006), pp. L53–L56. DOI: 10.1086/500544. eprint: astro-ph/0601348.

[163] C. A. Meakin and D. Arnett. "Active Carbon and Oxygen Shell Burning Hydrodynamics". In: *ApJ Lett.* 637 (Jan. 2006), pp. L53–L56. DOI: 10.1086/500544. eprint: arXiv:astro-ph/0601348.

[164] C. A. Meakin and D. Arnett. "Anelastic and Compressible Simulations of Stellar Oxygen Burning". In: *ApJ* 665 (Aug. 2007), pp. 690–697. DOI: 10.1086/519372. eprint: arXiv:astro-ph/0611317.

[165] C. A. Meakin and D. Arnett. "Turbulent Convection in Stellar Interiors. I. Hydrodynamic Simulation". In: *ApJ* 667 (Sept. 2007), pp. 448–475. DOI: 10.1086/520318. eprint: astro-ph/0611315.

[166] G. Meynet and A. Maeder. "Stellar evolution with rotation. VIII. Models at Z = 10^{-5} and CNO yields for early galactic evolution". In: *A&A* 390 (Aug. 2002), pp. 561–583. URL: http://adsabs.harvard.edu/cgi-bin/nph-bib_query?bibcode=2002A%26A...390..561M&db_key=AST.

[167] M. M. Miller Bertolami and L. G. Althaus. "Full evolutionary models for PG 1159 stars. Implications for the helium-rich O(He) stars". In: *AAP* 454 (Aug. 2006), pp. 845–854. DOI: 10.1051/0004-6361:20054723. eprint: astro-ph/0603846.

[168] T. Mishenina et al. "New insights on Ba overabundance in open clusters. Evidence for the intermediate neutron-capture process at play?" In: *MNRAS* 446 (Feb. 2015), pp. 3651–3668. DOI: 10.1093/mnras/stu2337. arXiv: 1411.1422 [astro-ph.SR].

[169] H. Mo, F. C. van den Bosch, and S. White. *Galaxy Formation and Evolution*. May 2010.

[170] M. Mollá et al. "Galactic chemical evolution: stellar yields and the initial mass function". In: *MNRAS* 451 (Aug. 2015), pp. 3693–3708. DOI: 10.1093/mnras/stv1102. arXiv: 1505.03341.

[171] J. F. Navarro and S. D. M. White. "Simulations of Dissipative Galaxy Formation in Hierarchically Clustering Universes - Part One - Tests of the Code". In: *MNRAS* 265 (Nov. 1993), p. 271. DOI: 10.1093/mnras/265.2.271.

[172] N. Nishimura, T. Takiwaki, and F.-K. Thielemann. "The r-process Nucleosynthesis in the Various Jet-like Explosions of Magnetorotational Core-collapse Supernovae". In: *ApJ* 810, 109 (Sept. 2015), p. 109. DOI: 10.1088/0004-637X/810/2/109. arXiv: 1501.06567 [astro-ph.SR].

[173] K. Nomoto, C. Kobayashi, and N. Tominaga. "Nucleosynthesis in Stars and the Chemical Enrichment of Galaxies". In: *ARAA* 51 (Aug. 2013), pp. 457–509. DOI: 10.1146/annurev-astro-082812-140956.

[174] T. Nugis and H. J. G. L. M. Lamers. "Mass-loss rates of Wolf-Rayet stars as a function of stellar parameters". In: *Astronomy and Astrophysics* 360 (Aug. 2000), pp. 227–244.

[175] B. E. J. Pagel. *Nucleosynthesis and Chemical Evolution of Galaxies*. Jan. 2009.

[176] Bill Paxton et al. "Modules for Experiments in Stellar Astrophysics (Mesa)". In: *The Astrophysical Journal Supplement Series* 192.1 (Jan. 2011), p. 3. ISSN: 0067-0049. DOI: 10.1088/0067-0049/192/1/3. URL: http://stacks.iop.org/0067-0049/192/i=1/a=3?key=crossref.4bfe81c8d21794a47ae04409880eee28.

[177] G. J. Peters and R. Hirschi. "The Evolution of High-Mass Stars". In: *Planets, Stars and Stellar Systems. Volume 4: Stellar Structure and Evolution*. Ed. by T. D. Oswalt and M. A. Barstow. 2013, p. 447. DOI: 10.1007/978-94-007-5615-1_9.

[178] M. Pignatari and R. Gallino. "Metallicity dependence of the s-process in massive stars: theoretical predictions ." In: *Mem. Soc. Astron. Italiana* 78 (2007), p. 543.

[179] M. Pignatari et al. "Carbon-rich presolar grains from massive stars. Subsolar 12C/13C and 14N/15N ratios and the mystery of 15N". In: *ArXiv e-prints* (June 2015). arXiv: 1506.09056 [astro-ph.SR].

[180] M. Pignatari et al. "NuGrid stellar data set. I. Stellar yields from H to Bi for stars with metallicities Z = 0.02 and Z = 0.01". In: *ArXiv e-prints* (July 2016). arXiv: 1307.6961 [astro-ph.SR].

[181] M. Pignatari et al. "NuGrid Stellar Data Set. I.Stellar Yields from H to Bi for Stars with Metallicities Z = 0.02 and Z = 0.01". In: *ApJS* 225, 24 (Aug. 2016), p. 24. DOI: 10.3847/0067-0049/225/2/24. arXiv: 1307.6961 [astro-ph.SR].

[182] M. Pignatari et al. "Production of Carbon-rich Presolar Grains from Massive Stars". In: *ApJL* 767, L22 (Apr. 2013), p. L22. DOI: 10.1088/2041-8205/767/2/L22. arXiv: 1303.3374 [astro-ph.SR].

[183] M. Pignatari et al. "The ^{12}C + ^{12}C Reaction and the Impact on Nucleosynthesis in Massive Stars". In: *ApJ* 762, 31 (Jan. 2013), p. 31. DOI: 10.1088/0004-637X/762/1/31. arXiv: 1212.3962 [astro-ph.SR].

[184] M. Pignatari et al. "The production of proton-rich isotopes beyond iron: The γ-process in stars". In: *International Journal of Modern Physics E* 25, 1630003-232 (Apr. 2016), pp. 1630003–232. DOI: 10.1142/S0218301316300034. arXiv: 1605.03690 [astro-ph.SR].

[185] A. J. T. Poelarends et al. "The Supernova Channel of Super-AGB Stars". In: *apj* 675 (Mar. 2008), pp. 614–625. DOI: 10.1086/520872. eprint: arXiv:0705.4643.

[186] D. H. Porter and P. R. Woodward. "Three-dimensional Simulations of Turbulent Compressible Convection". In: *ApJS* 127 (Mar. 2000), pp. 159–187.

[187] D. H. Porter, P. R. Woodward, and M. L. Jacobs. "Convection in Slab and Spheroidal Geometries". In: *Astrophysical Turbulence and Convection*. Ed. by J. R. Buchler and H. Kandrup. Vol. 898. New York Academy Sciences Annals. online at http://www.lcse.umn.edu/convsph. Feb. 2000, pp. 1–+.

[188] L. Portinari, C. Chiosi, and A. Bressan. "Galactic chemical enrichment with new metallicity dependent stellar yields". In: *AAP* 334 (June 1998), pp. 505–539. eprint: astro-ph/9711337.

[189] N. Prantzos. "An Introduction to Galactic Chemical Evolution". In: *EAS Publications Series*. Ed. by C. Charbonnel and J.-P. Zahn. Vol. 32. EAS Publications Series. Nov. 2008, pp. 311–356. DOI: 10.1051/eas:0832009. arXiv: 0709.0833.

[190] N. Prantzos, M. Hashimoto, and K. Nomoto. "The s-process in massive stars - Yields as a function of stellar mass and metallicity". In: *Astronomy and Astrophysics* 234 (Aug. 1990), pp. 211–229.

[191] C. M. Raiteri, M. Villata, and J. F. Navarro. "Simulations of Galactic chemical evolution. I. O and Fe abundances in a simple collapse model." In: *A&A* 315 (Nov. 1996), pp. 105–115.

[192] T. Rauscher and F.-K. Thielemann. "Astrophysical Reaction Rates From Statistical Model Calculations". In: *Atomic Data and Nuclear Data Tables* 75 (May 2000), pp. 1–351. DOI: 10.1006/adnd.2000.0834. eprint: arXiv:astro-ph/0004059.

[193] T. Rauscher et al. "Nucleosynthesis in Massive Stars with Improved Nuclear and Stellar Physics". In: *ApJ* 576 (Sept. 2002), pp. 323–348. DOI: 10.1086/341728. eprint: arXiv:astro-ph/0112478.

[194] M. Rayet et al. "The p-process in Type II supernovae." In: *Astronomy and Astrophysics* 298 (June 1995), pp. 517–+.

[195] B. E. Reddy, D. L. Lambert, and C. Allende Prieto. "Elemental abundance survey of the Galactic thick disc". In: *Monthly Notices of the Royal Astronomical Society* 367 (Apr. 2006), pp. 1329–1366. DOI: 10.1111/j.1365-2966.2006.10148.x. eprint: arXiv:astro-ph/0512505.

[196] D. Reimers. "Circumstellar absorption lines and mass loss from red giants". In: *Mem. Soc. Sci. Liege* 8 (1975), p. 369.

[197] C. Ritossa, E. García-Berro, and I. J. Iben. "On the Evolution of Stars that Form Electron-degenerate Cores Processed by Carbon Burning. V. Shell Convection Sustained by Helium Burning, Transient Neon Burning, Dredge-out, URCA Cooling, and Other Properties of an 11 M_solar Population I Model Star". In: *ApJ* 515 (Apr. 1999), pp. 381–397. URL: http://adsabs.harvard.edu/cgi-bin/nph-bib_query?bibcode=1999ApJ...515..381R.

[198] C. Ritter et al. "Convective-reactive nucleosynthesis of K, Sc, Cl and p-process isotopes in O-C shell mergers". In: (2017, in prep.).

[199] R. Ritter et al. "NuGrid stellar data set. I extension. Stellar yields from H to Bi for stars with metallicity Z=0.02, Z=0.01, Z = 0.006, Z=0.001 and Z = 0.0001". In: (2016).

[200] I. U. Roederer et al. "A Search for Stars of Very Low Metal Abundance. VI. Detailed Abundances of 313 Metal-poor Stars". In: *Astronomical Journal* 147, 136 (June 2014), p. 136. DOI: 10.1088/0004-6256/147/6/136. arXiv: 1403.6853 [astro-ph.SR].

[201] I. U. Roederer et al. "The Diverse Origins of Neutron-capture Elements in the Metal-poor Star HD 94028: Possible Detection of Products of i-Process Nucleosynthesis". In: *ApJ* 821, 37 (Apr. 2016), p. 37. DOI: 10.3847/0004-637X/821/1/37. arXiv: 1603.00036 [astro-ph.SR].

[202] C. E. Rolfs and W.S. Rodney. *Cauldrons in the cosmos*. 2005.

[203] D. Romano et al. "Quantifying the uncertainties of chemical evolution studies. II. Stellar yields". In: *AAP* 522, A32 (Nov. 2010), A32. DOI: 10.1051/0004-6361/201014483. arXiv: 1006.5863.

[204] P. Rosenfield et al. "Evolution of Thermally Pulsing Asymptotic Giant Branch Stars. IV. Constraining Mass loss and Lifetimes of Low Mass, Low Metallicity AGB Stars". In: *ApJ* 790, 22 (July 2014), p. 22. DOI: 10.1088/0004-637X/790/1/22. arXiv: 1406.0676 [astro-ph.SR].

[205] S. Rosswog et al. "The long-term evolution of neutron star merger remnants - I. The impact of r-process nucleosynthesis". In: *MNRAS* 439 (Mar. 2014), pp. 744–756. DOI: 10.1093/mnras/stt2502. arXiv: 1307.2939 [astro-ph.HE].

[206] I.-J. Sackmann and A. I. Boothroyd. "The Creation of Superrich Lithium Giants". In: *ApJ* 392 (1992), p. L71.

[207] E. E. Salpeter. "The Luminosity Function and Stellar Evolution." In: *ApJ* 121 (Jan. 1955), p. 161. DOI: 10.1086/145971.

[208] T. Sawala et al. "Bent by baryons: the low-mass galaxy-halo relation". In: *MNRAS* 448 (Apr. 2015), pp. 2941–2947. DOI: 10.1093/mnras/stu2753. arXiv: 1404.3724.

[209] T. Sawala et al. "The abundance of (not just) dark matter haloes". In: *MNRAS* 431 (May 2013), pp. 1366–1382. DOI: 10.1093/mnras/stt259. arXiv: 1206.6495 [astro-ph.CO].

[210] T. Sawala et al. "The APOSTLE simulations: solutions to the Local Group's cosmic puzzles". In: *MNRAS* 457 (Apr. 2016), pp. 1931–1943. DOI: 10.1093/mnras/stw145. arXiv: 1511.01098.

[211] L. Sbordone et al. "The metal-poor end of the Spite plateau. I. Stellar parameters, metallicities, and lithium abundances". In: *Astronomy and Astrophysics* 522, A26 (Nov. 2010), A26. DOI: 10.1051/0004-6361/200913282. arXiv: 1003.4510.

[212] J. M. Scalo, K. H. Despain, and R. K. Ulrich. "Studies of evolved stars. V - Nucleosynthesis in hot-bottom convective envelopes". In: *ApJ* 196 (Mar. 1975), pp. 805–817.

[213] C. Scannapieco et al. "Feedback and metal enrichment in cosmological smoothed particle hydrodynamics simulations - I. A model for chemical enrichment". In: *MNRAS* 364 (Dec. 2005), pp. 552–564. DOI: 10.1111/j.1365-2966.2005.09574.x. eprint: astro-ph/0505440.

[214] J. Schaye et al. "The EAGLE project: simulating the evolution and assembly of galaxies and their environments". In: *MNRAS* 446 (Jan. 2015), pp. 521–554. DOI: 10.1093/mnras/stu2058. arXiv: 1407.7040.

[215] M. Schmidt. "The Rate of Star Formation. II. The Rate of Formation of Stars of Different Mass." In: *ApJ* 137 (Apr. 1963), p. 758. DOI: 10.1086/147553.

[216] R. Schneider et al. "Dust production rate of asymptotic giant branch stars in the Magellanic Clouds". In: *MNRAS* 442 (Aug. 2014), pp. 1440–1450. DOI: 10.1093/mnras/stu861. arXiv: 1404.7132.

[217] SDSS Collaboration et al. "The Thirteenth Data Release of the Sloan Digital Sky Survey: First Spectroscopic Data from the SDSS-IV Survey MApping Nearby Galaxies at Apache Point Observatory". In: *ArXiv e-prints* (Aug. 2016). arXiv: 1608.02013.

[218] I. R. Seitenzahl et al. "Three-dimensional delayed-detonation models with nucleosynthesis for Type Ia supernovae". In: *MNRAS* 429 (Feb. 2013), pp. 1156–1172. DOI: 10.1093/mnras/sts402. arXiv: 1211.3015 [astro-ph.SR].

[219] S. Shen et al. "The History of R-Process Enrichment in the Milky Way". In: *ApJ* 807, 115 (July 2015), p. 115. DOI: 10.1088/0004-637X/807/2/115. arXiv: 1407.3796.

[220] L. Siess. "Evolution of massive AGB stars". In: *Astronomy and Astrophysics* 512 (Mar. 2010), A10. ISSN: 0004-6361. DOI: 10.1051/0004-6361/200913556. URL: http://www.aanda.org/10.1051/0004-6361/200913556.

[221] L. Siess. "Evolution of massive AGB stars. II. model properties at non-solar metallicity and the fate of Super-AGB stars". In: *Astronomy and Astrophysics* 476 (Dec. 2007), pp. 893–909. DOI: 10.1051/0004-6361:20078132.

[222] C. Sneden et al. "Iron-group Abundances in the Metal-poor Main-Sequence Turnoff Star HD˜84937". In: *ApJ* 817, 53 (Jan. 2016), p. 53. DOI: 10.3847/0004-637X/817/1/53. arXiv: 1511.05985 [astro-ph.SR].

[223] M. Spite et al. "First stars VI - Abundances of C, N, O, Li, and mixing in extremely metal-poor giants. Galactic evolution of the light elements". In: *A&A* 430 (Feb. 2005), pp. 655–668. DOI: 10.1051/0004-6361:20041274.

[224] E. Spitoni et al. "Are ancient dwarf satellites the building blocks of the Galactic halo?" In: *MNRAS* 458 (May 2016), pp. 2541–2552. DOI: 10.1093/mnras/stw519. arXiv: 1603.00344.

[225] R. J. Stancliffe et al. "Three-dimensional Hydrodynamical Simulations of a Proton Ingestion Episode in a Low-metallicity Asymptotic Giant Branch Star". In: *ApJ* 742, 121 (Dec. 2011), p. 121. DOI: 10.1088/0004-637X/742/2/121. arXiv: 1109.1289 [astro-ph.SR].

[226] M. Steinmetz and E. Mueller. "The formation of disk galaxies in a cosmological context: Populations, metallicities and metallicity gradients". In: *A&A* 281 (Jan. 1994), pp. L97–L100. eprint: astro-ph/9312010.

[227] O. Straniero, S. Cristallo, and L. Piersanti. "Heavy Elements in Globular Clusters: The Role of Asymptotic Giant Branch Stars". In: *ApJ* 785, 77 (Apr. 2014), p. 77. DOI: 10.1088/0004-637X/785/1/77. arXiv: 1403.0819.

[228] O. Straniero et al. In: *ApJ* 440 (1995), p. L85.

[229] T. Sukhbold and S. E. Woosley. "The Compactness of Presupernova Stellar Cores". In: *ApJ* 783, 10 (Mar. 2014), p. 10. DOI: 10.1088/0004-637X/783/1/10. arXiv: 1311.6546 [astro-ph.SR].

[230] F.-K. Thielemann, M. Arnould, and W. Hillebrandt. "Meteoritic anomalies and explosive neutron processing of helium-burning shells". In: *Astronomy and Astrophysics* 74 (Apr. 1979), pp. 175–185.

[231] F.-K. Thielemann, K. Nomoto, and K. Yokoi. "Explosive nucleosynthesis in carbon deflagration models of Type I supernovae". In: *Astronomy and Astrophysics* 158 (Apr. 1986), pp. 17–33.

[232] F.-K. Thielemann et al. "Massive Stars and Their Supernovae". In: *Lecture Notes in Physics, Berlin Springer Verlag*. Ed. by R. Diehl, D. H. Hartmann, and N. Prantzos. Vol. 812. Lecture Notes in Physics, Berlin Springer Verlag. 2011, pp. 153–232. arXiv: 1008.2144 [astro-ph.HE].

[233] F.-K. Thielemann et al. "Supernova Nucleosynthesis and Galactic Evolution". In: *From Twilight to Highlight: The Physics of Supernovae*. Ed. by W. Hillebrandt and B. Leibundgut. 2003, p. 331. DOI: 10.1007/10828549_46.

[234] F.-K. Thielemann et al. "What are the astrophysical sites for the r-process and the production of heavy elements?" In: *Progress in Particle and Nuclear Physics* 66 (Apr. 2011), pp. 346–353. DOI: 10.1016/j.ppnp.2011.01.032.

[235] F. X. Timmes, S. E. Woosley, and T. A. Weaver. "Galacti chemical evolution: Hygrogen through zinc". In: *APJS* 98 (June 1995), pp. 617–658. URL: http://adsabs.harvard.edu/cgi-bin/nph-bib_query?bibcode=1995ApJS...98..617T&db_key=AST.

[236] B. M. Tinsley. "Evolution of the Stars and Gas in Galaxies". In: *Fund. Cosmic Phys.* 5 (1980), pp. 287–388.

[237] N. Tominaga. "Aspherical Properties of Hydrodynamics and Nucleosynthesis in Jet-Induced Supernovae". In: *ApJ* 690 (Jan. 2009), pp. 526–536. DOI: 10.1088/0004-637X/690/1/526. arXiv: 0711.4815.

[238] M. Tosi. "AGB Stars and the Chemical Evolution of Galaxies". In: *Why Galaxies Care About AGB Stars: Their Importance as Actors and Probes*. Ed. by F. Kerschbaum, C. Charbonnel, & R. F. Wing. Vol. 378. Astronomical Society of the Pacific Conference Series. Nov. 2007, p. 353. eprint: arXiv:astro-ph/0701062.

[239] J. W. Truran and W. D. Arnett. "Explosive Nucleosynthesis and the Composition of Metal-Poor Stars". In: *Ap&SS* 11 (June 1971), pp. 430–442. DOI: 10.1007/BF00649636.

[240] C. Tur, A. Heger, and S. M. Austin. "On the Sensitivity of Massive Star Nucleosynthesis and Evolution to Solar Abundances and to Uncertainties in Helium-Burning Reaction Rates". In: *ApJ* 671 (Dec. 2007), pp. 821–827. DOI: 10.1086/523095. arXiv: 0705.4404.

[241] M. Ugliano et al. "Progenitor-explosion Connection and Remnant Birth Masses for Neutrino-driven Supernovae of Iron-core Progenitors". In: *ApJ* 757, 69 (Sept. 2012), p. 69. DOI: 10.1088/0004-637X/757/1/69. arXiv: 1205.3657 [astro-ph.SR].

[242] H. Umeda and K. Nomoto. "Variations in the Abundance Pattern of Extremely Metal-Poor Stars and Nucleosynthesis in Population III Supernovae". In: *ApJ* 619 (Jan. 2005), pp. 427–445. DOI: 10.1086/426097. eprint: arXiv:astro-ph/0308029.

[243] L. B. van den Hoek and M. A. T. Groenewegen. "VizieR Online Data Catalog: Yields of intermediate mass stars (van den Hoek+ 1997)". In: *VizieR Online Data Catalog* 412 (Oct. 1996), p. 30305.

[244] J. T. van Loon et al. "An empirical formula for the mass-loss rates of dust-enshrouded red supergiants and oxygen-rich Asymptotic Giant Branch stars". In: *A&A* 438 (July 2005), pp. 273–289. DOI: 10.1051/0004-6361:20042555. eprint: astro-ph/0504379.

[245] D. A. VandenBerg and P. B. Stetson. "On the Old Open Clusters M67 and NGC 188: Convective Core Overshooting, Color-Temperature Relations, Distances, and Ages". In: *PASP* 116 (Nov. 2004), pp. 997–1011. DOI: 10.1086/426340.

[246] E. Vassiliadis and P.R. Wood. In: *ApJ* 413 (1993), p. 641.

[247] K. A. Venn et al. "Nucleosynthesis and the Inhomogeneous Chemical Evolution of the Carina Dwarf Galaxy". In: *ApJ* 751, 102 (June 2012), p. 102. DOI: 10.1088/0004-637X/751/2/102. arXiv: 1204.0787.

[248] P. Ventura and F. D'Antona. "Hot bottom burning in the envelope of super asymptotic giant branch stars". In: *Monthly Notices of the Royal Astronomical Society* 410 (Feb. 2011), pp. 2760–2766. DOI: 10.1111/j.1365-2966.2010.17651.x.

[249] P. Ventura et al. "The Large Magellanic Cloud as a laboratory for hot bottom burning in massive asymptotic giant branch stars". In: *MNRAS* 450 (July 2015), pp. 3181–3190. DOI: 10.1093/mnras/stv918. arXiv: 1504.06098 [astro-ph.SR].

[250] P. Ventura et al. "Yields of AGB and SAGB models with chemistry of low- and high-metallicity globular clusters". In: *Monthly Notices of the Royal Astronomical Society* 431.4 (Apr. 2013), pp. 3642–3653. ISSN: 0035-8711. DOI: 10.1093/mnras/stt444. URL: http://mnras.oxfordjournals.org/cgi/doi/10.1093/mnras/stt444.

[251] J. S. Vink, A. de Koter, and H. J. G. L. M. Lamers. "Mass-loss predictions for O and B stars as a function of metallicity". In: *Astronomy and Astrophysics* 369 (Apr. 2001), pp. 574–588. DOI: 10.1051/0004-6361:20010127. eprint: astro-ph/0101509.

[252] M. Vogelsberger et al. "A model for cosmological simulations of galaxy formation physics". In: *MNRAS* 436 (Dec. 2013), pp. 3031–3067. DOI: 10.1093/mnras/stt1789. arXiv: 1305.2913.

[253] M. Vogelsberger et al. "Introducing the Illustris Project: simulating the coevolution of dark and visible matter in the Universe". In: *MNRAS* 444 (Oct. 2014), pp. 1518–1547. DOI: 10.1093/mnras/stu1536. arXiv: 1405.2921.

[254] T. P. Walker et al. "Primordial nucleosynthesis redux". In: *ApJ* 376 (July 1991), pp. 51–69.

[255] a. Weiss and J. W. Ferguson. "New asymptotic giant branch models for a range of metallicities". In: *Astronomy and Astrophysics* 508.3 (Dec. 2009), pp. 1343–1358. ISSN: 0004-6361. DOI: 10.1051/0004-6361/200912043. URL: http://www.aanda.org/10.1051/0004-6361/200912043.

[256] K. Werner and F. Herwig. "The Elemental Abundances in Bare Planetary Nebula Central Stars and the Shell Burning in AGB Stars". In: *PASP* 118 (Feb. 2006), pp. 183–204. DOI: 10.1086/500443.

[257] Robert P. C. Wiersma et al. "Chemical enrichment in cosmological, smoothed particle hydrodynamics simulations". In: *Monthly Notices of the Royal Astronomical Society* 399.2 (Oct. 2009), pp. 574–600. ISSN: 00358711. DOI: 10.1111/j.1365-2966.2009.15331.x. URL: http://mnras.oxfordjournals.org/cgi/doi/10.1111/j.1365-2966.2009.15331.x.

[258] L. A. Willson. "Mass Loss From Cool Stars: Impact on the Evolution of Stars and Stellar Populations". In: *ARAA* 38 (2000), pp. 573–611. DOI: 10.1146/annurev.astro.38.1.573.

[259] L. A. Willson. "What Do We Really Know about Mass Loss on the AGB?" In: *Why Galaxies Care About AGB Stars: Their Importance as Actors and Probes*. Ed. by F. Kerschbaum, C. Charbonnel, and R. F. Wing. Vol. 378. Astronomical Society of the Pacific Conference Series. Nov. 2007, p. 211. arXiv: 0704.3589.

[260] J. C. Wilson et al. "The Apache Point Observatory Galactic Evolution Experiment (APOGEE) high-resolution near-infrared multi-object fiber spectrograph". In: *Ground-based and Airborne Instrumentation for Astronomy III*. Vol. 7735. Proceedings of the SPIE. July 2010, p. 77351C. DOI: 10.1117/12.856708.

[261] P. R. Woodward, F. Herwig, and P.-H. Lin. "Hydrodynamic Simulations of H Entrainment at the Top of He-shell Flash Convection". In: *ApJ* 798, 49 (Jan. 2015), p. 49. DOI: 10.1088/0004-637X/798/1/49.

[262] S. E. Woosley, W. D. Arnett, and D. D. Clayton. "The Explosive Burning of Oxygen and Silicon". In: *ApJS* 26 (Nov. 1973), p. 231. DOI: 10.1086/190282.

[263] S. E. Woosley, A. Heger, and T. A. Weaver. "The evolution and explosion of massive stars". In: *Rev. Mod. Phys.* 74.4 (2002), p. 1015.

[264] S. E. Woosley and R. D. Hoffman. "The alpha-process and the r-process". In: *ApJ* 395 (Aug. 1992), pp. 202–239. DOI: 10.1086/171644.

[265] S. E. Woosley and W. M. Howard. "The p-process in supernovae". In: *ApJs* 36 (Feb. 1978), pp. 285–304. DOI: 10.1086/190501.

[266] S. E. Woosley and T. A. Weaver. "The Evolution and Explosion of Massive Stars. II. Explosive Hydrodynamics and Nucleosynthesis". In: *APJS* 101 (Nov. 1995), pp. 181+.

[267] R. M. Yates et al. "Modelling element abundances in semi-analytic models of galaxy formation". In: *MNRAS* 435 (Nov. 2013), pp. 3500–3520. DOI: 10.1093/mnras/stt1542. arXiv: 1305.7231.

[268] P. A. Young et al. "Finding Tracers for Supernova Produced ^{26}Al". In: *ApJ* 699 (July 2009), pp. 938–947. DOI: 10.1088/0004-637X/699/2/938.

[269] L. R. Yungelson. "Population synthesis For low and intermediate mass binaries". In: *Interacting Binaries: Accretion, Evolution, and Outcomes*. Ed. by L. Burderi et al. Vol. 797. American Institute of Physics Conference Series. Oct. 2005, pp. 1–10. DOI: 10.1063/1.2130209. eprint: astro-ph/0412635.